Two-Dimensional Materials for Nanoelectronic and Optoelectronic Applications

Hao Xu

A thesis submitted to UCL for the degree of

Doctor of Philosophy (PhD)

Department of Electronic and Electrical Engineering

UCL

March 2019

Statement of originality

I, Hao Xu, confirm that the work presented in this thesis is my own. Where information has been derived from other sources, I confirm that this has been indicated in the thesis.

Signed:

_____

Date:

_____

To Fang, Shuhan and My Parents,

*My Dear **VIP**s.*

Abstract

Date back to 2004, atomically thin graphene nanosheets were initially discovered with an innovative mechanical exfoliation method, and the research focused on two-dimensional (2D) materials has been triggered thoroughly since the Nobel Prize in Physics was awarded for the ground-breaking work regarding 2D graphene in 2010. Until now, almost one decade has elapsed and witnessed the fast development of 2D family and its expansion. In this PhD research project, the primary effort has been devoted to synthesising, characterising novel 2D materials, uncovering their nature properties and fabricating them for nanoelectronic and optoelectronic applications. The detailed key findings are listed below.

Few-layer black phosphorene quantum dots (BPQDs) were grown directly on Si substrates using the molecular beam epitaxy technique. Detailed experiments were carried out to evidence the formation of BPQDs and the results show that BPQDs follow the Frank-van der Merwe growth mode and the favoured few-layer growth trend with pyramid configuration.

Self-powered phototransistors enabled by spatially bandgap-graded $MoS_{2(1-x)}Se_{2x}$ homojunctions were achieved. The graded bandgaps, induced by the spatial Se-composition and thickness grading in plane, were varied from 1.83 eV to 1.73 eV, forming a homojunction with a built-in electric field. Consequently, a strong and sensitive photovoltaic effect controlled by gate voltage was demonstrated, enabling the homojunction phototransistors to deliver a photoresponsivity of 500 mA/W under the self-powered working mode.

By utilising the self-oxidised edge domains that inevitably formed in air, back-gated field-effect transistors (FETs) on SiO_2/Si substrates enabled by long-term air-exposed bilayer WSe_2 were fabricated and studied. Detailed material characterisations proved the formation of WO_x/WSe_2 heterojunctions around edges of WSe_2. With air-induced WO_x passivating dangling bonds at edges of WSe_2, the FETs possessed ohmic contact from 77 K to 300 K, high conductivity up to ~ 2600 S/m and ultra-low leakage gate current as small as ~ 10^{-12} A.

Few-layer MoS_2/glassy-graphene heterostructures on quartz were prepared, followed by the detailed material characterisations. Transparent photodetectors enabled by these novel

van der Waals heterostructures were excited by monochromatic lasers for probing their photoresponsive features, respectively. Notably, the interface between MoS_2 and glassy-graphene is ohmic contact, differing from the previously reported Schottky junction between MoS_2 and graphene. The highest specific detectivity of 1.8×10^{10} Jones and the best photoresponsivity of 12.3 mA/W were achieved.

Impact Statement

This PhD research project is concentrated on synthesis and material characterisations of two-dimensional (2D) materials for nanoelectronic and optoelectronic applications, which achieves 3 invited oral talks and 1 invited poster presentation in the international conferences. In addition, my PhD project yields 7 research papers published in the academic journals with global influence and high impact factor (IF), including *Advanced Materials* (IF 25.81), *Journal of the American Chemical Society* (IF 14.70), *etc*.

Regarding the work in chapter 3, few-layer black phosphorene quantum dots (BPQDs) were grown directly on Si substrates by molecular beam epitaxy. The results show that BPQDs follow the Frank-van der Merwe growth mode and the favoured few-layer growth trend with pyramid configuration. The realisation of BPQDs by epitaxy enables the synthesis of inch-sized low-dimensional black phosphorus with high purity and crystallinity, particularly promising for nanoelectronics and optoelectronics.

In terms of the work in chapter 4, until now, scientists around the world trying to develop well-controlled homo-/heterostructures still face some important issues. Here the choice of bandgap-graded 2D $MoS_{2(1-x)}Se_{2x}$ homojunction appears very promising as an building block for next generation 2D electronics or optoelectronics. In this work, bandgap-graded 2D $MoS_{2(1-x)}Se_{2x}$ homojunctions were prepared by a cost-effective chemical solution deposition method. The work combines numbers of structural, electronic and optical tools to show that: (i) high quality 2D $MoS_{2(1-x)}Se_{2x}$ homojunctions can be synthesised without any evidence of chemical disorders. (ii) This simple homojunction shows p-n junction-like properties. (iii) Devices fabricated from these homojunctions present remarkable tunability. On this basis, the 2D $MoS_{2(1-x)}Se_{2x}$ phototransistors are studied, and a high photoconductive gain, high detectivity, and self-powered operating mode are obtained, showing the advantages provided by the unique structure.

As for the work in chapter 5, to meet the demands of wearable devices, flexible electronics (FE) have attracted ever increasing attentions. Atomically thin transition metal dichalcogenides (TMDs) with tunable bandgaps provide potential solutions to integrated FE. Selenium based TMDs with relatively higher valence and conduction band edges compared with sulfur-based ones can be utilised for prospective applications in nanoelectronic and optoelectronic fields. However, they are sensitive to ambient

conditions and air-induced oxidation is inevitable. In this work, the self-assembled oxidised edge domains (WO_x) that inevitably formed in ambient conditions were strategically utilized and a series of back-gated field-effect transistors (FETs) were fabricated, which outperformed the pristine WSe_2 FETs. This work demonstrated a strategy overturning the disadvantage, inevitable edge oxidation, into an advantage, namely the nearly 3 times enhanced conductivity and ohmic contact FETs. It also opened new opportunities on the edge-engineering of 2D materials for various devices.

With respect to the work in chapter 6, transparent electronics and optoelectronics have attracted significant attention for their use in wearable electronics, flexible displays, and touch panels. Typically, large area graphene and metal (Ag, Cu) nanowire networks/grids have been considered as candidates for transparent devices. However, the gapless graphene and Schottky junction between graphene and other materials have limited its applications. Here, a unique few-layer MoS_2/glassy-graphene heterostructure was achieved, prepared by a facile layer-by-layer transfer technique. This work demonstrated ohmic contact formed at the interface between the MoS_2 and the glassy-graphene nanosheets and a high detectivity of 1.8×10^{10} Jones.

Acknowledgements

In the first place, I would like to sincerely thank my supervisor, Prof. Dr. Huiyun Liu. Clearly memorised, it was on 22nd January 2015 that Prof. Liu sent me the PhD admission offer. Since 28th September 2015, his advice, guidance and knowledge have been always the original power for advancing and boosting my research work. Undoubtedly, none of the achievement in my PhD career would have come true without his supervision and full support.

Secondly, I would like to thank my second supervisor, Prof. Dr. Jiang Wu, who provided me with much technical support and brilliant research ideas. Thirdly, I would like to thank my close collaborators, Prof. Dr. Zhengxiao Guo and Dr. Xiaoyu Han, who assisted my work a lot and upgraded my academic skills. Fourthly, I would like to acknowledge China Scholarship Council (CSC) and UCL student funding office that awarded me with UCL-CSC Joint Scholarship and support my whole PhD career in finance.

Also, I would like to show my gratitude to all the former and current members of the MBE Research Group: Dr. Siming Chen, Dr. Yunyan Zhang, Dr. Dongyoung Kim, Dr. Arthur Onno, Dr. Qi Jiang, Dr. Phu-Minh Lam, Dr. Mingchu Tang, Dr. Pamela Jurczak, Dr. João Valente, Dr. Xuezhe Yu, Kevin Lee, Xiao Li, Kai Shen, Fan Cui, Zizhuo Liu, Shun Chan, Ying Lu, Mengya Liao, Daqian Guo and Haotian Zeng. They provided me with decent advice and cooperation.

Additionally, I would like to show my gratitude to all the members of 2015 UCL-CSC Joint Scholarship Group: Qiushi Wu, Teng Dong, Zhicheng Liu, Jianxiong Zhao, Xiuyun Jiang, Xiangyu Zhang, Fang Xie, Yifei Bian, *et al*. Counting in Wei Liu, they are my precious friendship to enrich my research life that sometimes is struggling.

Finally, I would like to express my deepest and warmest thanks to my family, including my wife and daughter, my parents and in-laws, and my sister's family. Obviously and definitely, it was/is/will be always the persistent support, understanding, trust and care from my dear family that make all these realised and to be continued.

Table of Contents

List of Figures

List of Journal Publications and Conference Presentations

❖ Journal Publications

Corresponding author

1. **Hao Xu**, Xiaoyu Han, Xiao Dai, Wei Liu, Jiang Wu, Juntong Zhu, Dongyoung Kim, Guifu Zou, Kimberley A. Sablon, Andrei Sergeev, Zhengxiao Guo, Huiyun Liu, High Detectivity and Transparent Few-Layer MoS_2/Glassy-Graphene Heterostructure Photodetectors, ***Advanced Materials***, **30** (2018) 1706561.
   Impact factor: **25.81**, JCR Rank Q1

2. Juntong Zhu, **Hao Xu** (***shared 1st author***), Wan Zhang, Guifu Zou, Yushu Tang, Ruiqing Chai, Guozhen Shen, Jiang Wu, Jinho Choi1, Huiyun Liu, Jianyu Huang, Hongyou Fan, MoS_2-OH bilayer mediated substrate-independent growth of inch-sized monolayer MoS_2, ***Journal of the American Chemical Society***, **141** (2019) 5392-5401.
   Impact factor: **14.70**, JCR Rank Q1

3. Kai Shen, Xiao Li, **Hao Xu***, Mingqing Wang, Xiao Dai, Jian Guo, Ting Zhang, Shibin Li, Guifu Zou, Kwang-Leong Choy, Ivan P. Parkin, Zhengxiao Guo, Huiyun Liu, Jiang Wu, Enhanced performance of ZnO nanoparticles decorated all-inorganic $CsPbBr_3$ quantum dot photodetectors, 9.93(2019) ***Journal of Materials Chemistry A***, **7** (2019) 6134-6142.
   Impact factor: **10.73**, JCR Rank Q1

4. **Hao Xu***, Xiaoyu Han, Zhuangnan Li, Wei Liu, Xiao Li, Jiang Wu, Kimberley A. Sablon, Zhengxiao Guo, Huiyun Liu, Epitaxial growth of black phosphorus quantum dots directly on Si substrates, ***Advanced Materials Interfaces***, **5** (2018) 1801048.
   Impact factor: **4.71**, JCR Rank Q1

5. **Hao Xu***, Juntong Zhu, Guifu Zou, Wei Liu, Xiao Li, Gyeong Hee Ryu, Wenshuo

Xu, Xiaoyu Han, Zhengxiao Guo, Jamie H. Warner, Jiang Wu, Huiyun Liu, Self-powered Phototransistors Based On Spatially Composition-Graded Two-Dimensional $MoS_{2(1-x)}Se_{2x}$ Homojunctions, (2019) *in submission*.

6. **Hao Xu***, Xiaoyu Han, Wei Liu, Hehai Fang, Ping Liu, Xiao Li, Zhuangnan Li, Jian Guo, Fan Cui, Bing Xiang, Weida Hu, Ivan P. Parkin, Zhengxiao Guo, Jiang Wu, Huiyun Liu, Self-Passivated Bilayer WSe_2 For Field-Effect Transistors, (2019) *in submission*.

7. Xiao Li, **Hao Xu***(***shared 1st author***), Kai Shen, Xiao Dai, Jian Guo, Guifu Zou, Kwang-Leong Choy, Ivan P. Parkin, Zhengxiao Guo, Huiyun Liu, Jiang Wu, Highly conductive and transparent chemical sensors enabled by large-scale glassy-graphene thin films, (2019) *in submission*.

❖ Conference Presentations

Including 3 invited talks.

1. **Hao Xu**, Xiaoyu Han, Xiao Dai, Wei Liu, Kimberley A. Sablon, Jiang Wu, Dongyoung Kim, Juntong Zhu, Zhengxiao Guo, Guifu Zou, Huiyun Liu, "Large-Scale 2D Glassy-Graphene Thin Films for Transparent Photodetectors and Chemical Sensor Arrays", *2019 International Forum on Graphene in Shenzhen*, China (**oral talk**).

2. **Hao Xu**, Xiaoyu Han, Xiao Dai, Wei Liu, Kimberley A. Sablon, Jiang Wu, Dongyoung Kim, Juntong Zhu, Zhengxiao Guo, Guifu Zou, Huiyun Liu, "Novel MoS_2/glassy-graphene heterostructures for photoresponsive devices", *Smart NanoMaterials 2018 Conference*, Paris, France (**invited talk**).

3. **Hao Xu**, Juntong Zhu, Xiaoyu Han, Wei Liu, Kimberley A. Sablon, Guifu Zou, Zhengxiao Guo, Jiang Wu, Huiyun Liu, Bandgap-Graded $MoS_{2(1-x)}Se_{2x}$ Nanosheets for High-Performance and Self-Powered Phototransistors, *the 3rd Graphene & emerging 2D materials for Photonics Applications Conference*, 2018, Coventry, UK (**invited talk**).

4. **Hao Xu**, Xiaoyu Han, Xiao Dai, Wei Liu, Guifu Zou, Zhengxiao Guo, Kimberley A. Sablon, Jiang Wu, Huiyun Liu, High Detectivity and Transparent Photodetectors Enabled by Novel Atomically Thin Heterostructures, *The first Cambridge One Belt One Road Initiative International Conference*, 2018, Cambridge, UK (**invited talk**).

5. **Hao Xu**, Xiaoyu Han, Xiao Dai, Wei Liu, Kimberley A. Sablon, Jiang Wu, Dongyoung Kim, Juntong Zhu, Zhengxiao Guo, Guifu Zou, Huiyun Liu, "Novel MoS_2/glassy-graphene heterostructures for photoresponsive devices", *TMD-UK **2018** International Conference*, University of Sheffield, UK (**poster**).

6. **Hao Xu**, Xiaoyu Han, Xiao Dai, Wei Liu, Kimberley A. Sablon, Jiang Wu, Dongyoung Kim, Juntong Zhu, Zhengxiao Guo, Guifu Zou, Huiyun Liu, "Novel MoS_2/glassy-graphene heterostructures for photoresponsive devices", *2018*

International Forum on Graphene in Shenzhen, China (**oral talk**).

7. **Hao Xu**, Xiaoyu Han, Xiao Dai, Wei Liu, Jiang Wu, Juntong Zhu, Dongyoung Kim, Guifu Zou, Kimberley A. Sablon, Andrei Sergeev, Zhengxiao Guo, Huiyun Liu, High Detectivity and Transparent Few-Layer MoS_2/Glassy-Graphene Heterostructure Photodetectors, *UK-China 2D materials conference*, Jan **2018**, National Graphene Institute, the University of Manchester, UK (**invited poster**).

8. **Hao Xu**, Wei Liu, Xiaoyu Han, Jiang Wu, Dongyoung Kim, Xiao Dai, Juntong Zhu, Zhengxiao Guo, Guifu Zou, Huiyun Liu, "Novel MoS_2/glassy-graphene heterostructures for photoresponsive devices", *TMD-UK **2017** International Conference*, University of Sheffield, UK (**poster**).

9. **Hao Xu**, Wei Liu, Jiang Wu, Sanjeev Kumar, Xiao Dai, Juntong Zhu, Guifu Zou, Huiyun Liu, "Electrical characteristic of nanosheet MoS_2/glassy-graphene heterostructures", *Semiconductor and Integrated OptoElectronics Conference* **2017**, Cardiff University, UK (**oral talk**).

Chapter 1 Introduction

1.1 History and basics of graphene and its analogue: glassy-graphene

The first discovery of graphene by Andre Geim and Konstantin Novoselov using a mechanical exfoliation method in 2004, which led to the 2010 Nobel Prize in Physics, has completely triggered the research focused on 2D materials worldwide.[1] As a result, the number of academic publications involved graphene, including synthesis, characterisations, fabrication, practical applications, *etc*., has increased exponentially since then. The enormous interest in graphene has accelerated the development of graphene commercialisation and expanded graphene- and graphene-related-based product market as well,[2] for instance, tennis racket by Head, phone touch screen and transparent electrodes by Samsung,[3] *etc*. Such a popularity has been perceived in not only academic research at the labs but also application patents associated with industrial markets, as shown in Figure 1.1.[2] From the inset, it can be seen obviously that the number of patents on graphene has increased significantly in the past decade.

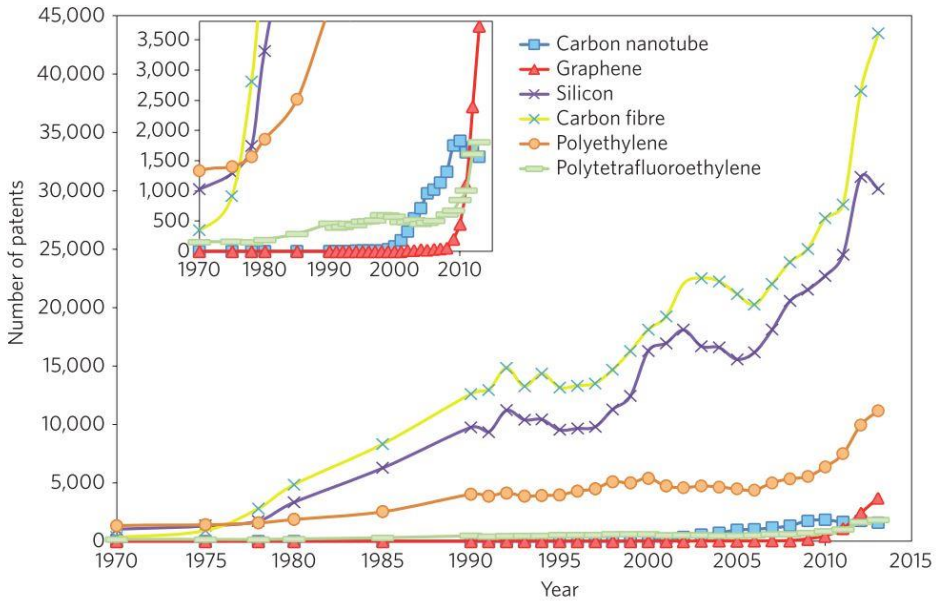

Figure 1.1 Number of patents for different materials from 1970. The inset shows a zoom-in view for carbon-related materials. The patent number of graphene has increased exponentially in the past decade. The image was from Ref. 2.

This famous 2D material originated from a conventional carbon-based material family. Graphene, composed of a flat monolayer of carbon atoms packed into a 2D honey comb lattice, was derived from well-known graphite and a 2D form of graphite. In terms of this family relationship, graphene has been studied for nearly seventy years since the early published paper about the band theory of graphite.[4,5] In the past, the research on materials from this family was focused on 0D fullerenes, 1D carbon nanotubes and 3D (bulk) graphite. The corresponding crystal structures of them are shown in figure 1.2.[6] As can be seen, graphene is viewed as the basic and essential component for the other three graphitic carbon materials. For instance, it can be wrapped up into 0D fullerenes, rolled up for 1D carbon nanotubes, and vertically stacked for 3D graphite.

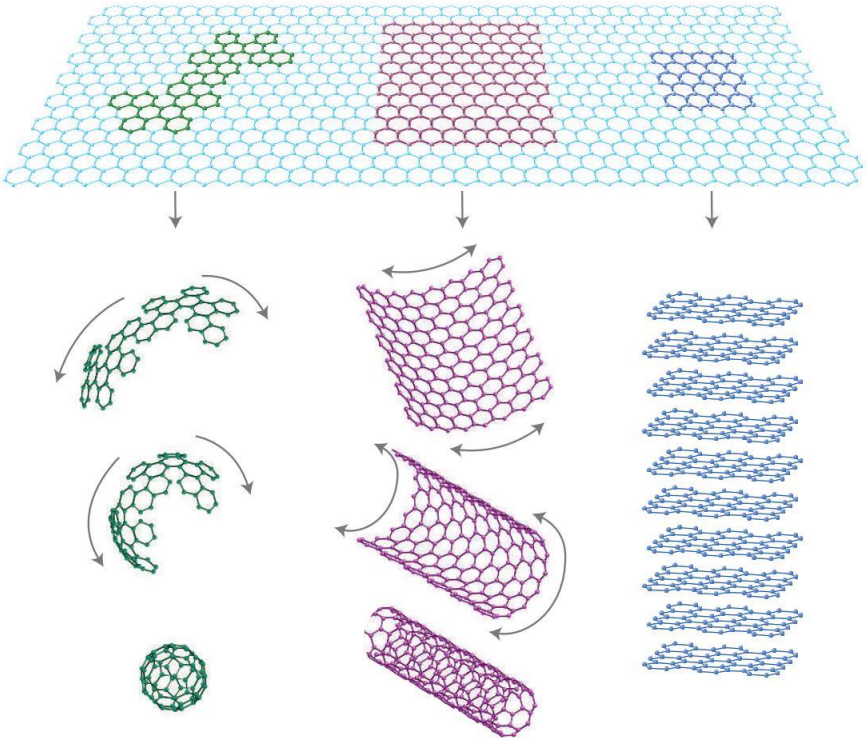

Figure 1.2 Schematic crystal structure of 2D graphene (top), 0D fullerene (bottom left), 1D carbon nanotube (bottom middle) and 3D graphite, respectively. Three different processing methods transform graphene into three forms of graphitic carbon materials. The image was from Ref. 6.

Since 2004 when pristine graphene was isolated by the mechanical exfoliation method, many other synthesis approaches have been developed to produce graphene, which aimed at growing nanosheets with less cost, higher material quality (like mobility, flexibility and thermal conductivity), larger scale, *etc*. The first introduced 'Scotch tape method',[7] which is now still widely accepted, briefly speaking, involved using the adhesive tape to peel off layered highly orientated pyrolytic graphite (HOPG), followed by depositing onto a SiO_2/Si substrate to obtain multilayer or even monolayer graphene. Besides this mechanical exfoliation method, graphene can be produced from reduction of graphene oxide (GO) by using chemical reduction as well,[8] while it showed harmful impact on the environment. Epitaxial growth using MBE under ultra-high vacuum is another option, which had high crystallinity although the cost is high.[9] Chemical vapour deposition (CVD) technique has been reported as the most popular method for growing graphene with large scale production.[10-12]

In the fields of material science and condensed matter physics, graphene is a rapidly rising star, which possesses many exceptionally intrinsic properties and thus holds great potential for next generation applications of electronics and photonics. As for its electronic properties, graphene is semi-metallic and has massless Dirac fermions as the carriers.[13] Furthermore, graphene has a high electron mobility of 2.5×10^5 $cm^2V^{-1}s^{-1}$, thermal conductivity of 3000 WmK^{-1} and optical transmittance of 97.7%.[14-16] The photonic properties of graphene are promising as well. Although graphene is atomically thin, it has broadband photoresponse and can absorb photons from the visual lights to infrared range which can be tuned by external gate voltage.[17,18] More than a decade of research centred on graphene has demonstrated that graphene is able to be employed and qualified for the applications with remarkable performance, including field effect transistors (FETs), longer-lasting batteries, solar cells, photodetectors, display panels and so on.[18-22]

In parallel with the extensive efforts devoted to graphene, the graphene-like materials have been gaining attentions as well. Graphene nanoribbons were prepared and fabricated to FETs with about 10^7 on-off ratio at room temperature.[23] Recently, a type of ultra-smooth glassy-graphene in large scale has been successfully synthesised by Zou *et al*.[24] using polymer-assisted deposition (PAD) method, and revealed to be an intermediate state between pristine graphene and amorphous glassy carbon in terms of physical and chemical properties (such as lattice structure, Raman spectra, thermal conductivity, *etc*.), inheriting intriguing properties from both of them.[1,25] Glassy-graphene has a layered structure which could contain both sp^2 and sp^3 bonds, differing from graphene only containing sp^2 in theory or glassy carbon that is amorphous.[26]

Figure 1.3 illustrates the evolution process of crystal structure from glassy carbon to glassy-graphene then to graphene. Compared with traditional glassy-carbon, glassy-graphene is better crystallised and has higher electrical conductivity and better flexibility. Compared with graphene, glassy-graphene has better chemical and thermal inertness. On the other hand, it is worth mentioning that glassy-graphene is much more cost-effective than graphene in terms of synthesis. Exhibiting good conductivity, flexibility, chemical inertness and transparency, glassy-graphene nanosheet has great perspective in the applications of future electronics.

Figure 1.3 Schematic diagrams of crystal structures of glassy-carbon (left), glassy-graphene (middle) and graphene (right), respectively. The lines in the images denote distribution of carbon atoms. The images were cited from Ref. 24.

Figure 1.4a shows the high resolution transmission electron microscopy (HR-TEM) image of amorphous glassy carbon synthesised by PAD method, from which we can clearly observe the connected carbon atom rings which were poorly ordered. Figure 1.4b shows the HR-TEM image of graphene synthesised by PAD approach as well. Apparently, the lattice structure of graphene is well oriented, showing regular honeycomb configuration. As for glassy-graphene, the HR-TEM result is displayed in figure 1.5. As can be seen, the crystal structure of glassy-graphene shows twisted lattice structure, and is much better crystallised than glassy carbon but still has disordered lattice areas.

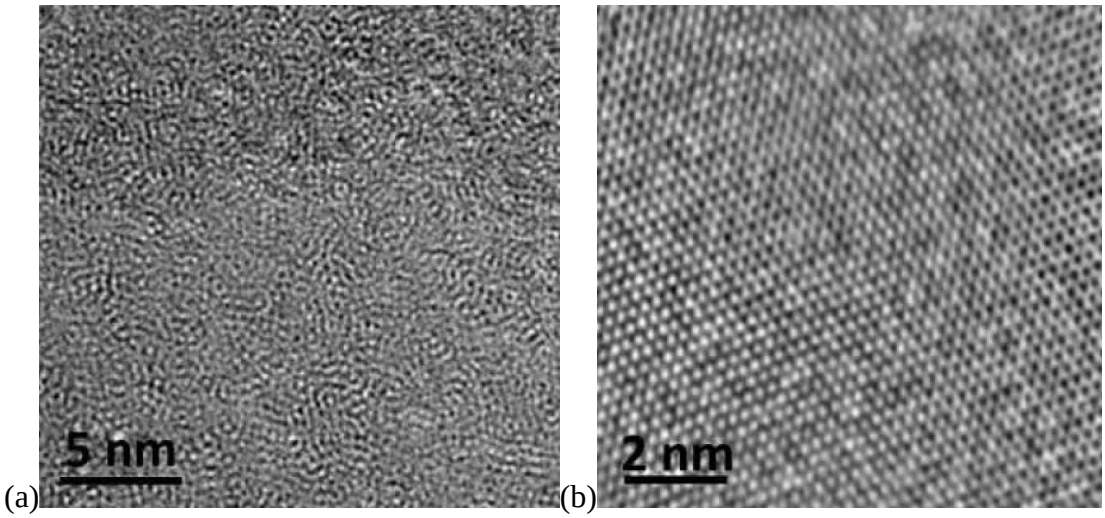

(a) (b)

Figure 1.4 HR-TEM images of amorphous glassy carbon (a) and well-crystallised graphene (b). The scales bars are labelled inside.

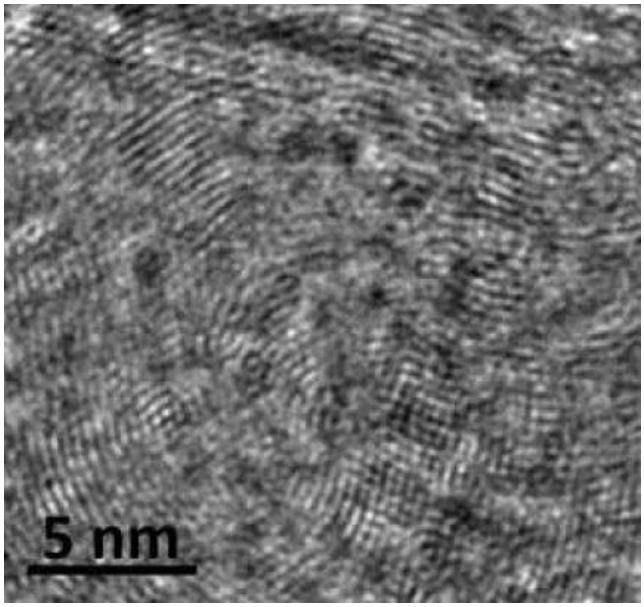

Figure 1.5 HR-TEM images of glassy-graphene. The scales bar is shown inside. This structure shows the bent and curved lattice plane, which is the most distinguished feature from graphene.

Raman spectroscopy, as a powerful and non-invasive characterisation method, was used to analyse the disorder in glassy carbon, glassy-graphene and graphene, respectively.[27-29] In pure graphene (without doping or oxidation) with perfect honeycomb lattice structure, the phonon energy shift caused by laser excitation (for instance, 532 nm) creates two main peaks in Raman spectra: peak G at 1580 cm^{-1} and peak 2D at 2690 cm^{-1}.[26] The former Raman peak is a primary in-plane vibrational mode while the latter one is a second-order overtone of a different in-plane phonon vibration. It is worth noting that the first-order peak D cannot be observed in pristine graphene due to crystal symmetries.

However, as the density of disorder in pristine graphene increases (such as in glassy carbon and glassy-graphene), the Raman intensity associated with disorder in crystal structures obviously increases: peak D at 1350 cm^{-1}, peak G at 1620 cm^{-1}, and peak D+G at 2940 cm^{-1}. At the same time, the values of FWHM and I_{2D}/I_G ratio will change as well.[29]

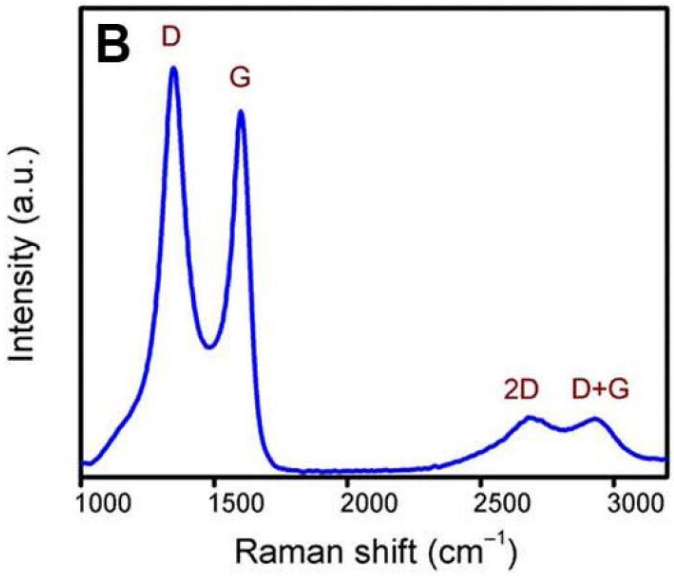

Figure 1.6 Raman spectrum of large-scale glassy carbon thin film, resolving the four Raman-active peaks. The figure was from Ref. 24.

Figure 1.6 shows the Raman spectrum of glassy carbon, in which peak D has the strongest intensity, indicating the large disordered area. Although peak 2D was detected, it was as very weak. Figure 1.7 shows the Raman spectrum of as-grown graphene. As expected, the two sharp peaks of G and 2D were both observed, indicating the well-ordered lattice structure.[30] The Raman spectrum of glassy-graphene is shown in figure 1.8. Similar to that of glassy carbon, four peaks were all observed, however, the relative peak intensity changed significantly, getting closer to that of graphene. Peak G and 2D reveals the presence of sp^2 bonds in glassy-graphene, while the relatively strong peak D still indicates disorder in glassy-graphene. Another pronounced difference is that the value of I_{2D}/I_G ratio is much larger than that of glassy carbon, revealing crystallisation of glassy-graphene compared with glassy carbon is enhanced.[26]

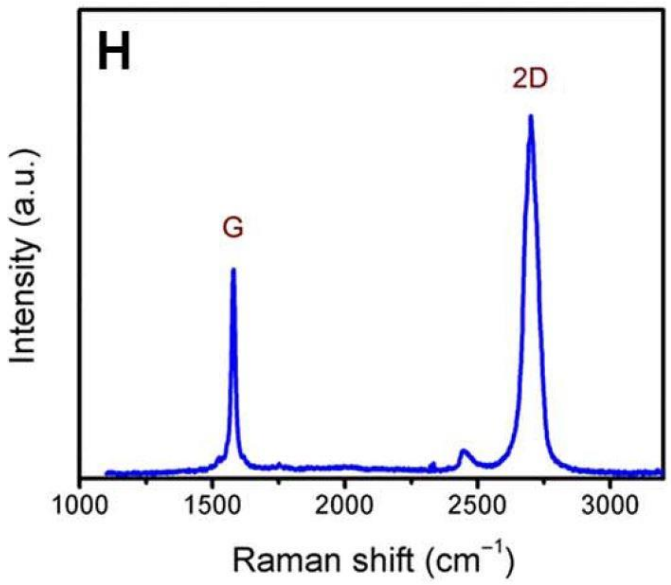

Figure 1.7 Raman spectrum of few-layer as-grown graphene thin films, resolving the two fingerprint peaks. The figure was from Ref. 24.

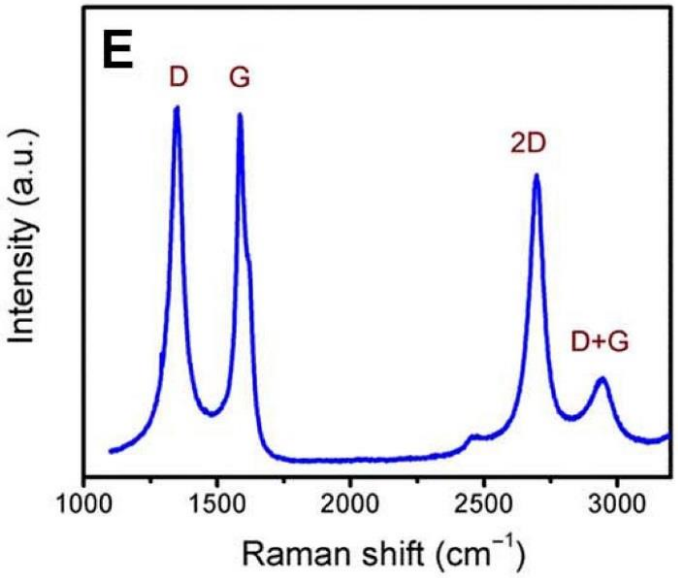

Figure 1.8 Raman spectrum of few-layer glassy-graphene thin film, resolving the four characteristic peaks. The figure was from Ref. 24.

1.2 History and basics of transition metal dichalcogenides (TMDs)

Compared with conventional 3D (bulk) materials, 2D materials possess following novel properties.[31] Firstly, as the thickness is reduced to several nanometre (or less) level, quantum confinement phenomenon in 2D materials becomes much more obvious compared with their bulk forms, which will lead to unusual electronic and optical properties.[32] Secondly, their naturally passivated surfaces make it possible and easy to create various layered 2D material-based heterojunctions that are connected with van der Waals force, without considering the issue of lattice mismatch.[33] Thirdly, these atomically thin materials can interact strongly with incident light.[34] Fourthly, as reported, 2D materials allow us to achieve smaller transistors and thus to pack more transistors on a microchip, which hold the potential to grow into silicon to extend the lifeline of Moore's law.[35] Consequently, the tremendous success of graphene inspire researchers to explore more related 2D materials.

Look beyond graphene family, transition metal dichalcogenides (TMDs) are another typical layered 2D materials. TMDs contain a diverse group of materials, whose crystal structures contain a similarly basic block consist of a transition metal atom attached to two atoms from group VI of the periodic table. Their bulk form materials have been well studied and historically used as additives to lubricants as they can decrease friction.[36,37] With the advent of graphene in 2004, they caught researchers' attention again because of their layered structures combined by van der Waals force and 2D form.[1,38,39]

1.2.1 Molybdenum disulphide (MoS_2)

MoS_2, as a member of TMDs family, is a representative 2D semiconductor, which is 0.65 nm thick for monolayer.[40] Crystal MoS_2 is composed of vertically stacked layers, each of which has hexagonal or rhombohedral symmetry. This single layer structure can be viewed as a layer of molybdenum (Mo) atoms sandwiched between two layers of Sulphur (S) atoms, as depicted in figure 1.9. Due to the weak van der Waals force between each layer of MoS_2, it can be isolated by the same 'Scotch tape method' as is done for graphene.

It was found that MoS_2 has an intrinsic direct band gap of 1.8 eV for monolayer and an indirect band gap of 1.06 eV for bulk. Owing to strong quantum confinement effect in the out-of-plane direction, the band gap changes as the thickness varies, together with a transition from direct to indirect band gap.[41] An example of MoS_2 nanosheets on SiO_2/Si substrate is displayed in Figure 1.10.

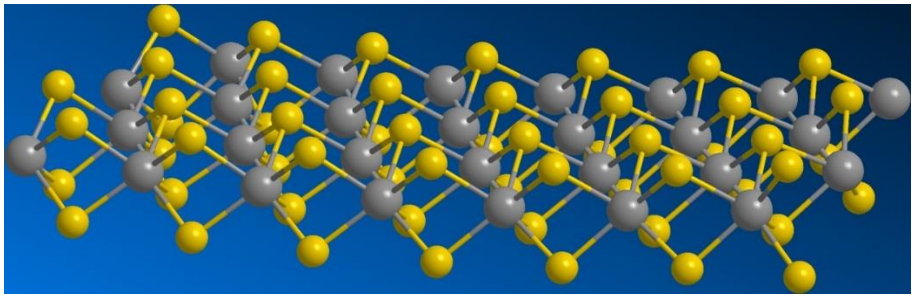

Figure 1.9 Schematic crystal structure of monolayer MoS_2. Each monolayer has a thickness of 0.65 nm and is combined with van der Waals force. The grey balls represent Mo atoms and the yellow balls represent S atoms. The monolayer form possesses a direct bandgap of 1.8 eV.

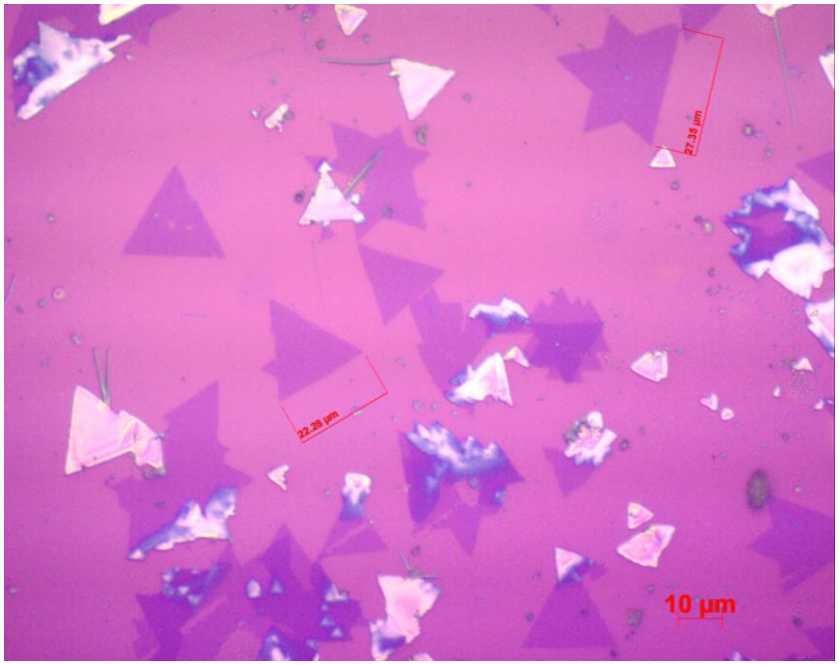

Figure 1.10 Optical microscopy image of few-layer MoS_2 nanosheets on SiO_2/Si substrate. The bright (white) domains depict multilayer MoS_2.

The intrinsic feature of band gap makes MoS_2 potential in optoelectronic applications. In particular, it is worth mentioning here that MoS_2 exhibits optical band gap in the range of 1-2 eV, which makes it suitable for visible lights and near-infrared absorption and emission. Tsai *et al*. reported that p-n junction based on n-type monolayer MoS_2 transferred onto p-type Si substrate was used to fabricate solar cells that achieved a power conversion efficiency of 5.23%.[42] Photodetectors based on few-layer MoS_2 with high broad photogain and fast optical switching behaviour was reported.[43] Besides, optoelectronic properties in devices based on MoS_2 have also been shown to be tuneable. Lee *et al*. fabricated phototransistors based on MoS_2 nanosheets with thickness-modulated optical energy gap, in which phototransistors with different thickness showed different photodetecting capabilities.[44]

With such atomically thin bodies, MoS_2 nanosheets can also be attractive for high-performance electronic devices. Recently, FETs with low-frequency noise built on bilayer MoS_2 was achieved by Xie *et al*.[45] Radisavljevic *et al*. reported that single-layer MoS_2 had mobility of at least 200 $cm^2V^{-1}s^{-1}$, which was comparable to that of graphene nanoribbon.[40] The FETs based on the single-layer MoS_2 exhibited current on/off ratios of 1×10^8 at room temperature and ultra-low standby power dissipation. Meanwhile, MoS_2 has been widely explored as a potential channel material replacement for traditional Si.[46] Remarkably, Desai *et al*. reported MoS_2 transistors with only 1 nm gate lengths using carbon nanotubes as the gate electrodes.[47] As scaling of Si based transistors is facing challenges, this achievement suggests that MoS_2 can be a potential alternative to Si.

1.2.2 Tungsten diselenide (WSe_2)

Tungsten diselenide WSe_2 is another typical member in TMDs family, which shares the same rhombohedral symmetry with crystal MoS_2 but with Mo sites substituted with W atoms and S sites replaced with Se atoms in the lattice structure. WSe_2 exhibits a direct bandgap of 1.6 eV for the monolayer form and 1.2 eV for the bulk form, and the bandgap decreases as layer number increases.[48,49] Different from pristine MoS_2, pristine WSe_2 based FETs possess p-type gate modulation features.[50] In addition, WSe_2 is sensitive to ambient conditions, so property degradation is unavoidable when exposed to air for long-term, especially at high temperature.[51] Figure 1.11 depicts few-layer WSe_2 nanosheets on SiO_2/Si substrate.

(a)

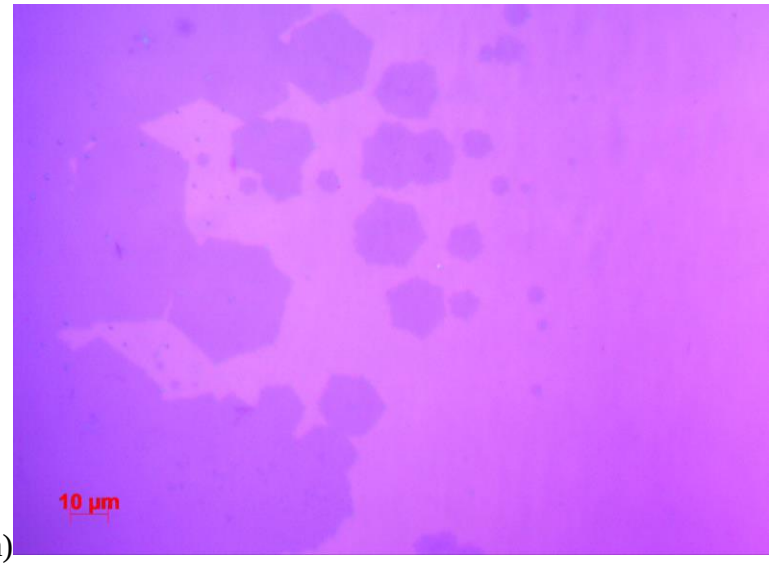

(b)

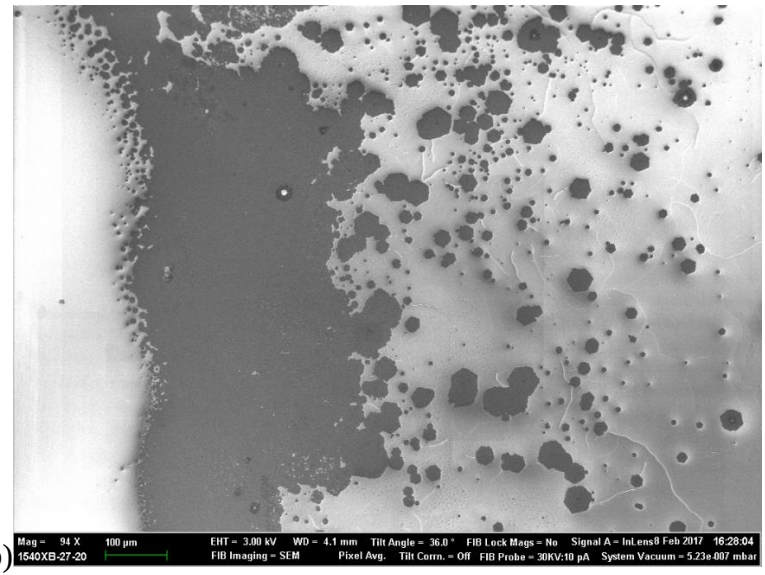

Figure 1.11 (a) Optical microscopy image and (b) SEM image of few-layer WSe_2 nanosheets on SiO_2/Si substrates grown by CVD method, as illustrated by the hexagonal or triangular domains. The scale bar is 100 µm for the SEM image.

1.2.3 Ternary TMDs

In addition to the binary TMDs presented in section 1.2.1 and 1.2.2, recently, ternary TMDs, such as $MoS_{2(1-x)}Se_{2x}$, $Mo_{1-x}W_xS_2$, $WSe_{2(1-x)}S_{2x}$, *etc*., emerge as a new class of 2D materials with artificially modulated bandgaps and resulted varied features, distinguishing them from conventional binary TMDs.[52-54] The bandgap can be

continuously tuned with gradually changed doped-element composition proportion. In-plane elemental implantation enables spatial composition gradient and thus resulted in spatial bandgap gradient. Consequently, this leads to the formation of spatial homojunctions or heterojunctions within a single 2D domain without additional processing, such as wet/dry transfer and subsequent mechanical stacking.[55] Such one-step preparation for 2D junctions possessing photovoltaic and rectifying features can simplify the future device design and fabrication enabled by 2D materials. Figure 1.12 exhibits the few-layer $MoS_{2(1-x)}Se_{2x}$ nanosheets on SiO_2/Si substrate, shaped in triangles and the shape showing no obvious difference from binary TMDs.

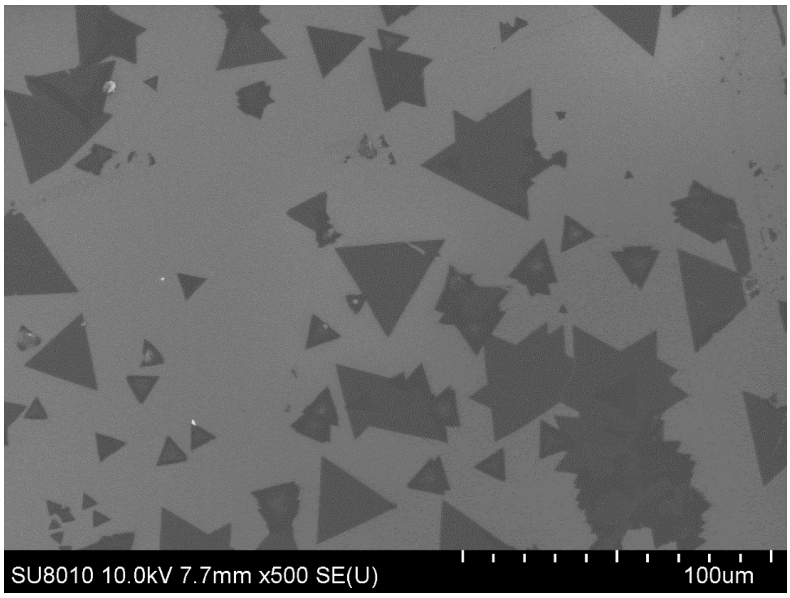

Figure 1.12 SEM image illustrating few-layer $MoS_{2(1-x)}Se_{2x}$ nanosheets on SiO_2/Si substrate.

1.3 History and basics of black phosphorene (BP)

Black phosphorus was first discovered in 1914 and is the most stable form at room temperature compared with other phosphorus allotropes (such as red, violet and white phosphorus).[56-58] Similarly, black phosphorus was restudied after the breakthrough achieved in graphene in 2004.[1] Due to its layered crystal structure and two-dimensionality, black phosphorus not only shares similar properties with graphene but also possesses novel physics features associated with natural bandgap of 0.3 eV for bulk form.[57] Black

phosphorene (BP), referred as monolayer or few-layer of black phosphorus, was first prepared and studied by experimental methods in 2014 by Liu *et al*, opening up a new page of an unexplored 2D material which used to be familiar to researchers for its bulk form.[59]

BP, with thickness of 0.85 nm for single layer, has a layered structure which is held together by weak van der Waals force, indicating that mechanical exfoliation method is available for isolation of BP.[60] Differing from bulk black phosphorus that forms with several crystalline structures, BP is crystallised in orthorhombic lattice, as depicted in figure 1.13, whose lattice parameters a and b equal to 4.62 Å and 3.35 Å, respectively.[59,61] Each phosphorus atom is covalently bonded with three adjacent atoms to form a puckered honeycomb configuration, unlike flat honeycomb structure of graphene.

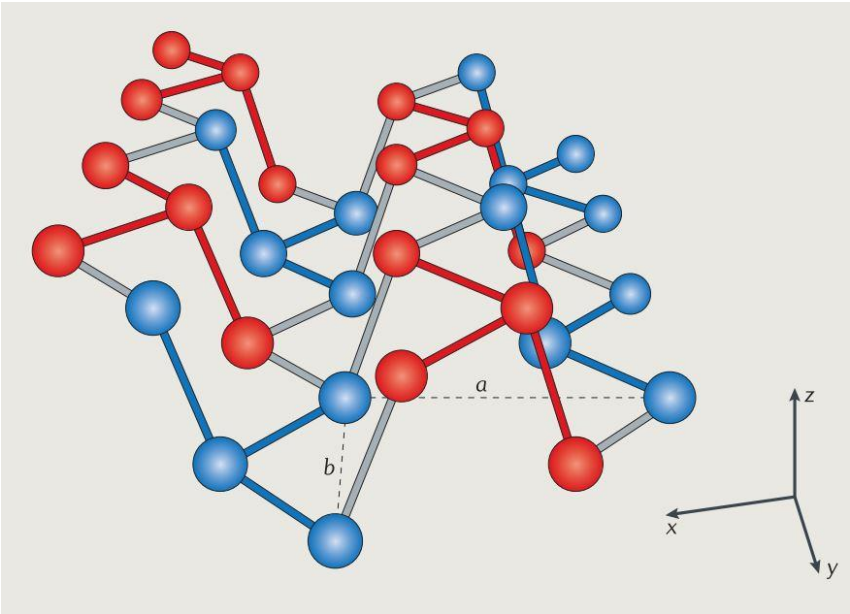

Figure 1.13 Schematic crystal structure of monolayer BP that crystallised in orthorhombic lattice structure. The image was from Ref. 61.

2D materials (such as graphene, MoS_2, *etc*.) have a variety of bottom-up synthesis methods (including MBE, CVD, *etc*.), however, as for growth of BP, especially for large-scale growth, it is challenging and undeveloped, which is mainly due to the complicated chemistry features of phosphorus. Only a few papers have reported BP growth using bottom-up method. Currently reported synthesis methods were mainly based on phase

transition principle (from red phosphorus to black phosphorus) under high-pressure condition.[62,63] Mechanical exfoliation method, as an up-bottom preparation method, is widely used to obtain BP nanosheets. The conventional exfoliation approach was optimised by a modification that employed a silicon-based transfer layer to acquire higher yield of atomically thin nanosheets.[64]

Theoretical calculation results show that BP is a 2D semiconductor with a band gap of 0.3 eV for bulk and 2.0 eV for monolayer.[65] Distinguished from 2D TMDs, the direct band gap exists in BP with any number of layers. This unique band structure independently from thickness allows for few-layer or multi-layer BP based devices have specific performance as monolayer BP device do. BP is the second elemental 2D material after presence of graphene and of particular interest for electronic and optoelectronic applications. It has been demonstrated that BP based devices have remarkable anisotropic properties resulting from structural anisotropy.[59] BP FETs have excellent performance, including a high field-effect mobility near 1000 $cm^2V^{-1}s^{-1}$ and an on-off ratios of up to 10^5 at room temperature.[63] Few-layer BP photodetector with in-plane p-n junction was reported, and had high photoresponsivity up to 180 mA/W and external quantum efficiency of 0.75%.[66]

On the other hand, BP is very unstable when exposed to the ambient environment according to the recent study results. Thus, much effort has been devoted to study the stability of BP under ambient conditions and effective protection techniques against ambient degradation. The methods including depositing AlO_x overlayers onto BP surface by atomic scalable deposition (ALD), encapsulating BP with graphene under van der Waals passivation, *etc*., have been proposed.[67]

1.4 History and basics of 2D van der Waals heterostructures

With interest of 2D materials increasing, another relevant research field has been developed and gained attention over the past five years.[35] It deals with van der Waals heterostructures that are prepared by vertically stacking different kinds of 2D materials onto each other and devices based on these 2D heterostructures. As mentioned before, there is no dangling bond on the surface of layered 2D materials that are held together by

weak van der Waals force, thus it is possible to transfer one such 2D material onto top of another one to create a stacked structure, as shown in figure 1.14. In-plane atoms are still combined with strong covalent bonds while weak van der Waals force connects each layer of 2D material and sufficient enough to keep the heterojunction stable. According to this basic principle, it is possible to build multilayer 2D heterostructures.

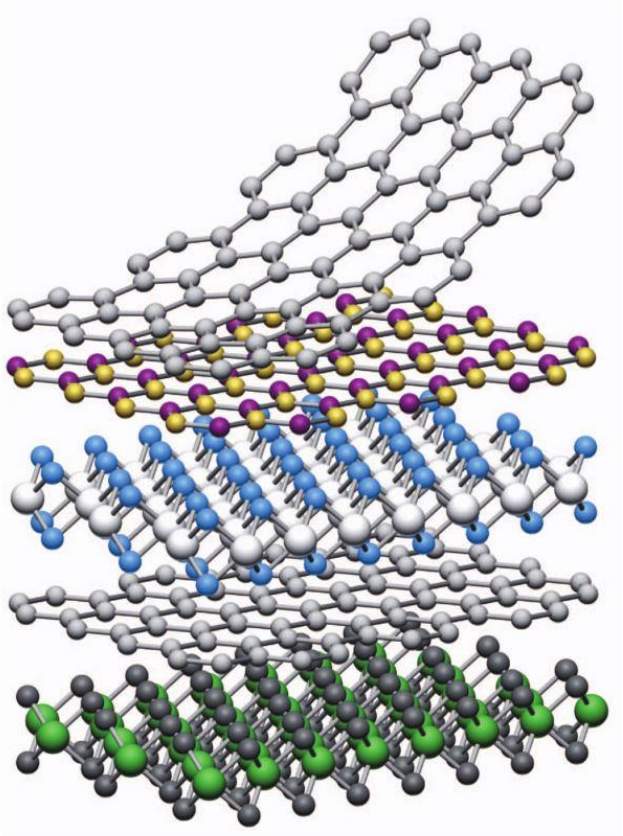

Figure 1.14 Schematic structure of vertically stacking 2D heterostructures. Each layer represents one kind of 2D materials. From top to bottom, they are graphene, boron nitride (BN), MoS_2, graphene and WSe_2, respectively. The image was from Ref. 35.

Theoretically, this artificially assembled hybrid structure can inherit properties from the designer 2D materials. For instance, if the 2D heterostructure is based on graphene/MoS_2, then the hybrid structure can possess properties of both high mobility for electronics applications (from graphene) and band gap (from MoS_2) for optoelectronics applications. With the presence of 2D heterostructures, researchers can fabricate multi-functional devices in atomic scale. Transistors based on graphene-MoS_2 heterostructures using Schottky barrier existing at the interface between graphene and MoS_2 were reported by

Tian *et al*.[68] Zhang *et al*. reported photodetectors also based on graphene-MoS_2 heterostructures with ultra-high gain.[34] Yu *et al*. reported heterostructures based on multi-layers of 2D materials by vertically stacking for logic transistors and complementary inverters.[69]

1.5 Basics for photodetectors

Photodetectors enabled by semiconducting materials is a kind of device detecting optical signal then changing it into electrical signal. This conversion in a photodetector is primarily involved with three processes: generation of photoexcited carriers, transport of photoexcited carriers, and communication with the connected circuit to output signal in the form of photocurrent. Photodetectors possess extensive applications in practical use, such as invisible ultraviolet (UV) detecting, visible light imaging, invisible infrared (IR) sensing, *etc*.[70] Accordingly, remarkable figures of merits, including high photoresponsivity, high specific detectivity, fast photoresponsive speed, low dark current and noise, are essential for these optoelectronic applications when working at the particular spectrum wavelength. Additionally, high-performance photodetectors are also required to meet the following points: low-energy consumption during optical detecting, small threshold voltage for triggering operation, and environmental inertness with good stability.[43]

1.5.1 Wavelengths of different optical signal

Electromagnetic radiation (optical signal) is formed in various ways, such as X-rays, UV, visible light, IR radiation, *etc*. They differ significantly in wavelength (nm) or frequency (Hz) and in coupling with optical substance, like atmosphere, which is illustrated with electromagnetic spectra in Figure 1.15. Notably, there is no restrict or absolute boundary between the adjacent spectra. For instance, visible light is usually defined within the spectra wavelength range from 400 nm to 700 nm, with which human eyes are able to respond. UV, visible and IR sources show continuously increasing wavelength and some optical sources radiate both visible and IR light. In addition, IR photodetectors, which are mainly used for sensing signal wavelength longer than visible light but shorter than the microwave ones, can also be applied to detect visible light.

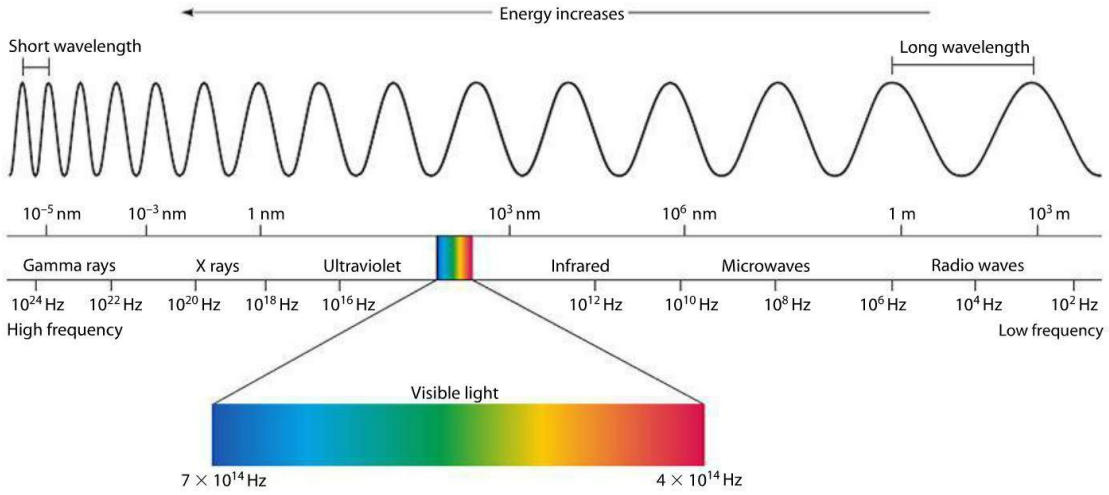

Figure 1.15 The electromagnetic spectra with energy increased from the right side to the left side, depicting different optical bands. Reprint with no permission required: https://www.miniphysics.com/electromagnetic-spectrum_25.html.

1.5.2 Figures of merits for photodetectors

In general, the following parameters are mainly used for assessing and comparing photodetector performance when operating at specific wavelength and under particular conditions.

- *Photoresponsivity (R)*:

  The photoresponsivity R with the unit of mA/W, as the most straightforward performance parameter, reveals how much photocurrent is generated under each unit optical power excitation. It is defined as the ratio between obtained net photocurrent (I_{ph}) under the specific biased voltage and input optical power (P_{in}) at the active domain of the device. It can be expressed by the equation below:

$$R = \frac{\mathrm{I}_{ph}}{\mathrm{P}_{in}} = \frac{\mathrm{I}_{light} - \mathrm{I}_{dark}}{\mathrm{P}_{d} \times S}$$

  Here, I_{light} , I_{dark} P_d and S represent measured current under light illumination, dark current obtained in the dark box, input power density and active domain size, respectively.

- *External quantum efficiency (EQE)*:

  The external quantum efficiency EQE describes the efficiency that how many photogenerated electron-hole pairs contribute to photocurrent excited by the unit

number of input photons. Here, photocurrent (I_{ph}) is obtained by subtracting dark current (I_{dark}) from output electrical signal under illumination (I_{light}). The total number of photogenerated carriers equals to the value of photocurrent divided by the unit electron charge. Besides, the total number of input photons equals to the value of input optical power (P_{in}) divided by the single photon energy. Accordingly, the EQE ratio value can be calculated based on the following equation:

$$EQE = \frac{\mathrm{I}_{ph}/e}{\mathrm{P}_{in}/h\upsilon} = R\frac{hc}{\upsilon\lambda}$$

Here, e, h, υ and λ represent elementary charge (1.6×10^{-19} C), Planck's constant (6.626×10^{-34} Js), frequency of incident light and wavelength of incident light, respectively. Evidently, photodetectors enabled by materials with better optical absorption capability have larger potential to obtain higher EQE value.

- *Internal quantum efficiency (IQE)*:

  As for internal quantum efficiency IQE, it is defined as the ratio between the quantity of photoexcited carriers contributing to photocurrent and the quantity of absorbed photons by photodetectors. The number of absorbed photons can be calculated by subtracting optical reflection or transmission induced photo loss from the number of input photons. Particularly for atomically thin materials, the optical interference phenomenon is inevitable and cannot be ignored.

- *Photoresponsive time (τ)*:

  The photoresponsive time τ reveals how fast photodetectors can react to incident optical signal. It can be extracted from photocurrent on/off dynamic measurements. It is divided into two parts: the rise time τ_r and the decay time τ_d. Photodetectors possessing both very small τ_r and τ_d (down to μs or ns) are much desired for optoelectronic applications, such as optical communication, military imaging, *etc*.

- *Signal to noise ratio (SNR)*:

  The signal to noise ratio SNR is defined as the ratio between signal power and noise power, which is required to be larger than 1 to discriminate genuine optical signal from background noise. Notably, noise is unavoidable during optical signal detection, which limits or degrades the photodetector performance by generating random fluctuation into output signal, and thus large SNR value is of much

importance for good photodetectors, especially those enabled by low-dimensional materials.

- *Noise equivalent power (NEP)*:

  Noise equivalent power NEP with the unit of W is relevant to optical detection sensitivity and defined as the required minimum input optical power (P_{in}) to obtain the SNR of 1. It can be calculated from: NEP = noise/photoresponsivity.

- *Specific detectivity (D^*)*:

  The specific detectivity D^* with the unit of cm·Hz$^{1/2}$ /W (Jones) is an importance performance parameter to assess and compare photodetectors enabled by different materials and device configurations. When the dark current induced shot noise is the primary noise during photodetection process, D^* can be determined by the following equation:

$$D^* = R(S/2eI_{dark})^{1/2} \tag{1.1}$$

1.6 Basics for field-effect transistors (FETs)

Field-effect transistor (FET) is an electronic device, which is the fundamental component of complex logic building blocks in integrated circuits nowadays, such as complementary metal-oxide-semiconductor (CMOS) switch, flat panel display modules, *etc*. The classical configuration of a FET is mainly composed of three electrode terminals, including gate, drain and source, and three materials with varied electrical conductivity, including conductive, semiconductive and dielectric materials.

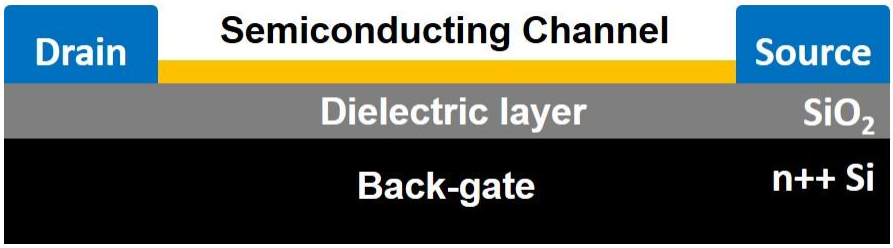

Figure 1.16 Schematic diagram (side-view) of a back-gated FET based on the semiconducting thin film.

Thin film based FET is a representative member in FET family. In general, in terms of back-gated thin film FETs, the dielectric layer is located between conductive substrates and semiconducting materials, and conductive metal electrodes are deposited on surface of semiconducting materials directly, as depicted in Figure 1.16. The channel current modulation in FETs between drain and source terminals (I_{ds}) is realised by varying the electric field between gate and source terminals (V_{gs}) to change the electrical conductivity of the channel, enabling FETs to work as gate-voltage controlled current sources or gate-voltage controlled resistors. According to the polarity of channels and resulted gate modulation features, FETs can be divided into n-type and p-type ones.

Output curves and transfer curves are the two dominant FET characterisation results for testing device performance. The former one resolves drain-source current as a function of sweeping channel biased voltage at specific gate voltage (denoted as I_{ds}-$V_{ds}|V_{gs}$, in which I_{ds} and V_{ds} correspond to y axis and x axis, respectively, and V_{gs} is varied for each I_{ds}-V_{ds} curve), while the latter one reveals drain-source current as a function of sweeping gate voltage at particular channel biased voltage (denoted as I_{ds}-$V_{gs}|V_{ds}$, in which I_{ds} and V_{gs} correspond to y axis and x axis, respectively, and V_{ds} is varied for each I_{ds}-V_{gs} curve). The following parameters can be extracted from output and transfer curves to further assess and compare FET performance based on different materials and configurations.

- *ON/OFF ratio*:

  This ratio is defined between the maximum value and the minimum value of drain-source current at specific drain-source voltage and gate voltage. The state of ON represents the FET working with larger current value and stronger current driving capability while the state of OFF means the FET works with smaller current value and obviously reduced electrical conductivity. Accordingly, the larger ON/OFF ratio is preferred for practical applications, especially for switch circuits.

- *Threshold voltage (V_T)*:

  The threshold voltage V_T is defined as the value of applied V_{gs} when significant carriers are accumulated close to the interface between semiconducting layer and

dielectric layer. This value can be deduced from transfer curves in linear scale when a small drain-source voltage is applied using the linear extrapolation method.

- *Turn-on voltage (V_{on})*:

The turn-on voltage V_{on} is equal to the V_{gs} when drain-source current starts to raise up, which can be extracted from transfer curves in logarithmic scale.

- *Subthreshold swing (SS)*:

The subthreshold swing SS value with the unit of mV/dec corresponds to the required V_{gs} when drain-source current increased by ten times, as calculated below:

$$SS = [\frac{d(log_{10} I_{ds})}{dV_{gs}}]^{-1}$$

Therefore, a small SS value is desired for energy-friendly and high-efficiency applications.

- *Transconductance (g_m)*:

The transconductance g_m with the unit of S is defined as the ratio between the changed output current value and changed input voltage value, as expressed below:

$$g_m = \frac{dI_{ds}}{dV_{ds}}$$

- *Field-effect mobility (μ)*:

The field-effect mobility μ with the unit of cm^2/Vs demonstrates the ability of a FET to drive dominant carriers in response to an external electric field, and it is one of the most frequently used parameter for comparing FET performance. The value of μ can be obtained using the following equation:

$$\mu = \frac{dI_{ds}}{dV_{ds}} \times \frac{L}{WC_i V_{ds}} = g_m \times \frac{L}{WC_i V_{ds}} \quad (1.2)$$

Here, L, W and C_i represent channel length, channel width and capacitance of the dielectric layer, respectively.

1.7 Thesis structure

This thesis consists of seven chapters, which is focused on 2D materials (including BPQDs, TMDs and 2D heterostructures) for nanoelectronic and optoelectronic applications, such as photodetectors, phototransistors and FETs.

Chapter 1 reviews the discovery and development of graphene and its analogue of glassy-graphene, and reveals their difference and similarity of properties. Beyond graphene, TMDs family, including binary and ternary TMDs, BP and vertically stacked 2D van der Waals heterostructures are introduced, describing their respective crystal structures and intrinsic features. The reported typical applications enabled by theses 2D materials are reviewed. Subsequently, fundamental knowledge for photodetectors and FETs are presented in section 1.5 and 1.6, respectively.

Chapter 2 introduces the involved experimental methods, including material growth using the MBE technique, material characterisations, device fabrication and device measurements. The configurations and operation principles of involved experimental equipment are covered. In addition, the obtained results by using relevant systems are illustrated as examples.

Chapter 3 presents the work focused on the MBE growth of few-layer BP quantum dots on Si(100) and Si(111) substrates, revealing the BP crystallisation preference and possibility of large-scale synthesis for BP. Detailed material characterisations are covered to demonstrate the formation of BP quantum dots on the surface terraces of Si substrates.

Chapter 4 details the work about spatially bandgap-graded $MoS_{2(1-x)}Se_{2x}$ homojunctions based phototransistors, which exhibit self-powered high-performance. Material characterisations and device measurements are presented in detail to evidence the existence of spatially graded bandgaps within a single homojunction domain. In the main text, it is demonstrated that the in-plane bandgap gradient is resulted from spatial Se-

composition and thickness grading, so a strong and sensitive photovoltaic effect controlled by gate voltage is achieved.

Chapter 5 is a presentation for the work of robust FETs enabled by bilayer self-passivated WSe_2 nanosheets. A series of material characterisation and device measurement results are presented and discussed, respectively. In the main text, the existence of WO_x/WSe_2 heterojunctions around edges of bilayer WSe_2 is proven. The FETs possess ohmic contact and exhibit n-type behaviour, high conductivity, ultra-low leakage gate current and noticeable robustness for large bias.

Chapter 6 details the results of combined use of glassy-graphene and TMDs, namely, 2D MoS_2/glassy-graphene heterostructures and transparent photodetectors based on them. The wet transferring method for preparing 2D heterostructure is described, followed by a series of material characterisations to demonstrate the formation of the heterojunctions. In addition, device measurements for the transparent photodetectors enabled by these novel van der Waals heterostructures are presented, which are conducted by using monochromatic lasers to probe their photoresponsive features.

Chapter 7 is a conclusion for the performed work in my PhD project, and also proposes the future work.

1.8 Reference

(1) Novoselov, K. S.; Geim, A. K.; Morozov, S. V.; Jiang, D.; Zhang, Y.; Dubonos, S. V.; Grigorieva, I. V.; Firsov, A. A. Electric Field Effect in Atomically Thin Carbon Films. *Science* **2004**, *306*, 666–669. http://doi: 10.1126/science.1102896.

(2) Zurutuza, A.; Marinelli, C. Challenges and Opportunities in Graphene Commercialization. *Nat. Nanotechnol.* **2014**, *9* (10), 730–734. https://doi.org/10.1038/nnano.2014.225.

(3) Bae, S.; Kim, H.; Lee, Y.; Xu, X.; Park, J.-S.; Zheng, Y.; Balakrishnan, J.; Lei, T.; Ri Kim, H.; Song, Y. Il; et al. Roll-to-Roll Production of 30-Inch Graphene Films for Transparent Electrodes. *Nat. Nanotechnol.* **2010**, *5* (8), 574–578. https://doi.org/10.1038/nnano.2010.132.

(4) Wallace, P. R. The Band Theory of Graphite. *Phys. Rev.* **1947**, *71* (9), 622–634. https://doi.org/10.1103/PhysRev.71.622.

(5) State, T.; Brgnsmck, X. Band Structure of Graphite. *Phys. Rev.* **1958**, *330*, 272–279. https://doi.org/10.1103/PhysRev.109.272.

(6) Randviir, E. P.; Brownson, D. A. C.; Banks, C. E. A Decade of Graphene Research: Production, Applications and Outlook. *Mater. Today* **2014**, *17* (9), 426–432. https://doi.org/10.1016/j.mattod.2014.06.001.

(7) Yi, M.; Shen, Z. A Review on Mechanical Exfoliation for the Scalable Production of Graphene. *J. Mater. Chem. A* **2015**, *3* (22), 11700–11715. https://doi.org/10.1039/C5TA00252D.

(8) Gilje, S.; Kaner, R. B.; Wallace, G. G.; Li, D. A. N.; Mu, M. B.; Muller, M. B.; Gilje, S.; Kaner, R. B.; Wallace, G. G. Processable Aqueous Dispersions of Graphene Nanosheets. *Nat. Nanotechnol.* **2008**, *3* (2), 101–105. https://doi.org/10.1038/nnano.2007.451.

(9) Park, J.; Mitchel, W. C.; Grazulis, L.; Smith, H. E.; Eyink, K. G.; Boeckl, J. J.; Tomich, D. H.; Pacley, S. D.; Hoelscher, J. E. Epitaxial Graphene Growth by Carbon Molecular Beam Epitaxy (CMBE). *Adv. Mater.* **2010**, *22* (37), 4140–4145. https://doi.org/10.1002/adma.201000756.

(10) Kumari, A.; Prasad, N.; Bhatnagar, P. K.; Mathur, P. C.; Yadav, A. K.; Tomy, C. V.; Bhatia, C. S. Electrical Transport Properties of Polycrystalline CVD Graphene on SiO2/Si Substrate. *Diam. Relat. Mater.* **2014**, *45*, 28–33. https://doi.org/10.1016/j.diamond.2014.03.003.

(11) Gupta, P.; Dongare, P. D.; Grover, S.; Dubey, S.; Mamgain, H.; Bhattacharya, A.; Deshmukh, M. M. A Facile Process for Soak-and-Peel Delamination of CVD Graphene from Substrates Using Water. *Sci. Rep.* **2014**, *4*, 3882. https://doi.org/10.1038/srep03882.

(12) Yoon, J.; Park, W.; Bae, G. Y.; Kim, Y.; Jang, H. S.; Hyun, Y.; Lim, S. K.; Kahng, Y. H.; Hong, W. K.; Lee, B. H.; et al. Highly Flexible and Transparent Multilayer MoS2 Transistors with Graphene Electrodes. *Small* **2013**, *9* (19), 3295–3300. https://doi.org/10.1002/smll.201300134.

(13) Novoselov, K. S.; Geim, A. K.; Morozov, S. V; Jiang, D.; Katsnelson, M. I.; Grigorieva, I. V; Dubonos, S. V; Firsov, A. A. Two-Dimensional Gas of Massless Dirac Fermions in Graphene. *Nature* **2005**, *438* (7065), 197–200. https://doi.org/10.1038/nature04233.

(14) Mayorov, a. S.; Gorbachev, R. V; Morozov, S. V; Britnell, L.; Jalil, R.; Ponomarenko, L. a; Novoselov, K. S.; Watanabe, K.; Taniguchi, T.; Geim, a. K. Direct Evidence for Micron-Scale Ballistic Transport in Encapsulated Graphene at Room Temperature. *1103.4510* **2011**, 2396–2399. https://doi.org/10.1021/nl200758b.

(15) Balandin, A. A. Thermal Properties of Graphene and Nanostructured Carbon Materials. *Nat. Mater.* **2011**, *10* (8), 569. https://doi.org/10.1038/nmat3064.

(16) Nair, R. R.; Blake, P.; Grigorenko, a. N.; Novoselov, K. S.; Booth, T. J.; Stauber, T.; Peres, N. M. R.; Geim, a. K. Fine Structure Constant Defines Visual Transperency of Graphene. *Science* **2008**, *320* (June), 2008. https://doi.org/10.1126/science.1156965.

(17) Zhang, B. Y.; Liu, T.; Meng, B.; Li, X.; Liang, G.; Hu, X.; Wang, Q. J. Broadband High Photoresponse from Pure Monolayer Graphene Photodetector. *Nat. Commun.* **2013**, *4* (May), 1811. https://doi.org/10.1038/ncomms2830.

(18) Xia, F.; Mueller, T.; Lin, Y.; Valdes-Garcia, A.; Avouris, P. Ultrafast Graphene Photodetector. *Nat. Nanotechnol.* **2009**, *4* (12), 839–843. https://doi.org/10.1038/nnano.2009.292.

(19) Sagar, A. S. Graphene-Based Field-Effect Transistors. **2011**.

(20) Zhao, X.; Hayner, C. M.; Kung, M. C.; Kung, H. H. In-Plane Vacancy-Enabled High-Power Si-Graphene Composite Electrode for Lithium-Ion Batteries. *Adv. Energy Mater.* **2011**, *1* (6), 1079–1084. https://doi.org/10.1002/aenm.201100426.

(21) Ye, Y.; Dai, L. Graphene-Based Schottky Junction Solar Cells. *J. Mater. Chem.*

2012, No. September, 24224–24229. https://doi.org/10.1039/c2jm33809b.

(22) Bonaccorso, F.; Sun, Z.; Hasan, T.; Ferrari, A. C. Graphene Photonics and Optoelectronics. *Nat. Photonics* **2010**, *4* (August), 611–622. https://doi.org/10.1038/nphoton.2010.186.

(23) Li, X.; Wang, X.; Zhang, L.; Lee, S.; Dai, H. Chemically Derived Ultramooth Graphene Nanoribbon Semiconductors. *Science* **2008**, *319* (5867), 1229–1232. https://doi.org/10.1126/science.1150878.

(24) Dai, X.; Wu, J.; Qian, Z.; Wang, H.; Jian, J.; Cao, Y.; Rummeli, M. H.; Yi, Q.; Liu, H.; Zou, G. Ultra-Smooth Glassy Graphene Thin Films for Flexible Transparent Circuits. *Sci. Adv.* **2016**, *2* (November), e1601574. https://doi.org/10.1126/sciadv.1601574.

(25) Bauer, J.; Schroer, a.; Schwaiger, R.; Kraft, O. Approaching Theoretical Strength in Glassy Carbon Nanolattices. *Nat. Mater.* **2016**, *8* (February). https://doi.org/10.1038/nmat4561.

(26) Ferrari, A. C. Raman Spectroscopy of Graphene and Graphite: Disorder, Electron–phonon Coupling, Doping and Nonadiabatic Effects. *Solid State Commun.* **2007**, *143* (1-2), 47–57. https://doi.org/10.1016/j.ssc.2007.03.052.

(27) Neumann, C.; Reichardt, S.; Venezuela, P.; Drögeler, M.; Banszerus, L.; Schmitz, M.; Watanabe, K.; Taniguchi, T.; Mauri, F.; Beschoten, B.; et al. Raman Spectroscopy as Probe of Nanometre-Scale Strain Variations in Graphene. *Nat. Commun.* **2015**, *6* (May), 8429. https://doi.org/10.1038/ncomms9429.

(28) Malard, L. M.; Pimenta, M. a.; Dresselhaus, G.; Dresselhaus, M. S. Raman Spectroscopy in Graphene. *Phys. Rep.* **2009**, *473* (5-6), 51–87. https://doi.org/10.1016/j.physrep.2009.02.003.

(29) Graf, D.; Molitor, F.; Ensslin, K.; Stampfer, C.; Jungen, a.; Hierold, C.; Wirtz, L. Spatially Resolved Raman Spectroscopy of Single- and Few-Layer Graphene. *Nano Lett.* **2007**, *7* (2), 238–242. https://doi.org/10.1021/nl061702a.

(30) Dresselhaus, M. S.; Jorio, A.; Hofmann, M.; Dresselhaus, G.; Saito, R. Perspectives on Carbon Nanotubes and Graphene Raman Spectroscopy. *Nano Lett.* **2010**, *10* (3), 751–758. https://doi.org/Doi 10.1021/Nl904286r.

(31) Xia, F.; Wang, H.; Xiao, D.; Dubey, M.; Ramasubramaniam, A. Two-Dimensional Material Nanophotonics. *Nat. Photonics* **2014**, *8* (12), 899–907. https://doi.org/10.1038/nphoton.2014.271.

(32) Mak, K. F.; McGill, K. L.; Park, J.; McEuen, P. L. The Valley Hall Effect in MoS2 Transistors. *Science* **2014**, *344* (6191), 1489–1492. https://doi.org/10.1126/science.1250140.

(33) Rathi, S.; Lee, I.; Lim, D.; Wang, J.; Ochiai, Y.; Aoki, N.; Watanabe, K.; Taniguchi, T.; Lee, G.-H.; Yu, Y.-J.; et al. Tunable Electrical and Optical Characteristics in Monolayer Graphene and Few-Layer MoS2 Heterostructure Devices. *Nano Lett.* **2015**, *15* (8), 5017–5024. https://doi.org/10.1021/acs.nanolett.5b01030.

(34) Zhang, W.; Chuu, C.-P.; Huang, J.-K.; Chen, C.-H.; Tsai, M.-L.; Chang, Y.-H.; Liang, C.-T.; Chen, Y.-Z.; Chueh, Y.-L.; He, J.-H.; et al. Ultrahigh-Gain Photodetectors Based on Atomically Thin Graphene-MoS2 Heterostructures. *Sci. Rep.* **2014**, *4*, 3826. https://doi.org/10.1038/srep03826.

(35) Geim, A. K.; Grigorieva, I. V. Van Der Waals Heterostructures. *Nature* **2013**, *499* (7459), 419–425. https://doi.org/10.1038/nature12385.

(36) Waghray, H.; Lee, T. S.; Tatarchuk, B. J. A Study of the Tribological and Electrical Properties of Sputtered and Burnished Transition Metal Dichalcogenide Films. *Surf. Coatings Technol.* **1995**, *76-77* (PART 2), 415–420. https://doi.org/10.1016/0257-8972(95)02564-2.

(37) Rapoport, L.; Leshcinsky, V.; Lvovsky, M.; Nepomnyashchy, O.; Volovik, Y.; Tenne, R. Mechanism of Friction of Fullerenes. *Ind. Lubr. Tribol.* **2002**, *54* (4), 171–176. https://doi.org/10.1108/00368790210431727.

(38) Frindt, R. F. Single Crystals of MoS2 Several Molecular Layers Thick. *J. Appl. Phys.* **1966**, *37* (4), 1928–1929. https://doi.org/10.1063/1.1708627.

(39) Novoselov, K. S.; Jiang, D.; Schedin, F.; Booth, T. J.; Khotkevich, V. V; Morozov, S. V; Geim, a K. Two-Dimensional Atomic Crystals. *Proc. Natl. Acad. Sci. U. S. A.* **2005**, *102* (30), 10451–10453. https://doi.org/10.1073/pnas.0502848102.

(40) Radisavljevic, B.; Radenovic, A.; Brivio, J.; Giacometti, V.; Kis, A. Single-Layer MoS2 Transistors. *Nat. Nanotechnol.* **2011**, *6* (3), 147–150. https://doi.org/10.1038/nnano.2010.279.

(41) Mak, K. F.; Lee, C.; Hone, J.; Shan, J.; Heinz, T. F. Atomically Thin MoS2: A New Direct-Gap Semiconductor. *Phys. Rev. Lett.* **2010**, *105* (13), 136805. https://doi.org/10.1103/PhysRevLett.105.136805.

(42) Tsai, M. L.; Su, S. H.; Chang, J. K.; Tsai, D. S.; Chen, C. H.; Wu, C. I.; Li, L. J.;

Chen, L. J.; He, J. H. Monolayer MoS2 Heterojunction Solar Cells. *ACS Nano* **2014**, *8* (8), 8317–8322. https://doi.org/10.1021/nn502776h.

(43) Tsai, D.-S.; Liu, K.-K.; Lien, D.-H.; Tsai, M.-L.; Kang, C.-F.; Lin, C.-A.; Li, L.-J.; He, J.-H. Few Layer MoS2 with Broadband High Photogain and Fast Optical Switching for Use in Harsh Environments. *ACS Nano* **2013**, *7* (5), 3905–3911. https://doi.org/10.1021/nn305301b.

(44) Lee, H. S.; Min, S.-W.; Chang, Y.-G.; Park, M. K.; Nam, T.; Kim, H.; Kim, J. H.; Ryu, S.; Im, S. MoS2 Nanosheet Phototransistors with Thickness-Modulated Optical Energy Gap. *Nano Lett.* **2012**, *12* (7), 3695–3700. https://doi.org/10.1021/nl301485q.

(45) Xie, X.; Sarkar, D.; Liu, W.; Kang, J.; Marinov, O.; Deen, M. J.; Banerjee, K. Low-Frequency Noise in Bilayer MoS2 Transistor. *ACS Nano* **2014**, *8* (6), 5633–5640. https://doi.org/10.1021/nn4066473.

(46) Sarkar, D.; Xie, X.; Liu, W.; Cao, W.; Kang, J.; Gong, Y.; Kraemer, S.; Ajayan, P. M.; Banerjee, K. A Subthermionic Tunnel Field-Effect Transistor with an Atomically Thin Channel. *Nature* **2015**, *526* (7571), 91–95. https://doi.org/10.1038/nature15387.

(47) Desai, S. B.; Madhvapathy, S. R.; Sachid, A. B.; Llinas, J. P.; Wang, Q.; Ahn, G. H.; Pitner, G.; Kim, M. J.; Bokor, J.; Hu, C.; et al. MoS2 Transistors with 1-Nanometer Gate Lengths. *Science* **2016**, *354* (6308), 2–6.

(48) Huang, J.; Yang, L.; Liu, D.; Chen, J.; Fu, Q.; Xiong, Y.; Lin, F.; Xiang, B. Large-Area Synthesis of Monolayer WSe2 on a SiO2/Si Substrate and Its Device Applications. *Nanoscale* **2015**, *7* (9), 4193–4198. https://doi.org/10.1039/c4nr07045c.

(49) Yang, L.; Fu, Q.; Wang, W.; Huang, J.; Huang, J.; Zhang, J.; Xiang, B. Large-Area Synthesis of Monolayered MoS2(1-x)Se2x with a Tunable Band Gap and Its Enhanced Electrochemical Catalytic Activity. *Nanoscale* **2015**, *7* (23), 10490–10497. https://doi.org/10.1039/c5nr02652k.

(50) Zhang, W.; Chiu, M.-H.; Chen, C.-H.; Chen, W.; Li, L.; Wee, A. T. S.; Monolayers, W.; Zhang, W.; Chiu, M.-H.; Chen, C.-H.; et al. Role of Metal Contacts in High- Performance Phototransistors Based on WSe2 Monolayers. *ACS Nano* **2014**, *8* (Xx), 8653–8661. https://doi.org/10.1021/nn503521c.

(51) Park, J. H.; Vishwanath, S.; Liu, X.; Zhou, H.; Eichfeld, S. M.; Fullerton-Shirey, S. K.; Robinson, J. A.; Feenstra, R. M.; Furdyna, J.; Jena, D.; et al. Scanning

Tunneling Microscopy and Spectroscopy of Air Exposure Effects on Molecular Beam Epitaxy Grown WSe2 Monolayers and Bilayers. *ACS Nano* **2016**, *10* (4), 4258–4267. https://doi.org/10.1021/acsnano.5b07698.

(52) Li, H.; Duan, X.; Wu, X.; Zhuang, X.; Zhou, H.; Zhang, Q.; Zhu, X.; Pan, A.; Duan, X. Growth of Alloy MoS2xSe2(1−x) Nanosheets with Fully Tunable Chemical Compositions and Optical Properties. *J. Am. Chem. Soc.* **2014**, *136*, 3756–3759.

(53) Dumcenco, D. O.; Kobayashi, H.; Liu, Z.; Huang, Y.-S.; Suenaga, K. Visualization and Quantification of Transition Metal Atomic Mixing in Mo1−xWxS2 Single Layers. *Nat. Commun.* **2013**, *4*, 1351. https://doi.org/10.1038/ncomms2351.

(54) Huang, J.; Wang, W. H.; Fu, Q.; Yang, L.; Zhang, K.; Zhang, J. Y.; Xiang, B. Stable Electrical Performance Observed in Large-Scale Monolayer WSe2(1-x)S2x with Tunable Band Gap. *Nanotechnology* **2016**, *27* (13), 13LT01. https://doi.org/10.1088/0957-4484/27/13/13lt01.

(55) Zheng, S.; Sun, L.; Yin, T.; Dubrovkin, A. M.; Liu, F.; Liu, Z.; Shen, Z. X.; Fan, H. J. Monolayers of WxMo1-xS2 Alloy Heterostructure with in-Plane Composition Variations. *Appl. Phys. Lett.* **2015**, *106* (6), 063113. https://doi.org/10.1063/1.4908256.

(56) Bridgman, P. W. Two New Modifications of Phosphorus. *J. Am. Chem. Soc.* **1914**, *36* (7), 1344–1363. https://doi.org/10.1021/ja02184a002.

(57) Keyes, R. W. The Electrical Properties of Black Phosphorus. *Phys. Rev.* **1953**, *92* (3), 580–584. https://doi.org/10.1103/PhysRev.92.580.

(58) Bullett, D. W. Valence-Band Structures of Phosphorus Allotropes. *Solid State Commun.* **1985**, *55* (3), 257–260. https://doi.org/10.1016/0038-1098(85)90728-8.

(59) Liu, H.; Neal, A. T. Phosphorene : An Unexplored 2D Semiconductor with a High Hole Mobility. *ACS Nano* **2014**, *8* (4), 4033–4041. https://doi.org/10.1021/nn501226z.

(60) Jia, Y.; Xia, F.; Wang, H. Rediscovering Black Phosphorus as an Anisotropic Layered Material for Optoelectronics and Electronics. *Nat. Commun.* **2014**, *5*, 1–6. https://doi.org/10.1038/ncomms5458.

(61) Carvalho, A.; Wang, M.; Zhu, X.; Rodin, A. S.; Su, H.; Castro Neto, A. H. Phosphorene: From Theory to Applications. *Nat. Rev. Mater.* **2016**, *1*, 16061. https://doi.org/10.1038/natrevmats.2016.61.

(62) Li, X.; Deng, B.; Wang, X.; Chen, S.; Vaisman, M.; Karato, S.; Pan, G.; Larry Lee, M.; Cha, J.; Wang, H.; et al. Synthesis of Thin-Film Black Phosphorus on a Flexible Substrate. *2D Mater.* **2015**, *2* (3), 031002. https://doi.org/10.1088/2053-1583/2/3/031002.

(63) Li, L.; Yu, Y.; Ye, G. J.; Ge, Q.; Ou, X.; Wu, H.; Feng, D.; Chen, X. H.; Zhang, Y. Black Phosphorus Field-Effect Transistors. *Nat. Nanotechnol.* **2014**, *9* (5), 1–17. https://doi.org/10.1038/nnano.2014.35.

(64) Castellanos-gomez, A.; Vicarelli, L.; Prada, E.; Island, J. O.; Narasimha-Acharya, K. L.; Blanter, S. I.; Groenendijk, D. J.; Buscema, M.; Steele, G. A.; Alvarez, J. V; et al. Isolation and Characterization of Few-Layer Black Phosphorus. *2D Mater.* **2014**, *1*, 025001. https://doi.org/10.1088/2053-1583/1/2/025001.

(65) Tran, V.; Soklaski, R.; Liang, Y.; Yang, L. Layer-Controlled Band Gap and Anisotropic Excitons in Few-Layer Black Phosphorus. *Phys. Rev. B - Condens. Matter Mater. Phys.* **2014**, *89* (23), 1–6. https://doi.org/10.1103/PhysRevB.89.235319.

(66) Yu, X.; Zhang, S.; Zeng, H.; Wang, Q. J. Lateral Black Phosphorene P-N Junctions Formed via Chemical Doping for High Performance near-Infrared Photodetector. *Nano Energy* **2016**, *25*, 34–41. https://doi.org/10.1016/j.nanoen.2016.04.030.

(67) Eswaraiah, V.; Zeng, Q.; Long, Y.; Liu, Z. Black Phosphorus Nanosheets: Synthesis, Characterization and Applications. *Small* **2016**, *12* (26), 3480–3502. https://doi.org/10.1002/smll.201600032.

(68) Tian, H.; Tan, Z.; Wu, C.; Wang, X.; Mohammad, M. A.; Xie, D.; Yang, Y.; Wang, J.; Li, L.-J.; Xu, J.; et al. Novel Field-Effect Schottky Barrier Transistors Based on Graphene-MoS2 Heterojunctions. *Sci. Rep.* **2014**, *4*, 5951. https://doi.org/10.1038/srep05951.

(69) Yu, W. J.; Li, Z.; Zhou, H.; Chen, Y.; Wang, Y.; Huang, Y.; Duan, X. Vertically Stacked Multi-Heterostructures of Layered Materials for Logic Transistors and Complementary Inverters. *Nat. Mater.* **2013**, *12* (3), 246–252. https://doi.org/10.1038/nmat3518.

(70) Sze, S. M.; Ng, K. K. *Physics of Semiconductor Devices*, Third Edit.; John Wiley & Sons, Inc.: Hoboken, New Jersey, 2007.

Chapter 2 Experimental Methods

2.1 Molecular beam epitaxy (MBE)

Molecular Beam Epitaxy (MBE) growth technique has been well studied and used for growing nanoscale two-dimensional (2D) materials, such as graphene, silicene, germanene, blue phosphorene, *etc*.[1-6] To the best knowledge, no published literature has reported synthesis of BP using MBE method or other bottom-up growth approach without introducing the high-pressure conditions to date.[7-9] Accordingly, MBE technique was employed for synthesising the novel 2D material in this work. Direct MBE growth of black phosphorene quantum dots (BPQDs) on wafer-sized Si substrates instead of phase conversion under high pressure was proposed, followed by detailed material characterisation. Evidently, wafer-scale synthesis of 2D materials using MBE method is of much significance for future practical applications, especially for fabricating large-scale device arrays.[10-12]

2.1.1 Basics of MBE operations

The so-called epitaxy refers to the deposition of a material upon a crystalline substrate so that the deposited material will copy the crystalline structure of the underlying substrate, leading to a highly crystallised grown epilayers. The respective deposition process is called homoepitaxy when the epilayers are of the same composition as the substrate (such as GaAs on GaAs growth) and heteroepitaxy when the deposited material and the substrate are of different nature (such as GaAs on Si growth), as illustrated in figure 2.1. Multiple epitaxial growth techniques have been well developed, including such as Liquid Phase Epitaxy (LPE), MBE and Metal-Organic Chemical Vapour Deposition (MOCVD). Due to the versatility and precision, MBE is a technique of the most importance for the development of new pioneering materials and structures, such as nanoscale BPQDs studied here.

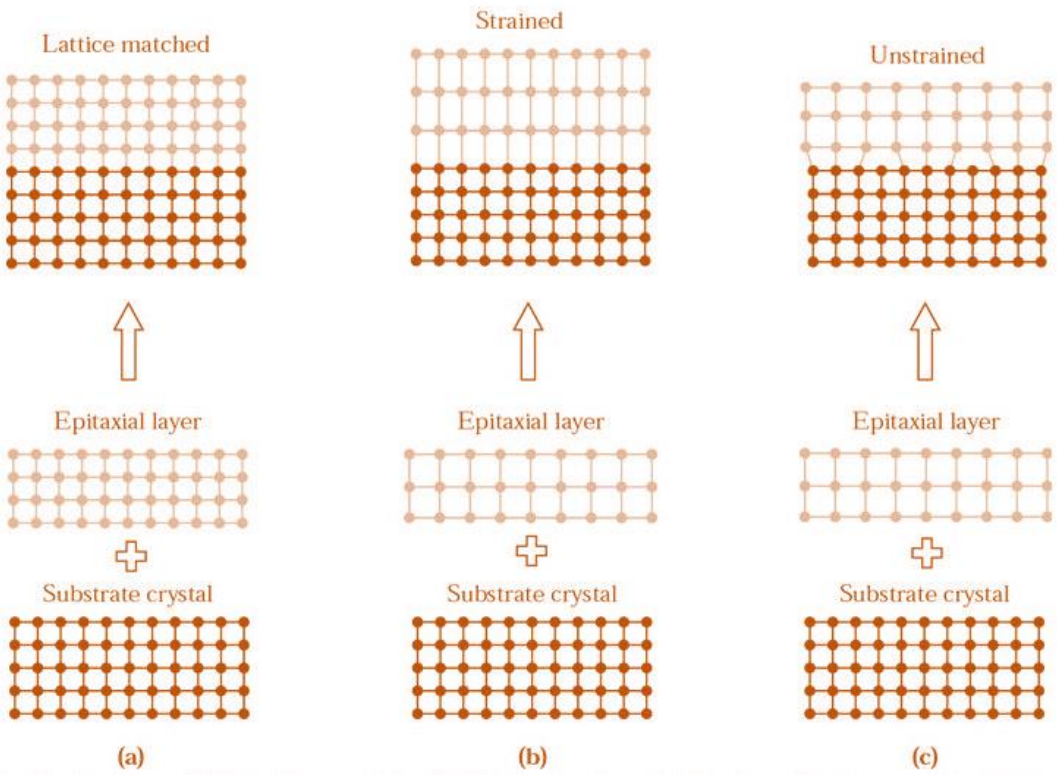

Figure 2.1 Schematic illustration of homoepitaxy (a) and heteroepitaxy with strained (b) and relaxed epilayers (c), respectively.

MBE is an ultra-high vacuum (UHV) epitaxial growth method developed by Alfred Y. Cho and John R. Arthur in the late 1960s.[13,14] The overall concept is straightforward: high purity materials are evaporated with precisely controlled flux rates onto a crystalline substrate maintained at a controlled temperature under UHV conditions. Because of the UHV environment in the growth chamber, the mean free path of the homo-atomic chemical species evaporating from the ultra-high purity source materials (such as Ga, As_2, P_4, *etc*.) will be orders of magnitude longer than the distance to the substrate. Evaporation from the sources, maintained in effusion cells, can therefore be considered rectilinear, hence the "molecular beam" qualification of the technology. These molecular beams are directed towards the substrate and, upon collision with the substrate surface, chemical species can be weakly adsorbed on the surface and dissociated into individual atoms. These individual atoms will then migrate to a suitable lattice site and be incorporated in the growing film, leading to the epitaxial growth.

The UHV, coupled with ultra-high purity elemental source materials and proper preparation of the substrate to obtain a clean surface at the atomic level, ensures a minimal contamination of the epitaxial grown film. Careful monitoring of the effusion cells temperatures and of the opening and closing sequence of the shutters in front of them allows for a very accurate control over each molecular beam flux rate. The growth rates can thus be precisely controlled from the beam flux rates and the substrate temperature.

Very slow growth rates (1 to 2 monolayer per second) can be easily realised by tweaking the effusion cells temperature. Conversely the individual shutters of the effusion cells present way shorter opening and closing times, typically below a tenth of a second. This allows for extremely sharp interfaces with abrupt modification of the epilayer composition at the atomic layer scale. Very fine architectures can therefore be obtained, leading to devices exploiting the quantum properties of such very low dimension structures. In order to provide the purity, the precision and the flexibility are required for such a fine-tuning of growth parameters, and a specific reactor architecture is essential as described below.

2.1.2 MBE configuration

An MBE system consists in interconnected modular building blocks under high or ultra-high vacuum. A typical system will at least comprise a load-lock, a preparation chamber and a growth chamber. The III-V MBE system used at UCL also includes a phosphorus recovery system in order to collect hazardous phosphorus residues from P-based III-V compounds growth. The chambers are separated using UHV gate valves to avoid cross contamination between them and allow different pressures in each chamber when loading and preparing wafers.

Under standard MBE operations, the load-lock is the only chamber not always maintained under vacuum. Its role is to enable the loading and unloading of wafers in and out the MBE system while keeping the UHV environment in the other chambers. It is equipped with a high vacuum pump to pump down from atmosphere to high vacuum pressures levels (about 10^{-7} torr). In the case of the MBE system used at UCL a cryogenic pump is also used to provide better vacuum capabilities. Inside the load-lock two quartz infrared tube lamps are used to heat up newly loaded wafers to about 100 °C to 200 °C in order to perform a preliminary outgassing of water and other volatile chemical species from the surface of the wafers, thus avoiding contamination of the preparation and growth chambers from the wafer. Once the wafers outgassed and the high vacuum obtained in the load-lock, the samples can be transferred to the preparation chamber.

The preparation chamber acts as a buffer between the high vacuum obtained in the load-lock and the UHV inside the growth chamber. It is equipped with an ion pump to pump down from high to ultra high vacuum. Similarly to the load-lock, the preparation chamber is equipped with a heating stage, which can heat wafers up to 600 °C. This second pre-growth high temperature outgassing ensures desorption of almost all the evaporable contaminants from the surface of the wafers before entering the growth chamber. Removal of the thin oxide layer present on the surface of wafers can also be performed in the preparation chamber although most growers prefer to perform this step inside the growth chamber where a better control over the oxide removal process can be achieved.

The growth chamber is the most important and the most sensitive part of the MBE system as the high-precision high-quality epitaxial growth is performed there. Figure 2.2 shows

the usual configuration of a growth chamber.[15] The substrate wafer is placed in the centre of the chamber on a substrate holder. The substrate holder rotates perpendicularly to the growth direction in order to ensure a homogenous epitaxy. A substrate heater, mounted behind the substrate holder, is used to heat up the sample wafer. Temperatures over 1000°C, suitable for oxide removal of Si substrates, can be reached. An ion gauge is mounted on the back of the substrate holder and the substrate heater to measure the pressure within the growth chamber and calibrate flux rates. The substrate holder, substrate heater and ion gauge are mounted together on a manipulator used to precisely position them inside the chamber. Three positions are usually used during MBE growth operations:

1. Substrate holder facing the effusion cells during growth with the ion gauge protected behind the growth stage,
2. Substrate holder facing the exchange port to load/unload wafers from/to the preparation chamber,
3. Ion gauge facing the effusion cells for calibration of the flux rates with the substrate holder protected behind the growth stage.

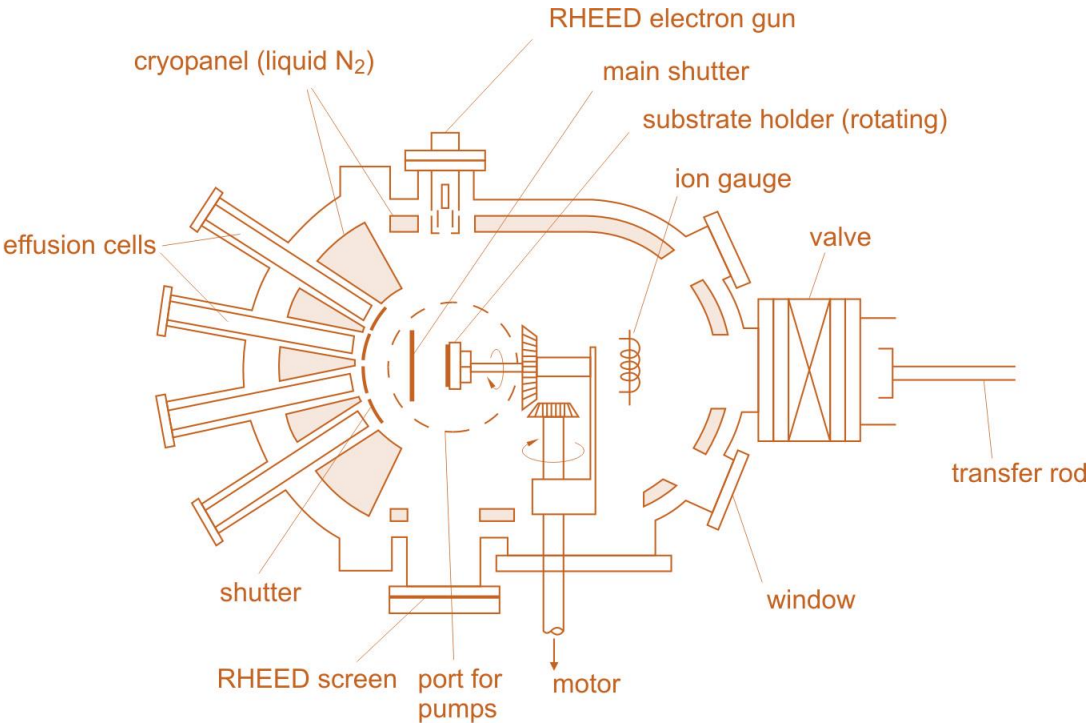

Figure 2.2 Schematic diagram of a classical MBE growth chamber. The image was taken from Ref. 15.

Effusion cells are mounted opposite to the substrate holder in its growth position so that the growth wafer sits at the focal point of the cells. In order to avoid contamination from flakes falling into them or onto the wafer, the effusion cells are attached as horizontally as possible. On top of the ion pump and cryogenic pump ensuring the UHV environment, with background pressures in the 10^{-10} to 10^{-11} torr, a cryopanel surrounds the chamber and separates the effusion cells in order to avoid possible cross-contamination between the sources and to trap contaminants such as water and hydrocarbons on the walls of the growth chamber. The cryopanel consists in a shroud in which a very low temperature coolant such as liquid nitrogen circulates.

The III-V MBE system used here has eleven effusions cells: two Ga, two Al, two In, one As, one Sb and one P cells for growth plus one Si and one Be cells for doping. The growth rate is governed by the group III elements flux rates. Having two cells for each group III element enables different cell temperatures and therefore different growth rates for the same element during one growth run. The high-purity source materials are placed in pyrolytic boron-nitride crucibles inside the effusion cells where their temperature is controlled with an accuracy of ±1 °C. Each material requires a specific effusion cell architecture, involving one, two or three temperature zones. Fast actuation time mechanical shutter are placed in front of each cell to abruptly start or interrupt the deposition of a given material, enabling brusque modifications in material composition and sharp interfaces within the grown sample.

2.1.3 Control of growth chamber conditions

The background pressure inside the growth chamber is monitored using the ion gauge placed at the back of the growth stage, as described earlier. Using the manipulator, the ion gauge can also be directed toward the effusion cells where it can be used to calibrate beams flux rates. In this configuration one cell is calibrated at a time by opening the shutter in front of it and observing the difference between the background pressure and the beam-on pressure measured by the ion gauge.

Thermocouples are used to measure the temperature of the different zones of the effusion cells as well as the temperature of the substrate. Over 450°C, a pyrometer mounted outside of the growth chamber is also used to measure the temperature of the substrate.

The pyrometer performs an optical measurement of the substrate temperature through a viewport by analysing the blackbody radiation from the growth wafer, thus enabling a remote measurement. During each growth run, the known oxide desorption temperature of the wafer used is recorded to add precision to the substrate temperature measurements from the thermocouple and the pyrometer.

2.2 Material characterisations

Special care is essential for the air-sensitive materials during characterisations, such as BPQDs. Since as-grown BPQDs on Si substrates are very reactive to the ambient environment after taking out from the MBE growth chamber, all the conducted characterisations for phosphorus films were finished within 1 hour, followed by preservation in the container filled with pure nitrogen gas. The samples were stored in the box filled with N_2 to avoid air-induced degradation. As for other 2D materials, such as glassy-graphene thin films, MoS_2 nanosheets and $MoS_{2(1-x)}Se_{2x}$ nanosheets, they are stable under ambient conditions when performing material characterisations.

2.2.1 Atomic force microscopy (AFM)

Atomic force microscopy (AFM) is one of the most versatile and powerful microscopy technology for studying materials at nanoscale level. There are three main imaging modes: contact, tapping and non-contact mode, respectively. Operation of AFM systems, for instance, in contact mode, is described below. A sharp tip fixed to a flexible cantilever is put in contact with the surface to be analysed. A laser beam is irradiated on the cantilever and a position-sensitive photodetector measures the deflection of the laser due to the bending of the cantilever, as illustrated in figure 2.3. The stage on which the sample is mounted slowly moves in the horizontal plane under the tip-cantilever ensemble so that the tip slowly brushes the surface. A feedback loop ensures a constant bending of the cantilever by moving the sample up and down depending on position on of the tip on the surface, thus recording the measured height of the sample surface. The major issue of this mode possibly introduces damages to the surface due to the tip grazing it as well as possible distortions in the final image.

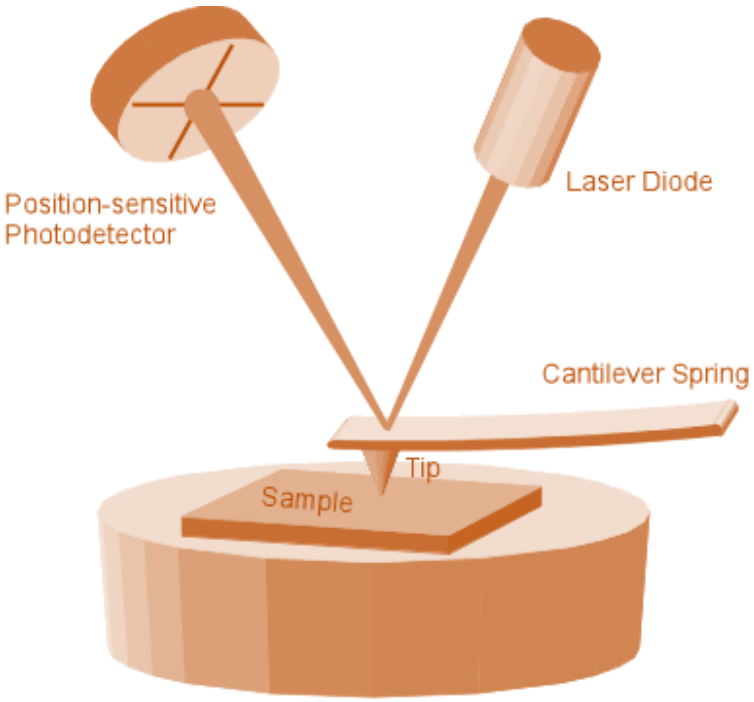

Figure 2.3 Schematic illustration of an AFM operation system.

Tapping mode was used for characterising surface morphology of materials. Instead of direct contact of the tip with sample surface, the cantilever is set to oscillate vertically at a determined frequency. As the tip-cantilever ensemble is brought down on the surface, the oscillating tip will tap the surface, leading to a reduced oscillation amplitude because of the energy dissipated with each tapping. Similarly to the contact mode, a feedback loop ensures constant oscillation amplitude by moving the stage and the sample vertically, thus recording the surface morphology of the sample.

Figure 2.4 and 2.5 show obtained AFM profiles of MoS_2 and glassy-graphene, respectively. Based on the AFM height profile results, the thickness of samples can be determined. Figure 2.6 displays the AFM result of figure 2.5 in a 3D view.

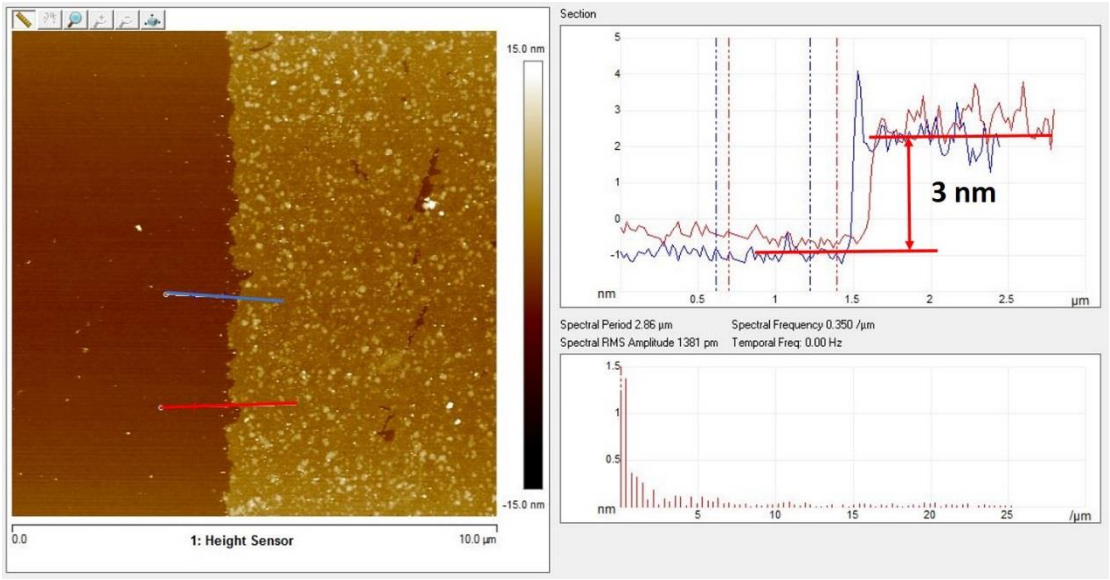

Figure 2.4 AFM image of $MoS_2/SiO_2/Si$ (left). The right figure shows the step height along the blue and red lines in the left figure, revealing the thickness of 3 nm.

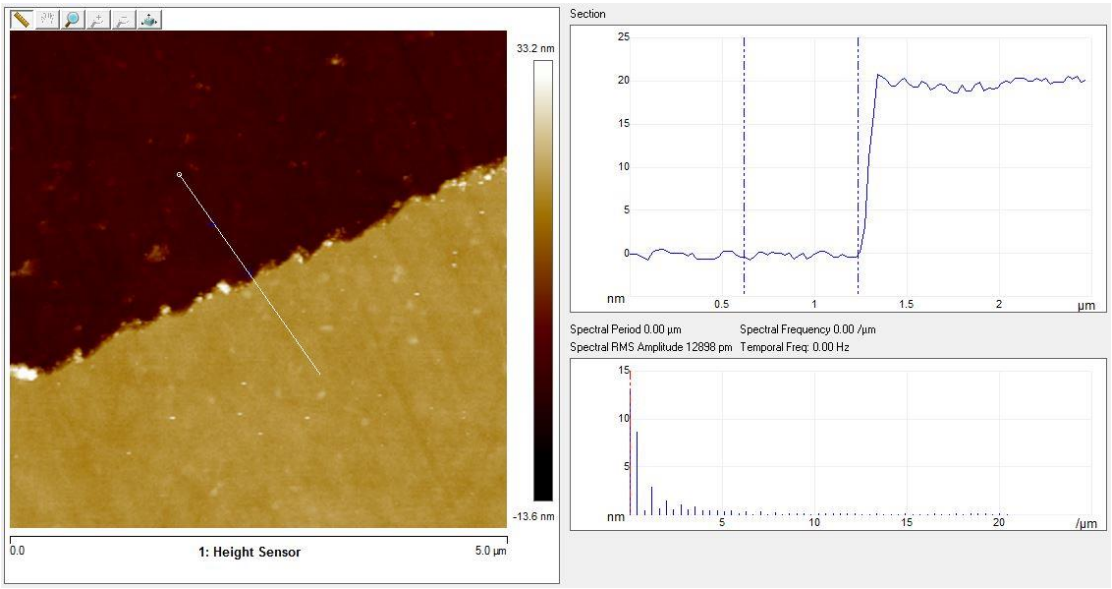

Figure 2.5 AFM image of g-graphene/quartz (left). The right figure shows the step height along the white line in the left figure, revealing the thickness of 20 nm.

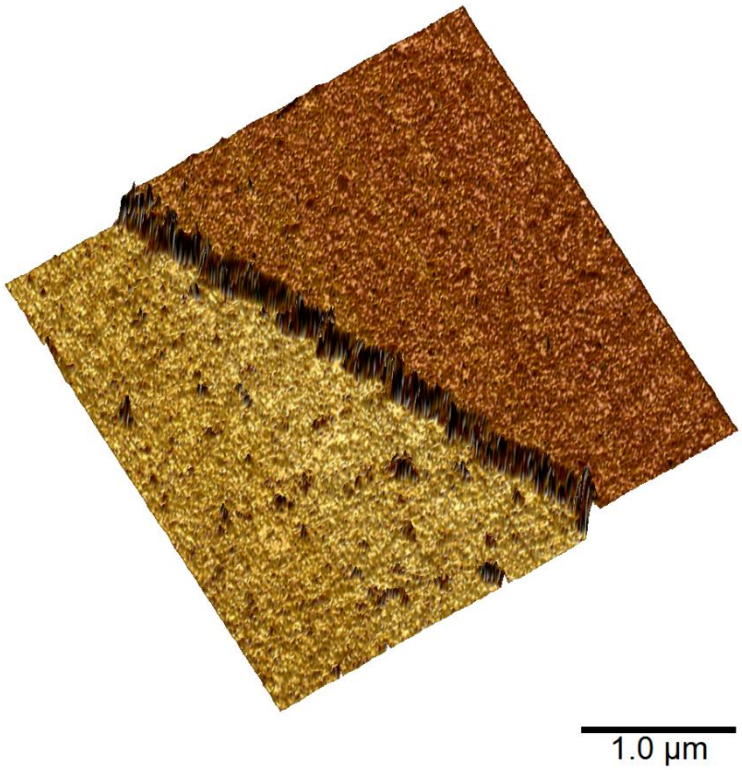

Figure 2.6 3D view of the AFM height profile of 20 nm glassy-graphene/quartz.

2.2.2 Raman spectroscopy

Raman spectroscopy is a spectroscopic technology using Raman scattering to observe phonon (periodic oscillation of atoms in a crystal) vibration in materials, revealing chemical and structural information of materials. It is a commonly used characterisation method in chemistry and material science. Raman scattering is an inelastic scattering caused by monochromatic light and happened when incident light (such as visible, near IR or near ultraviolet (UV) *etc*.) interacts with phonons of materials, leading to light photon energy being shifted up or down.

This energy shift provides information about Raman-active phonon modes in materials, which can be observed in Raman spectra. In Raman spectra, each resolved peak corresponds to one specific Raman-active phonon mode, and the frequency (wavenumber) and full width at half maximum (FWHM) of Raman peak are associated with inherent properties of materials, such as purity, thickness, doping level, *etc*. For instance, Raman spectrum of MoS_2/glassy-graphene heterostructure is shown in figure 2.7. As can be seen,

each peak was labelled with a particular Raman-active modes, and peak 2D and peak D+G were overlapped due to changed crystal structure and thickness.

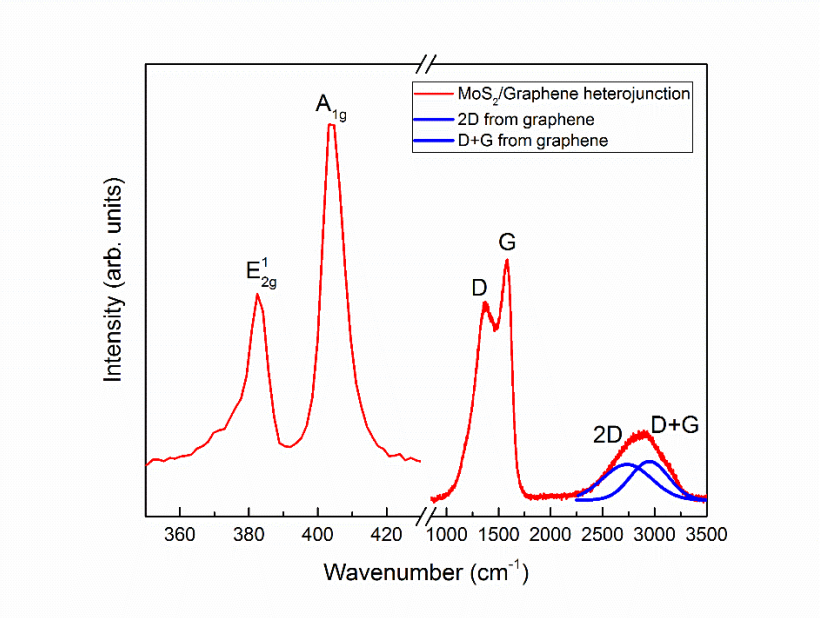

Figure 2.7 Raman spectrum of MoS_2/glassy-graphene heterostructure. The blue curves represent the fitted peaks.

During the process of incident laser irradiation, photons from the laser are absorbed by the sample and then reemitted, resulting in three different scattering modes: Rayleigh scattering, Stokes Raman scattering and anti-Stokes Raman scattering, in which the former one is an elastic process and the latter two are inelastic processes. In Rayleigh scattering, the reemitted light has the same frequency as the incident light, without frequency changed. In Stokes Raman scattering, partial energy (corresponding frequency of v_m) from incident light photons is absorbed by the Raman-active phonon modes, leading to the frequency of scattered light reduced by v_m. In anti-Stokes Raman scattering, oppositely, the frequency of scattered light is increased by v_m, resulting from released excessive energy of already excited Raman-active phonon modes.

A classical Raman system is composed of five main components: excitation source (laser), sample illumination system and light collection optics, microscope, wavelength selector (filter or spectrophotometer), and detector (photodiode array or charge-coupled device (CCD)), as shown in figure 2.8.[16]

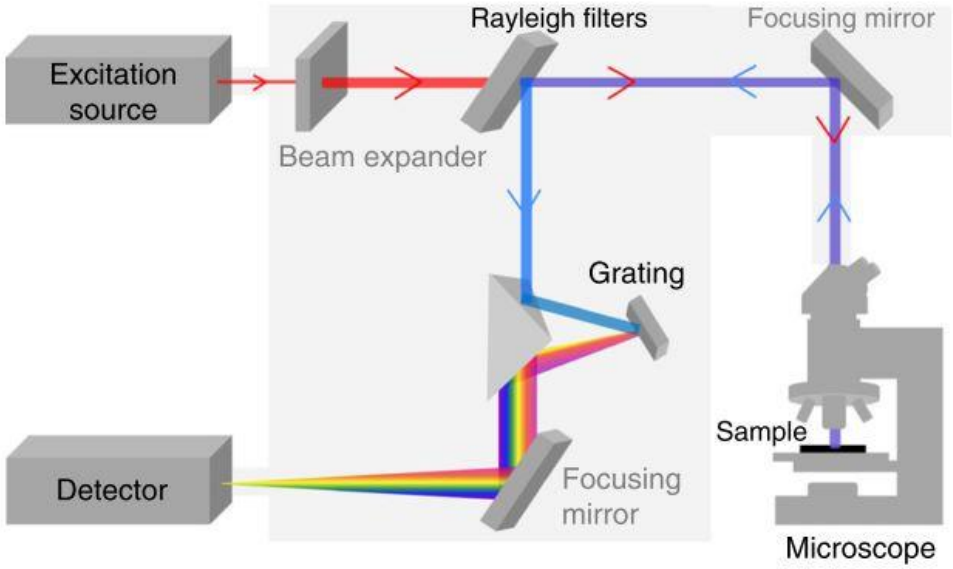

Figure 2.8 Schematic diagram of Raman spectrometer system. The image was taken from Ref. 16.

2.2.3 X-ray photoelectron spectroscopy (XPS)

X-ray photoelectrons spectroscopy (XPS) is a quantitative spectroscopic technique and used for characterising the surface chemistry of electrically conducting and non-conducting materials, which is one of the most widely used surface analysis techniques. It can provide valuable quantitative and chemical state information from the surface (average depth of analysis is about 5 nm) of studied materials. It is able to analyse elemental composition of samples with a sensitivity of up to 0.1%. In addition, angle-resolved XPS can investigate material thickness and depth distribution of different chemical species.

When an X-ray beam (we use Al Kα here) irradiates the surface of samples under a UHV condition (up to 10^{-9} millibar), X-ray photons will hit and then transfer their energy to electrons in samples. As a result, excited photoelectrons will emit from their initial states with kinetic energy associated with the incident X-ray photons and intrinsic binding energy of the atoms. The energy and intensity of the emitted photoelectrons are detected and analysed to determine the elemental concentrations of samples. These photoelectrons originate from a depth of less than 10 nm therefore the information obtained is from

within this depth. A typical XPS system mainly consists of a source of X-ray (commonly Al Kα or Mg Kα), a UHV chamber, lens system, electron analyser and electron multiplier, as illustrated below. The schematic configuration of XPS system is shown in figure 2.9.

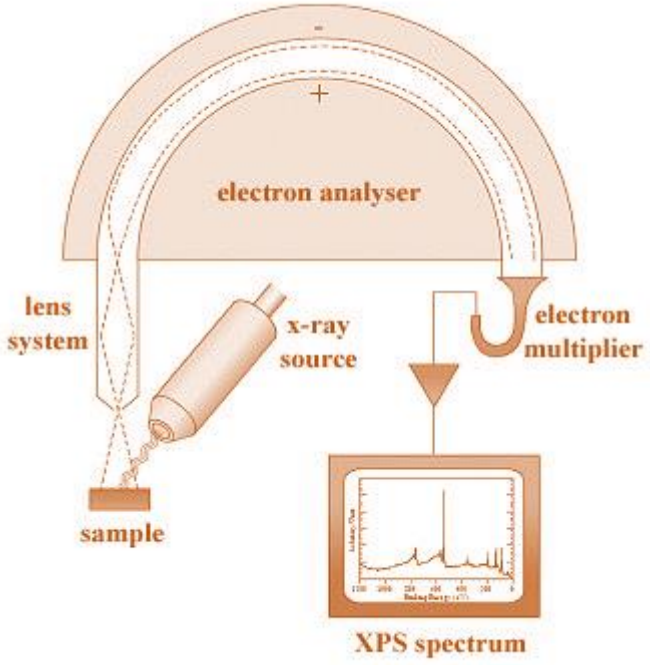

Figure 2.9 Schematic diagram of a typical XPS system.

2.2.4 Transmission electron microscopy (TEM)

Transmission electron microscopy (TEM) is a microscopy imaging technique using electron beam instead of light (optical microscopy) transmitted through target thin samples. The prepared target samples have thickness of less than 100 nm, alternatively, they are suspended on a grid. Due to smaller de Broglie wavelength of electrons than wavelength of photons, TEM is capable of imaging in significantly higher resolution than conventional optical microscopy, which is able to capture fine profile as small as a single atom (see figure 2.10). TEM now has become a major characterisation method in physical and chemical research areas.

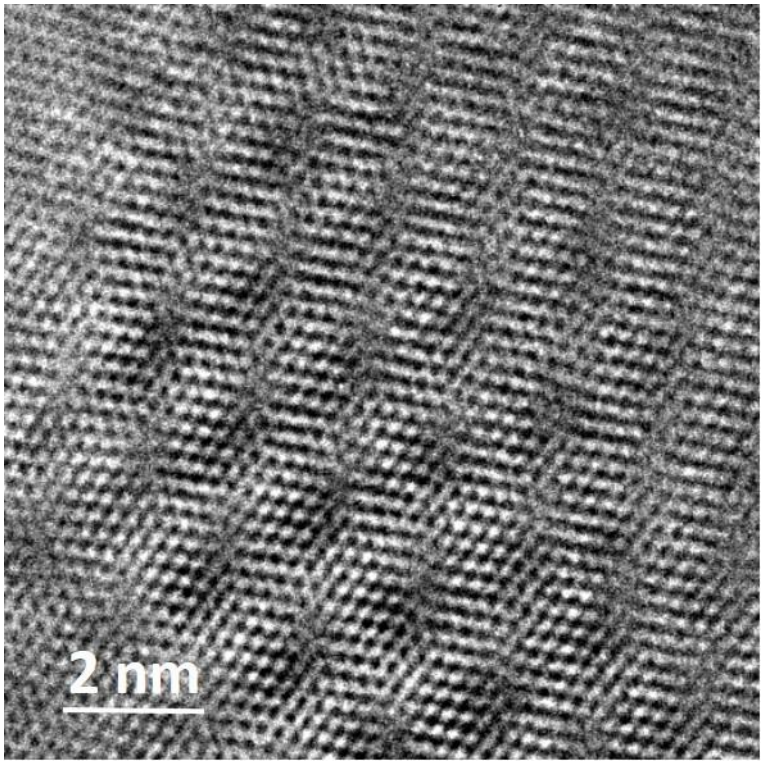

Figure 2.10 TEM figure of MoS_2 nanosheet synthesised by PAD method, showing clear crystal structure in atomic level.

TEM operation principle is described below and the schematic configuration of TEM system is shown in figure 2.11. Generally, TEM operates on the same mechanism as the optical microscopy does but uses electrons instead of photons. Electrons are emitted from an emission source, which can be a tungsten filament or needle, and travel through vacuum column in the microscope. In this process, the electrons are focused into a very thin beam by multiple electromagnetic lenses, after which electron beam transmits through the target specimen with different density (caused by such as defect, doping, *etc*.). Consequently, some of electrons are scattered and disappear from the electron beam. The remained unscattered electrons arrive the bottom of the microscope and hit a fluorescent screen (or CCD), giving rise to an image of the target specimen.

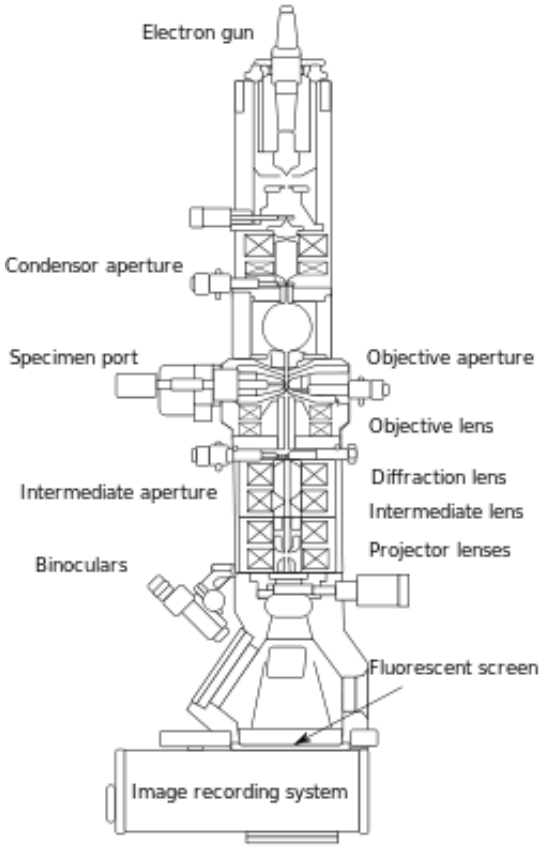

Figure 2.11 Schematic configuration of a typical TEM system. Reprint with permission: https://commons.wikimedia.org/wiki/File:Scheme_TEM_en.svg.

2.2.5 Photoluminescence (PL)

Photoluminescence (PL) is an important analysis technique as, contrary to structural characterisation tools such as AFM, XRD and TEM, it gives direct information on the optoelectronic properties of the grown sample before its processing into devices.

A PL setup usually consists in a laser with a bandgap higher than the expected bandgap of the measured sample, a sample stage or holder, an optical system including lenses and a monochromator and a detector coupled with a signal analyser software. The laser is beamed on the sample, exciting electrons from the valence to the conduction band and leading to a high concentration of free electrons and holes in the sample. These free carriers will recombine after some time, in particular through band-to-band radiative emission. These reemitted photons are collected by the optical system and focused on the detector. The monochromator decompose the incoming emitted light by wavelength,

giving access to the spectral response of the sample. The peak of the wavelength-dependent intensity of the PL spectrum gives the bandgap of the sample. In the case of a more complex structure including multiple materials or low dimension structures such as quantum wells or quantum dots, multiple peaks will be observed, each peak corresponding to a different structure or material.

Moreover, as radiative recombinations compete with non-radiative ones inside the photo-excited sample, comparing the amplitude of the PL peaks between different samples gives information on the relative material quality and defect densities between the samples. Indeed, the non-radiative recombination rate is directly related to the defect density whereas the radiative recombination rate is mainly governed by the material band structure. As a result the PL peak amplitude informs on the ratio between the radiative and the non-radiative recombination rates. Comparing different samples made of the same material; the sample with the highest material quality exhibits the strongest PL peak and can thus be determined.

2.3 Device fabrication

2.3.1 General process

All the fabrication mentioned in this thesis was performed in the cleanroom of London Centre for Nanotechnology (LCN). As thickness of 2D materials is down to few nanometres, they are weak and fragile during the fabrication process, for instance, cleaning with sonication, peel-off when dipped into acetone solution, *etc*., which needs to optimise traditional recipes for general use.

General process was performed before further device fabrication, as listed below:

1. Cleaving samples into square chips using a diamond-tipped scriber. For glassy-graphene on quartz samples, scribing process was repeated for at least 7 times to avoid cracking when cleaving. For MoS_2 on SiO_2/Si samples, repeating scribing process for 3 times was enough to cut off the substrates.

2. Cleaning samples with three different solutions by the following order: acetone with sonication for 1 min, then rinsed by isopropanol (IPA) and finally deionised (DI) water.
3. Baking samples at 115 °C on the hotplate for 1 min.

2.3.2 Photolithography

Photolithography is a widely used technique in device microfabrication process, especially for nanotechnology, which is capable of covering samples selectively based on a predesigned photo-mask with photoresist (a kind of optical-active chemical species). With this processing, specific areas on samples are covered by photoresist after exposed under UV light, and protected when performing metal deposition or etching. The photolithography machine of Karl Suss MJB3 Mask Aligner in LCN has a resolution of 1 μm in theory. The photoresist we used for our device fabrication is S1818 that will form a uniform layer onto samples with a thickness of approximate 1.8 μm.

Photolithography combined with subsequent metallization and lift-off is a commonly conducted process during device fabrication. The flow chart of this process is shown in figure 2.12. The photoresist (S1818 in the following experiments) is first spin coated onto as-cleaned sample with a spinning rate of 6000 rounds per second for 60 s, forming a transparent and even layer. Then sample is loaded into mask aligner under a photo-mask, exposed by UV light with specific time (the exact time is calculated based on the reflectivity and transparency of samples). The sample is soaked into developing solution (such as MF-319 and MF-26A) to remove exposed photoresist, revealing target areas of the sample. At next step, sample is loaded into metallization system (such electron-beam evaporator, thermal evaporator, etc.) for depositing contact metals, followed by soaking into 1165 solution (or acetone) to finish lift-off.

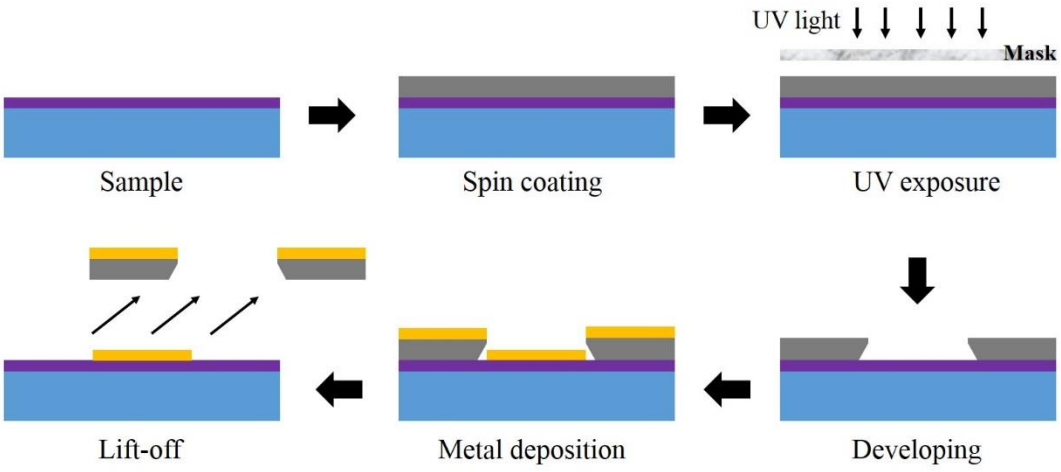

Figure 2.12 Flow chart of common photolithography-metallisation-lift off process.

2.3.3 Dry and wet etching

Plasma etching uses plasma treatment and is a kind of dry etching techniques widely used in nanotechnology fabrication. Particular plasma etching source is selected and accelerated to gain energy, then shot onto sample surface and collide with atoms on sample surface, then interact (physically or chemically) with them. As plasma is in high speed and high energy conditions, three different processes, including excitation, dissociation and ionisation, can happen, depending on the selected etching source. In addition, for instance, if the etching source can chemically react with sample, then the plasma processing will produce volatile etch products that will be removed away by the plasms etching system.

According to the following chemical reaction formula (2.1), in this case, a Diener Plasma Asher was employed and oxygen (O_2) was used as the plasma etching source to etch away unwanted glassy-graphene, as illustrated in figure 2.13. Figure 2.14 shows the microscopy image of patterned glassy-graphene/quartz after O_2 plasma etching.

$$C + O_2 \rightarrow CO_2 \tag{2.1}$$

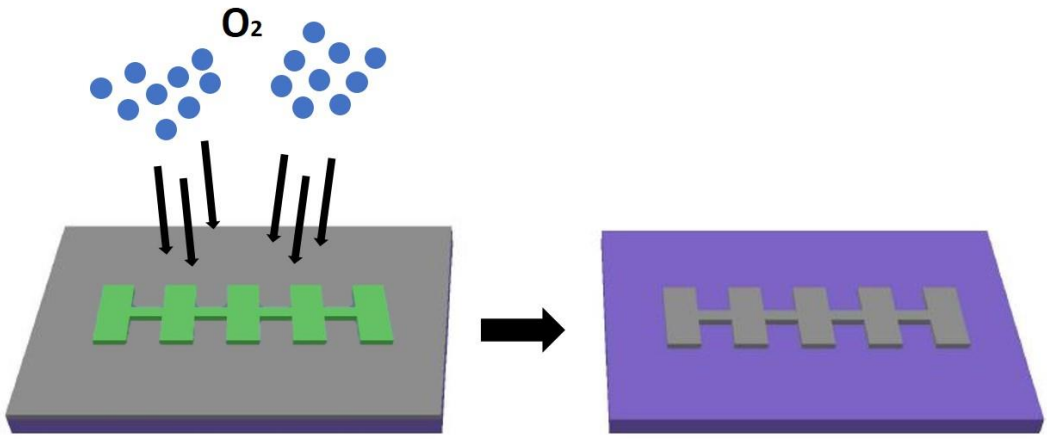

Figure 2.13 Schematic diagram of oxygen plasma etching at the glassy-graphene thin film. The green and grey patterns denote covered photoresist and g-graphene, respectively.

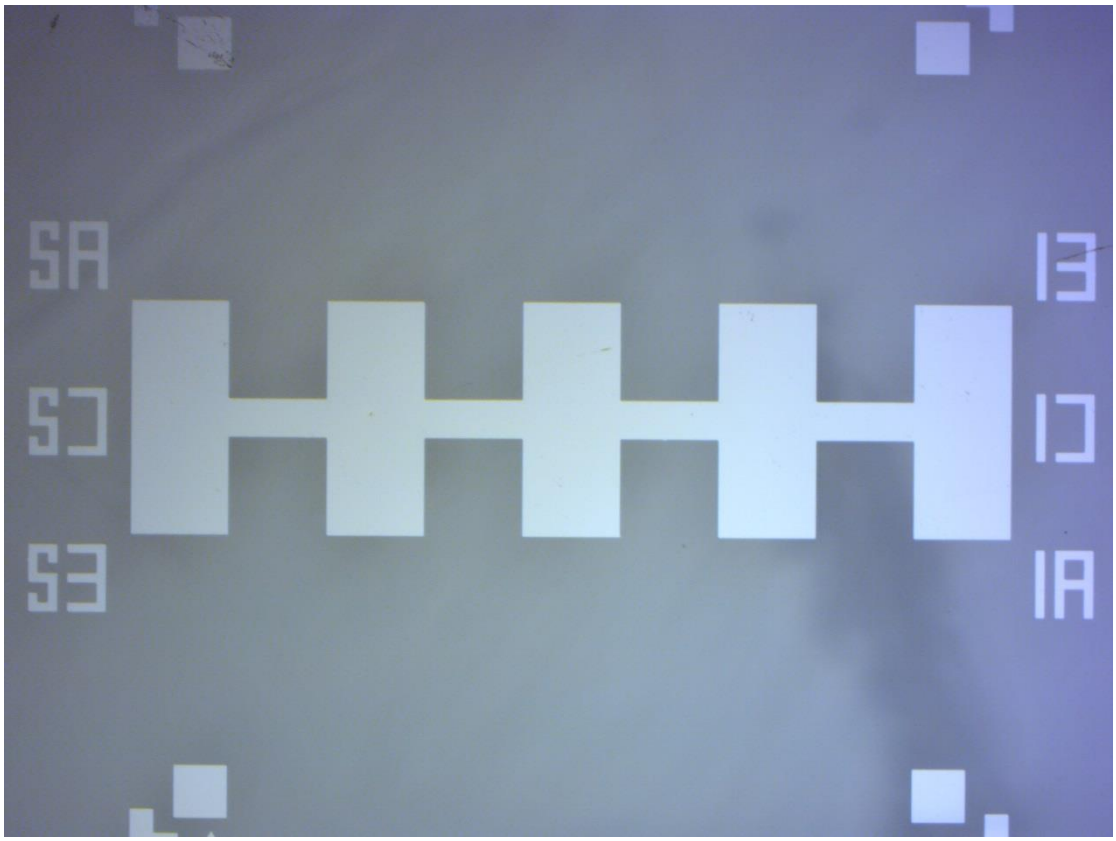

Figure 2.14 Optical microscope image of patterned glassy-graphene nanosheet on quartz.

On the other hand, wet etching is employed, which is a material removal process and is involved with chemical solutions to etch away materials. Based on the following chemical reaction (2.2), in our device fabrication, 1 M KOH solution at 80 °C was used to etch the interface between MoS_2 and SiO_2 to separate them.

$$KOH + SiO_2 \xrightarrow{80\ ^\circ C} K_2SiO_3 + K_2Si_4O_5 + H_2O \quad (2.2)$$

2.3.4 Electron beam lithography

Electron beam lithography (EBL), using a focused electron beam for exposing, is a powerful patterning technique for creating nano-patterns or nanostructures down to nm-scale that are out of the resolution of conventional photolithography. EBL is employed in my research to pattern metal electrodes of photodetectors, phototransistors and field-effect transistors enabled by 2D material nanosheets. The lithography process is similar to the one used for photolithography. A plastic electron beam sensitive resist layer of Poly(methyl methacrylate) (PMMA) is spin-coated onto the sample first. It can be spin-coated easily and uniformly on the sample surface. The desired patterns are exposed with local electron beam equipped in the EBL system.

The PMMA is an e-beam sensitive material with long polymer chains that break at a certain dose of e-beam exposure. The higher e-beam energy has a smaller effective cross section, so it penetrates the PMMA and scatters less, which allows for much finer features to be created. PMMA comes with different molecular weights and can be dissolved in different solvents. The electron beam dose needed to break the PMMA chains depends on its molecular weight: PMMA with low molecular weight is more sensitive to e-beam exposure than one with larger molecular weight. For depositing thick metal layers or large structures, it is useful to use PMMA with double layers.

The PMMA resist is deposited on the sample at first. The pre-designed patterns using AutoCAD (pattern design software) are written into the PMMA resist with the electron beam in a scanning electron microscope. The electron beam comes to a halt and transfers its kinetic energy to break the chemical bonds of the PMMA. It can be easily removed by a developer using 1:3 solution of MIBK and IPA. After EBL patterning, metallisation is

performed. Afterwards, the remaining PMMA resist and metal is dissolved in 1165 solution for the lift-off treatment.

2.3.5 Metal contact pad deposition

Electron-beam evaporation technique is used to deposit metal contact pads onto as-processed samples. It is a powerful physical vapour deposition process, allowing us depositing very thin metal onto target materials. In the evaporation system, electrons are generated from a filament applied with electrical current and a high energy electric field. Then the electrons are focused into a beam by magnets and travel towards the metal of interest. As a result, the metal begins to melt and then evaporate after the electron beam hit it and transfer the energy to it.

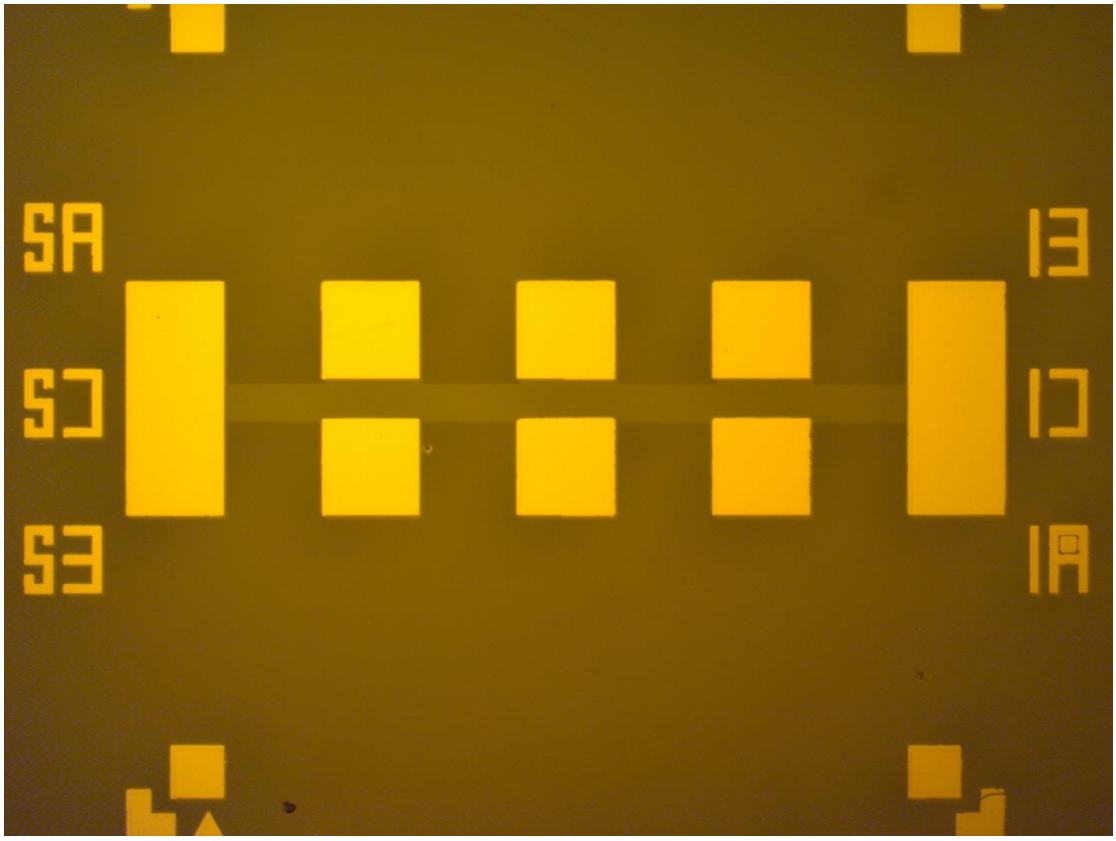

Figure 2.15 Optical microscope image of patterned g-graphene nanosheet with Ti/Au Ohmic contact pads.

The machine of A500 electron beam evaporator in LCN can fine control metal deposition rate. The vacuum in the evaporation chamber can reach up to 10^{-8} mBar level to ensure good metal-material Ohmic contacts. Considering metal work function, we select Titanium (Ti) as the adhesion layer to 2D material, and the target deposition thickness is 10 nm to avoid break 2D nanosheets. Subsequently, 50 nm Gold (Au) is deposit onto 10 nm Ti to form good Ohmic contact. Figure 2.15 exhibits an optical microscope image of patterned g-graphene with Ti/Au Ohmic contact pads.

2.3.6 Wire bonding

GE varnish is used to glue chips to the 20 pin non-magnetic ceramic chip carriers. Chips mounted with GE varnish can be removed by using a 1:1 mixture of ethanol: trichloroethylene solution. We used the wire-bonder in LCN to connect the metal pads on the dvices to the pads on the chip carrier, using Au wire (with a diameter of 25 μm). A digital image of a bonded chip glued in a logic chip carrier (LCC) and wired up LCC is shown in Figure 2.16.

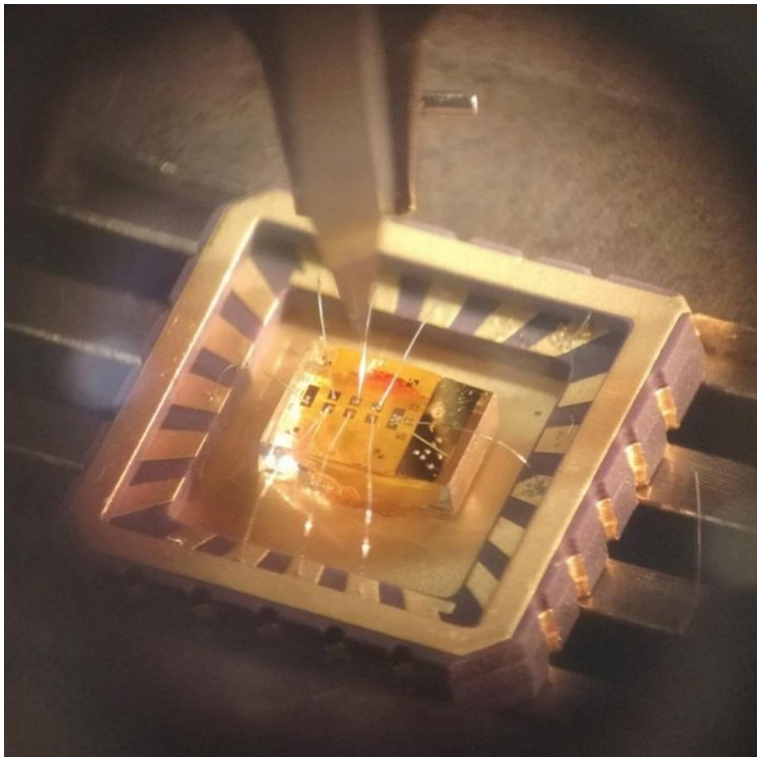

Figure 2.16 Digital photograph of glassy-graphene device wire-bonded to LCC.

2.4 Device performance characterisations

Keithley 4200 semiconductor characterisation system is employed to characterize photoexcited current-voltage (I-V) curves of devices under dark and monochromatic light illumination conditions, respectively. Blue, green and red laser pointers, whose wavelength is 405 nm, 532 nm and 656 nm, respectively, are used as the monochromatic light sources. The I-V curves under solar illumination is traced using a calibrated solar simulator to irradiate devices. The solar simulator approximates the AM 1.5G spectrum with a power density of around 1000 W/m^2. As for the electrical performance characterisations for field-effect transistors, four-terminal test mode is employed to obtain output curves and transfer curves. The four probe stations are connected to drain, source, gate and ground terminals, respectively.

2.5 References

(1) Manzeli, S.; Ovchinnikov, D.; Pasquier, D.; Yazyev, O. V.; Kis, A. 2D Transition Metal Dichalcogenides. *Nat. Rev. Mater.* **2017**, *2*, 17033. https://doi.org/10.1038/natrevmats.2017.33.

(2) Garcia, J. M.; Wurstbauer, U.; Levy, A.; Pfeiffer, L. N.; Pinczuk, A.; Plaut, A. S.; Wang, L.; Dean, C. R.; Buizza, R.; Van Der Zande, A. M.; et al. Graphene Growth on H-BN by Molecular Beam Epitaxy. *Solid State Commun.* **2012**, *152* (12), 975–978. https://doi.org/10.1016/j.ssc.2012.04.005.

(3) Park, J.; Mitchel, W. C.; Grazulis, L.; Smith, H. E.; Eyink, K. G.; Boeckl, J. J.; Tomich, D. H.; Pacley, S. D.; Hoelscher, J. E. Epitaxial Graphene Growth by Carbon Molecular Beam Epitaxy (CMBE). *Adv. Mater.* **2010**, *22* (37), 4140–4145. https://doi.org/10.1002/adma.201000756.

(4) Zhang, J. L.; Zhao, S.; Han, C.; Wang, Z.; Zhong, S.; Sun, S.; Guo, R.; Zhou, X.; Gu, C. D.; Yuan, K. Di; et al. Epitaxial Growth of Single Layer Blue Phosphorus: A New Phase of Two-Dimensional Phosphorus. *Nano Lett.* **2016**, *16* (8), 4903–4908. https://doi.org/10.1021/acs.nanolett.6b01459.

(5) Derivaz, M.; Dentel, D.; Stephan, R.; Hanf, M. C.; Mehdaoui, A.; Sonnet, P.; Pirri, C. Continuous Germanene Layer on Al(111). *Nano Lett.* **2015**, *15* (4), 2510–2516. https://doi.org/10.1021/acs.nanolett.5b00085.

(6) De Crescenzi, M.; Berbezier, I.; Scarselli, M.; Castrucci, P.; Abbarchi, M.; Ronda, A.; Jardali, F.; Park, J.; Vach, H. Formation of Silicene Nanosheets on Graphite. *ACS Nano* **2016**, *10* (12), 11163–11171. https://doi.org/10.1021/acsnano.6b06198.

(7) Stephan, R.; Hanf, M. C.; Derivaz, M.; Dentel, D.; Asensio, M. C.; Avila, J.; Mehdaoui, A.; Sonnet, P.; Pirri, C. Germanene on Al(111): Interface Electronic States and Charge Transfer. *J. Phys. Chem. C* **2016**, *120* (3), 1580–1585. https://doi.org/10.1021/acs.jpcc.5b10307.

(8) Morishita, T.; Spencer, M. J. S.; Kawamoto, S.; Snook, I. K. A New Surface and Structure for Silicene: Polygonal Silicene Formation on the Al(111) Surface. *J. Phys. Chem. C* **2013**, *117* (42), 22142–22148. https://doi.org/10.1021/jp4080898.

(9) Smith, J. B.; Hagaman, D.; Ji, H.-F. Growth of 2D Black Phosphorus Film from Chemical Vapor Deposition. *Nanotechnology* **2016**, *27* (21), 215602.

https://doi.org/10.1088/0957-4484/27/21/215602.

(10) Mahjouri-Samani, M.; Lin, M.-W.; Wang, K.; Lupini, A. R.; Lee, J.; Basile, L.; Boulesbaa, A.; Rouleau, C. M.; Puretzky, A. A.; Ivanov, I. N.; et al. Patterned Arrays of Lateral Heterojunctions within Monolayer Two-Dimensional Semiconductors. *Nat. Commun.* **2015**, *6*, 7749. https://doi.org/10.1038/ncomms8749.

(11) Xia, F.; Wang, H.; Xiao, D.; Dubey, M.; Ramasubramaniam, A. Two-Dimensional Material Nanophotonics. *Nat. Photonics* **2014**, *8* (12), 899–907. https://doi.org/10.1038/nphoton.2014.271.

(12) Novoselov, K. S.; Fal'ko, V. I.; Colombo, L.; Gellert, P. R.; Schwab, M. G.; Kim, K. A Roadmap for Graphene. *Nature* **2012**, *490* (7419), 192–200. https://doi.org/10.1038/nature11458.

(13) Cho, A. Y. Epitaxial Growth of Gallium Phosphide on Cleaved and Polished (111) Calcium Fluoride. *J. Appl. Phys.* **1970**, *41* (2), 782. https://doi.org/Doi 10.1063/1.1658749.

(14) Cho, A. Y. Morphology of Epitaxial Growth of Gaas by a Molecular Beam Method - Observation of Surface Structures. *J. Appl. Phys.* **1970**, *41* (7), 2780–2786. https://doi.org/Doi 10.1063/1.1659315.

(15) H. Ibach; H. Luth. *An Introduction to Principles of Materials Science*; Springer Science & Business Media, 2009.

(16) Butler, H. J.; Ashton, L.; Bird, B.; Cinque, G.; Curtis, K.; Dorney, J.; Esmonde-White, K.; Fullwood, N. J.; Gardner, B.; Martin-Hirsch, P. L.; et al. Using Raman Spectroscopy to Characterize Biological Materials. *Nat. Protoc.* **2016**, *11* (4), 664–687. https://doi.org/10.1038/nprot.2016.036.

Chapter 3 MBE Growth of Few-Layer Back Phosphorene Quantum Dots

3.1 Research Background and Result Overview

3.1.1 Research background

In contrast to corresponding three-dimensional (3D) configurations, two-dimensional (2D) materials are scaled down with thickness and possess novel physical and chemical features, one major reason for which is originated from the quantum confinement effect. Substantial effort has been devoted to studying them and exploring their practical applications in photonics, electronics and optoelectronics fields.[1-3] Since the first discovery of graphene by the mechanical exfoliation method in 2004, more materials have been introduced to the 2D family, including black phosphorene (BP), hexagonal boron nitride (h-BN), transition metal dichalcogenides (TMDs), MXenes, silicene, germanene, *etc*.[4-12]. Different techniques have been developed to synthesise 2D materials, which are

mainly divided into two categories: bottom-up growth and up-down deposition. Epitaxial growth and chemical liquid deposition are representative methods of them, respectively. In terms of practical use, such as chemical sensors, photodetectors, field-effect transistors, light emitting diodes, *etc*., promising 2D materials synthesised with high quality is of much significance, especially for large-scale thin films. Single-crystalline or poly-crystalline lattice structures deliver distinctive impacts on nm-scale device performance. Thanks to the more precise control during material synthesis, epitaxial growth techniques, such as chemical vapour deposition (CVD) and molecular beam epitaxy (MBE), have been extensively employed for preparing 2D material nanoflakes and thin films, including pristine graphene, TMDs, stanene and silicene. [13-16]

BP nanosheets with graphene-like layered crystal structures were first discovered by mechanical exfoliation in 2014, since which it has drawn increasing attention due to intriguing properties.[8,9] For instance, BP possesses a tunable bandgap that can be changed by layer number, doping types and strain. In addition, pristine BP with p-type gate tunability, high carrier mobility and intrinsic anisotropy in electron conductance, were also demonstrated.[17,18] Notably, BP is inevitable to undergo performance degradation when exposed to ambient conditions. Figure 3.1 shows that the mechanically exfoliated BP nanosheets were etched away by air layer by layer after storing in ambient conditions for more than four weeks, with almost no BP left on the substrate surface. The clearly observed droplets were resulted from absorbed water from air due to strong hydrophilicity of BP.

Currently, BP nanosheets were mostly synthesised using top-down methods that are relatively poor in quality control, including mechanical and liquid exfoliation.[19-23] Although preparing BP by phase transition from red phosphorus powders has been realised , it was conducted under very harsh experimental conditions, namely high pressure and high temperature.[24,25] To date, no published work has reported that BP was grown by the MBE technique, while it has been successfully introduced to prepare blue phosphorene nanosheets, a novel allotrope of BP.[26,27] Therefore, studying BP synthesis using a bottom-up technique with good crystalline and thickness control is essential, especially for further inch-scale synthesis.

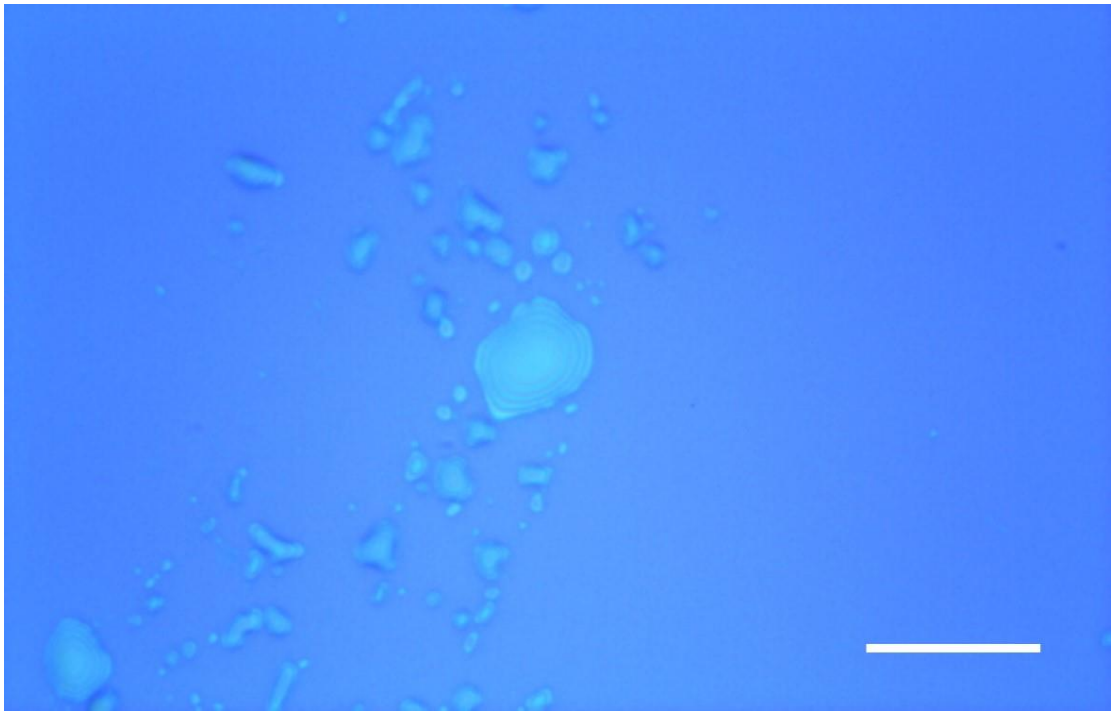

Figure 3.1 Optical microscopy image of non-encapsulated BP nanosheets on the SiO_2/Si substrate after exposing to ambient conditions for more than four weeks. The nanosheets were prepared by mechanical exfoliation method. The scale bar is 10 µm.

3.1.2 Result overview

Few-layer black phosphorene quantum dots (BPQDs) were grown on 3-inch Si substrates directly using MBE technique for the first time. Epitaxial growth of BPQDs with phase transition from white phosphorus was performed on Si(111) and Si(100), and the full deoxidisation for the substrates to remove the native surface oxides was carried out at 20 °C and 15 °C, respectively. Detailed material characterisations were conducted to evidence the existence of BPQDs on Si substrates, including atomic force microscopy (AFM), X-ray photoelectron spectroscopy (XPS) and Raman spectroscopy measurements. The obtained AFM images revealed that the BPQDs on Si(111) exhibited an average radius of 27.5 ± 5 nm and height of 3.1 ± 0.6 nm, shaped in a uniform pyramid configuration, and the edge steps on the Si(111) surface were the preferred sites for BPQD crystallisation. In contrast, AFM results indicated that the BPQDs on non-deoxidised Si(100) were distributed densely and randomly with an average radius between 8 and 14 nm and height between 1 and 2 nm. This was caused by the absence of surface steps on

Si(100) with covered native oxides. The ambient degradation of BPQDs was also studied by exposing samples to air for more than 6 months.

In addition to widely used top-down method, such as mechanical and liquid exfoliation, this work demonstrated a bottom-up method for BP synthesis, which was achieved by phase transition from white phosphorus using a standard MBE system. The successful epitaxial growth of BPQDs provided a good understanding for the BP crystallisation ways and possibility of wafer-size synthesis for further practical applications for electronics and optoelectronics.

3.2 Experimental Methods

3.2.1 MBE growth

A Veeco Gen930 MBE system was used to grow BPQDs on commercially purchased Si(111) and Si(100) wafers. All growth runs were performed by Dr. Jiang Wu. After being thermally outgassed at 600 °C for one hour in the preparation chamber, the wafers were then transferred into a growth chamber in an ultrahigh vacuum equipped with a valved cracker white phosphorus cell. White phosphorus, as one of the most common phosphorus allotropes, is composed of tetrahedral P_4 molecules and each molecule is made up of four phosphorus atoms. As for Si(111) wafers, surface deoxidisation was conducted by heating at > 950 °C for 30 min, which was not performed for Si(100) wafers. When the temperature of wafers was cooled down to 15 ~ 20 °C, the BPQD deposition was conducted by evaporating white phosphorus to the substrate surface. In a cracking zone with high temperature up to 900 °C, the white phosphorus molecules started to crack. It can be expected the P_4 molecules unfolded into buckled structures at the particular sites of substrate surface where can provide stable deposition beds. BP on Si substrates can be obtained when the reformed buckled structures possessed the same bond length and angle as the BP structure. The total deposition time of BPQDs was approximately 20 min, during which the beam flux was maintained at ~ 1×10^{-6} torr. The wafer samples were taken out from the vacuum chamber after epitaxial growth, followed by storing them in a N_2-filled box immediately for the subsequent material characterisations.

3.2.2 Material characterisations

AFM measurements were performed under the tapping-mode in ambient conditions, in a Veeco Dimension V Scanning Probe Microscope System. The surface morphology was scanned under a frequency of 1 Hz using a silicon tip with resonance frequency of 146 ~ 236 kHz, which was finished within 5 min to avoid ambient degradation of BPQDs as much as possible. XPS was used to analyse elemental composition via detecting chemical bonds, in a Thermo Fisher Escalab 250Xi system equipped with an Al-Kα source. Raman spectroscopy measurements were carried out in a Renishaw inVia micro-Raman spectrometer system equipped with a ×50 objective lens. 532 nm laser was chosen as the excitation light source, and its power was set as small as 0.1 mW to avoid local heating impact on BPQDs. For the same purpose, the time for each scattering cycle was only 10 s, which was repeated for 3 times.

3.3 Results and Discussion

Figure 3.2 illustrates a 3D view of a few-layer BPQD, crystallised in a stacked and pyramid-shaped structure. Due to the inherent trend of ambient degradation,[20,28] BPQDs/Si were loaded into the AFM system to scan surface morphology as soon as taken out from the N_2-filled box. Native steps and terraces were clearly observed on the fully deoxidised Si(111) substrate surface, as shown in Figure 3.3. It was obviously noticed that BPQDs were preferable to nucleate at the steps of terraces. This feature was also reported when epitaxially growing self-assembled InAs QDs on GaAs substrates, during which natural surface reconstruction was happened on Si(111) surface.[29]

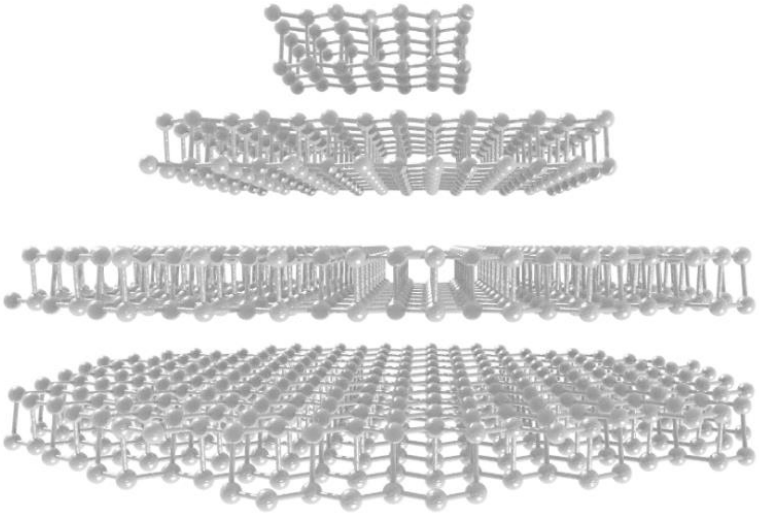

Figure 3.2 3D schematic diagram (side-view) of few-layer BPQDs.

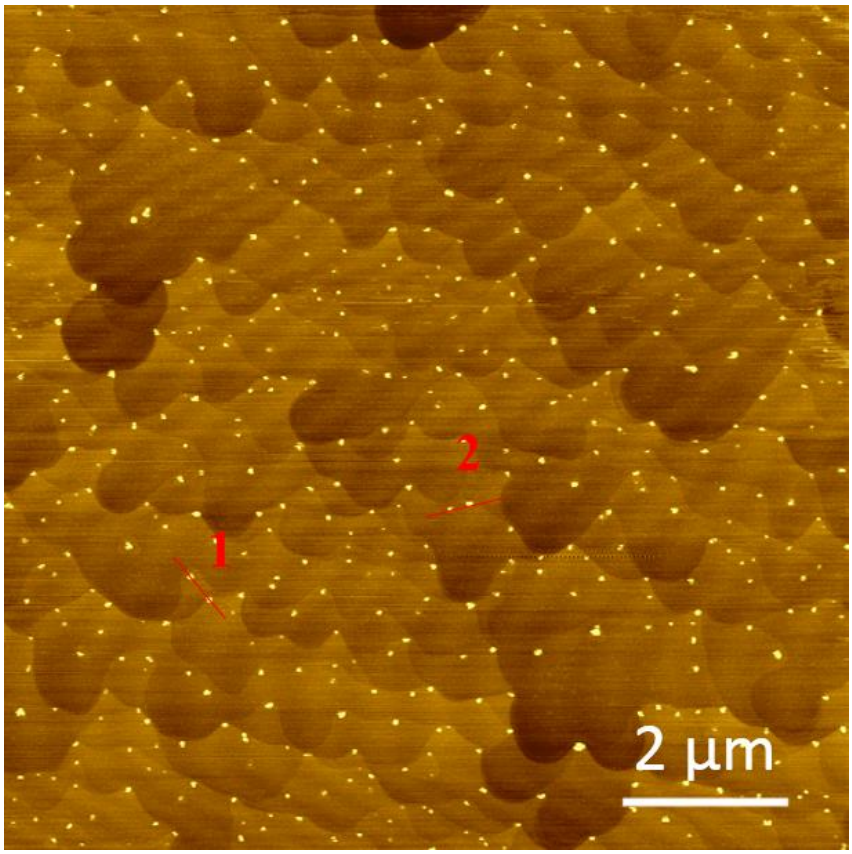

Figure 3.3 AFM image shows the surface morphology of BPQDs on Si(111) substrate, the distribution of the BPQDs and the Si surface steps.

The step-preferred nucleation behaviour in the heterogeneous systems can be explained by the capillarity theory of nucleation, based on which the step edges reduced surface energy of P clusters and thus provided P adatoms with deposition sites. As a result, the BPQD epitaxial growth process could be directed by the edges. In contrast, BPQDs were distributed densely and randomly when grown on Si(100) with native oxide covered on substrate surface and no surface step was observed, as illustrated in Figure 3.4.

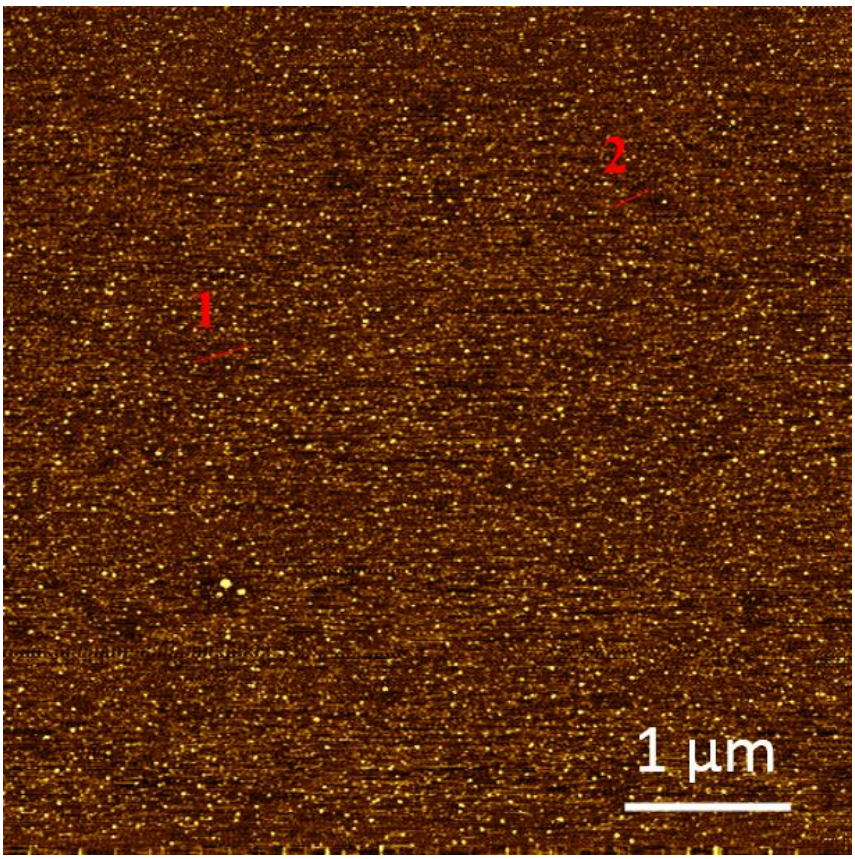

Figure 3.4 AFM image shows the surface morphology of BPQDs on Si(100) substrate and the distribution of the BPQDs. Different from the AFM image shown in Figure 3.3, no surface step was observed here.

Moreover, statistical AFM analysis, which was carried out with the Gwyddion software (a scanning probe microscopy data analysis tool) by setting specific threshold values within selected areas, was introduced to study the surface morphology of BPQDs quantitatively. Figure 3.5 reveals that the BPQDs/Si(111) exhibited an average radius of 27.5 ± 5 nm and height of 3.1 ± 0.6 nm. Height profiles (Figure 3.6) along line 1 and line

2 marked in Figure 3.3 suggested that the BPQDs were shaped in a uniform pyramid configuration when grown on fully deoxidised Si(111) substrates.

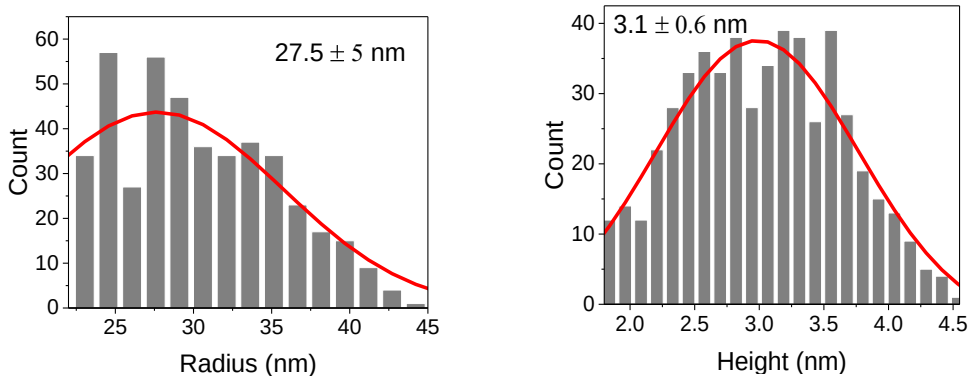

Figure 3.5 The statistical distribution of radius (left) and height (right) of BPQDs on Si(111) substrates. The fitted red curves illustrate the data trend.

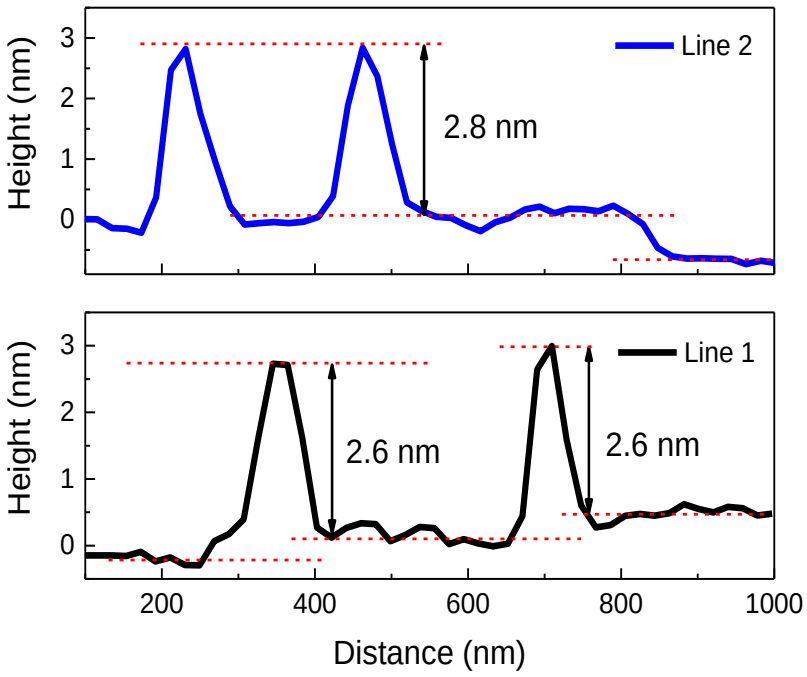

Figure 3.6 Height profiles of BPQDs/Si(111) along line 1 and line 2 labelled in Figure 3.3. The red dashed lines illustrate the Si(111) surface steps.

As compared, the BPQDs/Si(100) showed an average radius between 8 and 14 nm and height between 1 and 2 nm, as displayed in Figure 3.7. According to the height profiles (see Figure 3.8) along line 1 and line 2 labelled in Figure 3.4, the BPQDs/Si(100) were also shaped in a pyramid structure but with smaller thickness. To sum up, the epitaxial growth of few-layer BPQDs could follow the Frank-van der Merwe mode.

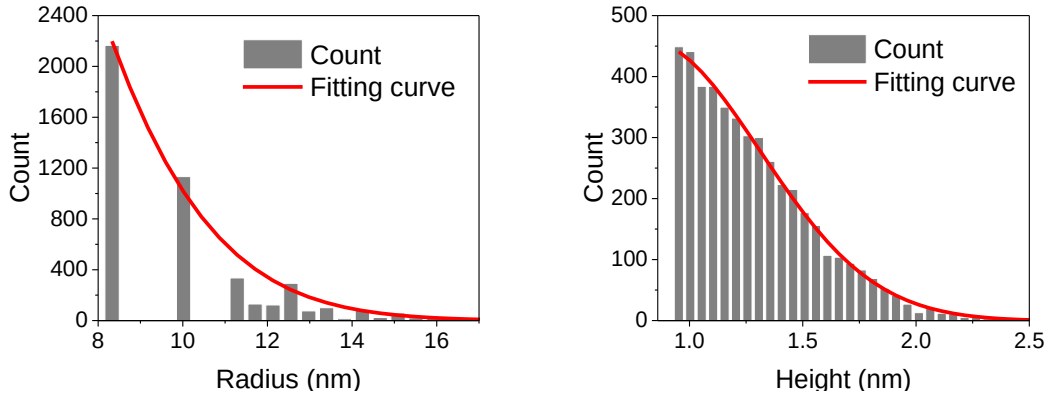

Figure 3.7 The statistical distribution of radius (left) and height (right) of BPQDs on Si(100) substrates. The fitted red curves illustrate the data trend.

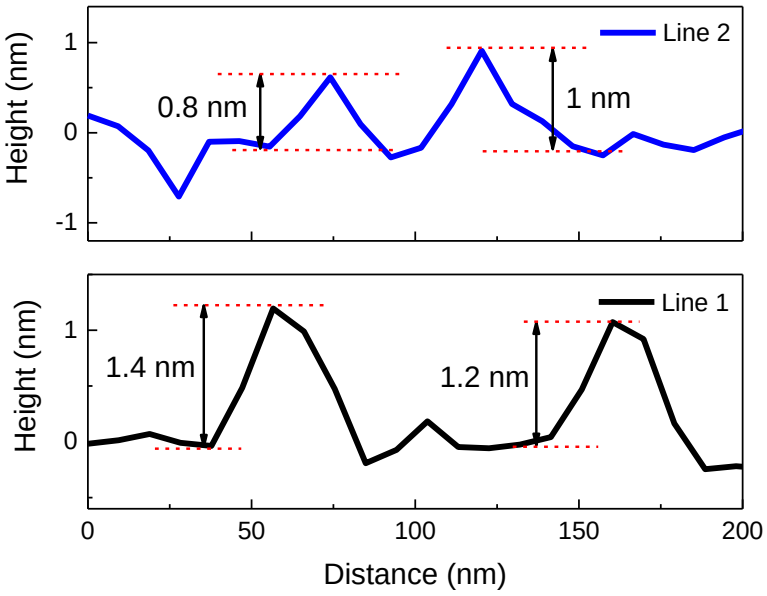

Figure 3.8 Height profiles of BPQDs/Si(100) along line 1 and line 2 labelled in Figure 3.4, suggesting the pyramid configuration and smaller thickness than those grown on Si(111).

To further validate the successful directly epitaxial growth of BPQDs on Si substrates, Raman spectroscopy measurement was carried out. Similarly, the as-grown samples were kept in N_2-filled box before loading into Raman scattering system. Figure 3.9 shows the Raman spectrum of BPQDs on Si(111) substrate, in comparison with that of the Si substrate. Considering the high Raman cross-sections of the 3-inch monocrystalline Si substrate wafer and the low optical absorption of BPQDs, it was reasonable to observe strong background Raman signals from the Si(111) substrate.[30-32] Nonetheless, the three eigen-peaks can still be clearly resolved at 366, 436 and 463 cm^{-1}, and they were correspondingly assigned to out-of-plane A_g^1, in-plane B_{2g} and in-plane A_g^2 phonon modes originated from BPQDs, indicating the deposition of BPQDs on Si(111) substrate.[19,33]

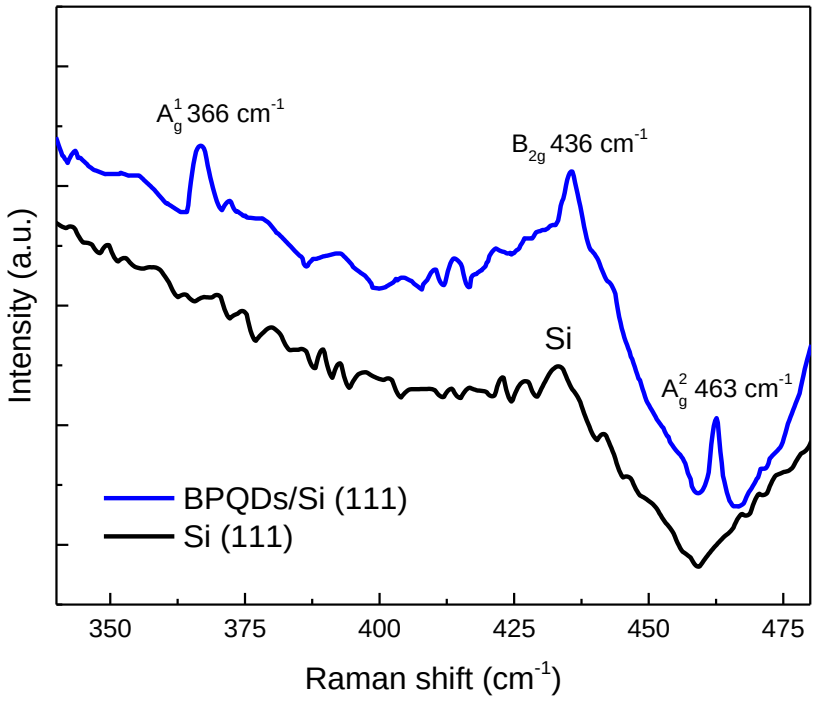

Figure 3.9 Raman spectrum of BPQDs/Si(111), compared with that of Si(111) substrate. The eigen-peaks of BPQDs were labelled with wavenumber.

XPS was also employed to analyse the elemental composition of the MBE grown samples. In Figure 3.10, the XPS spectrum of BPQDs/Si(111) illustrates that the fingerprints of

crystallised BPQDs were evidently resolved at ~ 29.3 eV and ~ 130.4 eV, corresponding to spin-orbit split doublets of $2p_{3/2}$ and $2p_{1/2}$, respectively.[34,35] Because the sample underwent about 1 day air-exposure, a peak at 133.7 eV resulted from air-induced oxidation was observed, and it was assigned to phosphate species (PO_x).[36]

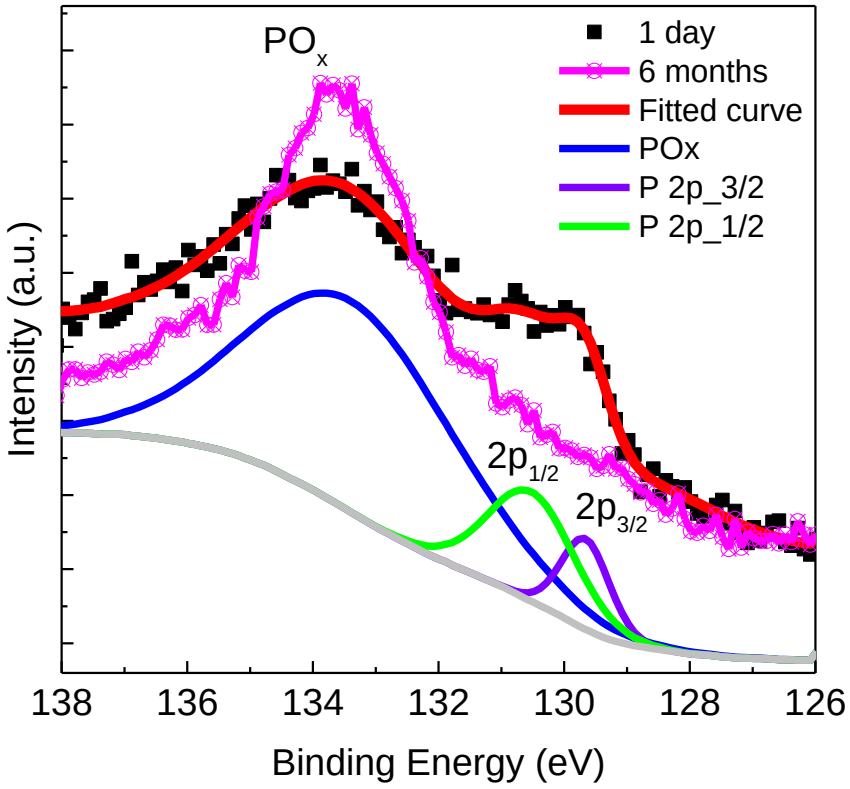

Figure 3.10 XPS spectra of BPQDs grown on Si(111), obtained after different air-exposure time. The solid and scattered curves denote fitted and experimental results, respectively.

Air-exposure induced degradation of MBE grown BPQDs/Si was studied below. The magenta curve plotted in Figure 3.10 shows the obtained XPS spectrum of BPQDs after 6 month air-exposure, in which all the eigen-peaks of BPQDs disappeared and only the PO_x peak was observed. This ambient degradation was caused by air-induced layer-by-layer etching and long-term oxidation,[28,37] which was resolved in AFM images as well.

Figure 3.11 and 3.12 display the surface morphology comparison between the as-grown and the air-exposed BPQDs on Si(111) and Si(100), respectively. Comparatively, water-like droplets dominated the substrate surface after ambient exposure.

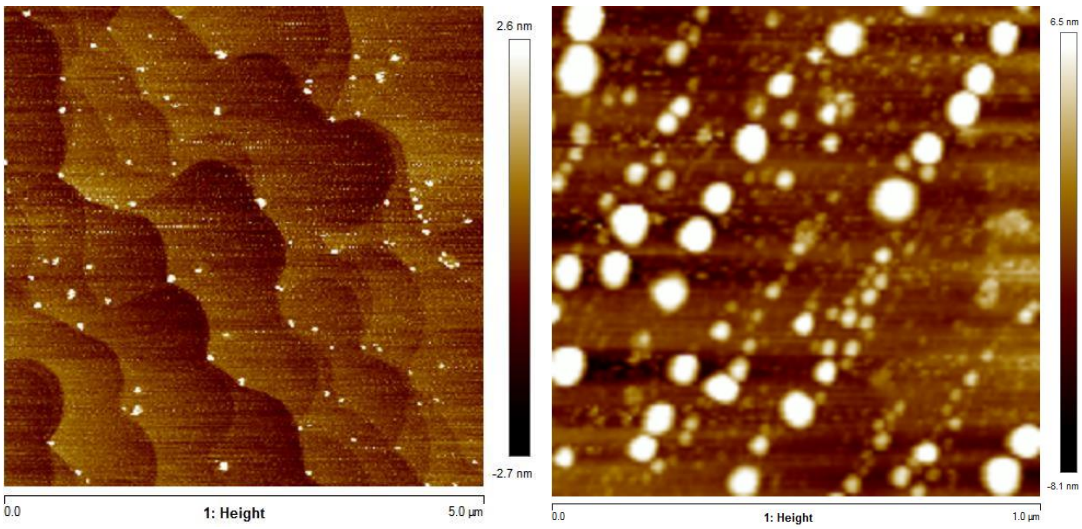

Figure 3.11 AFM images show the surface morphology of as-grown (left) and air-exposed for 6 months (right) BPQDs/Si(111). The surface step became fuzzy and large water-like droplets were observed after 6 month air-exposure.

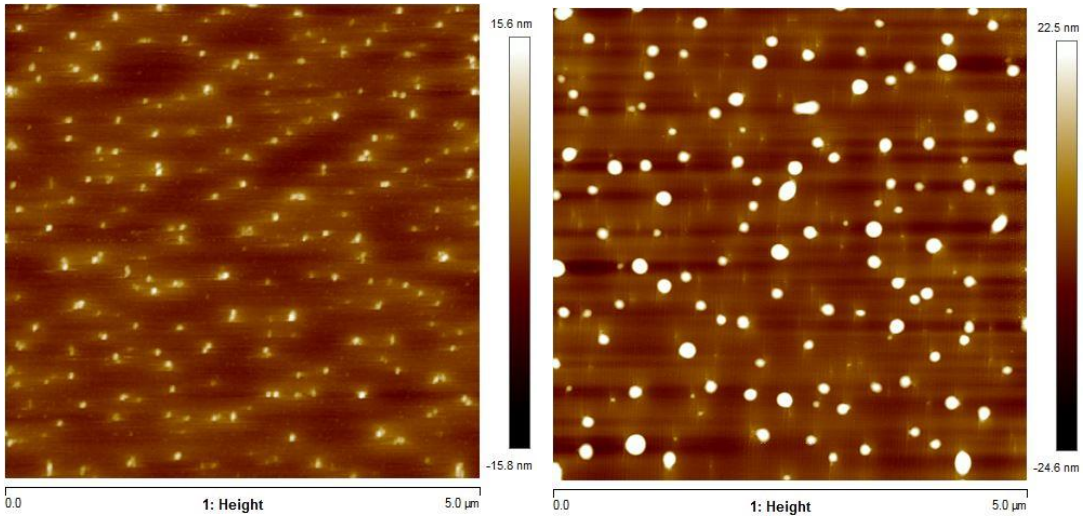

Figure 3.12 AFM images show the surface morphology of as-grown (left) and air-exposed for 6 months (right) BPQDs/Si(100). Large water-like droplets were observed on the surface of the air-exposed sample.

3.4 Conclusions

To summarise, by phase transition of white phosphorus, few-layer BPQDs were directly grown on both Si(100) and Si(111) substrates using the bottom-up technique of MBE. Detailed material characterisations, including AFM, Raman spectroscopy and XPS were carried out to demonstrate the successful deposition of BPQDs on Si substrates. When growing on fully-deoxidised Si(111), BPQDs shaped in a uniform and pyramid structure with an average radius of 27.5 ± 5 nm and height of 3.1 ± 0.6 nm were crystallised, which were mostly distributed along surface step edges. When growing on non-deoxidised Si(100), BPQDs with an average radius between 8 and 14 nm and height between 1 and 2 nm were obtained, which was shaped in a smaller pyramid configuration. Long-term air-exposure induced degradation of BPQDs was validated by XPS and AFM results.

3.5 References

(1) Geim, A. K.; Novoselov, K. S. The Rise of Graphene. *Nat. Mater.* **2007**, *6*, 183–191. https://doi.org/http://dx.doi.org/10.1038/nmat1849.

(2) Novoselov, K. S.; Fal'ko, V. I.; Colombo, L.; Gellert, P. R.; Schwab, M. G.; Kim, K. A Roadmap for Graphene. *Nature* **2012**, *490* (7419), 192–200. https://doi.org/10.1038/nature11458.

(3) Castellanos-Gomez, A. Why All the Fuss about 2D Semiconductors? *Nat. Photonics* **2016**, *10* (4), 202–204. https://doi.org/10.1038/nphoton.2016.53.

(4) Novoselov, K. S.; Geim, A. K.; Morozov, S. V.; Jiang, D.; Zhang, Y.; Dubonos, S. V.; Grigorieva, I. V.; Firsov, A. a. Electric Field Effect in Atomically Thin Carbon Films. *Science.* **2004**.

(5) Mak, K. F.; Lee, C.; Hone, J.; Shan, J.; Heinz, T. F. Atomically Thin MoS2: A New Direct-Gap Semiconductor. *Phys. Rev. Lett.* **2010**, *105* (13), 136805. https://doi.org/10.1103/PhysRevLett.105.136805.

(6) Watanabe, K.; Taniguchi, T.; Kanda, H. Direct-Bandgap Properties and Evidence for Ultraviolet Lasing of Hexagonal Boron Nitride Single Crystal. *Nat. Mater.* **2004**, *3*, 404.

(7) Michael, N.; Murat, K.; Volker, P.; Jun, L.; Junjie, N.; Min, H.; Lars, H.; Yury, G.; W., B. M. Two-Dimensional Nanocrystals Produced by Exfoliation of Ti3AlC2. *Adv. Mater.* **2011**, *23* (37), 4248–4253. https://doi.org/doi:10.1002/adma.201102306.

(8) Li, L.; Yu, Y.; Ye, G. J.; Ge, Q.; Ou, X.; Wu, H.; Feng, D.; Chen, X. H.; Zhang, Y. Black Phosphorus Field-Effect Transistors. *Nat. Nanotechnol.* **2014**, *9* (5), 1–17. https://doi.org/10.1038/nnano.2014.35.

(9) Liu, H.; Neal, A. T. Phosphorene : An Unexplored 2D Semiconductor with a High Hole Mobility. *ACS Nano* **2014**, *8* (4), 4033–4041. https://doi.org/10.1021/nn501226z.

(10) Fortin-Deschênes, M.; Waller, O.; Menteş, T. O.; Locatelli, A.; Mukherjee, S.; Genuzio, F.; Levesque, P. L.; Hébert, A.; Martel, R.; Moutanabbir, O. Synthesis of Antimonene on Germanium. *Nano Lett.* **2017**, *17* (8), 4970–4975. https://doi.org/10.1021/acs.nanolett.7b02111.

(11) Shao, Y.; Liu, Z.-L.; Cheng, C.; Wu, X.; Liu, H.; Liu, C.; Wang, J.-O.; Zhu, S.-Y.; Wang, Y.-Q.; Shi, D.-X.; et al. Epitaxial Growth of Flat Antimonene

Monolayer: A New Honeycomb Analogue of Graphene. *Nano Lett.* **2018**, *18* (3), 2133–2139. https://doi.org/10.1021/acs.nanolett.8b00429.

(12) Zhu, Z.; Cai, X.; Yi, S.; Chen, J.; Dai, Y.; Niu, C.; Guo, Z.; Xie, M.; Liu, F.; Cho, J.-H.; et al. Multivalency-Driven Formation of Te-Based Monolayer Materials: A Combined First-Principles and Experimental Study. *Phys. Rev. Lett.* **2017**, *119* (10), 106101. https://doi.org/10.1103/PhysRevLett.119.106101.

(13) Garcia, J. M.; Wurstbauer, U.; Levy, A.; Pfeiffer, L. N.; Pinczuk, A.; Plaut, A. S.; Wang, L.; Dean, C. R.; Buizza, R.; Van Der Zande, A. M.; et al. Graphene Growth on H-BN by Molecular Beam Epitaxy. *Solid State Commun.* **2012**, *152* (12), 975–978. https://doi.org/10.1016/j.ssc.2012.04.005.

(14) Derivaz, M.; Dentel, D.; Stephan, R.; Hanf, M. C.; Mehdaoui, A.; Sonnet, P.; Pirri, C. Continuous Germanene Layer on Al(111). *Nano Lett.* **2015**, *15* (4), 2510–2516. https://doi.org/10.1021/acs.nanolett.5b00085.

(15) Vogt, P.; De Padova, P.; Quaresima, C.; Avila, J.; Frantzeskakis, E.; Asensio, M. C.; Resta, A.; Ealet, B.; Le Lay, G. Silicene: Compelling Experimental Evidence for Graphenelike Two-Dimensional Silicon. *Phys. Rev. Lett.* **2012**, *108* (15), 155501. https://doi.org/10.1103/PhysRevLett.108.155501.

(16) Blackman, E. G.; Mamajek, E. E.; Cottrell, R. D.; Watkeys, M. K.; Bauch, D.; Hernlund, J. W.; Coltice, N.; Magnetism, R. Epitaxial Growth of a Monolayer WSe2-MoS2 Lateral P-N Junction with an Atomically Sharp Interface. *Science (80-.).* **2015**, *349*, 524–528.

(17) Batmunkh, M.; Bat-Erdene, M.; Shapter, J. G. Phosphorene and Phosphorene-Based Materials – Prospects for Future Applications. *Adv. Mater.* **2016**, *28* (39), 8586–8617. https://doi.org/10.1002/adma.201602254.

(18) Carvalho, A.; Wang, M.; Zhu, X.; Rodin, A. S.; Su, H.; Castro Neto, A. H. Phosphorene: From Theory to Applications. *Nat. Rev. Mater.* **2016**, *1*, 16061. https://doi.org/10.1038/natrevmats.2016.61.

(19) Lee, H. U.; Park, S. Y.; Lee, S. C.; Choi, S.; Seo, S.; Kim, H.; Won, J.; Choi, K.; Kang, K. S.; Park, H. G.; et al. Black Phosphorus (BP) Nanodots for Potential Biomedical Applications. *Small* **2016**, *12* (2), 214–219. https://doi.org/10.1002/smll.201502756.

(20) Shao, J.; Xie, H.; Huang, H.; Li, Z.; Sun, Z.; Xu, Y.; Xiao, Q.; Yu, X.-F.; Zhao, Y.; Zhang, H.; et al. Biodegradable Black Phosphorus-Based Nanospheres for in Vivo Photothermal Cancer Therapy. *Nat. Commun.* **2016**, *7*, 12967.

https://doi.org/10.1038/ncomms12967.

(21) Sofer, Z.; Bouša, D.; Luxa, J.; Mazanek, V.; Pumera, M. Few-Layer Black Phosphorus Nanoparticles. *Chem. Commun.* **2016**, *52* (8), 1563–1566. https://doi.org/10.1039/C5CC09150K.

(22) Zhang, X.; Xie, H.; Liu, Z.; Tan, C.; Luo, Z.; Li, H.; Lin, J.; Sun, L.; Chen, W.; Xu, Z.; et al. Black Phosphorus Quantum Dots. *Angew. Chemie - Int. Ed.* **2015**, *54* (12), 3653–3657. https://doi.org/10.1002/anie.201409400.

(23) Sun, Z.; Xie, H.; Tang, S.; Yu, X. F.; Guo, Z.; Shao, J.; Zhang, H.; Huang, H.; Wang, H.; Chu, P. K. Ultrasmall Black Phosphorus Quantum Dots: Synthesis and Use as Photothermal Agents. *Angew. Chemie - Int. Ed.* **2015**, *54* (39), 11526–11530. https://doi.org/10.1002/anie.201506154.

(24) Li, X.; Deng, B.; Wang, X.; Chen, S.; Vaisman, M.; Karato, S.; Pan, G.; Larry Lee, M.; Cha, J.; Wang, H.; et al. Synthesis of Thin-Film Black Phosphorus on a Flexible Substrate. *2D Mater.* **2015**, *2* (3), 031002. https://doi.org/10.1088/2053-1583/2/3/031002.

(25) Smith, J. B.; Hagaman, D.; Ji, H.-F. Growth of 2D Black Phosphorus Film from Chemical Vapor Deposition. *Nanotechnology* **2016**, *27* (21), 215602. https://doi.org/10.1088/0957-4484/27/21/215602.

(26) Zhu, Z.; Tomanek, D. Semiconducting Layered Blue Phosphorus: A Computational Study. *Phys. Rev. Lett.* **2014**, *112* (17), 1–5. https://doi.org/10.1103/PhysRevLett.112.176802.

(27) Zhang, J. L.; Zhao, S.; Han, C.; Wang, Z.; Zhong, S.; Sun, S.; Guo, R.; Zhou, X.; Gu, C. D.; Yuan, K. Di; et al. Epitaxial Growth of Single Layer Blue Phosphorus: A New Phase of Two-Dimensional Phosphorus. *Nano Lett.* **2016**, *16* (8), 4903–4908. https://doi.org/10.1021/acs.nanolett.6b01459.

(28) Favron, A.; Gaufrès, E.; Fossard, F.; Phaneuf-L'Heureux, A.-L.; Tang, N. Y.-W.; Lévesque, P. L.; Loiseau, A.; Leonelli, R.; Francoeur, S.; Martel, R. Photooxidation and Quantum Confinement Effects in Exfoliated Black Phosphorus. *Nat. Mater.* **2015**, *14* (8), 826–832. https://doi.org/10.1038/nmat4299.

(29) Patella, F.; Sgarlata, A.; Arciprete, F.; Nufris, S.; Szkutnik, P. D.; Placidi, E.; Fanfoni, M.; Motta, N.; Balzarotti, A. Self-Assembly of InAs and Si/Ge Quantum Dots on Structured Surfaces. *J. Phys. Condens. Matter* **2004**, *16* (17), S1503–S1534. https://doi.org/10.1088/0953-8984/16/17/005.

(30) Khorasaninejad, M.; Walia, J.; Saini, S. S. Enhanced First-Order Raman Scattering from Arrays of Vertical Silicon Nanowires. *Nanotechnology* **2012**, *23* (27), 275706. https://doi.org/10.1088/0957-4484/23/27/275706.

(31) Hammouda, A.; Canizarès, A.; Simon, P.; Boughalout, A.; Kechouane, M. Improving the Sensitivity of Raman Signal of ZnO Thin Films Deposited on Silicon Substrate. *Vib. Spectrosc.* **2012**, *62* (September), 217–221. https://doi.org/10.1016/j.vibspec.2012.07.004.

(32) Castellanos-gomez, A.; Vicarelli, L.; Prada, E.; Island, J. O.; Narasimha-Acharya, K. L.; Blanter, S. I.; Groenendijk, D. J.; Buscema, M.; Steele, G. A.; Alvarez, J. V; et al. Isolation and Characterization of Few-Layer Black Phosphorus. *2D Mater.* **2014**, *1*, 025001. https://doi.org/10.1088/2053-1583/1/2/025001.

(33) Eswaraiah, V.; Zeng, Q.; Long, Y.; Liu, Z. Black Phosphorus Nanosheets: Synthesis, Characterization and Applications. *Small* **2016**, *12* (26), 3480–3502. https://doi.org/10.1002/smll.201600032.

(34) Bullett, D. W. Valence-Band Structures of Phosphorus Allotropes. *Solid State Commun.* **1985**, *55* (3), 257–260. https://doi.org/10.1016/0038-1098(85)90728-8.

(35) Woomer, A. H.; Farnsworth, T. W.; Hu, J.; Wells, R. A.; Donley, C. L.; Warren, S. C. Phosphorene: Synthesis, Scale-Up, and Quantitative Optical Spectroscopy. *ACS Nano* **2015**, *9* (9), 8869–8884.

(36) Wood, J. D.; Wells, S. A.; Jariwala, D.; Chen, K.; Cho, E.; Sangwan, V. K.; Liu, X.; Lauhon, L. J.; Marks, T. J.; Hersam, M. C. Effective Passivation of Exfoliated Black Phosphorus Transistors against Ambient Degradation. *Nano Lett.* **2014**, *14*, 6964–6970.

(37) Island, J. O.; Steele, G. A.; Zant, H. S. J. Van Der; Castellanos-gomez, A. Environmental Instability of Few-Layer Black Phosphorus. *2D Mater.* **2015**, *2* (011002), 1–6. https://doi.org/10.1088/2053-1583/2/1/011002.

Chapter 4 In-Plane Bandgap-Graded $MoS_{2(1-x)}Se_{2x}$ Homojunctions for Self-Powered Phototransistors

4.1 Research Background and Result Overview

4.1.1 Research background

Semiconducting two-dimensional (2D) transition metal dichalcogenides (TMDs), formulated as MX_2 (M = Mo, W; X = S, Se, Te), possess tunable bandgaps, which can be tuned not only across the range from UV to NIR spectral region but also from indirect to direct ones as thickness varied. These intriguing features have drawn considerable attention for promising applications in nanoelectronic and optoelectronic fields, such as field-effect transistors (FETs), photodetectors, lasers, memories, light emission diodes (LEDs), *etc.*[1-11] In order to optimise the already outstanding properties of TMD family members and obtain high-performance devices based on them for practical use, further bandgap engineering has been employed. For most cases, it has been achieved by

fabricating vertically-stacked or in-plane heterostructures, such as exfoliated-restacked $MoTe_2/MoS_2$ and epitaxially-grown WS_2-$MoSe_2$.[12-16]

Recently, *in-situ* controlling the elemental concentration within the same domain of ternary TMDs, such as $Mo_{1-x}W_xS_2$, $WS_{2x}Se_{2(1-x)}$, $MoS_{2(1-x)}Se_{2x}$, *etc*., has been employed to modulate the bandgaps, demonstrated another prospective way to change bandgaps and provided heterostructure fabrication with more design flexibility.[17-20] Nonetheless, most reported ternary alloys within a single domain showed a specific composition value, which needed further processing, such as wet or dry transferring, to prepare hetero- or homojunctions for devices. The spatially in-plane bandgap-graded alloys get rid of this weakness by *in-situ* forming a homojunction possessing continuously tuned band structures, without abrupt changes as in the case of heterojunctions, and give rise to a lower adjacent barrier height thus is more energy-friendly for nano-devices, such as lower operation-voltage and higher electrical conductivity.[21-24]

Notably, such homojunctions provide various nanoelectronic and optoelectronic devices with a novel platform and more design possibility, thanks to the graded-bandgap within a single nanosheet domain. For instance, grading of stoichiometry has been already introduced to 0D materials to obtain graded-bandgaps, which was used for fabricating solar cells with energy harvesting.[25,26] Bandgap-graded 1D alloys have been systemically studied, and they exhibited competitive or even superior performance to conventional 1D materials as well.[27-29] In terms of 2D TMDs with spatial bandgap gradient, however, studies were only limited to material synthesis and device applications based on them remained unexplored to date.[30,31] Although the fabrication of in-plane bandgap-graded 2D materials is rather rewarding, it is challenge to form desired heterostructures, e.g. p-n junctions, for electronic and optoelectronic applications.

4.1.2 Result overview

In this work, high-performance and self-powered phototransistors based on the spatially bandgap-graded $MoS_{2(1-x)}Se_{2x}$ homojunctions, which were synthesised by a simple and cost-effective chemical solution deposition (CSD) method, were systemically studied. The composition gradient and Se atom distribution in the alloys were clearly resolved by annular dark field (ADF) imaging. The graded bandgaps, originated from the spatial Se-

composition grading and graded thickness within a single alloy domain, were tuned from 1.83 eV to 1.73 eV, giving rise to the formation of a homojunction with a built-in electric field. As a result, a strong and sensitive photovoltaic effect controlled by gate voltage was demonstrated, enabling the homojunction phototransistors to deliver a photoresponsivity of 500 mA/W under the self-powered working mode. When working under biased conditions, the devices yielded a remarkable photoresponsivity of 8.4 A/W, a specific detectivity of 2.2 $\times 10^{12}$ Jones, an ultrahigh photoconductive gain of 10^6 ~10^7, and a fast photoresponsive time in the order of ~50 ms. This work demonstrated high-performance phototransistors enabled by $MoS_{2(1-x)}Se_{2x}$ homojunctions with spatial Se-composition and thickness gradient, and provided an easy and competitive solution to the bandgap engineering of 2D materials for device applications.

4.2 Experimental Methods

4.2.1 Material characterisations

Annular dark field scanning transmission electron microscopy (ADF-STEM) imaging was carried out at room temperature in a JEOL ARM200F under 200 kV. This measurement was performed by Dr. Gyeong Hee Ryu from University of Oxford. A 30 µm cathode-luminescence (CL) aperture with a convergence semi-angle of 22.5 mrad and a beam current of 35 Pa were used for imaging. The acquisition angles of these images were 72.8 – 271 mrad. Dwell time for each pixel was typical 32 µs.

The surface morphology of $MoS_{2(1-x)}Se_{2x}$ alloy nanosheets was characterised using a FEI Scios scanning electron microscopy (SEM) system at 15 kV, and thickness was identified by a Bruker Dimension Icon atomic force microscopy (AFM) system working at the tapping-mode. A Thermo Fisher Escalab 250Xi XPS (X-ray photoelectron spectroscopy) system was employed to characterise chemical composition of homojunction alloys. High resolution transmission electron microscopy (HRTEM) imaging was performed by Dr. Juntong Zhu from Soochow University on a field emission FEI Tecnai F20 TEM (transmission electron microscopy) system at 200 kV.

Selected area electron diffraction (SAED) characterisation was carried out by Dr. Gyeong Hee Ryu from University of Oxford on a FEI Tecnai T12 TEM system working at 120 kV. Raman scattering and micro-photoluminescence (micro-PL) spectra/mapping were collected with a confocal Raman spectrometer (Horiba Jobin Yvon HR Evolution) equipped with a 532 nm laser as the excitation light source. The size of 532 nm laser spot was ~ 1 μm and the laser power on the sample surface was kept below 1 mW to avoid local heating effect.

4.2.2 Device fabrication

Photolithography and subsequent Ti/Au (10 nm/100 nm) metallisation were first introduced to make metal position labels and cross alignment on SiO_2/Si substrates, preparing for the followed EBL processing. Afterwards, drain and source electrodes for phototransistors were patterned using EBL, followed by Ti/Au (10 nm/50 nm) metallisation using an electron-beam evaporator system and standard lift-off. The back-gate was enabled by heavily n-doped Si substrates. Then the devices were wire-bonded to logic chip carrier (LCC) using gold wire.

4.2.3 Device characterisations

The gate-tunable electrical and visible light excited photoresponsive measurements were carried out at ambient conditions, using a Keithley 4200 semiconductor parameter analyser equipped with a white light and monochromic laser sources. The lasers were unfocused with a spot size of ~1.5 mm in diameter. The measured effective power density for the 405 nm, 532 nm and 650 nm monochromic lasers during the measurements was 137.5 μW/mm^2, 123.9 μW/mm^2 and 99.3 μW/mm^2, respectively.

The photoresponsivity was calculated based on the equation 4.1 below.

$$R = \frac{I_{pc}}{PS} \tag{4.1}$$

Here, R, I_{pc}, P and S are defined as photoresponsivity, net photocurrent ($I_{pc} = I_{laser} - I_{dark}$), laser power density and active area of a photodetector, respectively.

Specific detectivity (D^*) of phototransistors was calculated from the equation 1.1 aforementioned:

$$D^* = R\sqrt{\frac{S}{2qI_{dark}}}$$

where q is the elementary charge equal to 1.6×10^{-19} C.

The electron mobility μ of 0.65 $cm^2V^{-1}s^{-1}$ was deduced by the equation 1.2 aforementioned:

$$\mu = \frac{dI_{ds}}{dV_{bg}}\frac{L}{WC_iV_{ds}}$$

Here, L (3.4 μm), W (2 μm) and C_i (1.15×10^{-4} F/m^2) represent the channel length, the channel width and the capacitance between the channel and the back gate, respectively. $\tau_{transit}$ was defined as below:[3]

$$\tau_{transit} = \frac{L^2}{\mu V_{ds}} \quad (4.2)$$

Here, μ and L denote the electron mobility and the channel length, respectively. Thus, the transient time was calculated to be ~ 10^{-7} s.

4.3 Results and Discussion

A simple and cost-effective CSD method was used for synthesising $MoS_{2(1-x)}Se_{2x}$ nanosheets on (300 nm) SiO_2/Si substrates, which was carried out by Dr. Juntong Zhu from Soochow University. As displayed in Figure 4.1, a precursor solution prepared by KOH and ammonium molybdate was first spin-coated onto pre-processed cleaned SiO_2/Si substrates, which was then loaded into a tube furnace. In the atmosphere filled with Ar/H_2 (5% H_2), the S/Se powders at the upstream position and the as-processed substrates at the middle position were heated up to 280 °C and 650 °C independently within 60 min, respectively. After keeping the substrates at 650 °C for 30 min and subsequently naturally cooling down to the room temperature, $MoS_{2(1-x)}Se_{2x}$ alloy nanosheets grown on SiO_2/Si

substrates with uniform thickness and homojunctions were correspondingly obtained. Firstly, the as-grown materials with uniform thickness and few-layer nature were characterised below in detail.

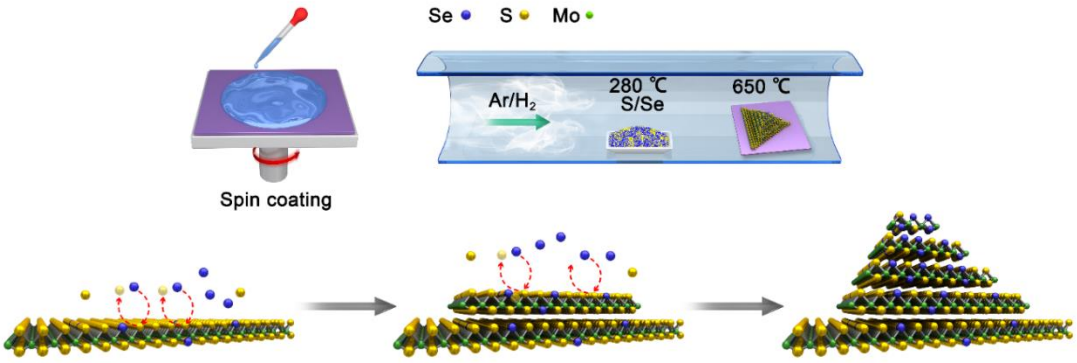

Figure 4.1 Schematic flowchart of $MoS_{2(1-x)}Se_{2x}$ alloy nanosheet synthesis on SiO_2/Si substrates. The configuration of few-layer-nanosheet/multilayer-pyramid of the as-grown alloy is illustrated here.

Figure 4.2a shows the as-grown few-layer $MoS_{2(1-x)}Se_{2x}$ alloy nanosheets with uniform thickness, when the aqueous solution was dissolved with 0.12 g KOH and 0.05 g ammonium molybdate. In contrast, the samples with a configuration of thickness-graded pyramid on few-layer nanosheet within single domains were grown when the aqueous solution dissolved with 0.06 g KOH and 0.05 g ammonium molybdate, as shown in Figure 4.2b. Both the HR-TEM and SAED results revealed that the as-grown samples were highly crystalline, as shown in Figure 4.3.

(a) 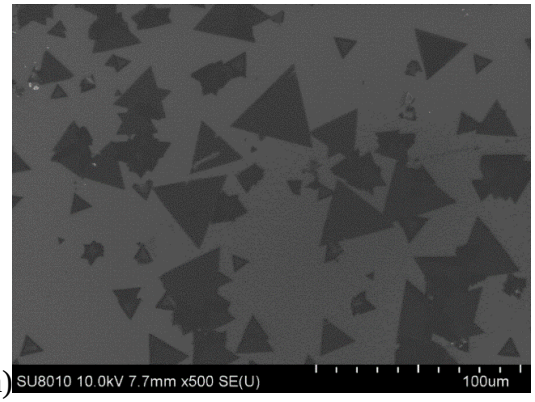

(b) 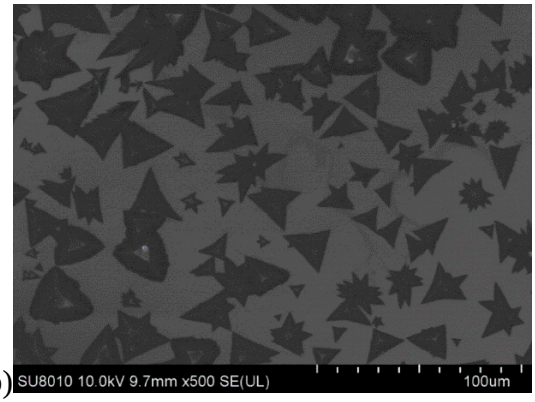

Figure 4.2 SEM images of the as-synthesised $MoS_{2(1-x)}Se_{2x}$ alloy nanosheets (a) with a few-layer configuration and uniform thickness, and (b) with a nanosheet/pyramid configuration within a single domain. As observed, the thickness and configuration of the as-grown samples changed when the aqueous solution dissolved with different concentration KOH and ammonium molybdate.

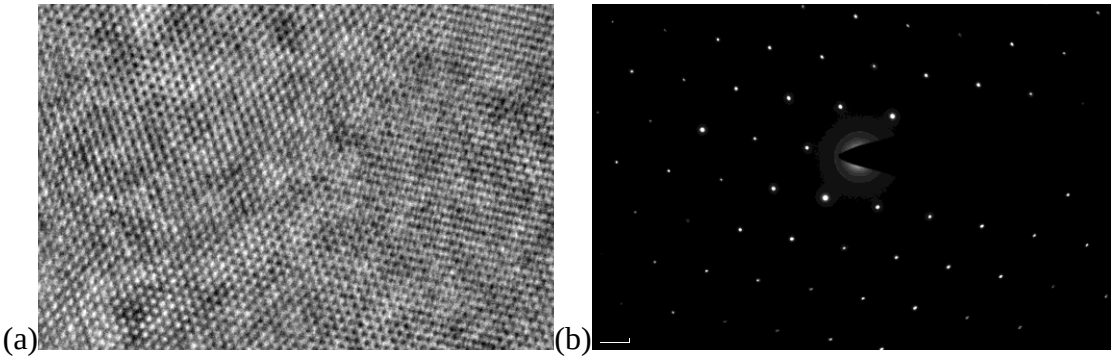

Figure 4.3 HR-TEM (a) and SAED (b) images of few-layer $MoS_{2(1-x)}Se_{2x}$ alloy nanosheets, indicating high crystallinity.

Raman spectroscopy measurement was also performed to study intrinsic phonon oscillation features of alloy nanosheets with different Se-composition. In Figure 4.4, the obtained Raman spectrum of $MoS_{2(1-x)}Se_{2x}$ alloy nanosheets clearly resolved the fingerprint of crystallised $MoS_{2(1-x)}Se_{2x}$ alloys, compared with pure $MoSe_2$ and MoS_2 nanosheets when x =1 and x = 0, respectively. This confirmed that Se atoms were successfully implanted. In addition, the obtained XPS spectra with comparison between as-grown samples and pure MoS_2 nanosheets, shown in Figure 4.5, identified the binding energy of Mo, S and Se, respectively, indicating the value of x in the as-grown samples was around 0.1.

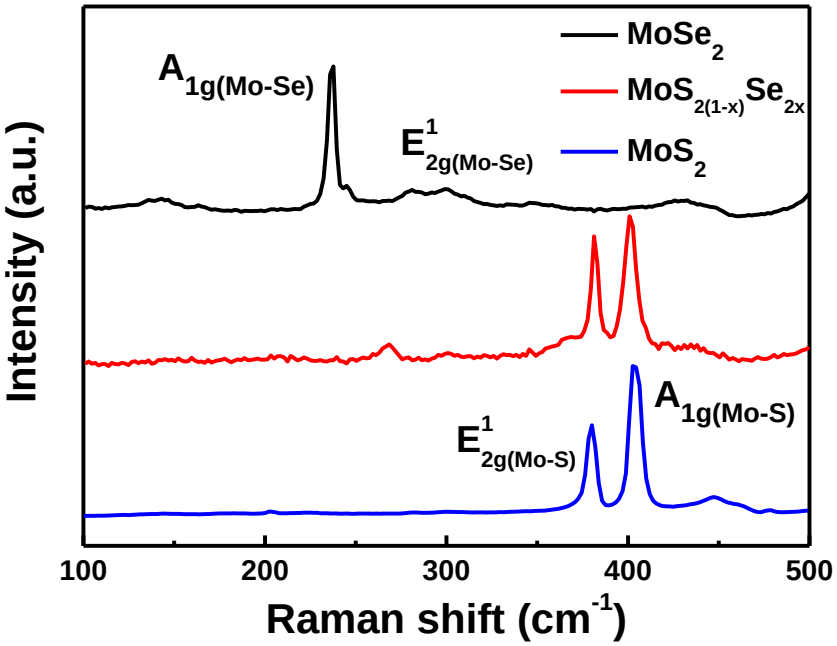

Figure 4.4 Raman spectrum of few-layer $MoS_{2(1-x)}Se_{2x}$ alloy nanosheets, compared with those of pure $MoSe_2$ and MoS_2 nanosheets when x = 1 and x = 0, respectively.

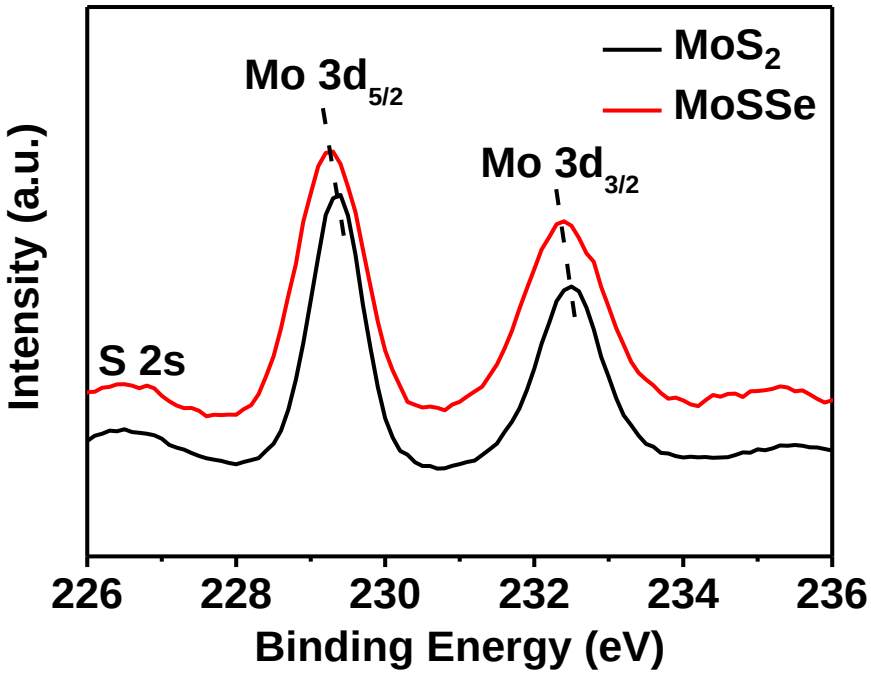

(a)

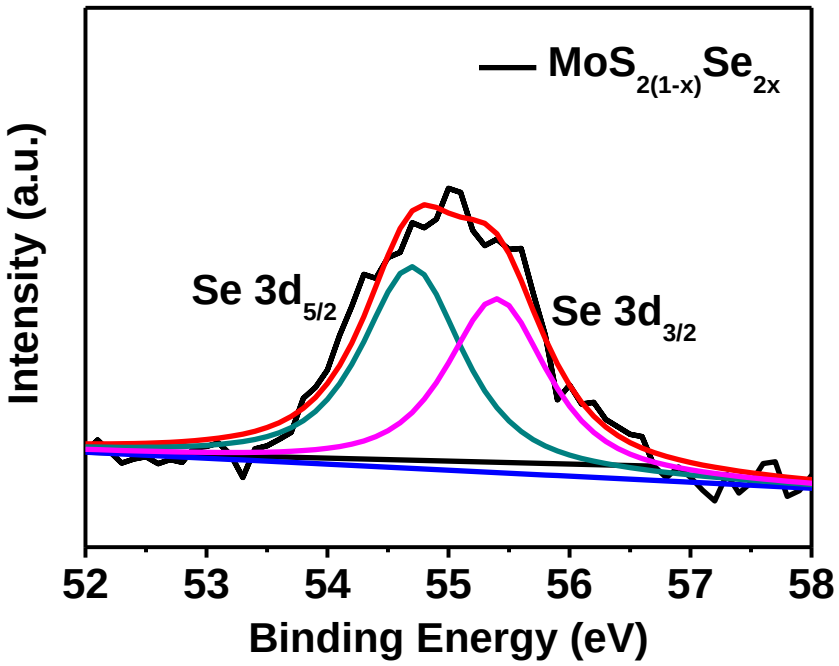

(b)

Figure 4.5 (a) XPS spectrum of the few-layer $MoS_{2(1-x)}Se_{2x}$ alloy nanosheets, identifying the binding energy of Mo and S. (b) XPS identified binding energy of Se, showing the fitted peaks and the measured curve.

Moreover, detailed material characterisations were performed below for as-grown samples with homojunctions shaped in nanosheet/pyramid structures. AFM image, in Figure 4.6a, exhibited the surface morphology of a homojunction domain, showing a stacked configuration comprised of a thin and smooth edge at the bottom and a thick centre at the top. Figure 4.6b shows the height profiles along line 1 and line 2 labelled in Figure 4.6a, demonstrating the 3L nature for the edge alloy with uniform thickness and pyramid configuration for the central multi-layer alloy with thickness gradient.[7]

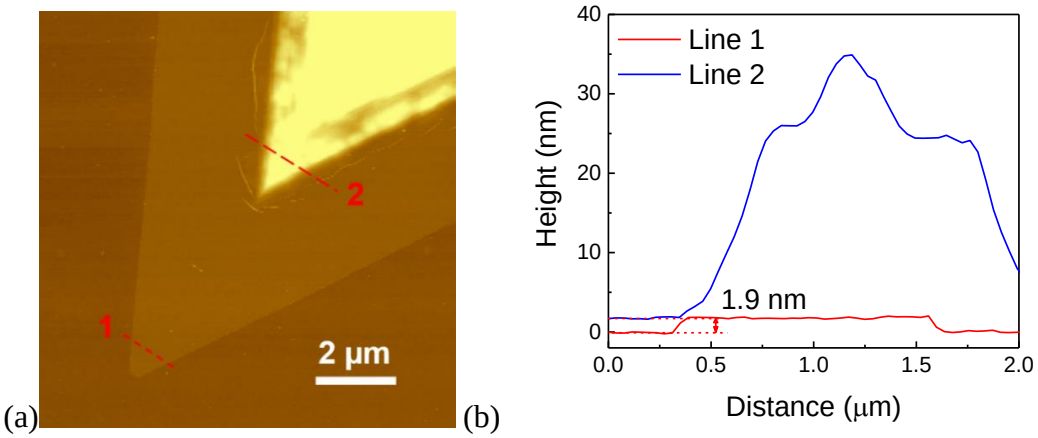

Figure 4.6 (a) AFM image mapping the surface morphology of the nanosheet/pyramid configuration of a $MoS_{2(1-x)}Se_{2x}$ alloy nanosheet. (b) Height profiles along line 1 and line 2 marked in (a), revealing the 3-layer nature of the bottom nanosheet with uniform thickness and the upper multilayer pyramid structure.

To identify distribution and concentration of the specific atoms in 2D materials, ADF-STEM was used to study $MoS_{2(1-x)}Se_{2x}$ alloy nanosheets. Both the ADF-STEM image and the inset of digital diffractogram in Figure 4.7a suggest the monolayer $MoS_{2(1-x)}Se_{2x}$ nanosheet on the bottom of a domain with homojunctions possessed high crystallinity. Se atoms, which have a higher intensity (grey contrast) than S atoms, are integrated at the positions of S atoms and the further zoom-in view of ADF-STEM image, as displayed in Figure 4.7b, also validated S atoms were substituted by Se atoms.

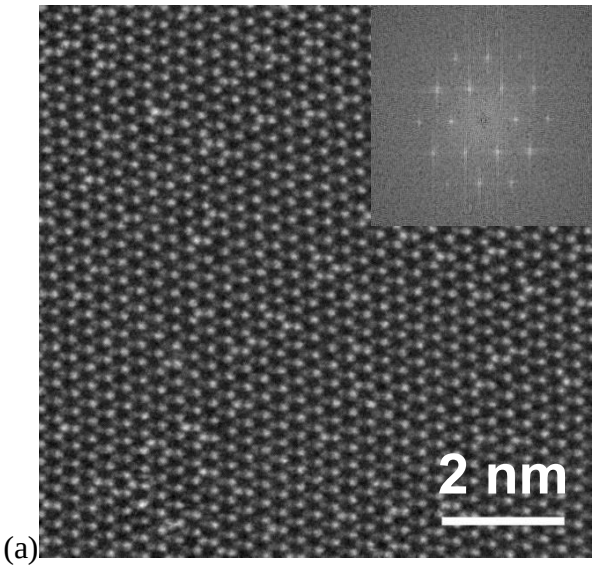

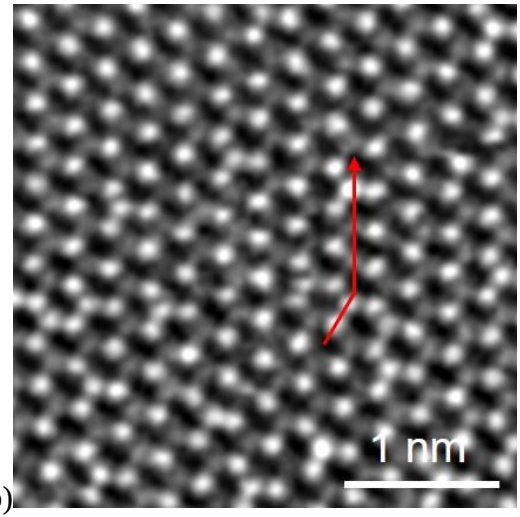

(b)

Figure 4.7 (a) ADF-STEM image and digital diffraction (the inset) of the monolayer nanosheet at the bottom of the $MoS_{2(1-x)}Se_{2x}$ homojunction alloy. (b) Zoom-in view of ADF-STEM image, illustrating different contrast levels of atoms and Se substitution.

Figure 4.8a illustrates the varied gray values of Mo, S and Se atoms along the red route marked in Figure 4.7b. The grey values were obtained by the Gwyddion software along the selected route. As can be seen, in comparison with the referenced Mo atoms, S_2 units show the smaller gray value while the units of S + Se (induced by single Se substitution) have similar one. It is worth noting that Se_2 units (induced by double Se substitution) show the larger gray value, well consistent with the formerly reported results.[20]

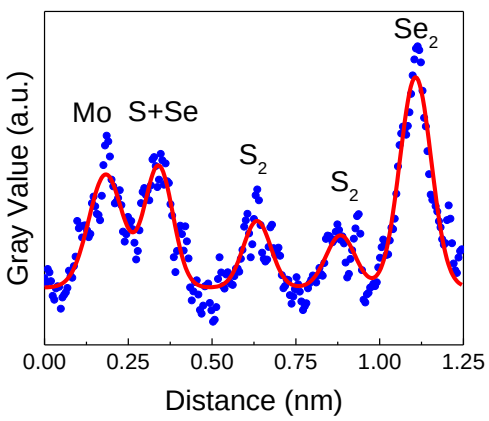

(a)

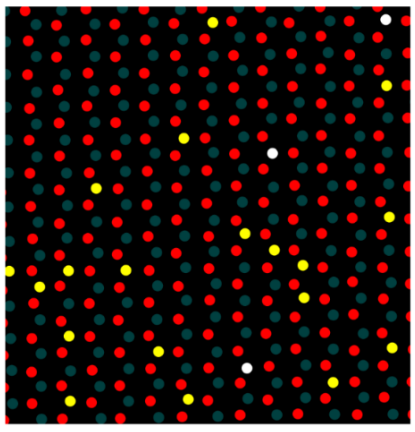

(b)

Figure 4.8 (a) Gray values (a.u.) of different atoms distributed along the red-route marked in Figure 4.7b. (b) The schematic map of Mo, S, Se atom distribution within a selected

domain, showing the positions where the single and double S atoms were substituted by Se atoms. The red, dark gray, yellow and white dots denote Mo atoms, S_2 units, S + Se units and Se_2 units, respectively.

As a result, the schematic diagram (see Figure 4.8b), extracted from Figure 4.7b, exhibits the positions straightforwardly where single or double Se was replaced. The ADF-STEM results were well observed in another homojunction alloy domain, as displayed in Figure 4.9.

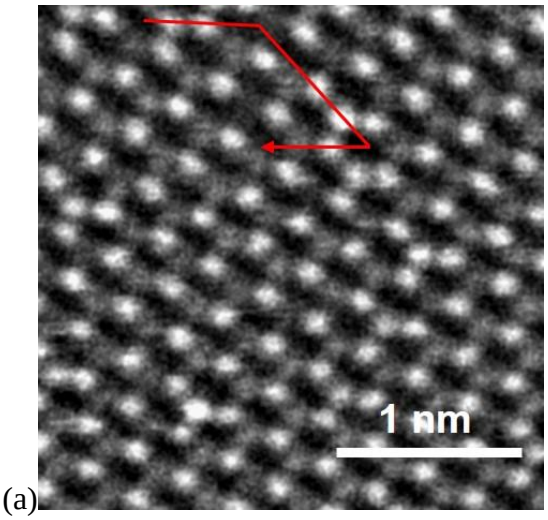

(a)

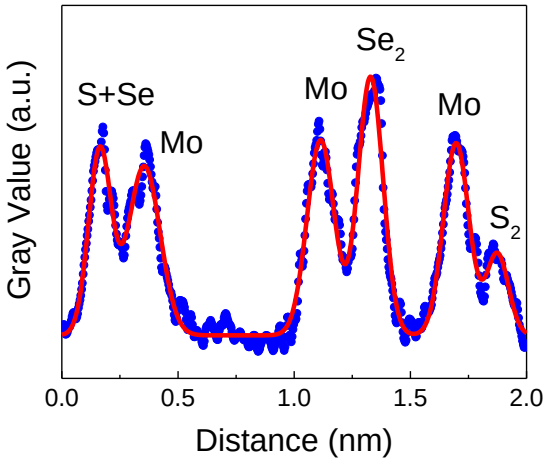

(b)

Figure 4.9 (a) ADF-STEM image of the other monolayer nanosheet at the bottom of the $MoS_{2(1-x)}Se_{2x}$ homojunction alloy. (b) Gray values of different atoms distributed along the red-route marked in (a).

Besides, energy-dispersive X-ray spectroscopy (EDS) was used to further study the distribution of Mo, S and Se atoms from the atomically thin edge to the thick centre of the alloys. A domain (Figure 4.10a) located at the bottom of the multilayer pyramid structure (see Figure 4.6a) was selected for EDS study. Figure 4.10b, measured at the framed region marked in Figure 4.10a, obviously illustrated more Mo, S and Se signal was detected (white dots) as moving from the right side to the left side, which can be resulted from accumulated signal layer by layer as thickness continuously increased (from the right to the left) and further implied the spatial thickness grading in the alloy.

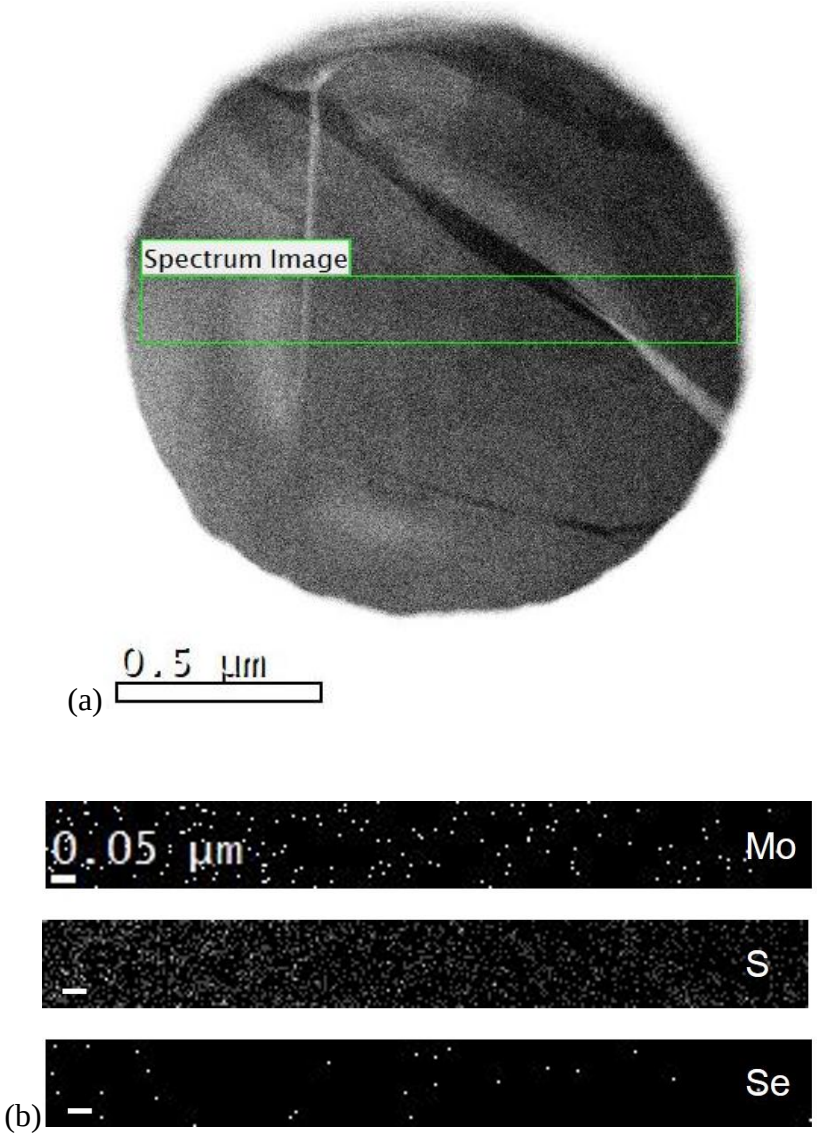

Figure 4.10 (a) SI survey image. The framed area was selected for EDS imaging. The thickness of this homojunction alloy domain increases along the direction from the right side to the left side. (b) EDS mapping results of Mo, S and Se atoms within the framed

areas shown in (a), respectively. The thickness increases from the right side to the left side and the scale bar is 50 nm.

Raman spectroscopy and micro-PL studies using a 532 nm laser as the excitation light source in a confocal Raman spectrometer system, were performed to explore the spatial composition and thickness grading influenced optical properties. Figure 4.12 displays the position-dependent Raman spectra of the alloy domain with a nanosheet/pyramid configuration displayed in Figure 4.11a, measured from the thin edge (dot a) to the thick centre (dot c).

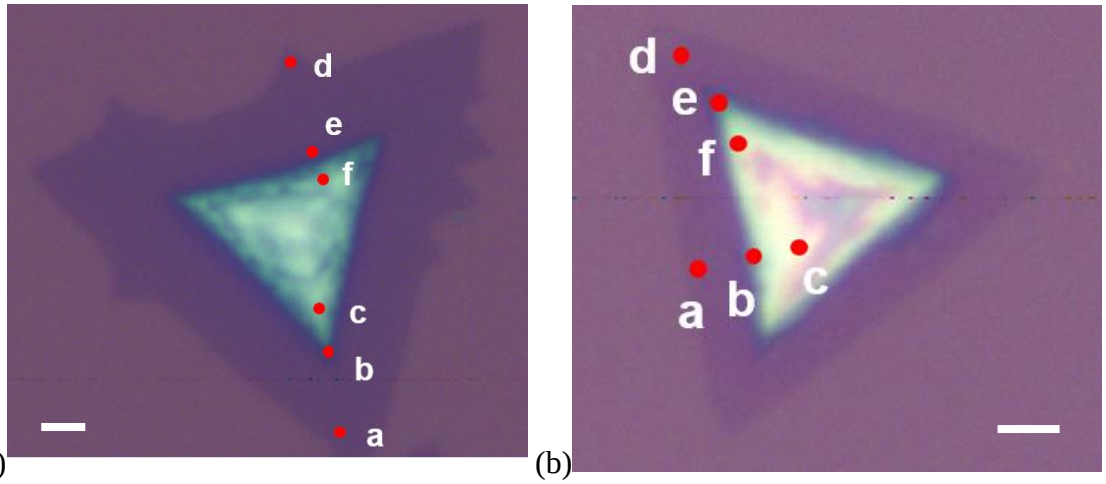

Figure 4.11 (a) Optical microscopy image of a $MoS_{2(1-x)}Se_{2x}$ alloy nanosheet with the nanosheet/pyramid configuration, namely, few-layer nanosheet on the bottom and thickness-graded multilayer on the centre. The scale bar is 2 µm. (b) Optical microscopy image of another different $MoS_{2(1-x)}Se_{2x}$ alloy nanosheet with homojunctions. The scale bar is 1 µm.

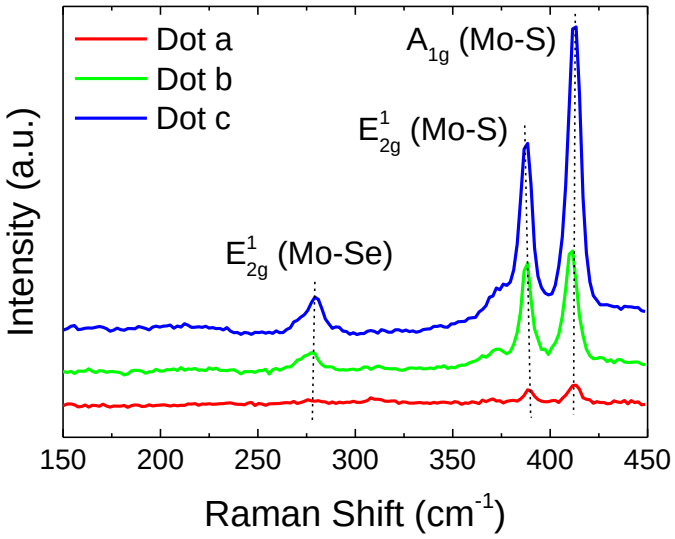

Figure 4.12 Raman spectra of the $MoS_{2(1-x)}Se_{2x}$ alloy nanosheet, excited by a 532 nm laser. They were measured at the sites of dot a, dot b and dot c, labelled at Figure 4.11a. The black dashed lines illustrate the peak position changing tendency.

In the Raman spectrum (Figure 4.12) measured at dot ***a*** labelled in Figure 4.11a, the Raman shift difference between the two dominant characteristic peaks of crystallised MoS_2 (in-plane E^1_{2g} mode and out-of-plane A_{1g} mode) is 23 cm^{-1}, indicating the 3L nature of the edge area (well agreeing with the AFM height results shown in Figure 4.6b).[32,33] From dot ***a*** at thin edge to dot ***c*** at thick centre, this wavenumber difference is gradually increased to 26 cm^{-1} with E^1_{2g} mode red-shifted and A_{1g} mode blue-shifted. Since natural cooling down process at ambient conditions was carried out in the end during material synthesis, the red-shift of the E^1_{2g} mode can be mainly originated from the varied concentration of S and the increased number of layers, rather than strain.[32-34] For the A_{1g} mode, the blue-shift is originated from the stronger electron coupling with increased electron concentration, which could also reveal the increasing content of Se in the centre of the nanosheet/pyramid domain.[35]

According to the previously reported results, for pure few-layer $MoSe_2$ nanosheets, the in-plane E^1_{2g} mode is red-shifted and its intensity decreases as the number of layers increases.[36] Oppositely, from dot ***a*** to dot ***c***, the $MoSe_2$-like mode (at ~273 cm^{-1}) observed in the alloy domain shows a slight blue-shift (Figure 4.12) or unnoticeable shift (Figure

4.14) but apparently enhanced intensity as thickness increased. In terms of pure $MoS_{2(1-x)}Se_{2x}$ alloy without thickness variation, it was reported that the peak intensity of the $MoSe_2$-like mode increased as concentration of Se rised, showing the same variation tendency as the nanosheet/pyramid alloy nanosheets.[17,19,37]

This analysis above considering thickness variation and spatial composition gradient indicates that a Se-composition gradient can be formed from dot ***a*** to dot ***c***, which was further confirmed by the measurement from dot ***d*** at the thin edge to dot ***f*** at the thick centre (see Figure 4.13) and also observed in an entirely different 2D flake (see Figure 4.11b, 4.14 and 4.15).

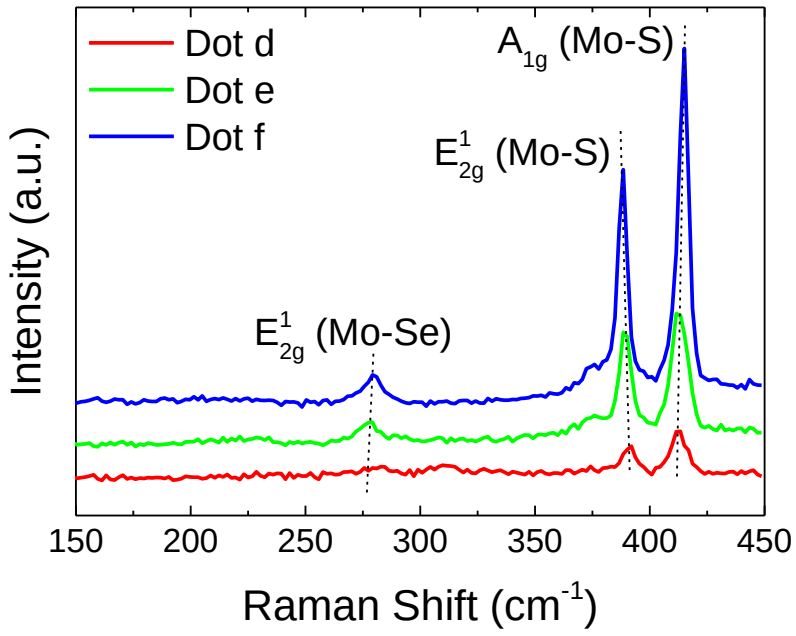

Figure 4.13 Raman spectra of the $MoS_{2(1-x)}Se_{2x}$ alloy nanosheet. They were measured at the sites of dot d, dot e and dot f, labelled at Figure 4.11a. The black dashed lines illustrate the peak position changing tendency.

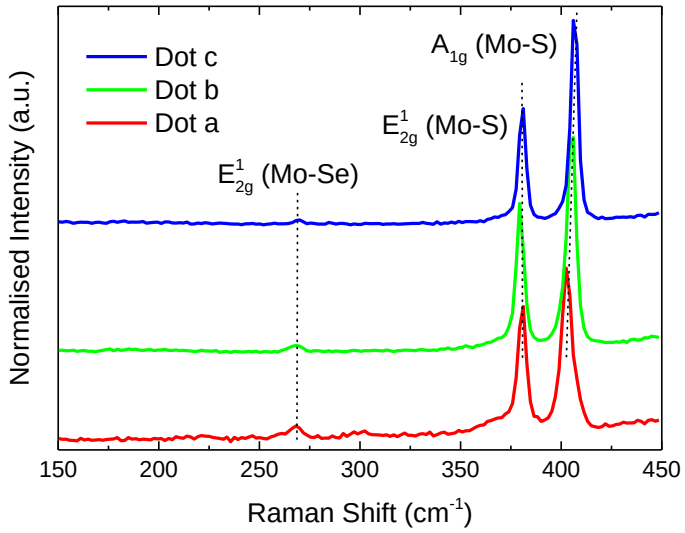

Figure 4.14 Raman spectra of the $MoS_{2(1-x)}Se_{2x}$ alloy nanosheet, excited by a 532 nm laser. They were measured at the sites of dot a, dot b and dot c, labelled at Figure 4.11b. The black dashed lines illustrate the peak position changing tendency.

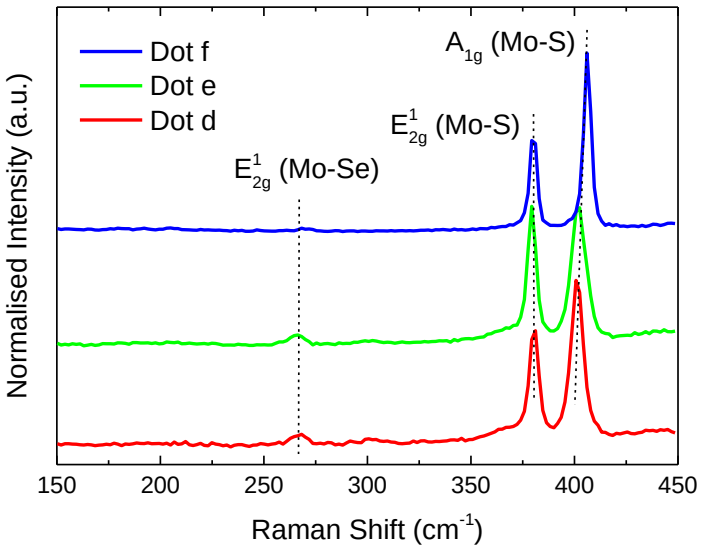

Figure 4.15 Raman spectra of the $MoS_{2(1-x)}Se_{2x}$ alloy nanosheet, excited by a 532 nm laser. They were measured at the sites of dot d, dot e and dot f, labelled at Figure 4.11b. The black dashed lines illustrate the peak position changing tendency.

Figure 4.16 and 4.17 exhibits the corresponding Raman intensity maps of the E_{2g}^1 (Mo-Se), E_{2g}^1 (Mo-S) and A_{1g} (Mo-S) oscillation modes, respectively. Obviously, the Raman peak intensity of them all increases as the layer number increases from the edge to the centre. Notably, as the thickness continuously increased, the optical interference involved with the coupling of the excitation laser and the emitted Raman scattering near the centre. Consequently, the Raman peak intensity gradually reduces when moving close to the centre for all the three phonon modes, further confirming the nanosheet/pyramid structure.[33,38] To sum up for the Raman spectroscopy study, the spatial Se-composition gradient and thickness grading both can play significant roles in Raman scattering properties.

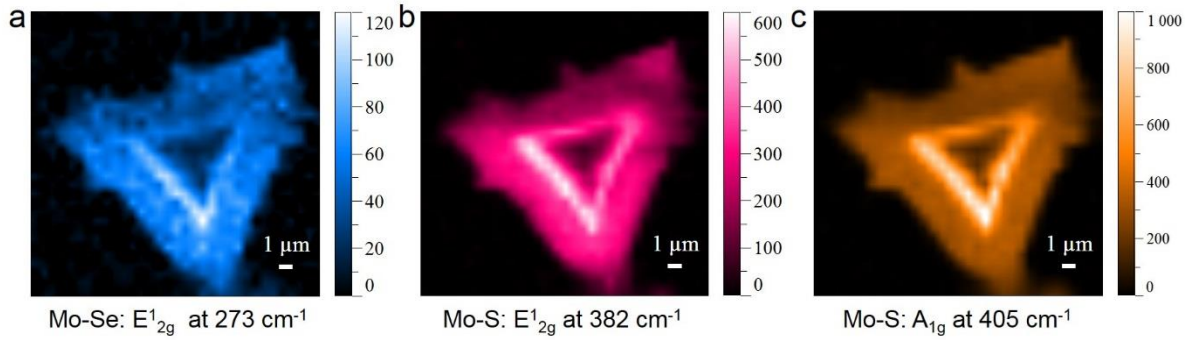

Figure 4.16 Raman intensity maps of the homojunction alloy domain shown in Figure 4.11a for (a) E_{2g}^1 (Mo-Se) at 273 cm^{-1}, (b) E_{2g}^1 (Mo-S) at 382 cm^{-1} and (c) A_{1g} (Mo-S) at 405 cm^{-1} modes, respectively. The configuration of nanosheet/pyramid was clearly resolved. A 532 nm laser was used as the excitation light source.

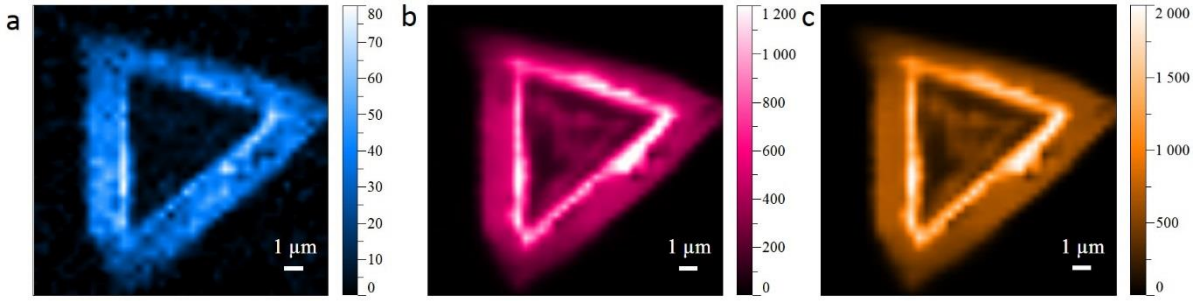

Figure 4.17 Raman intensity maps of the homojunction alloy domain shown in Figure 4.11b for (a) E_{2g}^1 (Mo-Se) at 273 cm^{-1}, (b) E_{2g}^1 (Mo-S) at 382 cm^{-1} and (c) A_{1g} (Mo-S) at

405 cm^{-1} modes, respectively. A 532 nm laser was used as the excitation light source. Similarly, the configuration of nanosheet/pyramid was clearly resolved.

Figure 4.19 shows the position-dependent micro-PL spectra and intensity map of the nanosheet/pyramid domain shown in Figure 4.18. As widely studied before, the thickness of the single crystalline binary MoS_2 has an obvious impact on its emission wavelength.[10,11] As soon as the thickness increased, the micro-PL spectra slightly red-shifted with a small degree less than 20 meV but with drastically dropped intensity. In contrast, from dot ***a*** at the thin edge to dot ***c*** at the thick centre (from dot ***d*** to dot ***f***), the peak red-shifted obviously from 677 nm (695 nm) to 715 nm (713 nm) (corresponding to 100 meV and 45 meV, respectively). Moreover, the peak intensity firstly underwent unobvious change (e.g., from dot ***a*** to dot ***c***) or even strengthened (e.g., from dot ***d*** to dot ***f***) as thickness increased, and afterwards it decreased to much smaller level when detected at the very central area, which was illustrated by the colour change of the pixels (see Figure 4.18b and 4.20b).

Such variation features agreed well with the case when more Se was introduced into binary MoS_2 with uniform thickness.[17,19,30,31,37] Therefore, the features of PL peak shift and intensity changing can be caused by the spatial composition and thickness gradient, further indicating more Se composition was implanted to the MoS_2 nanoflake when getting closer to the thick centre. The micro-PL results, which were was double confirmed in another nanosheet/pyramid 2D flake (see Figure 4.20 and 4.21), are also in good agreement with the Raman spectroscopy results resolving spatial composition and thickness gradient induced effects.

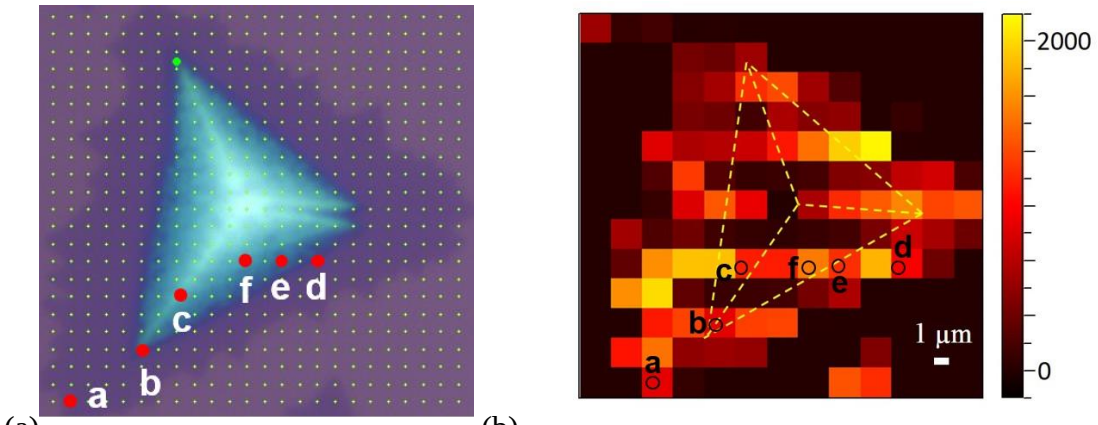

Figure 4.18 (a) Optical microscopy image of a $MoS_{2(1-x)}Se_{2x}$ alloy nanosheet with the nanosheet/pyramid configuration, selected for the following PL study. (b) PL intensity maps of the selected domain shown in (a). A 532 nm laser was used as the excitation light source. The dashed lines draw the central thick area.

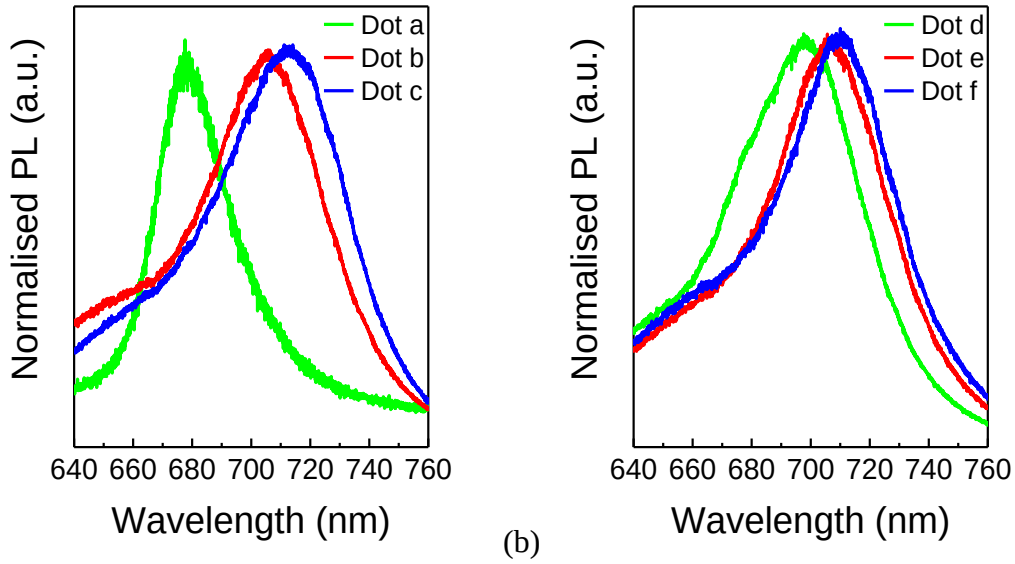

Figure 4.19 (a) Micro-PL spectra of the $MoS_{2(1-x)}Se_{2x}$ alloy nanosheet, excited by a 532 nm laser. They were measured at the sites of dot a, dot b and dot c, labelled at Figure 4.18a. (b) Micro-PL spectra of the $MoS_{2(1-x)}Se_{2x}$ alloy nanosheet. They were measured at the sites of dot d, dot e and dot f, labelled at Figure 4.18a.

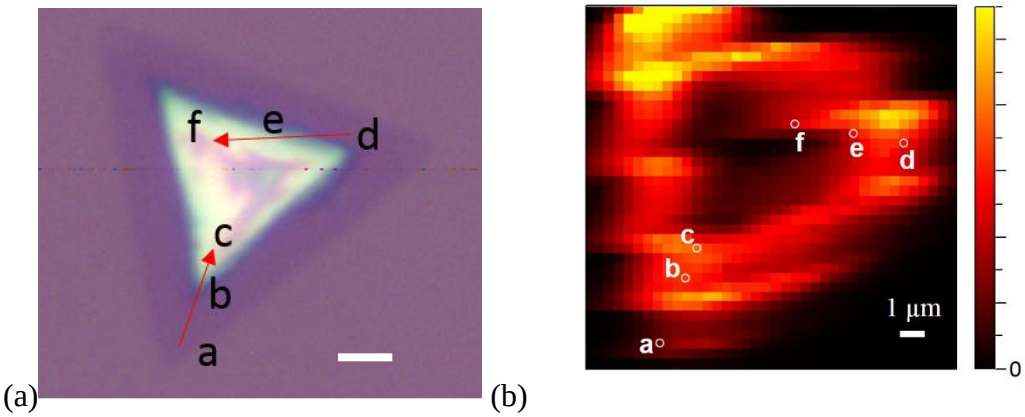

Figure 4.20 (a) Optical microscopy image of a $MoS_{2(1-x)}Se_{2x}$ alloy nanosheet with the nanosheet/pyramid configuration, selected for the following PL study. The scale bar is 1

μm. (b) PL intensity maps of the selected domain shown in (a). A 532 nm laser was used as the excitation light source.

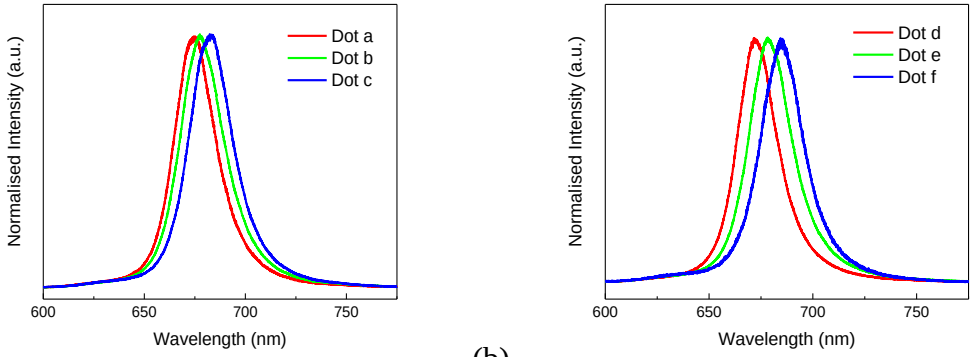

(a) (b)

Figure 4.21 (a) Micro-PL spectra of the $MoS_{2(1-x)}Se_{2x}$ alloy nanosheet, excited by a 532 nm laser. They were measured at the sites of dot a, dot b and dot c, labelled at Figure 4.20a. (b) Micro-PL spectra of the $MoS_{2(1-x)}Se_{2x}$ alloy nanosheet. They were measured at the sites of dot d, dot e and dot f, labelled at Figure 4.20a.

The presence of a spatial Se-composition and thickness gradient results in the bandgap-graded homojunction. As a result, a built-in electric field was formed. This is much desired for 2D devices as accurate spatial doping cannot be easily achieved in 2D nanosheets. Figure 4.22a shows the 3D view of a phototransistor based on the graded 2D homojunctions. The source and drain metal contacts were patterned by EBL and the subsequent e-beam evaporation of Ti/Au (10 nm/50 nm) for the electrode metallisation. Figure 4.22b shows the optical microscopy image of the selected nanosheet/pyramid homojunctions after metallisation.

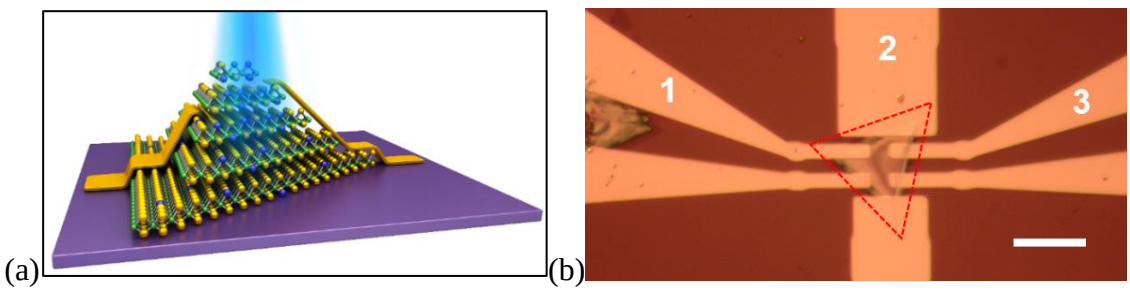

(a) (b)

Figure 4.22 (a) 3D view for the schematic diagram of a back-gated phototransistor based on the $MoS_{2(1-x)}Se_{2x}$ alloy nanosheet with the nanosheet/pyramid configuration. (b) Optical microscopy image of the phototransistor based on the nanosheet/pyramid structure on the SiO_2/Si substrate. The dashed triangle region denotes the nanosheet on the bottom. The scale bar is 20 μm and the three electrodes selected for the following measurements were marked as 1, 2 and 3.

Figure 4.23 shows the output curves of the phototransistor measured between metal contacts 1 and 3 under illumination (the channel distance > 3 μm). The two contacts worked as drain and source, respectively, and were marked in Figure 4.22b. The back-gate voltage was modulated from -3 V to 3 V. An obvious rectifying behaviour modulated by stepped gate voltage was illustrated owing to the intrinsic asymmetry of the nanosheet/pyramid homojunction.

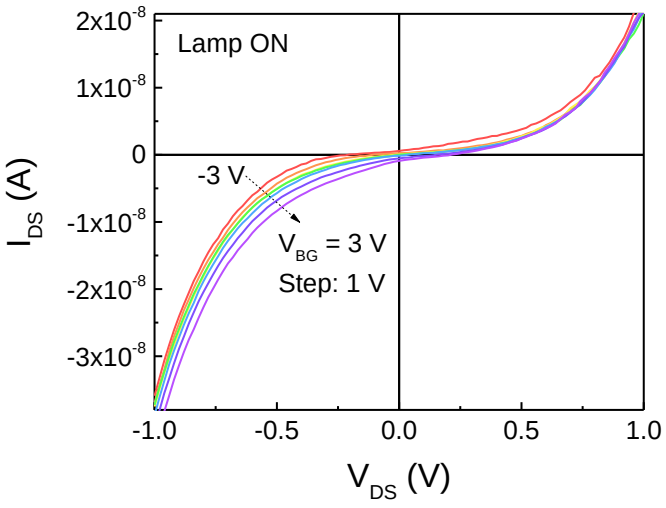

Figure 4.23 Drain-source output curves of the back-gated phototransistor, measured between contact 1 (drain) and contact 3 (source) when the lamp was on.

The irregularly changed rectifying features were also observed in different systems, which can be induced by the internal built-in electric field.[39,40] The enlarged linear and logarithmic plots of output curves were plotted in Figure 4.24 and 4.25 below, respectively, clearly resolving a gate-tunable photovoltaic effect. With the gate voltage

varying from the negative to the positive value, a consistently shifted V_{OC} from -0.22 V to 0.22 V was obtained.

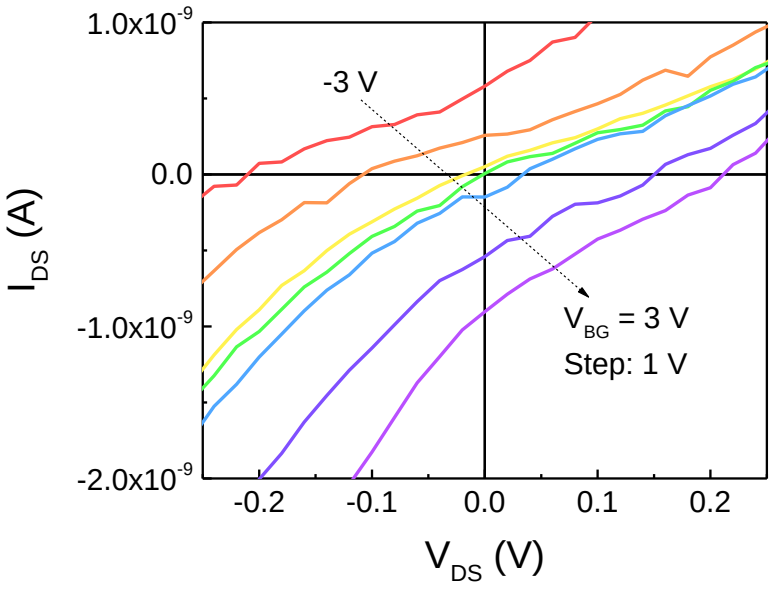

Figure 4.24 A magnified view of Figure 4.23 nearby the origin point to identify V_{oc} and I_{sc} in linear scale.

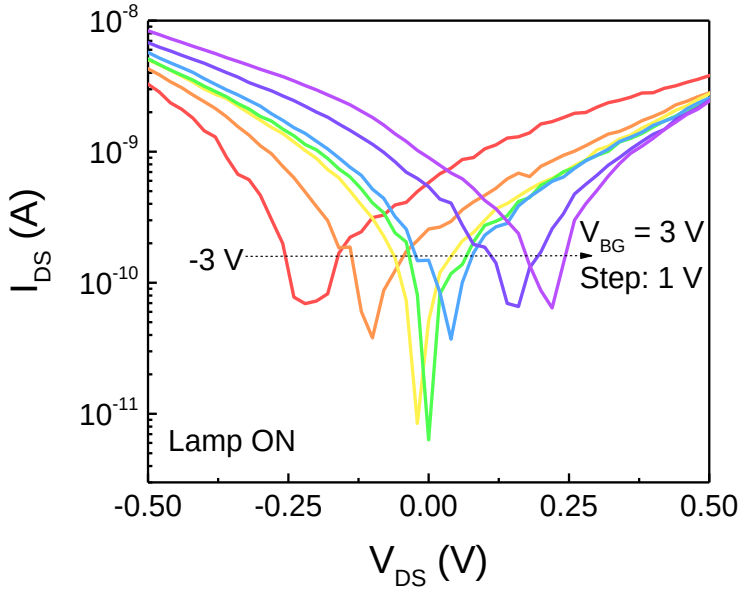

Figure 4.25 A magnified view of Figure 4.23 nearby the origin point to identify V_{oc} and I_{sc} in logarithmic scale.

Figure 4.26a, displaying the map of the drain-source current (the smallest current equal to the V_{OC}) in absolute value versus drain-source bias and back gate voltage, further revealed the back-gate voltage dependent V_{OC}. This behaviour was further confirmed on the same device by measuring between metal contacts 2 and 3 (the drain and source distance < 1 µm). Similarly, as shown in Figure 4.27, the output curves measured under illumination showed larger current and more apparent rectifying behaviour, which can be attributed to the shorter conducting channel distance and larger junction barrier under illumination. In addition, it is worth noting that the V_{OC} can be continuously tuned from -0.27 V to 0.26 V as the back-gate voltage changed from -6 V to 6 V (see Figure 4.26b, 4.27 – 4.29 from page 123 – 124).

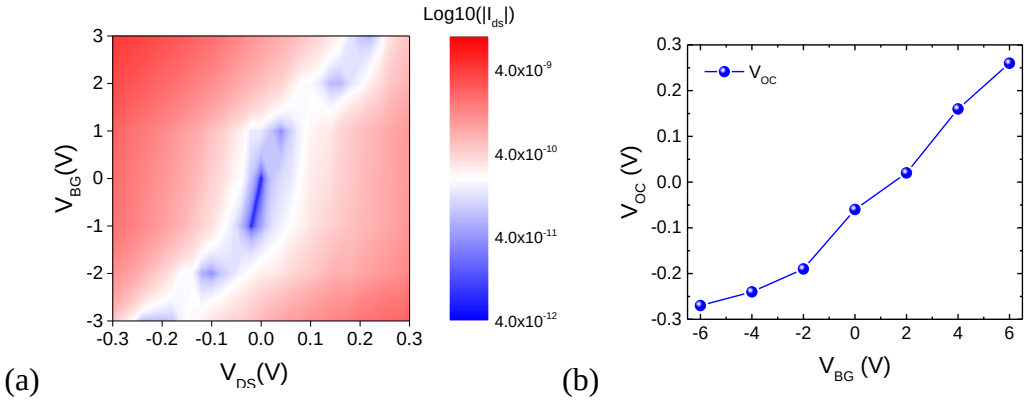

Figure 4.26 (a) The map of the minimum Ids as a function of V_{DS} and V_{BG}. The current was set in absolute value. (b) The Voc values of the phototransistor when measured between contact 1 and 2.

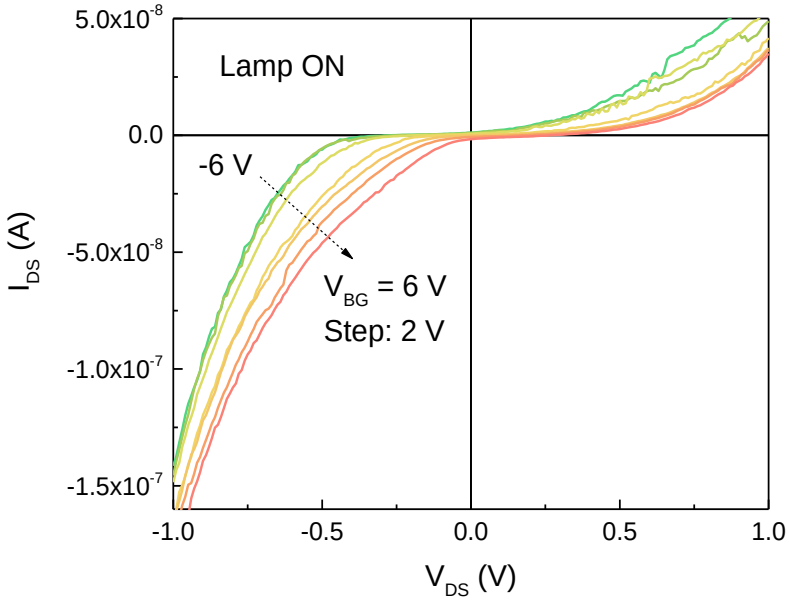

Figure 4.27 Drain-source output curves of the phototransistor between contacts 2 (drain) and 3 (source) under when the lamp illumination was on.

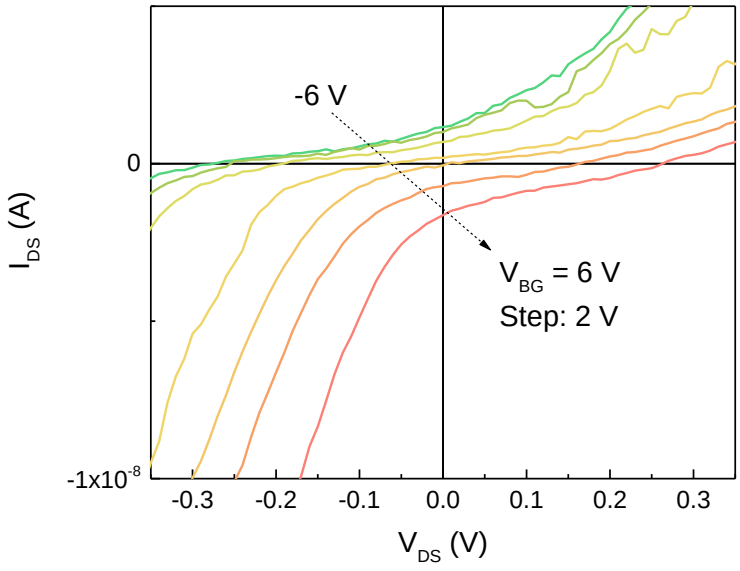

Figure 4.28 A magnified view of Figure 4.27 nearby the origin point to identify Voc and Isc in linear scale.

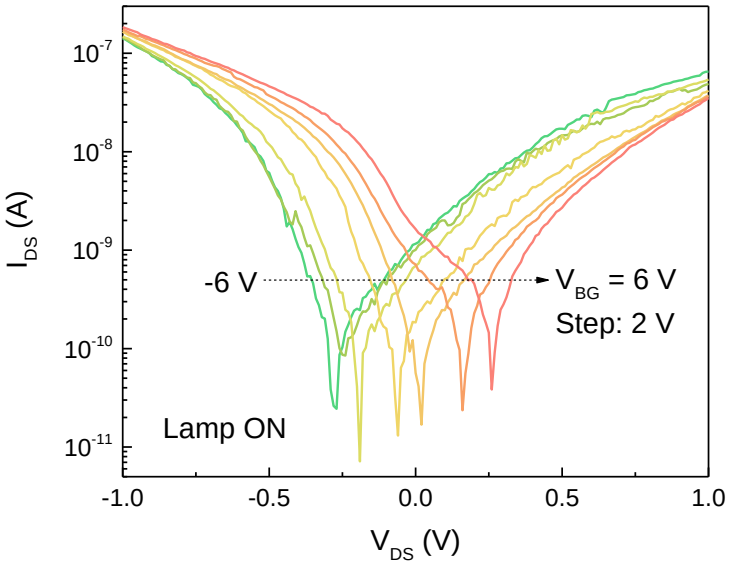

Figure 4.29 A magnified view of Figure 4.27 nearby the origin point to identify Voc and Isc in logarithmic scale.

When the back-gate voltage is zero, V_{OC} of -60 mV is achieved. In comparison, a device based on a non-graded 2D nanoflake without thickness variation, displayed in Figure 4.30, shows neither rectifying properties nor photovoltaic effect under illumination, as exhibited in Figure 4.31a. Therefore, this gate-modulated photovoltaic effect is attributed to the built-in electric field resulted from the spatially composition and thickness graded homojunctions, and it is stronger and more sensitive (larger V_{OC} and tuned by smaller back gate voltage) than the previously reported ones, which were enabled by perovskites/2D WSe_2 heterostructures (~ 0.19 V tuned by 60 V V_{BG}) and $MoSe_2$ homojunctions (~ -0.24 V tuned by -20 V V_{BG}) enabled by varied thickness.[40,41]

(a) 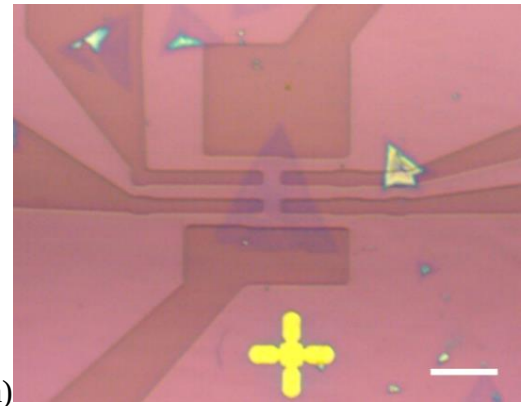 (b) 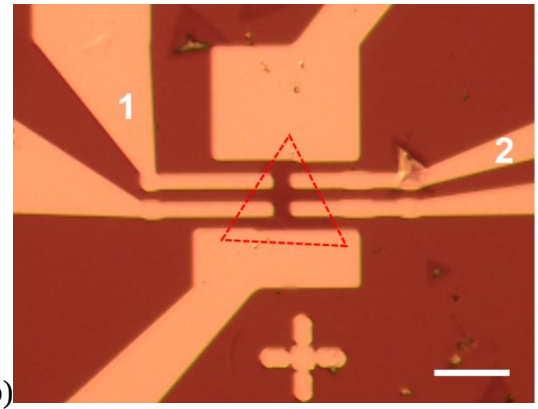

Figure 4.30 Optical microscopy image of the phototransistor based on the nanosheet without thickness variation on the SiO_2/Si substrate (a) after EBL patterning and (b) after metallisation. The dashed triangle region denotes the nanosheet domain. The scale bar is 10 µm for both figures and the two electrodes selected for the following measurements were marked as 1 and 2 and 3.

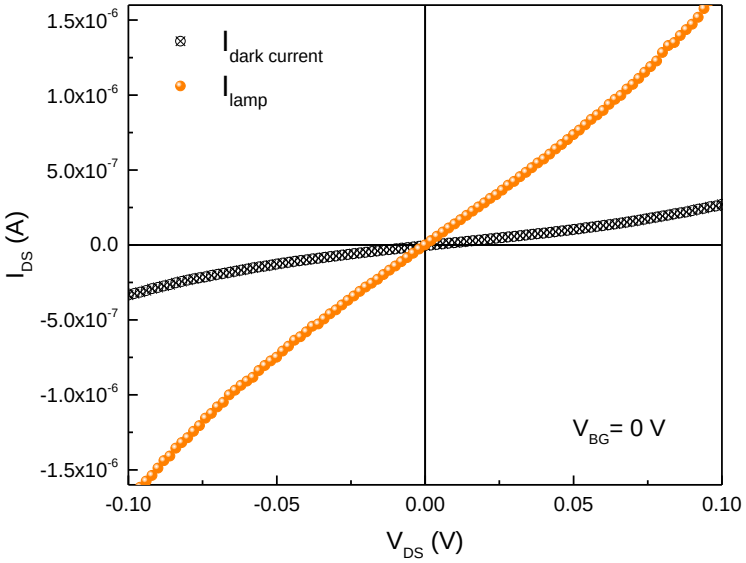

(a)

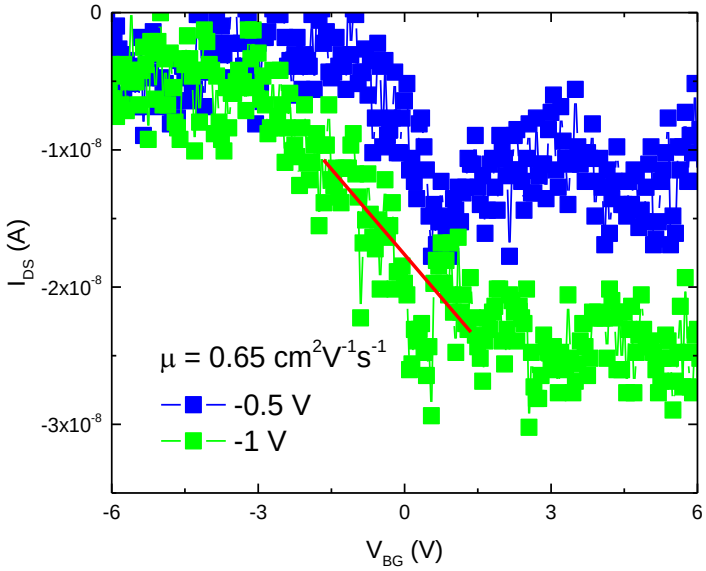

(b)

Figure 4.31 (a) Drain-source output curves with no gate modulation under dark and illumination, both of which passed through the origin point. (b) Transfer curves of the device with changing drain-source voltage.

According to the band structures of pristine MoS_2 and $MoSe_2$, the composition-graded alloy possesses a type II-like development band alignment.[21,22] Considering the potential offset caused by the asymmetry of the nanosheet/pyramid configuration, equivalent band diagrams are schematically shown in Figure 4.32.

When illumination is on under zero gate voltage, the photogenerated carriers were separated and collected by the built-in electric field, leading to modulated Fermi-level and a non-zero potential. When applied a negative gate voltage, the built-in electric field is amplified, giving rise to larger V_{OC}. Reversibly, by applying a positive gate voltage, the built-in electric field is compensated until being changed to a reversed direction, resulting in the reversed sign of V_{OC}.

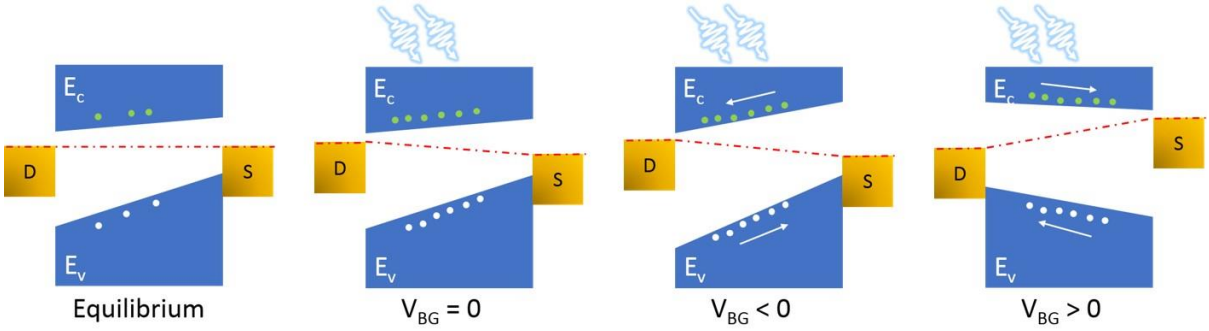

Figure 4.32 Schematic diagrams of homojunction band structures at equilibrium state, illumination and back-gate modulation. The concentration of Se increases from the left to the right. The dashed line represents the fermi level.

Moreover, the photoresponse performance of the device (measured between contact 1 (drain) and 3 (source)) was studied under illumination of 405 nm (blue), 532 nm (green) and 650 nm (red) lasers at ambient conditions. As displayed in Figure 4.33a, the dark current shows nearly linear and symmetric curve passing through the origin point, while the photocurrent exhibits evident wavelength selectivity with changing rectifying

properties and evident V_{OC}, further confirming the existence of the built-in electric field in the composition gradient homojunctions.

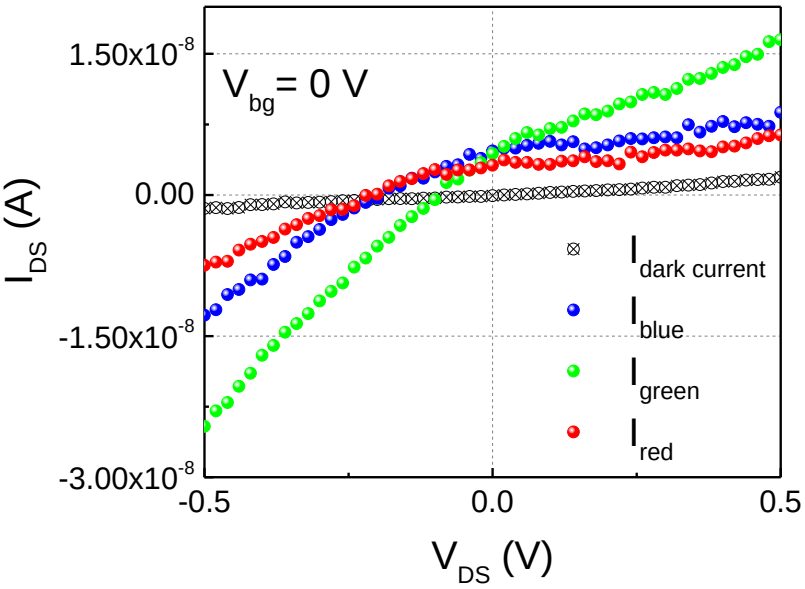

(a)

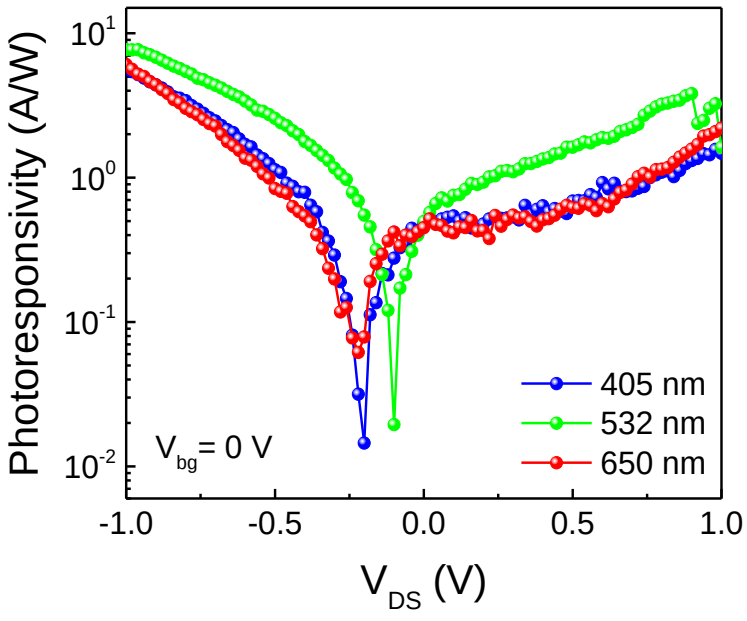

(b)

Figure 4.33 (a) The photocurrent curves excited by 405 nm, 532 nm and 650 nm laser illumination, in comparison with the dark current. (b) The corresponding photoresponsivity for 405 nm, 532 nm and 650 nm laser excitation.

The corresponding photoresponsivity was plotted in Figure 4.33b. The phototransistor can deliver the different *R* of 6.3 A/W, 8.4 A/W and 6.6 A/W when excited by 405 nm, 532 nm and 650 nm lasers under -1 V bias, respectively. Notably, the device under zero bias can still deliver the high *R* of 480 mA/W, 500 mA/W and 450 mA/W when illuminated by these three lasers, respectively. Due to the high responsivity, a high detectivity (D^*) of 2.2 $\times 10^{12}$ Jones was achieved for 532 nm laser excitation.

Figure 4.34a shows the time-resolved photoswitching dynamics of the phototransistor excited by different lasers under 1 V drain-source bias. The dynamic photoresponse was highly repeatable in many on/off cycles, indicating stability of the devices. The response time was evaluated by a typical rise time of 51 ms and fall time of 51 ms under 405 nm laser excitation (Figure 4.35). Figure 4.36 and 4.37 resolve rise and fall time for 532 nm and 650 nm laser excitation, respectively. The photoswitching characteristics of the device under different illuminations further demonstrate the wavelength selectivity and stability of the phototransistors enabled by the Se composition-graded alloys.

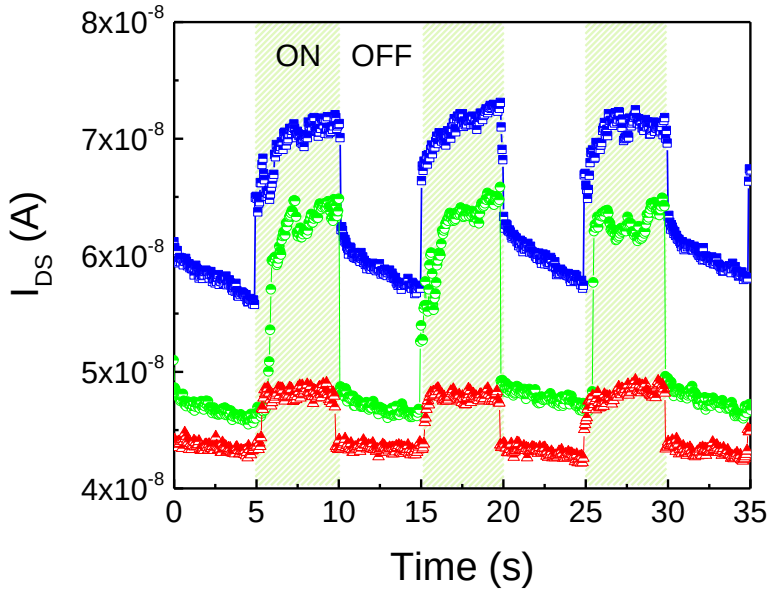

(a)

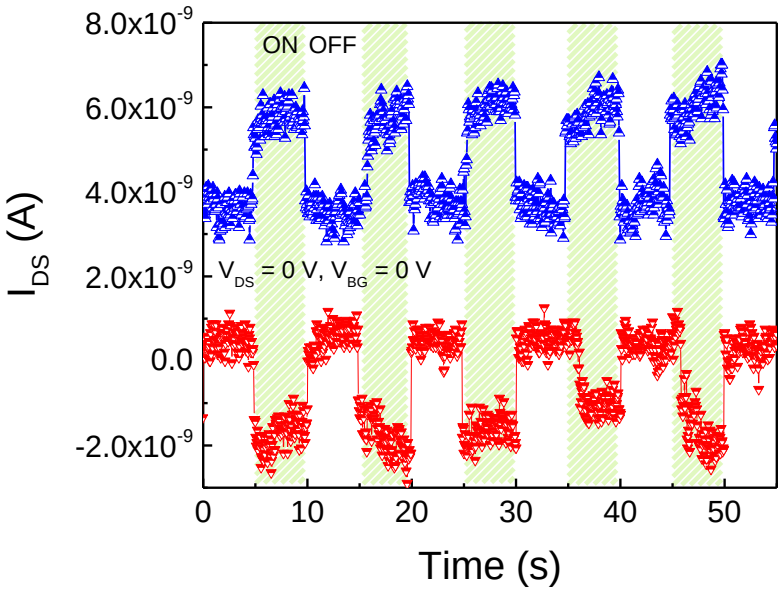

(b)

Figure 4.34 (a) Repeated ON/OFF photocurrent dynamics under 405 nm, 532 nm and 650 nm laser illumination. (b) The photoswitching dynamics (blue) of the phototransistor under zero bias and 405 nm laser illumination, exhibiting positive photoresponsive behaviour. The time gap between ON/OFF cycles was 5 s. After reversing the drain and source electrodes during the measurement, the devices also showed positive photoresponse (red).

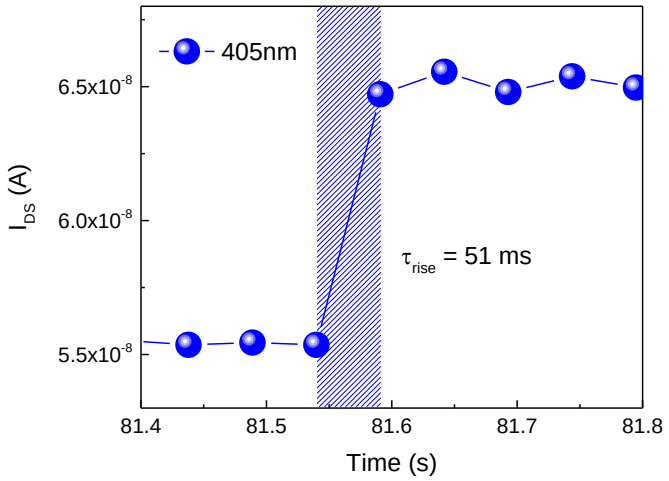

(a)

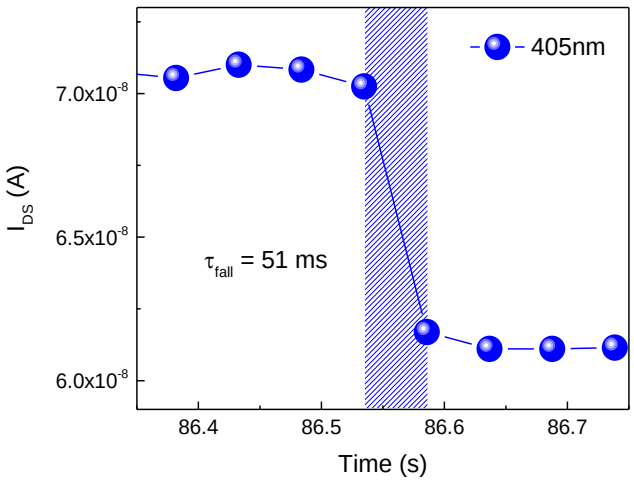

(b)

Figure 4.35 Enlarged view of one rise/fall loop of the repeated time-resolved photoresponsive behaviour, illustrating (a) the rise time of 51 ms and (b) the falling time of 51 ms for the 405 nm laser illumination. The drain-source biased voltage and back-gate voltage were 1 V and 0 V, respectively.

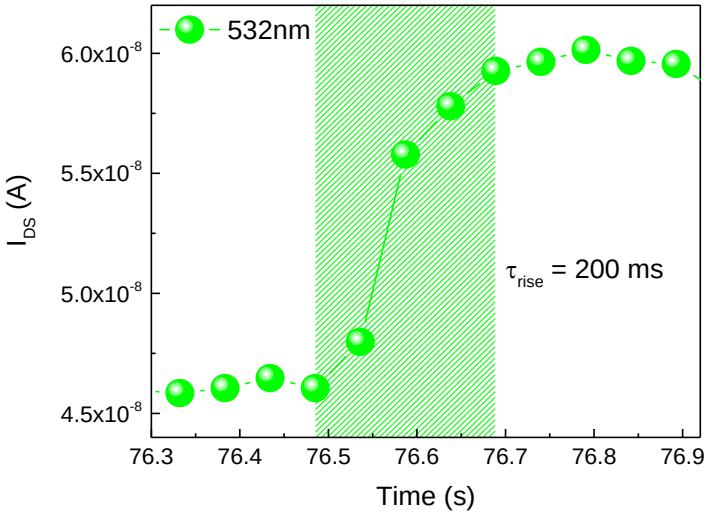

(a)

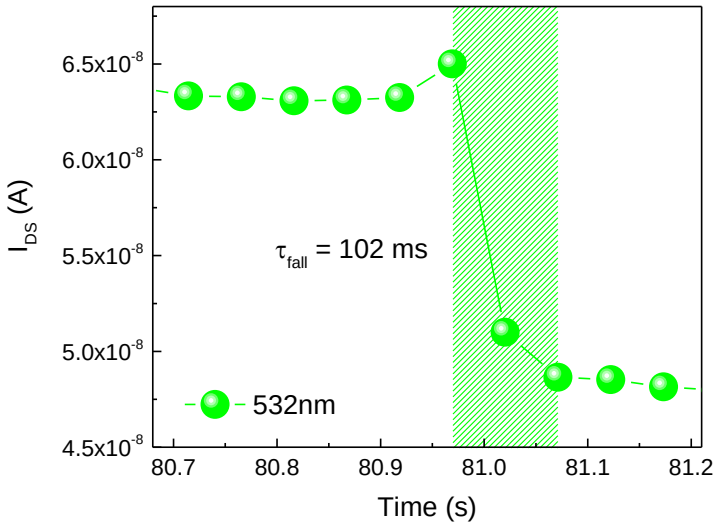

(b)

Figure 4.36 Enlarged view of one rise/fall loop of the repeated time-resolved photoresponsive behaviour, illustrating (a) the rise time of 200 ms and (b) the falling time of 102 ms for the 532 nm laser illumination. The drain-source biased voltage and back-gate voltage were 1 V and 0 V, respectively.

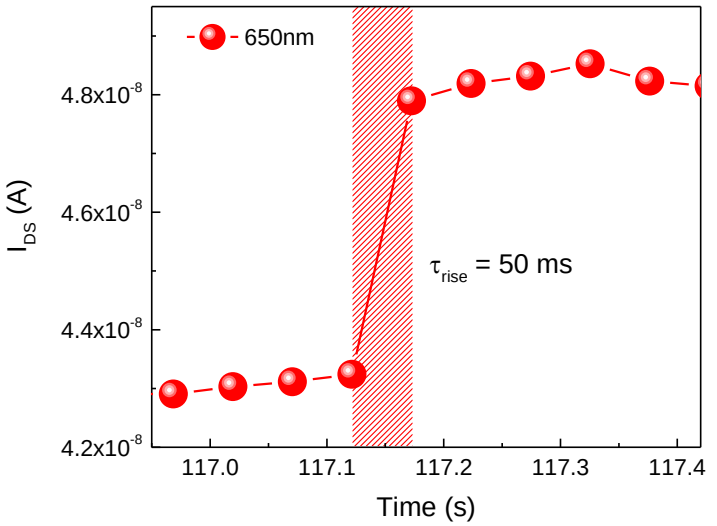

(a)

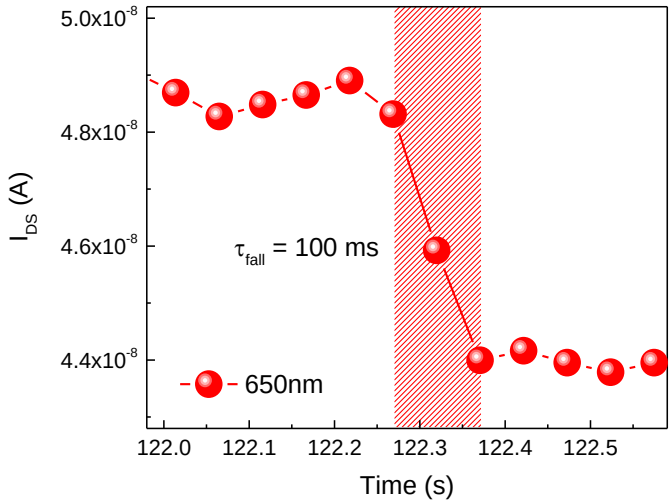

(b)

Figure 4.37 Enlarged view of one rise/fall loop of the repeated time-resolved photoresponsive behaviour, illustrating (a) the rise time of 50 ms and (b) the falling time of 100 ms for the 650 nm laser illumination. The drain-source biased voltage and back-gate voltage were 1 V and 0 V, respectively.

A long carrier lifetime τ_L on the order of 10^{-1} ~10^{0} s level can be extracted by fitting the following equation 4.5 and 4.6 (the fitting results shown in Figure 4.38 – 4.40).[42]

$$I(t) = \alpha e^{-t/\tau_L} \tag{4.5}$$

Here α is fitting parameter. As a result, a very high photoconductive gain (G) was estimated to be on the order of 10^{6} ~10^{7} from the equation below.

$$G = \frac{\tau_L}{\tau_{transit}} \tag{4.6}$$

Here $\tau_{transit}$ denotes carrier transit time that was deduced in Equation 4.4. More importantly, because of the internal built-in electric field, the phototransistors can work under zero bias, showing repeatable positive-photoresponse under illumination of 405 nm laser (see Figure 4.34b). This self-powered behaviour was also double confirmed under different laser illumination, e.g. 532 nm and 650 nm lasers (see Figure 4.41).

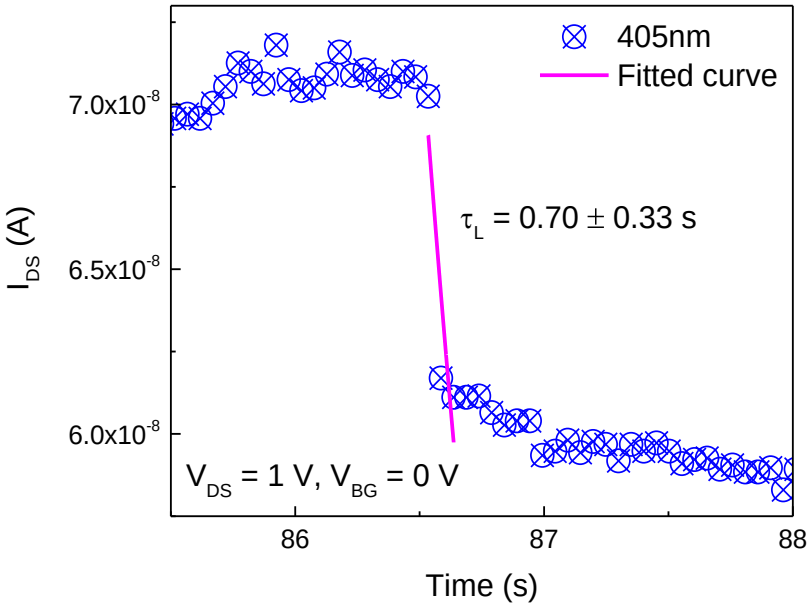

Figure 4.38 Lifetime of photogenerated carriers under 405 nm laser excitation. τ was exacted from Equation (4.5).

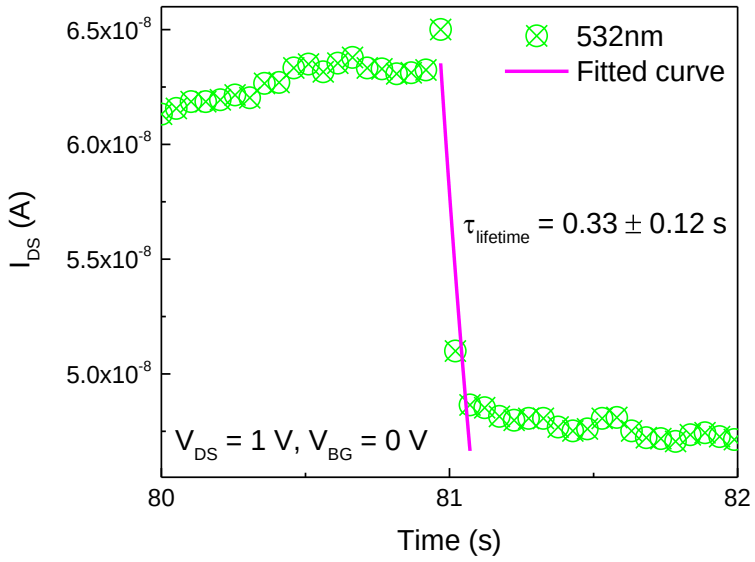

Figure 4.39 Lifetime of photogenerated carriers under 532 nm laser excitation. τ was exacted from Equation (4.5).

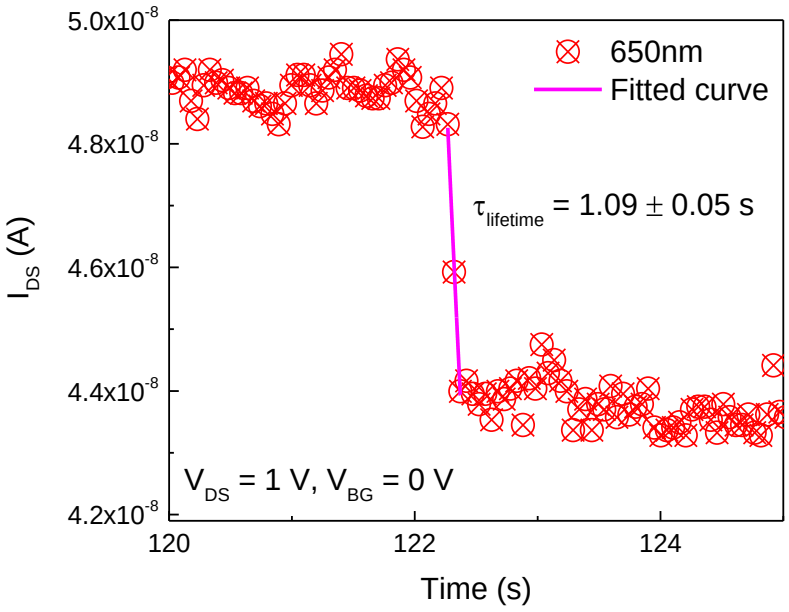

Figure 4.40 Lifetime of photogenerated carriers under 650 nm laser excitation. τ was exacted from Equation (4.5).

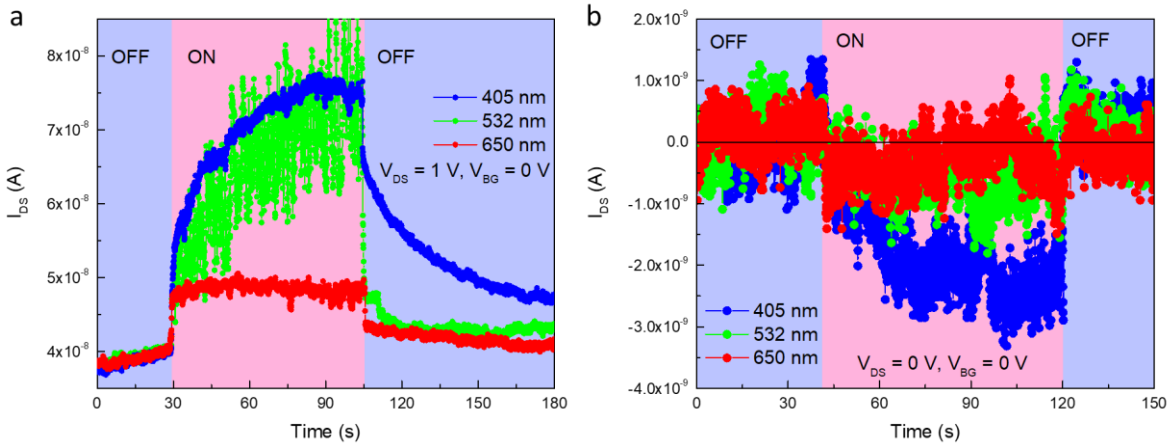

Figure 4.41 (a) The photoswitching characteristics of the phototransistors at V_{DS} = 1 V and V_{BG} = 0 V (b) The photoswitching behaviour of the unbiased phototransistors at V_{DS} = 0 V and V_{BG} = 0 V after reversing the drain and source electrodes.

4.4 Conclusions

To sum up, self-powered phototransistors based on novel bandgap-graded homojunctions, namely, spatially composition and thickness graded $MoS_{2(1-x)}Se_{2x}$ alloys, were fabricated and studied. The bandgap-graded homojunction materials were synthesised using a simple and cost-effective CSD approach. Detailed material characterisations were carried out to confirm the spatial Se composition gradient and the existence of homojunctions.

ADF-STEM was employed to image the spatial distribution of Se atoms and resolve the single/double Se substitution positions. Besides, EDS, Raman and micro-PL position-dependent spectroscopy and mapping were performed to confirm the Se-composition and thickness gradient within the single nanosheet domains. Based on the shifted peaks in micro-PL spectra, the bandgaps of the homojunction alloys can be continuously tuned from 1.83 eV to 1.73 eV, leading to the formation of an internal built-in electric field.

Consequently, the strong and sensitive gate-tunable photovoltaic effect was observed, enabling the phototransistors to work without applying external bias voltage. The highest achieved photoresponsivity of 500 mA/W (illuminated by 532 nm laser) was attained when working in the self-powered mode. The wavelength selectivity and dynamic stability were demonstrated, and the devices under 1 V bias delivered: a photoresponsivity of 8.4 A/W, a specific detectivity of 2.2×10^{12} Jones, a very high photoconductive gain of $10^6 \sim 10^7$, and a fast photoresponse time in the order of 50 ms.

Notably, in contrast to the most reported photodetectors based on 2D or multilayer TMDs, 2D layered semiconductors and artificial heterojunctions under similar measurement conditions, the figures of merit of the phototransistors based on $MoS_{2(1-x)}Se_{2x}$ homojunctions were competitive or even better, particularly in terms of showing the self-powered working mode.[43]

Overall, the realisation of the high-performance phototransistors based on such spatially bandgap-graded TMD homojunctions opens up new scope of bandgap engineering and device design, and provides bandgap engineering with more device design possibility and flexibility.

4.5 References

(1) Radisavljevic, B.; Radenovic, A.; Brivio, J.; Giacometti, V.; Kis, A. Single-Layer MoS2 Transistors. *Nat. Nanotechnol.* **2011**, *6* (3), 147–150. https://doi.org/10.1038/nnano.2010.279.

(2) Lopez-Sanchez, O.; Lembke, D.; Kayci, M.; Radenovic, A.; Kis, A. Ultrasensitive Photodetectors Based on Monolayer MoS2. *Nat. Nanotechnol.* **2013**, *8* (7), 497–501. https://doi.org/10.1038/nnano.2013.100.

(3) Baugher, B. W. H.; Churchill, H. O. H.; Yang, Y.; Jarillo-Herrero, P. Optoelectronic Devices Based on Electrically Tunable P-N Diodes in a Monolayer Dichalcogenide. *Nat. Nanotechnol.* **2014**, *9* (4), 262–267. https://doi.org/10.1038/nnano.2014.25.

(4) Ye, Y.; Wong, Z. J.; Lu, X.; Ni, X.; Zhu, H.; Chen, X.; Wang, Y.; Zhang, X. Monolayer Excitonic Laser. *Nat. Photonics* **2015**, *9* (11), 733–737. https://doi.org/10.1038/nphoton.2015.197.

(5) Chuang, H. J.; Chamlagain, B.; Koehler, M.; Perera, M. M.; Yan, J.; Mandrus, D.; Tománek, D.; Zhou, Z. Low-Resistance 2D/2D Ohmic Contacts: A Universal Approach to High-Performance WSe2, MoS2, and MoSe2 Transistors. *Nano Lett.* **2016**, *16* (3), 1896–1902. https://doi.org/10.1021/acs.nanolett.5b05066.

(6) Sangwan, V. K.; Lee, H. S.; Bergeron, H.; Balla, I.; Beck, M. E.; Chen, K. S.; Hersam, M. C. Multi-Terminal Memtransistors from Polycrystalline Monolayer Molybdenum Disulfide. *Nature* **2018**, *554* (7693), 500–504. https://doi.org/10.1038/nature25747.

(7) Xu, H.; Han, X.; Dai, X.; Liu, W.; Wu, J.; Zhu, J.; Kim, D.; Zou, G.; Sablon, K. A.; Sergeev, A.; et al. High Detectivity and Transparent Few-Layer MoS2/Glassy-Graphene Heterostructure Photodetectors. *Adv. Mater.* **2018**, *30*, 1706561. https://doi.org/10.1002/adma.201706561.

(8) Novoselov, K. S.; Geim, A. K.; Morozov, S. V; Jiang, D.; Katsnelson, M. I.; Grigorieva, I. V; Dubonos, S. V; Firsov, A. A. Two-Dimensional Gas of Massless Dirac Fermions in Graphene. *Nature* **2005**, *438* (7065), 197–200. https://doi.org/10.1038/nature04233.

(9) Zhang, Y.; Chang, T. R.; Zhou, B.; Cui, Y. T.; Yan, H.; Liu, Z.; Schmitt, F.; Lee, J.; Moore, R.; Chen, Y.; et al. Direct Observation of the Transition from Indirect

to Direct Bandgap in Atomically Thin Epitaxial MoSe2. *Nat. Nanotechnol.* **2014**, *9* (2), 111–115. https://doi.org/10.1038/nnano.2013.277.

(10) Eda, G.; Yamaguchi, H.; Voiry, D.; Fujita, T.; Chen, M.; Chhowalla, M. Photoluminescence from Chemically Exfoliated MoS2. *Nano Lett.* **2011**, *11* (12), 5111–5116. https://doi.org/10.1021/nl201874w.

(11) Splendiani, A.; Sun, L.; Zhang, Y.; Li, T.; Kim, J.; Chim, C. Y.; Galli, G.; Wang, F. Emerging Photoluminescence in Monolayer MoS2. *Nano Lett.* **2010**, *10* (4), 1271–1275. https://doi.org/10.1021/nl903868w.

(12) Zhang, Z.; Chen, P.; Duan, X.; Zang, K.; Luo, J.; Duan, X. Robust Epitaxial Growth of Two-Dimensional Heterostructures, Multiheterostructures, and Superlattices. *Science.* **2017**, *357*, 788–792. https://doi.org/10.1126/science.aan6814.

(13) Hong, X.; Kim, J.; Shi, S.-F.; Zhang, Y.; Jin, C.; Sun, Y.; Tongay, S.; Wu, J.; Zhang, Y.; Wang, F. Ultrafast Charge Transfer in Atomically Thin MoS2/WS2 Heterostructures. *Nat. Nanotechnol.* **2014**, *9* (August), 682–686. https://doi.org/10.1038/nnano.2014.167.

(14) Chen, Y.; Wang, X.; Wu, G.; Wang, Z.; Fang, H.; Lin, T.; Sun, S.; Shen, H.; Hu, W.; Wang, J.; et al. High-Performance Photovoltaic Detector Based on MoTe2/MoS2 Van Der Waals Heterostructure. *Small* **2018**, *14* (9), 1703293. https://doi.org/10.1002/smll.201703293.

(15) Huo, N.; Kang, J.; Wei, Z.; Li, S. S.; Li, J.; Wei, S. H. Novel and Enhanced Optoelectronic Performances of Multilayer MoS2-WS2 Heterostructure Transistors. *Adv. Funct. Mater.* **2014**, *24* (44), 7025–7031. https://doi.org/10.1002/adfm.201401504.

(16) Li, M.-Y.; Shi, Y.; Cheng, C.-C.; Lu, L.-S.; Lin, Y.-C.; Tang, H.-L.; Tsai, M.-L.; Chu, C.-W.; Wei, K.-H.; He, J.-H.; et al. Epitaxial Growth of a Monolayer WSe2-MoS2 Lateral P-N Junction with an Atomically Sharp Interface. *Science.* **2015**, *349* (6247), 524–528.

(17) Zhang, W.; Li, X.; Jiang, T.; Song, J.; Lin, Y.; Zhu, L.; Xu, X. CVD Synthesis of Mo(1−x)WxS2 and MoS2(1−x)Se2x Alloy Monolayers Aimed at Tuning the Bandgap of Molybdenum Disulfide. *Nanoscale* **2015**, *7* (32), 13554–13560. https://doi.org/10.1039/C5NR02515J.

(18) Duan, X.; Wang, C.; Fan, Z.; Hao, G.; Kou, L.; Halim, U.; Li, H.; Wu, X.; Wang, Y.; Jiang, J.; et al. Synthesis of WS2xSe2–2x Alloy Nanosheets with

Composition-Tunable Electronic Properties. *Nano Lett.* **2016**, *16* (1), 264–269. https://doi.org/10.1021/acs.nanolett.5b03662.

(19) Yang, L.; Fu, Q.; Wang, W.; Huang, J.; Huang, J.; Zhang, J.; Xiang, B. Large-Area Synthesis of Monolayered MoS2(1-x)Se2x with a Tunable Band Gap and Its Enhanced Electrochemical Catalytic Activity. *Nanoscale* **2015**, *7* (23), 10490–10497. https://doi.org/10.1039/c5nr02652k.

(20) Gong, Y.; Liu, Z.; Lupini, A. R.; Shi, G.; Lin, J.; Najmaei, S.; Lin, Z.; Elías, A. L.; Berkdemir, A.; You, G.; et al. Band Gap Engineering and Layer-by-Layer Mapping of Selenium-Doped Molybdenum Disulfide. *Nano Lett.* **2014**, *14* (2), 442–449. https://doi.org/10.1021/nl4032296.

(21) Kang, J.; Tongay, S.; Zhou, J.; Li, J.; Wu, J. Band Offsets and Heterostructures of Two-Dimensional Semiconductors. *Appl. Phys. Lett.* **2013**, *102* (1), 012111. https://doi.org/10.1063/1.4774090.

(22) Kang, J.; Li, J.; Li, S. S.; Xia, J. B.; Wang, L. W. Electronic Structural Moiré Pattern Effects on MoS2/MoSe2 2D Heterostructures. *Nano Lett.* **2013**, *13* (11), 5485–5490. https://doi.org/10.1021/nl4030648.

(23) Feng, C.; Zhang, Y.; Qian, Y.; Chang, B.; Shi, F.; Jiao, G.; Zou, J. Photoemission from Advanced Heterostructured AlxGa1-xAs/GaAs Photocathodes under Multilevel Built-in Electric Field. *Opt. Express* **2015**, *23* (15), 19478. https://doi.org/10.1364/OE.23.019478.

(24) Woo, K.; Kim, Y.; Yang, W.; Kim, K.; Kim, I.; Oh, Y.; Kim, J. Y.; Moon, J. Band-Gap-Graded Cu2ZnSn(S1-x,Sex)4 Solar Cells Fabricated by an Ethanol-Based, Particulate Precursor Ink Route. *Sci. Rep.* **2013**, *3*, 1–7. https://doi.org/10.1038/srep03069.

(25) Bailey, R. E.; Nie, S. Alloyed Semiconductor Quantum Dots: Tuning the Optical Properties without Changing the Particle Size. *J. Am. Chem. Soc.* **2003**, *125* (23), 7100–7106. https://doi.org/10.1021/ja035000o.

(26) Zhou, R.; Wan, L.; Niu, H.; Yang, L.; Mao, X.; Zhang, Q.; Miao, S.; Xu, J.; Cao, G. Tailoring Band Structure of Ternary CdSxSe1-X Quantum Dots for Highly Efficient Sensitized Solar Cells. *Sol. Energy Mater. Sol. Cells* **2016**, *155*, 20–29. https://doi.org/10.1016/j.solmat.2016.04.049.

(27) Pan, A.; Zhou, W.; Leong, E. S. P.; Liu, R.; Chin, A. H.; Zou, B.; Ning, C. Z. Continuous Alloy-Composition Spatial Grading and Superbroad Wavelength-Tunable Nanowire Lasers on a Single Chip. *Nano Lett.* **2009**, *9* (2), 784–788.

https://doi.org/10.1021/n1803456k.

(28) Li, L.; Lu, H.; Yang, Z.; Tong, L.; Bando, Y.; Golberg, D. Bandgap-Graded CdSxSe1-X Nanowires for High-Performance Field-Effect Transistors and Solar Cells. *Adv. Mater.* **2013**, *25* (8), 1109–1113. https://doi.org/10.1002/adma.201204434.

(29) Zhuang, X.; Ning, C. Z.; Pan, A. Composition and Bandgap-Graded Semiconductor Alloy Nanowires. *Adv. Mater.* **2012**, *24* (1), 13–33. https://doi.org/10.1002/adma.201103191.

(30) Li, H.; Zhang, Q.; Duan, X.; Wu, X.; Fan, X.; Zhu, X.; Zhuang, X.; Hu, W.; Zhou, H.; Pan, A.; et al. Lateral Growth of Composition Graded Atomic Layer MoS2(1-x)Se2x Nanosheets. *J. Am. Chem. Soc.* **2015**, *137* (16), 5284–5287. https://doi.org/10.1021/jacs.5b01594.

(31) Zheng, S.; Sun, L.; Yin, T.; Dubrovkin, A. M.; Liu, F.; Liu, Z.; Shen, Z. X.; Fan, H. J. Monolayers of WxMo1-xS2 Alloy Heterostructure with in-Plane Composition Variations. *Appl. Phys. Lett.* **2015**, *106* (6), 063113. https://doi.org/10.1063/1.4908256.

(32) Li, H.; Zhang, Q.; Yap, C. C. R.; Tay, B. K.; Edwin, T. H. T.; Olivier, A.; Baillargeat, D. From Bulk to Monolayer MoS2: Evolution of Raman Scattering. *Adv. Funct. Mater.* **2012**, *22* (7), 1385–1390. https://doi.org/10.1002/adfm.201102111.

(33) Lee, C.; Yan, H.; Brus, L. E.; Heinz, T. F.; Hone, J.; Ryu, S. Anomalous Lattice Vibrations of Single- and Few-Layer MoS2. *ACS Nano* **2010**, *4* (5), 2695–2700. https://doi.org/10.1021/nn1003937.

(34) Saito, R.; Tatsumi, Y.; Huang, S.; Ling, X.; Dresselhaus, M. S. Raman Spectroscopy of Transition Metal Dichalcogenides. *J. Phys. Condens. Matter* **2016**, *28* (35), 353002. https://doi.org/10.1088/0953-8984/28/35/353002.

(35) Lanzillo, N. A.; Glen Birdwell, A.; Amani, M.; Crowne, F. J.; Shah, P. B.; Najmaei, S.; Liu, Z.; Ajayan, P. M.; Lou, J.; Dubey, M.; et al. Temperature-Dependent Phonon Shifts in Monolayer MoS2. *Appl. Phys. Lett.* **2013**, *103* (9), 93102. https://doi.org/10.1063/1.4819337.

(36) Tonndorf, P.; Schmidt, R.; Böttger, P.; Zhang, X.; Börner, J.; Liebig, A.; Albrecht, M.; Kloc, C.; Gordan, O.; Zahn, D. R. T.; et al. Photoluminescence Emission and Raman Response of Monolayer MoS2, MoSe2, and WSe2. *Opt. Express* **2013**, *21* (4), 4908–4916. https://doi.org/10.1038/srep01608.

(37) Gong, Q.; Cheng, L.; Liu, C.; Zhang, M.; Feng, Q.; Ye, H.; Zeng, M.; Xie, L.; Liu, Z.; Li, Y. Ultrathin MoS2(1– x)Se2x Alloy Nanoflakes For Electrocatalytic Hydrogen Evolution Reaction. *ACS Catal.* **2015**, *5* (4), 2213–2219. https://doi.org/10.1021/cs501970w.

(38) O'Brien, M.; McEvoy, N.; Hanlon, D.; Hallam, T.; Coleman, J. N.; Duesberg, G. S. Mapping of Low-Frequency Raman Modes in CVD-Grown Transition Metal Dichalcogenides: Layer Number, Stacking Orientation and Resonant Effects. *Sci. Rep.* **2016**, *6* (August 2015), 19476. https://doi.org/10.1038/srep19476.

(39) Jariwala, D.; Sangwan, V. K.; Wu, C.-C.; Prabhumirashi, P. L.; Geier, M. L.; Marks, T. J.; Lauhon, L. J.; Hersam, M. C. Gate-Tunable Carbon Nanotube-MoS2 Heterojunction P-N Diode. *Proc. Natl. Acad. Sci.* **2013**, *110* (45), 18076–18080. https://doi.org/10.1073/pnas.1317226110.

(40) Cheng, H. C.; Wang, G.; Li, D.; He, Q.; Yin, A.; Liu, Y.; Wu, H.; Ding, M.; Huang, Y.; Duan, X. Van Der Waals Heterojunction Devices Based on Organohalide Perovskites and Two-Dimensional Materials. *Nano Lett.* **2016**, *16* (1), 367–373. https://doi.org/10.1021/acs.nanolett.5b03944.

(41) Yang, Y.; Huo, N.; Li, J. Gate Tunable Photovoltaic Effect in a MoSe2 Homojunction Enabled with Different Thicknesses. *J. Mater. Chem. C* **2017**, *5* (28), 7051–7056. https://doi.org/10.1039/C7TC01806A.

(42) Ma, Y.; Gu, Y.; Zhang, Y.; Chen, X.; Xi, S.; Boldizsar, Z.; Huang, L.; Zhou, L. Carrier Scattering and Relaxation Dynamics in N-Type In $_{0.83}$ Ga $_{0.17}$ As as a Function of Temperature and Doping Density. *J. Mater. Chem. C* **2015**, *3* (12), 2872–2880. https://doi.org/10.1039/C4TC02709D.

(43) Xie, C.; Mak, C.; Tao, X.; Yan, F. Photodetectors Based on Two-Dimensional Layered Materials Beyond Graphene. *Adv. Funct. Mater.* **2017**, *27* (19), 1603886. https://doi.org/10.1002/adfm.201603886.

Chapter 5 Bilayer Self-Passivated WSe_2 Nanosheets for Robust Field-Effect Transistors

5.1 Research Background and Result Overview

5.1.1 Research background

Nowadays, fuelled by the huge global market value of the Internet of Things, wearable devices, such as smart glasses, foldable screens, light emission diode (LED) integrated clothes, *etc*., have drawn ever increasing attention. This directly triggers the considerable study focused on flexible electronics, including flexible display, flexible sensors, flexible optoelectronic chips, flexible cells, *etc*., which is the key and essential technique for wearable devices.[1-3] Thanks to the outstanding properties, such as atomic scale thickness, transparency, mechanical strength, flexibility, good conductivity, tunable broadband absorption, *etc*., two-dimensional (2D) materials can come into play for the flexible devices and are believed to boost improvement of integrated flexible electronics.[4,5] As

representative 2D materials, layered semiconducting transition metal dichalcogenides (TMDs), unlike pristine gapless graphene, have thickness-dependent bandgaps that can be tuned across the spectral range from ultraviolet (UV) to near-infrared (NIR), showing prospective optoelectronic properties and promising applications in flexible electronics. Consequently, worldwide researchers have devoted extensive efforts to tailoring TMDs, including scaling down thickness, large-area synthesis, bandgap engineering by doping or strain, *etc*., to achieve high-performance devices for future practical use.[6-8] Notably, Se based TMDs are delegates to the TMD family, and they also share excellent properties with the S based ones, such as prospective applications in nanoelectronic and optoelectronic fields, while the latter one have been more widely studied.[9,10] Nevertheless, Se base TMDs are sensitive to ambient conditions and air-induced oxidation on material surface is unavoidable, particularly at high temperature.

Binary WSe_2 is a representative member of Se based TMDs, which inherently shows a direct bandgap of 1.6 eV for monolayer (ML) and indirect bandgap of 1.2 eV for bulk forms.[10,11] WSe_2 has been widely employed for fabricating field-effect transistors (FETs) and phototransistors, exhibiting evident p-type gate-tunable behaviour. Due to the intrinsic sensitivity to ambient conditions, WSe_2 also provides chances for studying oxidation, reduction and etching of TMDs when stored in ambient conditions for a long-term. The former studies revealed that air-induced oxidation occurring at edges of WSe_2 surface, which can obviously degrade device performance.[12,13] Both physical absorption and chemical reaction were observed on WSe_2 surface after long-term air exposure, leading to varied bandgaps, roughened surface, enlarged thickness, reduced carrier mobility and electrical conductivity. To study this inevitable air-induced oxidation process and use the resulted changed features, artificial oxidation was introduced to pristine WSe_2 nanosheets via air-heating, selectively forming in-plane WSe_2/WO_x heterojunctions and then demonstrating enhanced FET performance.[14]

5.1.2 Result overview

Here, by using the self-assembled oxidised edge domains that unavoidably formed under ambient conditions, a series of back-gated FETs on SiO_2/Si substrates enabled by long-term air-exposed bilayer (BL) WSe_2 with self-passivation were fabricated and studied. Detailed material characterisations, including scanning electron microscopy (SEM),

atomic force microscopy (AFM), current-sensing AFM (C-AFM), Raman spectroscopy and X-ray photoelectron spectroscopy (XPS), were carried out, and proved the existence of WO_x/WSe_2 heterojunctions around edges of BL WSe_2. It was found that the internal domains of WSe_2 nanosheets were nearly unaffected by ambient air and maintained pristine properties. With air-induced WO_x passivating dangling bonds at edges of WSe_2 and acting as a buffer layer between contact metals and WSe_2 nanosheets, the FETs possessed ohmic contact and exhibited n-type behaviour from 77 K to 300 K, high conductivity up to ~ 2600 S/m, ultra-low leakage gate current as small as ~ 10^{-12} A and noticeable robustness for large bias, instead of reported p-type gate tunable behaviour based on pristine WSe_2 nanosheets. This study may lead the way to further development of *in-situ* passivation and edge-engineering of electronic or optoelectronic devices based on 2D materials.

5.2 Experimental Methods

5.2.1 Material characterisations

The surface morphology of WSe_2 nanosheets and devices was obtained in a Carl Zeiss Orion NanoFab SEM system operated at 20 kV. A Bruker Dimension Icon AFM (atomic force microscopy) system working at tapping mode was used to identify nanosheet thickness. A Thermo Fisher Escalab 250Xi XPS (X-ray photoelectron spectroscopy) system was employed to characterise the elemental composition in long-term air-exposed WSe_2 nanosheets. Raman spectroscopy study was performed using a confocal Raman spectrometer (Horiba Jobin Yvon HR Evolution). The current-mapping measurements were conducted in a Keysight 5600LS AFM system with the current sensing mode under ambient conditions.

5.2.2 Device fabrication

Photolithography and subsequent Ti/Au (10 nm/50 nm) metallisation were first introduced to make metal position labels and cross alignment marks on SiO_2/Si substrates, preparing for the followed EBL processing. Afterwards, drain and source electrodes for phototransistors were patterned using EBL, followed by Ti/Au (10 nm/50 nm)

metallisation using an electron-beam evaporator system and standard lift-off. The back-gate was enabled by heavily n-doped Si substrates. Then the devices were wire-bonded to logic chip carrier (LCC) using gold wire.

5.2.3 Device measurement

The electrical measurements for output curves and transfer curves from 77 K to 300 K was conducted at the Lake Shore four-probe semiconductor analysing system, equipped with a Keithley 4200 semiconductor parameter analyser.

5.3 Results and Discussion

Bilayer fresh-WSe_2 (F-WSe_2) nanoflakes were grown on (300 nm) SiO_2/Si substrates directly using a chemical vapour deposition (CVD) method under atmospheric pressure, which was carried out by collaborators from University of Science and Technology of China and presented in their previous work.[12] The air-exposure induced oxidised-WSe_2 (O-WSe_2) nanoflakes were prepared by exposing as-grown F-WSe_2 samples to ambient air at room temperature for more than 6 months. Detailed material characterisations were conducted to study air-induced self-passivation effects by comparing F-WSe_2 and O-WSe_2 samples. Figure 5.1a shows a SEM image of an O-WSe_2 nanoflake. As can be seen clearly, the edges of the O-WSe_2 presented an apparently dimmer contrast than the internal area, which was caused by air-exposure induced oxidation (WO_x).[15,16] In contrast, the internal areas still showed relatively uniform contrast, and only protruded dots were randomly spotted, which can be resulted from adsorbates in the hexagonal domain based on previously reported results.[13]

AFM image (displayed in Figure 5.1b) illustrates surface topography of another O-WSe_2 nanoflake shaped in a triangle. This triangular domain shows primarily uniform thickness of ~ 2 nm, corresponding to a BL configuration. Similarly, thicker edges and randomly distributed dots at the internal areas were observed.[12,17] The height of the protrusion resulted from air-induced oxidation is ~ 1 nm, well agreeing with previous results.[13]

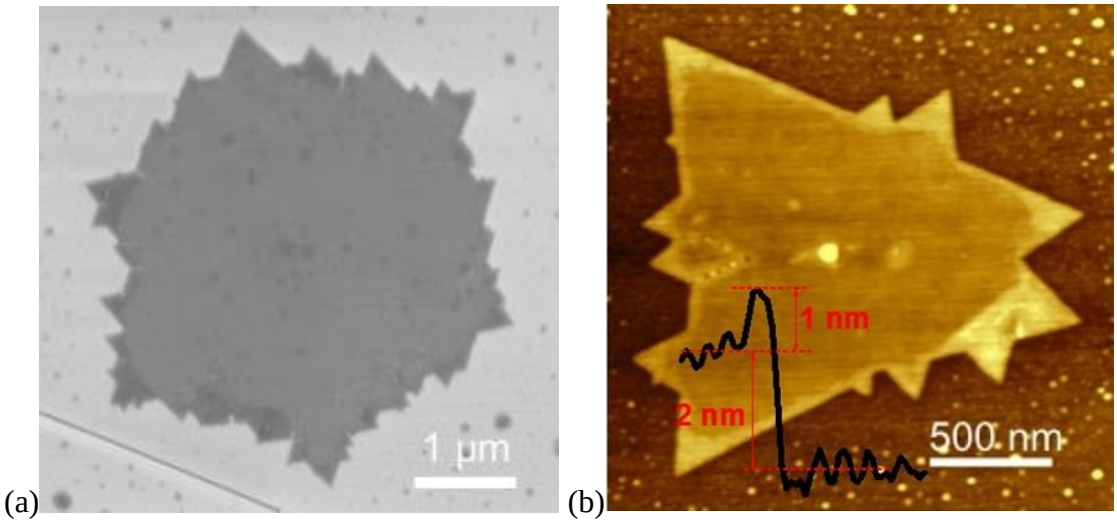

Figure 5.1 (a) SEM image of a hexagonal air-exposure induced O-WSe_2 nanosheet, with thicker edges. (b) The AFM image shows the surface morphology of another triangle O-WSe_2 domain. The inset height profile shows the thickness of 2 nm for the internal area and the thickness of 1 nm for the protruded edges.

Raman spectroscopy and XPS were employed to further validate the existence of air-exposure induced WO_x at nanosheet edges. Figure 5.2 shows the Raman spectra of the F-WSe_2 and O-WSe_2 nanoflakes, excited by a 514-nm laser. To avoid collecting Raman-active phonon signal from WO_x or adsorbates from air, the Raman scattering measurements for O-WSe_2 nanoflakes were carefully carried out in the internal and clean domains. As shown in Figure 5.2, no obvious Raman peak shift or peak broadening was observed, presumably the internal area of O-WSe_2 remained the same as the F-WSe_2. That is, the crystalline nature of internal areas of O-WSe_2 nanoflakes remained almost unaffected after long term air-exposure, as phonon oscillation is closely related to crystal structures and quality.[18-20] The Raman shift difference between the two Raman eigen-peaks of E^1_{2g} (in-plane) and A_{1g} (out-of-plane) is ~ 8 cm^{-1}, corresponding to BL nature and agreeing with the AFM results.[21]

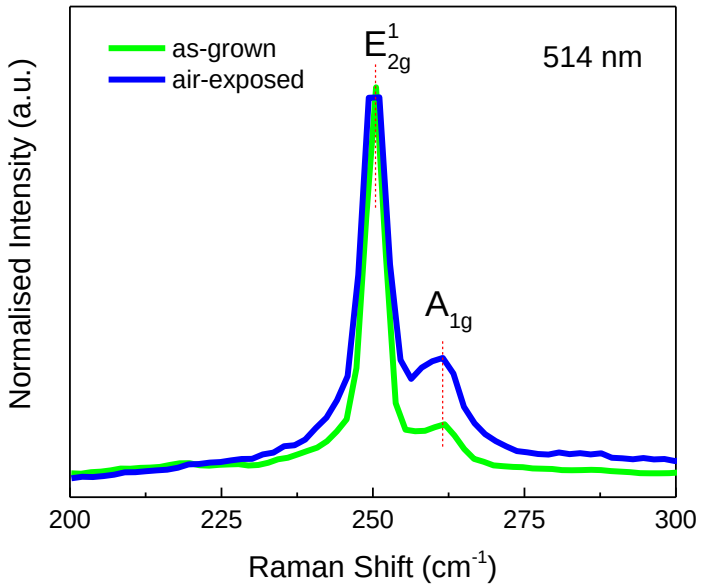

Figure 5.2 Raman spectra of as-grown (green curve) and air-exposed (blue curve) WSe_2 nanoflakes, measured under 514 nm laser excitation. No obvious peak shift was observed.

In terms of resonant Raman scattering (RRS), it can resolve more features of Raman-active phonon oscillation. When incident photon energy approximately equalled to the electronic absorption band of materials, the condition for RRS is obtained. As a result, it results in strong electron-phonon coupling together with the first-order Raman scattering, leading to enhanced phonon oscillation and generating additional Raman-active modes.[22,23] RRS spectrum of the O-WSe_2 nanoflake was obtained at edges when using an excitation source of 633-nm laser.[24] As shown in Figure 5.3, the two characteristic peaks located at 251.1 cm^{-1} (E^1_{2g}) and 259.3 cm^{-1} (A_{1g}) were also resolved when Raman scattering was under the off-resonant condition.

In addition, several new phonon oscillation modes were observed in the RRS spectrum. Compared with the previously reported Raman-active modes, red arrow labelled peaks located at 223.5 cm^{-1}, 237.6 cm^{-1}, 373.7 cm^{-1} and 394.4 cm^{-1} were clearly resolved from WSe_2 involved Raman modes, and blue arrow labelled peaks located at 128.8 cm^{-1}, 135.4 cm^{-1}, 156.1 cm^{-1} and 301.9 cm^{-1} were assigned to WO_x, indicating coexistence of WSe_2 and WO_x at edges of nanosheets.[15,24-28] Besides, a near-infrared excitation source of 785 nm laser was used to double confirm Raman-active phonon oscillation of internal

domains of O-WSe_2 nanoflakes. As expected, the two eigen-peaks were clearly observed with obviously strengthened A_{1g} mode, suggesting almost unaltered phonon oscillation after long term air-exposure as well. Both the Raman spectra obtained under 633 nm and 785 nm laser excitation identified the eigen-peaks of O-WSe_2 nanoflakes, while the 633 nm one also demonstrated the formation of WO_x/WSe_2 heterojunctions around edges of O-WSe_2 regarding to Raman-active oscillation.

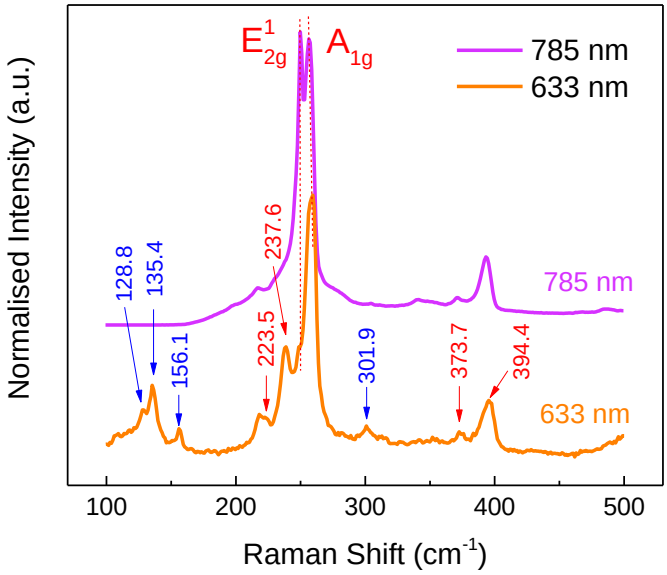

Figure 5.3 RRS spectra of WSe2 nanoflakes, using 633 nm (orange curve) and 785 nm (magenta) laser sources. The RRS was performed at the edges of nanoflakes for 633 nm excitation and at the internal areas for 785 nm excitation. The red and blue arrows point at the peaks originated from WSe_2 and WO_x involved Raman-active modes, respectively.

Figure 5.4 – 5.6 exhibit XPS results of W4f, Se3d and O1s obtained at the edges of O-WSe_2 nanosheets, respectively. In the as-grown F-WSe_2 XPS spectra (Ref. 12), the peaks of doublet W^{4+} $4f_{7/2}$ and W^{4+} $4f_{5/2}$ indexed to pristine WSe_2 were dominated. In contrast, the spectra of the O-WSe_2 edges (see Figure 5.4) were governed by the peaks of doublet W^{6+} $4f_{7/2}$ and W^{6+} $4f_{5/2}$, which were assigned to WO_x.[12,26,29] The peaks of Se3d resolved at 54.9 eV and 55.8 eV (Figure 5.5) kept the same as those observed in the as-grown F-WSe_2 nanoflakes, and the binding energy profile of O1s (Figure 5.6) was originated from air-exposure induced WO_x.[30]

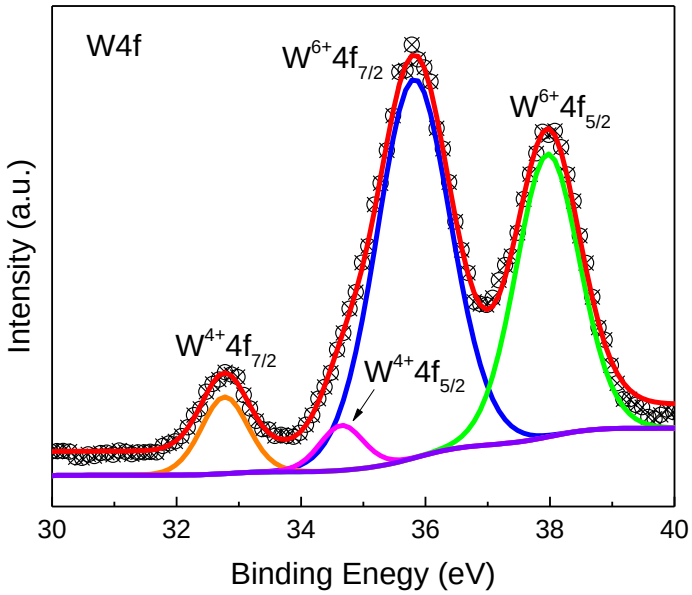

Figure 5.4 Binding energy profile of W4f. The scattered dots and solid red curve denote experimental data and fitted results, respectively.

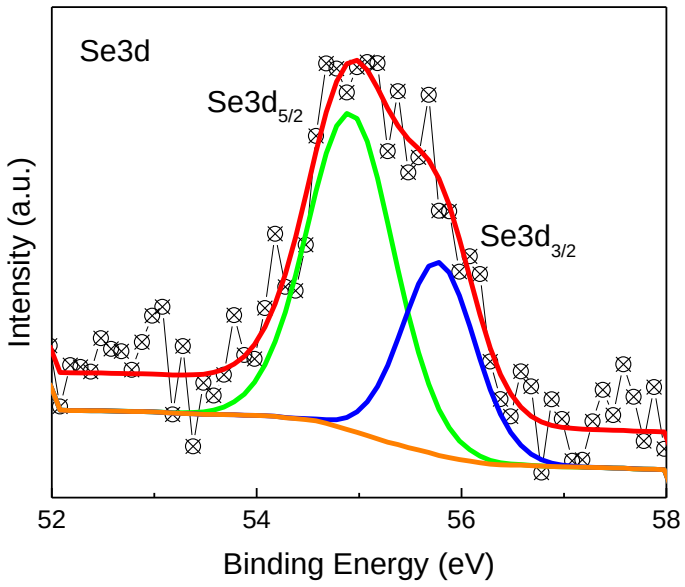

Figure 5.5 Binding energy profile of Se3d. The scattered dots and solid red curve denote experimental data and fitted results, respectively.

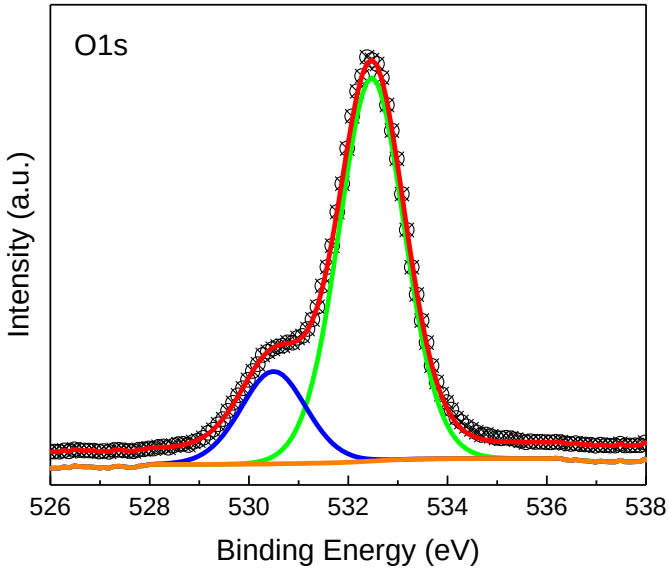

Figure 5.6 Binding energy profile of O1s. The scattered dots and solid red curve denote experimental data and fitted results, respectively.

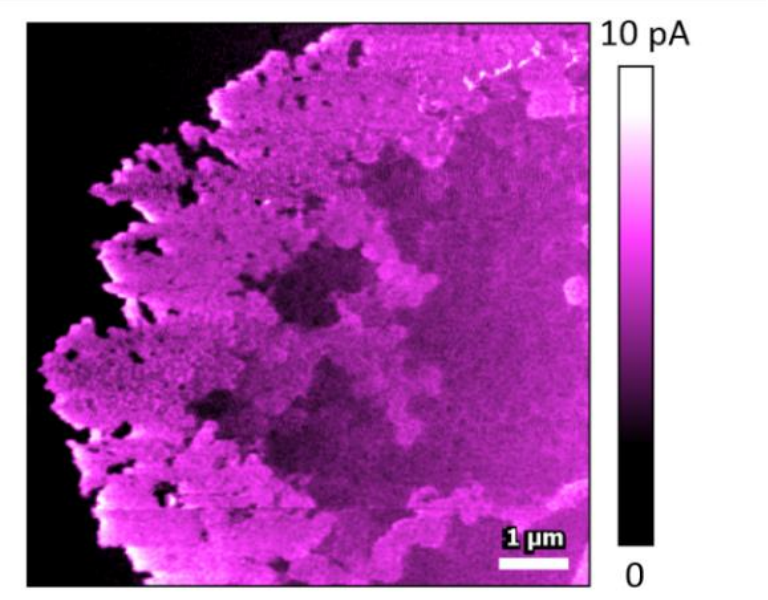

Figure 5.7 C-AFM map of WO_x/WSe_2 heterojunctions, showing electrical conductivity features of the surface. The scale bar is 1 µm.

Moreover, c-AFM equipped with a platinum coated tip operated under tapping mode was employed to image electrical conducting properties of the O-WSe_2, illustrated in Figure 5.7. Similar to the AFM image of surface morphology (shown in Figure 5.1b), the c-AFM map displays that internal uniform WSe_2 was surrounded by air-induced WO_x with better electrical conductivity at edges. According to the above detailed material characterisation results, it can be concluded that the O-WSe_2 is composed of internal areas keeping originally pristine properties while the edges covered by air-induced WO_x, forming the heterojunction of WO_x/WSe_2.

A series of back-gated FETs were fabricated based on the O-WSe_2 nanosheets using standard EBL and subsequent Ti/Au metallisation, whose schematic image is shown in Figure 5.8. The SEM image of an FET is exhibited in Figure 5.9a with two marked terminals as drain and source contacts. As a result, WO_x around nanosheet edges worked as an intermediate layer between Ti/Au contacts and WSe_2. The devices were then wire-bonded to a LCC with gold wires for the following measurements, as shown in Figure 5.9b. Output curves of the FET obtained at room temperature (see Figure 5.10) illustrates evident n-type dominant gate-tunable behaviour instead of the typical p-type property based on pristine WSe_2 nanosheets, which can be caused by the high concentration n-type carriers from the WO_x layer formed naturally in ambient air.[12,31,32] This switching from p-type to n-type was also consistent with the theoretical prediction.

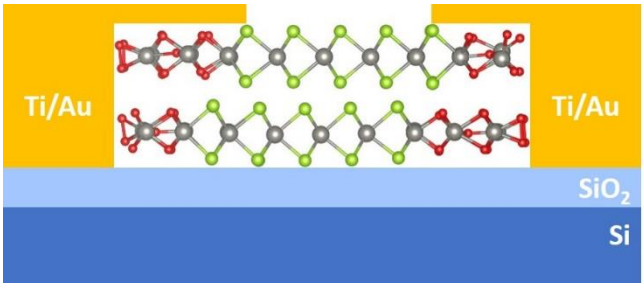

Figure 5.8 Schematic diagram (side-view) of a FET based on the bilayer O-WSe_2 nanosheet on SiO_2/Si substrate. The red, grey and green balls denote O, W and Se atoms, respectively. WO_x worked as intermediate layers between Ti/Au contacts and the WSe_2 nanosheet.

(a)

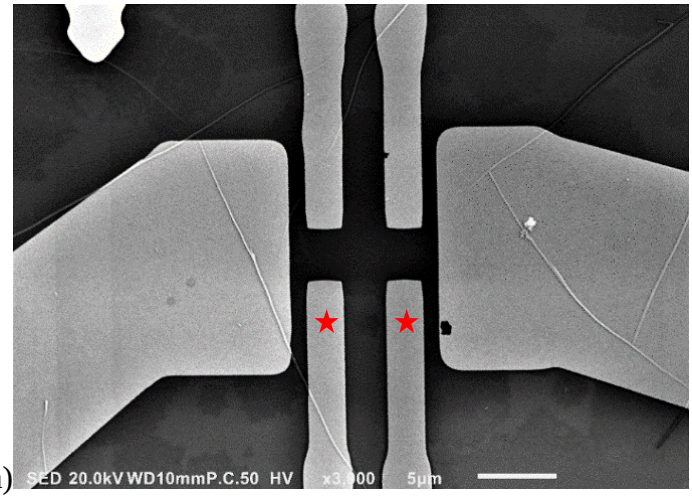

(b)

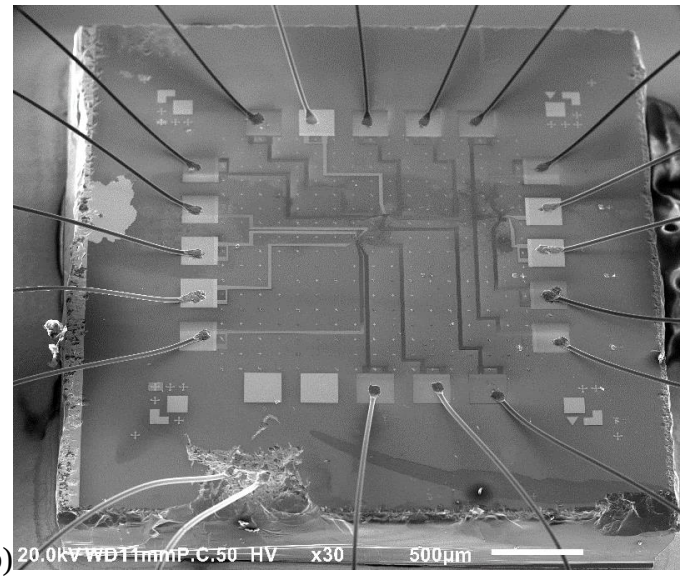

Figure 5.9 (a) SEM image (top-view) of the FET based on the bilayer O-WSe_2 nanosheet on SiO_2/Si substrate. The two terminals marked with stars were selected as drain and source terminals for measurements. The scale bar is 5 µm. (b) SEM image of the FETs wire-bonded (gold wires) to the LCC. The scale bar is 500 µm.

Notably, the I_{ds}-V_{ds} curves in Figure 5.10 exhibit a small degree of current modulation when back-gate voltage tuned from -80 to 80 V, which can be originated from low carrier mobility of WO_x.[33] Because of the WO_x acting as a buffer layer and involvement of WO_x in electron transfer from Ti/Au contacts to O-WSe_2, drain-source current showed a linear behaviour, revealing ohmic contacts at the drain and source electrodes, instead of the classical Schottky contact between Ti/Au and pristine WSe_2 nanosheets.[12,34,35] This ohmic

behaviour was further confirmed in another FET based on a different O-WSe_2 domain, illustrated in Figure 5.11 and 5.12.

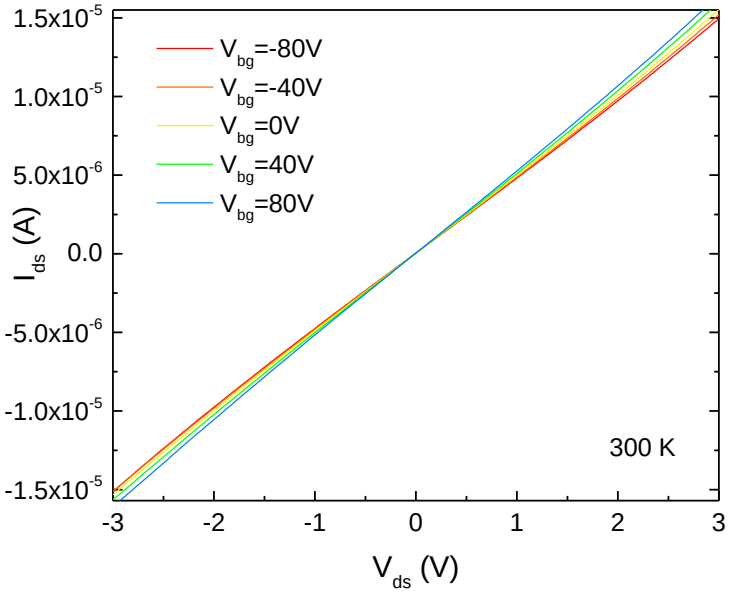

Figure 5.10 Output curves of the FET based on the bilayer O-WSe_2 nanosheet on SiO_2/Si substrate, measured at room temperature (300 K). The curves show obvious ohmic contact behaviour under different drain-source bias and back-gate.

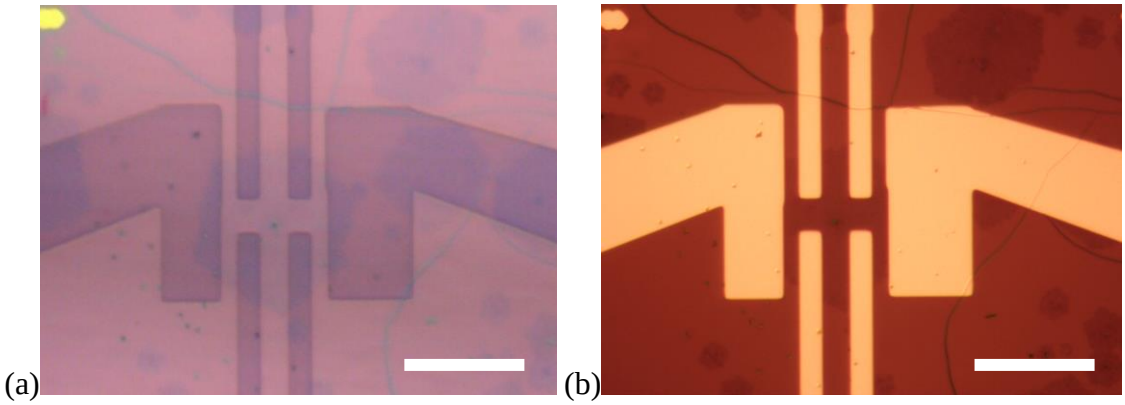

Figure 5.11 Optical microscopy images of the device based on another different bilayer O-WSe_2 nanosheet (a) after EBL patterning and (b) after Ti/Au metallisation. The scale bar for both images is 10 µm.

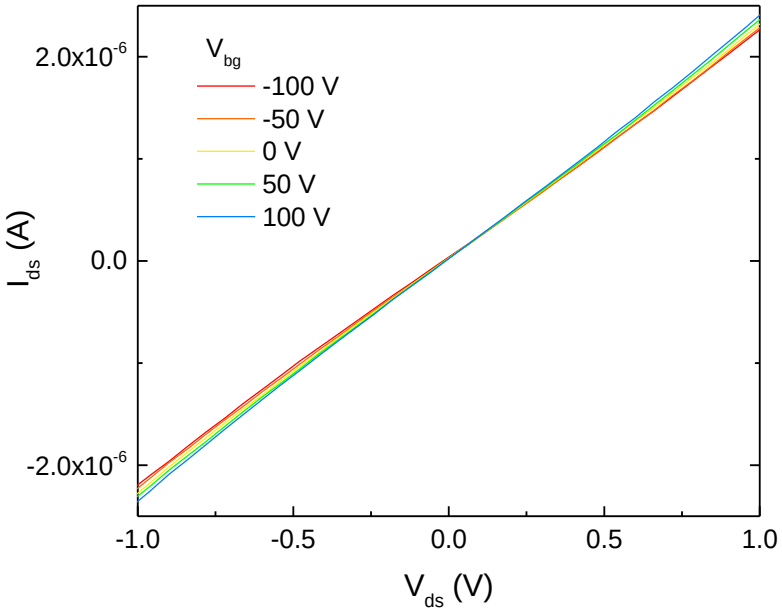

Figure 5.12 Output curves of the FET based on another different bilayer O-WSe_2 nanosheet, also measured at room temperature (300 K). The curves show obvious ohmic contact behaviour under different drain-source bias and back-gate.

The temperature-dependent output curves obtained with changing back-gate voltage were also studied. As depicted in Figure 5.13 – 5.15, the drain-source current increased as temperature rised for all the back-gate bias, although gate tunability was insensitive. The ohmic contact features kept under all the gate voltages and temperatures. The corresponding theoretical calculation results revealed that the linear IV curves were originated from the ohmic contact at the source and drain (Ti/Au-O-WSe_2 interfaces) and the barrier-less heterojunction (WO_x-WSe_2 interfaces). Temperature-dependent electrical conductivity was then extracted (Figure 5.16), exhibiting the same tunable trend as output curves. The largest conductivity as high as ~ 2600 S/m was achieved when applied 80 V gate bias at room temperature. According to the reported studies, such a high conductivity should be contributed by the air-exposure induced WO_x around the nanosheet edges.[33]

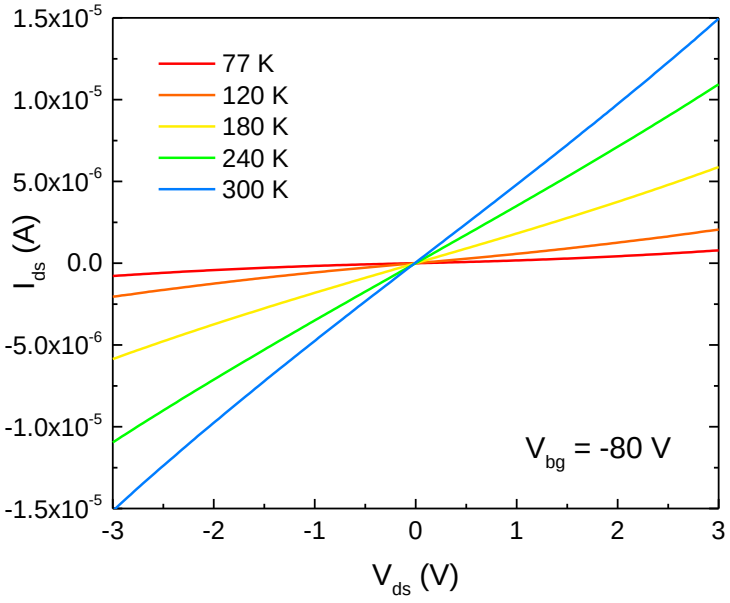

(a)

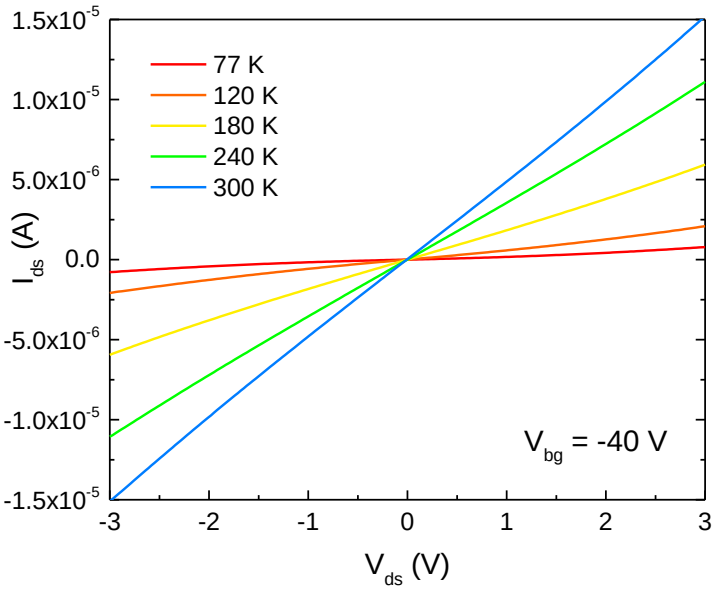

(b)

Figure 5.13 Temperature-dependent (from 77 K to 300 K) output curves of the FET, obtained at (a) V_{bg} = -80 V and (b) V_{bg} = -40 V. The curves show obvious ohmic contact behaviour under different drain-source bias and back-gate.

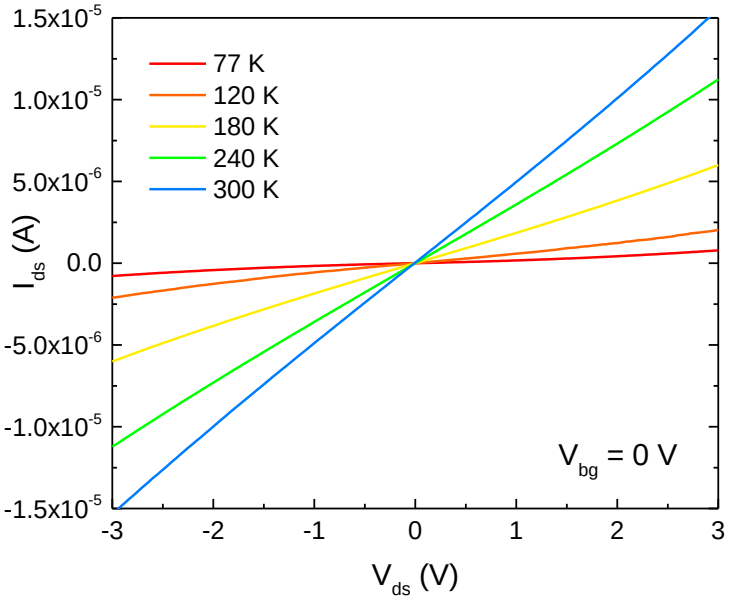

(a)

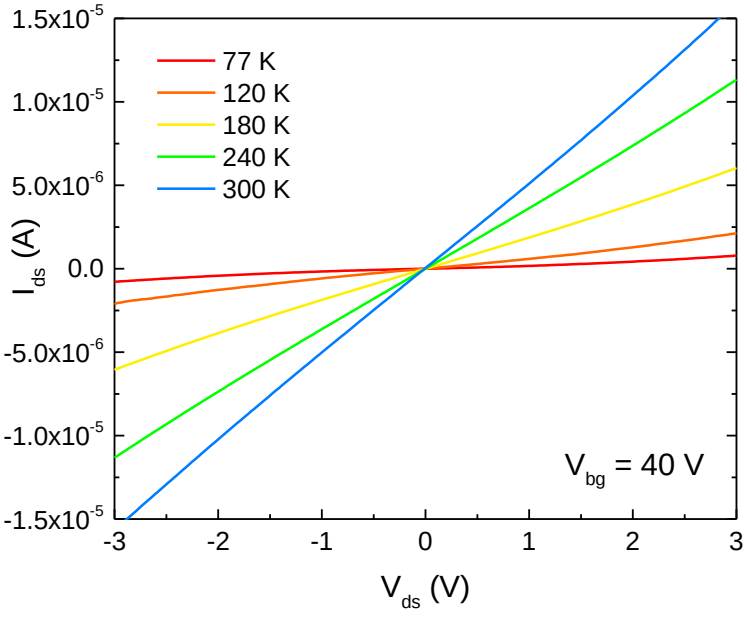

(a)

Figure 5.14 Temperature-dependent (from 77 K to 300 K) output curves of the FET, obtained at (a) V_{bg} = 0 V and (b) V_{bg} = 40 V. The curves show obvious ohmic contact behaviour under different drain-source bias and back-gate.

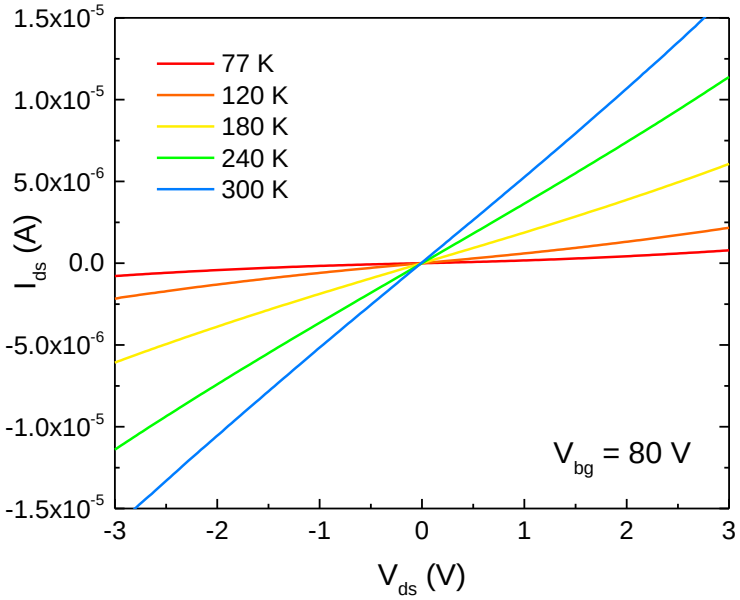

(b)

Figure 5.15 Temperature-dependent (from 77 K to 300 K) output curves of the FET, obtained at V_{bg} = 80 V. The curves show obvious ohmic contact behaviour under different drain-source bias and back-gate.

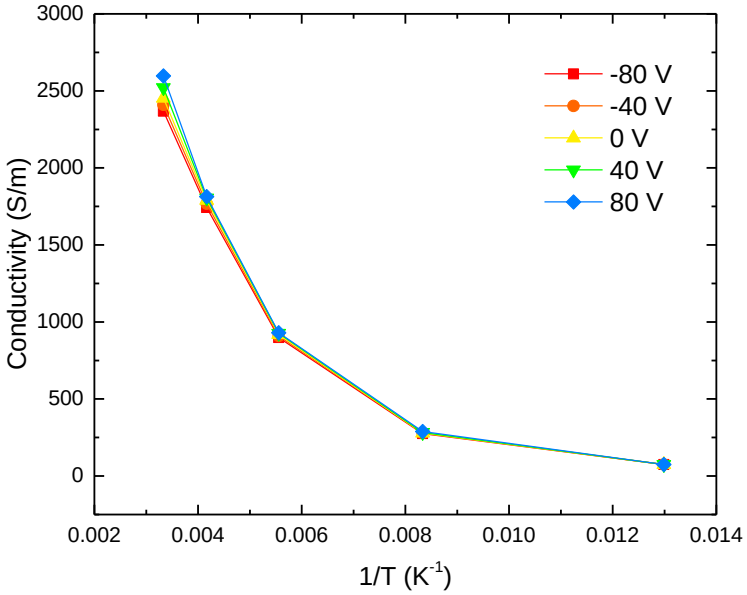

Figure 5.16 Electrical conductivity of the FET based on the bilayer O-WSe_2 nanosheet on SiO_2/Si substrate as a function of changing temperature from 77 K to 300 K.

Figure 5.17 and 5.18 illustrate transfer curves of FETs based on O-WSe_2 measured in response to varied temperature. Similarly, the n-type dominant behaviour and insensitive gate-dependence were apparently observed, and the current modulation was the most evident at room temperature (see Figure 5.18b). The corresponding leakage current (gate current I_{gs}) curves are shown in Figure 5.19 and 5.20. Notably, ultra-low I_{gs} between 10^{-14} and 10^{-13} A was achieved at 77 K and I_{gs} of 10^{-12} ~ 10^{-11} A was obtained from 120 K to 300 K, which can be entirely neglected and is much desired in energy-friendly device applications. Obviously, passivated electronic edge states by air-exposure induced oxidation of WSe_2 around edges made major contribution to such small leakage current. Benefited from the self-passivated edge states, the FET also exhibits robustness to extreme electrical test conditions, such as ultra-large voltage bias. Figure 5.21 demonstrates that atomically thin nanoflake based FET is able to successfully stand drain source bias as high as 8 V and huge back-gate voltage sweeping range from -100 V to 100 V, and still work in good conditions (small leakage current, Figure 5.22).

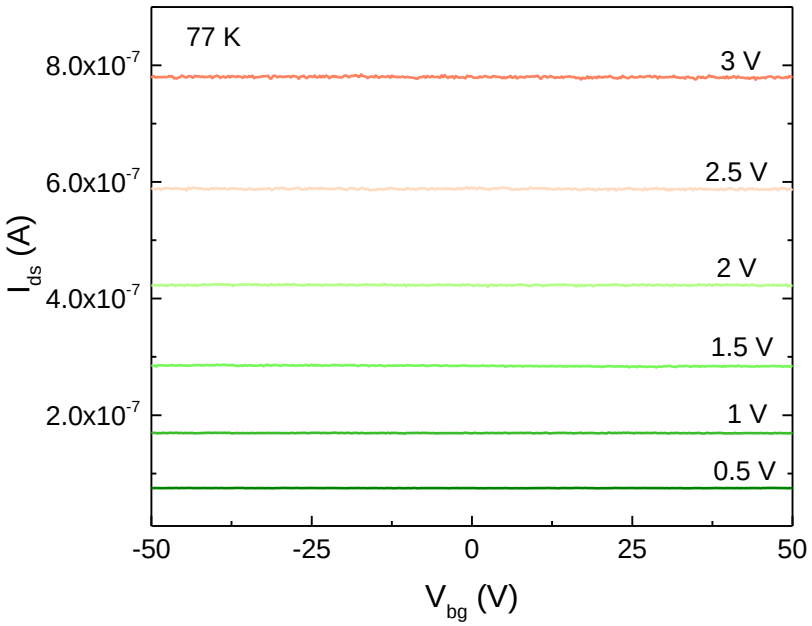

(a)

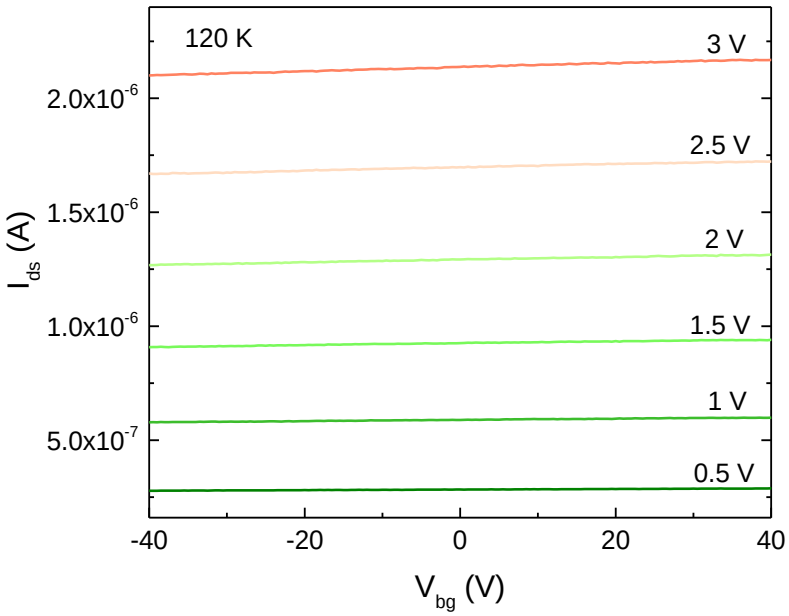

(b)

Figure 5.17 Transfer characteristics of the FET based on the bilayer O-WSe_2 nanosheet, measured (a) at 77 K and (b) 120 K.

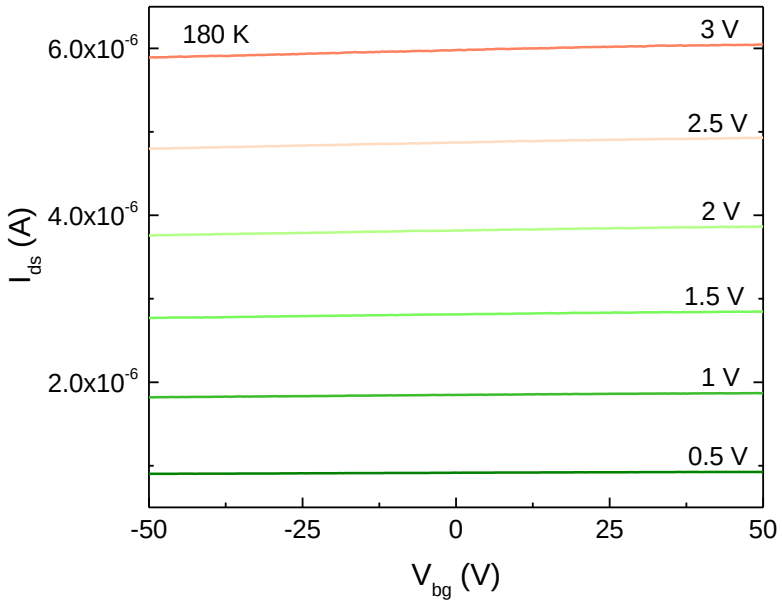

(a)

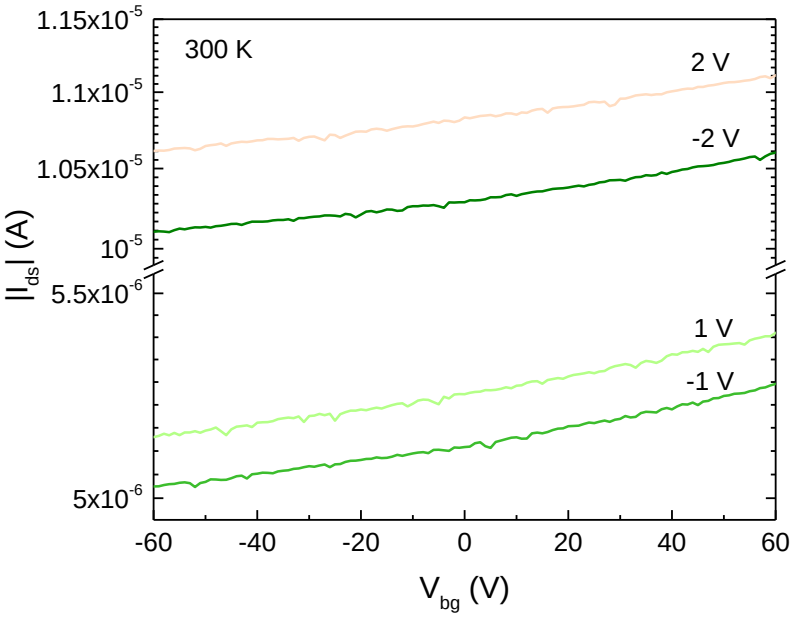

(b)

Figure 5.18 Transfer characteristics of the FET based on the bilayer O-WSe_2 nanosheet, measured (a) at 180 K and (b) 300 K.

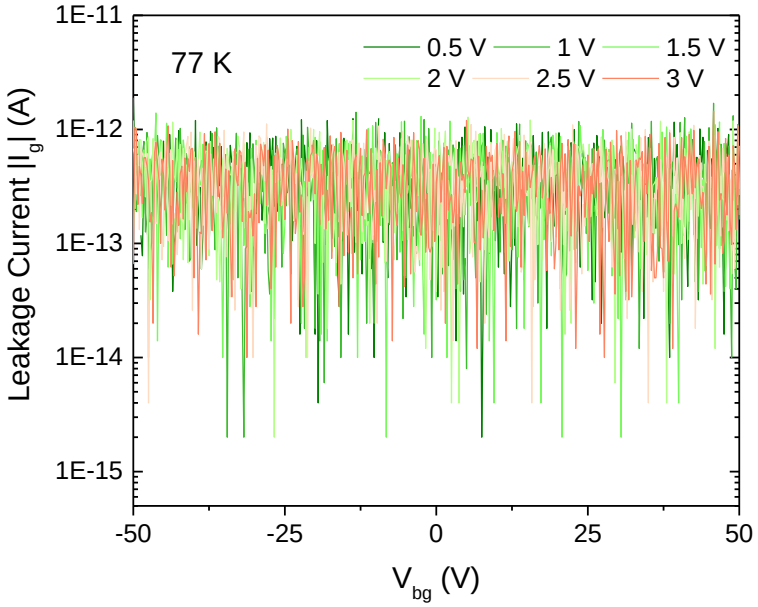

(a)

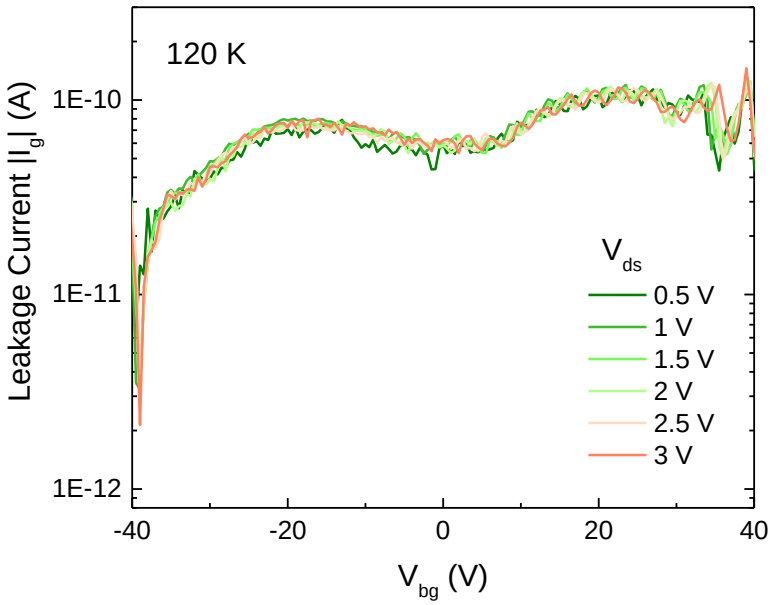

(b)

Figure 5.19 Leakage current (I_{gs}) characteristics as a function of back-gate voltage, obtained (a) at 77 K and (b) at 120 K.

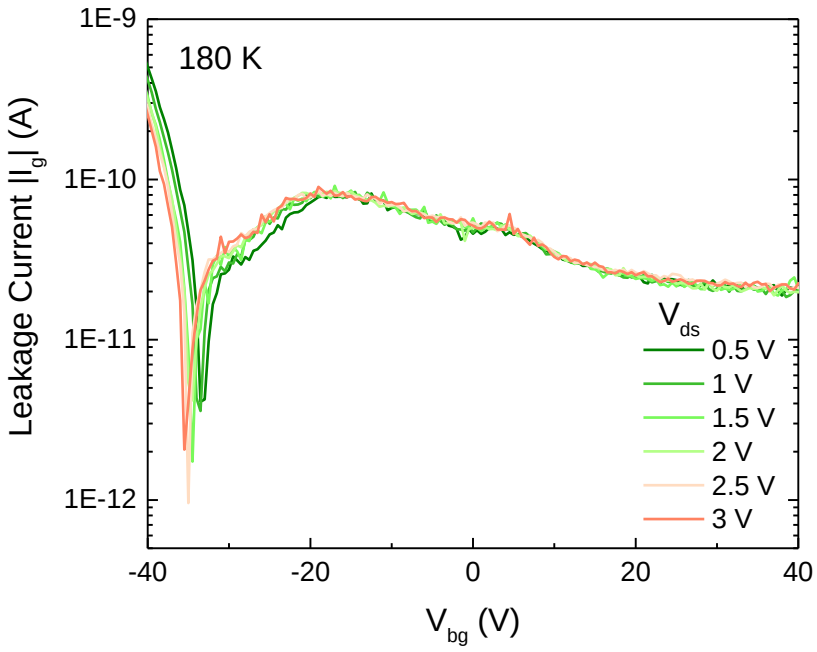

(a)

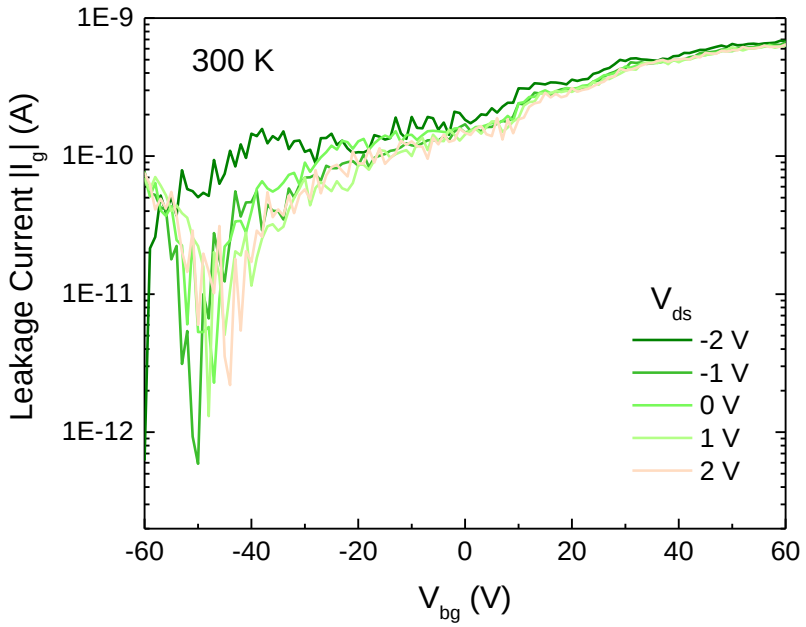

(b)

Figure 5.20 Leakage current (I_{gs}) characteristics as a function of back-gate voltage, obtained (a) at 180 K and (b) at 300 K.

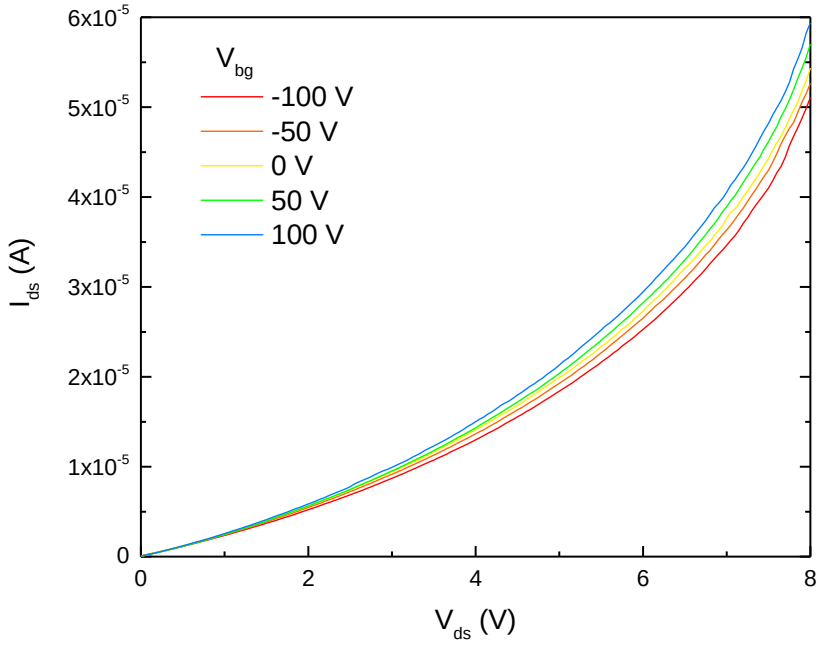

(a)

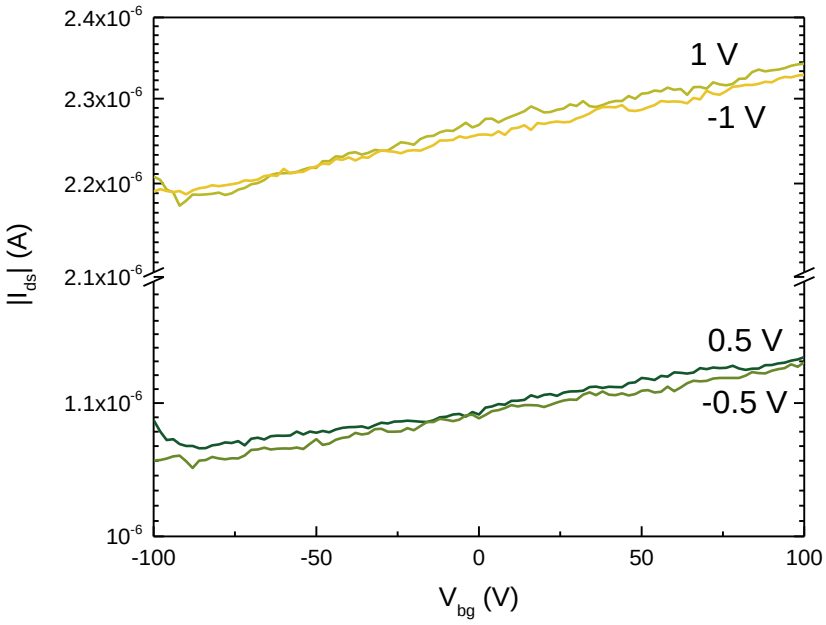

(b)

Figure 5.21 (a) Output characteristics of the FET under large drain-source bias up to 8 V and huge stepped back-gate voltage from -100 V and 100 V. (b) Transfer characteristics of the FET under large back-gate voltage sweeping from -100 V and 100 V.

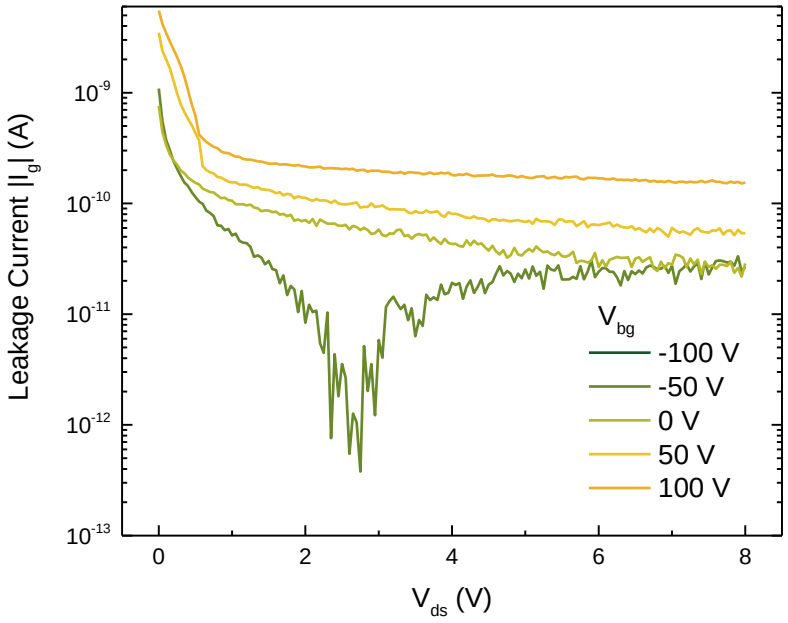

(a)

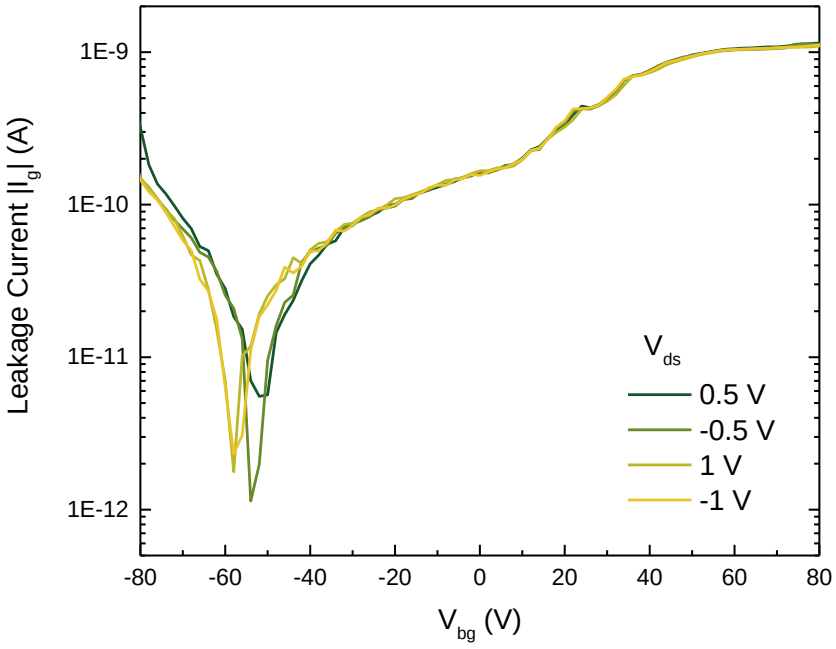

(b)

Figure 5.22 (a) Leakage current curves as a function of drain-source bias voltage when drain-source bias voltage swept from 0 V to 8 V. (b) Leakage current curves as a function of back-gate voltage sweeping from -100 V to 100 V.

5.4 Conclusions

In summary, back-gated FETs enabled by long-term air-exposure induced self-passivated BL WSe_2 nanoflakes were fabricated and studied for the first time. The self-assembled WO_x was used as an intermediate buffer layer between metal contacts and the internal WSe_2 domains. Systematic material characterisations, including SEM, AFM, c-AFM, Raman spectroscopy and XPS, were carried out to study long-term air-exposure impacts on as-grown pristine atomically thin WSe_2.

The results demonstrated the formation of WO_x/WSe_2 heterostructures around domain edges while internal domains remained as pristine ones. As-fabricated FETs showed evident n-type dominant gate-tunable behaviour and linear current-voltage relationship from 77 K to 300 K, instead of the behaviour of the reported FETs based on pristine WSe_2 nanosheets, which formed Schottky contacts and showed typical p-type properties.

Besides, a remarkable electrical conductivity up to ~ 2600 S/m was achieved. Due to self-passivated dangling bonds of edges via air-exposure, the FETs also exhibited ultra-low leakage current and robustness for ultra-high bias. The self-passivation of 2D WSe_2 nanosheet edges provides new chances for the edge-engineering of 2D materials for nanoelectronic and optoelectronic applications.

5.5 References

(1) Choi, C.; Choi, M. K.; Liu, S.; Kim, M. S.; Park, O. K.; Im, C.; Kim, J.; Qin, X.; Lee, G. J.; Cho, K. W.; et al. Human Eye-Inspired Soft Optoelectronic Device Using High-Density MoS2-Graphene Curved Image Sensor Array. *Nat. Commun.* **2017**, *8* (1), 1664. https://doi.org/10.1038/s41467-017-01824-6.

(2) Nassar, J. M.; Khan, S. M.; Villalva, D. R.; Nour, M. M.; Almuslem, A. S.; Hussain, M. M. Compliant Plant Wearables for Localized Microclimate and Plant Growth Monitoring. *npj Flex. Electron.* **2018**, *2* (1), 24. https://doi.org/10.1038/s41528-018-0039-8.

(3) Sarycheva, A.; Polemi, A.; Liu, Y.; Dandekar, K.; Anasori, B.; Gogotsi, Y. 2D Titanium Carbide (MXene) for Wireless Communication. *Sci. Adv.* **2018**, *4* (9), eaau0920. https://doi.org/10.1126/sciadv.aau0920.

(4) Akinwande, D.; Petrone, N.; Hone, J. Two-Dimensional Flexible Nanoelectronics. *Nat. Commun.* **2015**, *5*, 5678. https://doi.org/10.1038/ncomms6678.

(5) Novoselov, K. S.; Mishchenko, A.; Carvalho, A.; Castro Neto, A. H. 2D Materials and van Der Waals Heterostructures. *Science.* **2016**, *353* (6298), 9439. https://doi.org/10.1126/science.aac9439.

(6) Mak, K. F.; Shan, J. Photonics and Optoelectronics of 2D Semiconductor Transition Metal Dichalcogenides. *Nat. Photonics* **2016**, *10* (4), 216–226. https://doi.org/10.1038/nphoton.2015.282.

(7) Xie, C.; Mak, C.; Tao, X.; Yan, F. Photodetectors Based on Two-Dimensional Layered Materials Beyond Graphene. *Adv. Funct. Mater.* **2017**, *27* (19), 1603886. https://doi.org/10.1002/adfm.201603886.

(8) Xu, H.; Han, X.; Dai, X.; Liu, W.; Wu, J.; Zhu, J.; Kim, D.; Zou, G.; Sablon, K. A.; Sergeev, A.; et al. High Detectivity and Transparent Few-Layer MoS2/Glassy-Graphene Heterostructure Photodetectors. *Adv. Mater.* **2018**, *30*, 1706561. https://doi.org/10.1002/adma.201706561.

(9) Zhang, W.; Chiu, M.-H.; Chen, C.-H.; Chen, W.; Li, L.; Wee, A. T. S.; Monolayers, W.; Zhang, W.; Chiu, M.-H.; Chen, C.-H.; et al. Role of Metal Contacts in High- Performance Phototransistors Based on WSe2 Monolayers. *ACS Nano* **2014**, *8* (Xx), 8653–8661. https://doi.org/10.1021/nn503521c.

(10) Baugher, B. W. H.; Churchill, H. O. H.; Yang, Y.; Jarillo-Herrero, P.

Optoelectronic Devices Based on Electrically Tunable P-N Diodes in a Monolayer Dichalcogenide. *Nat. Nanotechnol.* **2014**, *9* (4), 262–267. https://doi.org/10.1038/nnano.2014.25.

(11) Fang, H.; Chuang, S.; Chang, T. C.; Takei, K.; Takahashi, T.; Javey, A. High-Performance Single Layered WSe2 P-FETs with Chemically Doped Contacts. *Nano Lett.* **2012**, *12* (7), 3788–3792. https://doi.org/10.1021/nl301702r.

(12) Huang, J.; Yang, L.; Liu, D.; Chen, J.; Fu, Q.; Xiong, Y.; Lin, F.; Xiang, B. Large-Area Synthesis of Monolayer WSe2 on a SiO2/Si Substrate and Its Device Applications. *Nanoscale* **2015**, *7* (9), 4193–4198. https://doi.org/10.1039/c4nr07045c.

(13) Park, J. H.; Vishwanath, S.; Liu, X.; Zhou, H.; Eichfeld, S. M.; Fullerton-Shirey, S. K.; Robinson, J. A.; Feenstra, R. M.; Furdyna, J.; Jena, D.; et al. Scanning Tunneling Microscopy and Spectroscopy of Air Exposure Effects on Molecular Beam Epitaxy Grown WSe2 Monolayers and Bilayers. *ACS Nano* **2016**, *10* (4), 4258–4267. https://doi.org/10.1021/acsnano.5b07698.

(14) Liu, B.; Zhang, A.; Chen, L.; Abbas, A. N.; Liu, Y.; Shen, C.; Wan, H.; Zhou, C. High-Performance WSe2 Field-E Ffect Transistors via Controlled Formation of In- Plane Heterojunctions. *ACS Nano* **2016**, *10*, 5153–5160. https://doi.org/10.1021/acsnano.6b00527.

(15) Liu, Y.; Tan, C.; Chou, H.; Nayak, A.; Wu, D.; Ghosh, R.; Chang, H. Y.; Hao, Y.; Wang, X.; Kim, J. S.; et al. Thermal Oxidation of WSe2 Nanosheets Adhered on SiO2/Si Substrates. *Nano Lett.* **2015**, *15* (8), 4979–4984. https://doi.org/10.1021/acs.nanolett.5b02069.

(16) Yamamoto, M.; Nakaharai, S.; Ueno, K.; Tsukagoshi, K. Self-Limiting Oxides on WSe2 as Controlled Surface Acceptors and Low-Resistance Hole Contacts. *Nano Lett.* **2016**, *16* (4), 2720–2727. https://doi.org/10.1021/acs.nanolett.6b00390.

(17) Tonndorf, P.; Schmidt, R.; Böttger, P.; Zhang, X.; Börner, J.; Liebig, A.; Albrecht, M.; Kloc, C.; Gordan, O.; Zahn, D. R. T.; et al. Photoluminescence Emission and Raman Response of Monolayer MoS2, MoSe2, and WSe2. *Opt. Express* **2013**, *21* (4), 4908–4916. https://doi.org/10.1038/srep01608.

(18) Xu, H.; Song, Y.; Pan, W.; Chen, Q.; Wu, X.; Lu, P.; Gong, Q.; Wang, S. Vibrational Properties of Epitaxial Bi4Te3 Films as Studied by Raman Spectroscopy. *AIP Adv.* **2015**, *5* (8), 87103.

(19) Xu, H.; Song, Y.; Gong, Q.; Pan, W.; Wu, X.; Wang, S. Raman Spectroscopy of Epitaxial Topological Insulator Bi2Te3 Thin Films on GaN Substrates. *Mod. Phys. Lett. B* **2015**, *29*, 1550075.

(20) Neumann, C.; Reichardt, S.; Venezuela, P.; Drögeler, M.; Banszerus, L.; Schmitz, M.; Watanabe, K.; Taniguchi, T.; Mauri, F.; Beschoten, B.; et al. Raman Spectroscopy as Probe of Nanometre-Scale Strain Variations in Graphene. *Nat. Commun.* **2015**, *6* (May), 8429. https://doi.org/10.1038/ncomms9429.

(21) Li, H.; Lu, G.; Wang, Y.; Yin, Z.; Cong, C.; He, Q.; Wang, L.; Ding, F.; Yu, T.; Zhang, H. Mechanical Exfoliation and Characterization of Single- and Few-Layer Nanosheets of WSe2, TaS2, and TaSe2. *Small* **2013**, *9* (11), 1974–1981. https://doi.org/10.1002/smll.201202919.

(22) Sourisseau, C.; Cruege, F.; Fouassier, M.; Alba, M. Second-Order Raman Effects, Inelastic Neutron Scattering and Lattice Dynamics in 2H-WS2. *Chem. Phys.* **1991**, *150* (2), 281–293. https://doi.org/10.1016/0301-0104(91)80136-6.

(23) Stacy, A. M.; Hodul, D. T. Raman Spectra of IVB and VIB Transition Metal Disulfides Using Laser Energies near the Absorption Edges. *J. Phys. Chem. Solids* **1985**, *46* (4), 405–409. https://doi.org/10.1016/0022-3697(85)90103-9.

(24) Bhatt, S. V.; Deshpande, M. P.; Sathe, V.; Rao, R.; Chaki, S. H. Raman Spectroscopic Investigations on Transition-Metal Dichalcogenides MX2 (M = Mo, W; X = S, Se) at High Pressures and Low Temperature. *J. Raman Spectrosc.* **2014**, *45* (10), 971–979. https://doi.org/10.1002/jrs.4580.

(25) Djaoued, Y.; Balaji, S.; Brüning, R. Electrochromic Devices Based on Porous Tungsten Oxide Thin Films. *J. Nanomater.* **2012**, *2012* (June 2016), 674168. https://doi.org/10.1155/2012/674168.

(26) Liu, F.; Chen, X.; Xia, Q.; Tian, L.; Chen, X. Ultrathin Tungsten Oxide Nanowires: Oleylamine Assisted Nonhydrolytic Growth, Oxygen Vacancies and Good Photocatalytic Properties. *RSC Adv.* **2015**, *5* (94), 77423–77428. https://doi.org/10.1039/C5RA12993A.

(27) Chen, H.-C.; Jan, D.-J.; Luo, Y.-S.; Huang, K.-T. Electrochromic and Optical Properties of Tungsten Oxide Films Deposited with DC Sputtering by Introducing Hydrogen. *Appl. Opt.* **2014**, *53* (4), A321–A329. https://doi.org/10.1364/AO.53.00A321.

(28) Guo, J.; Li, Y.; Zhu, S.; Chen, Z.; Liu, Q.; Zhang, D.; Moon, W.-J.; Song, D.-M.

Synthesis of WO3@Graphene Composite for Enhanced Photocatalytic Oxygen Evolution from Water. *RSC Adv.* **2012**, *2* (4), 1356–1363. https://doi.org/10.1039/C1RA00621E.

(29) Guo, J.; Shi, Y.; Bai, X.; Wang, X.; Ma, T. Atomically Thin MoSe2/graphene and WSe2/graphene Nanosheets for the Highly Efficient Oxygen Reduction Reaction. *J. Mater. Chem. A* **2015**, *3* (48), 24397–24404. https://doi.org/10.1039/C5TA06909B.

(30) Guo, T.; Ling, C.; Zhang, T.; Li, H.; Li, X.; Chang, X.; Zhu, L.; Zhao, L.; Xue, Q. High-Performance WO3-X-WSe2/SiO2/n-Si Heterojunction near-Infrared Photodetector via a Homo-Doping Strategy. *J. Mater. Chem. C* **2018**, *6*, 5821–5829. https://doi.org/10.1039/C8TC01497C.

(31) Fang, L.; Baik, S. J.; Kim, J. W.; Kang, S. J.; Seo, J. W.; Jeon, J. W.; Kim, Y. H.; Lim, K. S. Tunable Work Function of a WOx Buffer Layer for Enhanced Photocarrier Collection of Pin-Type Amorphous Silicon Solar Cells. *J. Appl. Phys.* **2011**, *109* (10), 104501. https://doi.org/10.1063/1.3583576.

(32) Zheng, H.; Ou, J. Z.; Strano, M. S.; Kaner, R. B.; Mitchell, A.; Kalantar-Zadeh, K. Nanostructured Tungsten Oxide - Properties, Synthesis, and Applications. *Adv. Funct. Mater.* **2011**, *21* (12), 2175–2196. https://doi.org/10.1002/adfm.201002477.

(33) Tan, C.; Liu, Y.; Chou, H.; Kim, J. S.; Wu, D.; Akinwande, D.; Lai, K. Laser-Assisted Oxidation of Multi-Layer Tungsten Diselenide Nanosheets. *Appl. Phys. Lett.* **2016**, *108* (8), 083112. https://doi.org/10.1063/1.4942802.

(34) Pudasaini, P. R.; Oyedele, A.; Zhang, C.; Stanford, M. G.; Cross, N.; Wong, A. T.; Hoffman, A. N.; Xiao, K.; Duscher, G.; Mandrus, D. G.; et al. High-Performance Multilayer WSe2 Field-Effect Transistors with Carrier Type Control. *Nano Res.* **2018**, *11* (2), 722–730. https://doi.org/10.1007/s12274-017-1681-5.

(35) Yang, T.; Zheng, B.; Wang, Z.; Xu, T.; Pan, C.; Zou, J.; Zhang, X.; Qi, Z.; Liu, H.; Feng, Y.; et al. Van Der Waals Epitaxial Growth and Optoelectronics of Large-Scale WSe2/SnS2 Vertical Bilayer P–n Junctions. *Nat. Commun.* **2017**, *8* (1), 1906. https://doi.org/10.1038/s41467-017-02093-z.

Chapter 6 Few-Layer MoS_2/Glassy-Graphene Heterostructures for Transparent Photodetectors

6.1 Research Background and Result Overview

6.1.1 Research background

The research focused on atomically thin two-dimensional (2D) materials, such as black phosphorene, transition metal dichalcogenides (TMDs), silicene, germanene, *etc*., has been triggered since the first achievement of mechanically prepared graphene nanosheets in 2004.[1-3] Various layered 2D semiconducting materials have been attained using experimental methods since then and more will be synthesised or theoretically predicted in the near future.[3] Graphene, as the most typical 2D material with superior electrical and optical properties in 2D family, exhibits prospective for future flexible electronics,

nanoelectronic and photonic applications.[4,5] In parallel with the extensive efforts devoted to studying pristine graphene for practical use, the graphene-like materials have been gaining attentions as well.

In 2016, a kind of glassy-graphene with ultra-smooth surface in large scale (7 cm × 10 cm) was successfully synthesised by Zou *et al*., and demonstrated to be an intermediate state between pristine crystal graphene and amorphous glassy carbon, inheriting outstanding properties from both of them.[6] Large-scale 2D materials make device arrays for all-2D integrated circuits possible. Notably, glassy-graphene is much more cost-effective than graphene in terms of synthesis. Possessing excellent conductivity, mechanical flexibility, chemical inertness and good transparency, glassy-graphene thin films have great perspective in the applications of future nanoelectronics and optoelectronics fields. In addition to graphene family, MoS_2, whose bulk form has been widely studied, is another representative layered 2D material from the TMD family. MoS_2 possesses a direct bandgap of 1.8 eV for the monolayer form, which is desired for optoelectronic applications.[7,8]

As interest growing and material kinds expanding, the research on graphene and other relevant 2D materials has moved from investigating an individual material to the 2D hybrid configurations created by vertically stacking different 2D materials onto others.[9] Wet transferring layered 2D materials in liquid solution and dry transferring using stamps are the major two kinds of methods introduced for creating such structures. The resulted artificial heterojunctions, in which the stacked materials are combined together via van der Waals force, can exhibit the properties from the stacked designer materials and are stable under ambient conditions. The graphene/MoS_2 heterostructure is a representative instance and was fabricated to solar cells, phototransistors, field-effect transistors and photodetectors, showing good and stable device performance.[10-13]

Most previously reported graphene-MoS_2 heterostructures (as reported in Ref. 10 – 13) formed Schottky contact at interfaces, even though ohmic contact is a necessary condition for power-friendly integrated logic circuits and plays a significant role in the true realisation of all-2D device systems.[14,15] On the other hand, both graphene and MoS_2 are appropriate candidates for transparent optoelectronic applications. This is such a fast developing field with much aesthetic value and allows for more versatility in the design

and use of applications.[16,17] In spite of this fact, only few literatures have reported that MoS_2/graphene heterostructures were used for transparent photodetectors so far.[18] Therefore, more efforts are needed for further exploring this promising heterostructure.

6.1.2 Result overview

Herein, few-layer MoS_2/glassy-graphene heterostructures (MGH) on quartz substrates were prepared with the layer-by-layer vertical stacking technique, followed by the detailed material characterisations. Transparent photodetectors enabled by these novel van der Waals heterostructures were excited by monochromatic 405 nm, 532 nm and 656 nm laser for probing their photoresponsive features, respectively, showing apparent wavelength selectivity. Based on the photocurrent characteristic results, it is notable that the interface between MoS_2 and glassy-graphene is ohmic contact, different from the previously reported one between MoS_2 and graphene where Schottky junction was formed.[10,12] For all the photodetectors, the highest specific detectivity of 1.8×10^{10} Jones and the best photoresponsivity of 12.3 mA/W were both achieved at the photodetector enabled by the MGH with 3 layer (3L) MoS_2 as illuminated by the 532 nm laser. In the on/off photocurrent dynamics results, stable device reproducibility was demonstrated and unusual negative photoresponse under the 532 nm light was observed, which could be associated with localised states in glassy-graphene thin films.

6.2 Experimental methods

6.2.1 MGH preparation

Few-layer MGH were created by $MoS_2/SiO_2/Si$ and glassy-graphene/quartz, and both of large-scale thin films were grown by the low cost polymer-assisted deposition (PAD) method, which were carried out by Dr. Xiao Dai and Dr. Juntong Zhu from Soochow University.[6,19] The flowchart of preparing the vertically stacked heterostructure process is shown in figure 6.1. The Poly(methyl methacrylate) (PMMA) was first spin-coated on $MoS_2/SiO_2/Si$ at speed of 4000 rpm for 60 s and then it was baked at 180 °C for 2 minutes. MoS_2 thin film covered by PMMA was detached from the SiO_2/Si substrate using KOH

solution with concentration of 1 M at 80 °C, and then it was soaked into the deionised (DI) water.

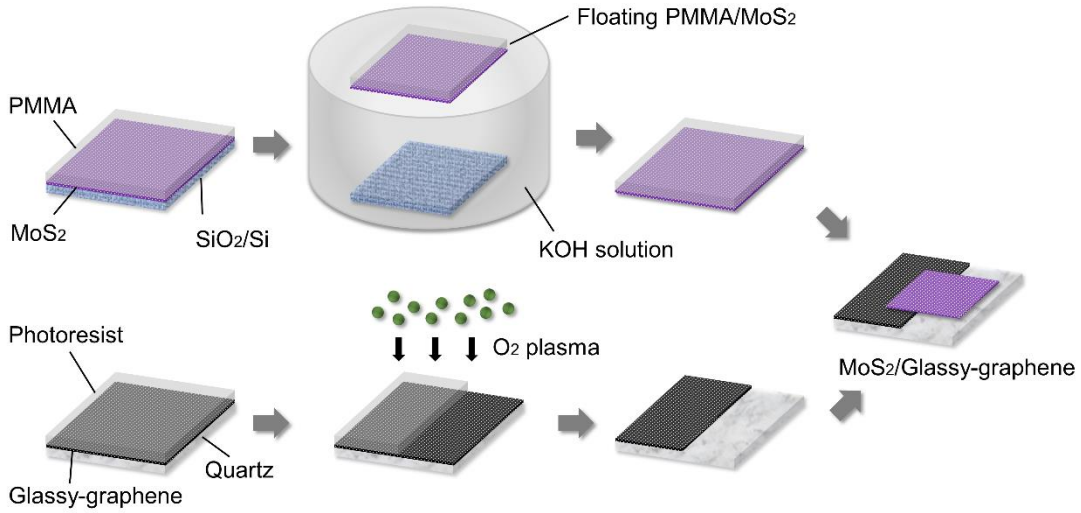

Figure 6.1 Schematic preparation flowchart of few-layer MGH. PMMA was used to protect the 2D thin films during wet transferring process.

The photoresist S1818 was spin-coated on glassy-graphene/quartz at speed of 6000 rpm for 60 s and then by baking at 115 °C for another 60 s. Treated by the standard ultraviolet photolithography processing, glassy-graphene mesa was shaped by oxygen plasma etching in the Diener Plasma Asher for 60 s. As-processed glassy-graphene thin film was employed as the substrate and transferred into the DI water to hold the MoS_2 thin film covered by PMMA. Subsequently, the MGH was baked at 180 °C for 5 minutes and then transferred into acetone to remove the residual PMMA. As shown in figure 6.2, the vertically stacked heterojunction on quartz substrate exhibits the well transparent feature.

6.2.2 Material characterisations

High resolution transmission electron microscopy (HR-TEM) was performed by Dr. Juntong Zhu from Soochow University in FEI Tecnai F20 system. Atomic force microscopy (AFM) imaging was conducted in a Veeco Dimension V Scanning Probe Microscope system using the tapping mode at ambient conditions. Optical microscopy

images were attained via the Olympus Reflection Microscope. Raman scattering measurement was carried out in a Renishaw inVia micro-Raman system equipped with a 532 nm laser as the excitation source and 1800 g/mm^2 grating via a ×50 objective lens. The power of excitation laser was set at approximately 1 mW to avoid the local heating effect.

Figure 6.2 Digital image illustrating the as-prepared MGH on quartz substrate with good transparency and in large-size, referenced by a ruler below.

6.2.3 Device fabrication

Positive photoresist S1818 was first spin-coated on MGH on quartz at the speed of 6000 rpm for 60 s and followed by baking at 115 °C for 60 s. Ti/Au contact pads with thickness of 10 nm/50 nm were created by standard ultraviolet photolithography patterning, electron-beam evaporator metallisation and the following lift-off treatment. Afterwards, the photodetectors were wire-bonded with gold wires to the logic chip carrier (LCC) for photoresponsive characterisation. Figure 6.3 displays the 3D view of the device enabled by the MGH/quartz with good transparency.

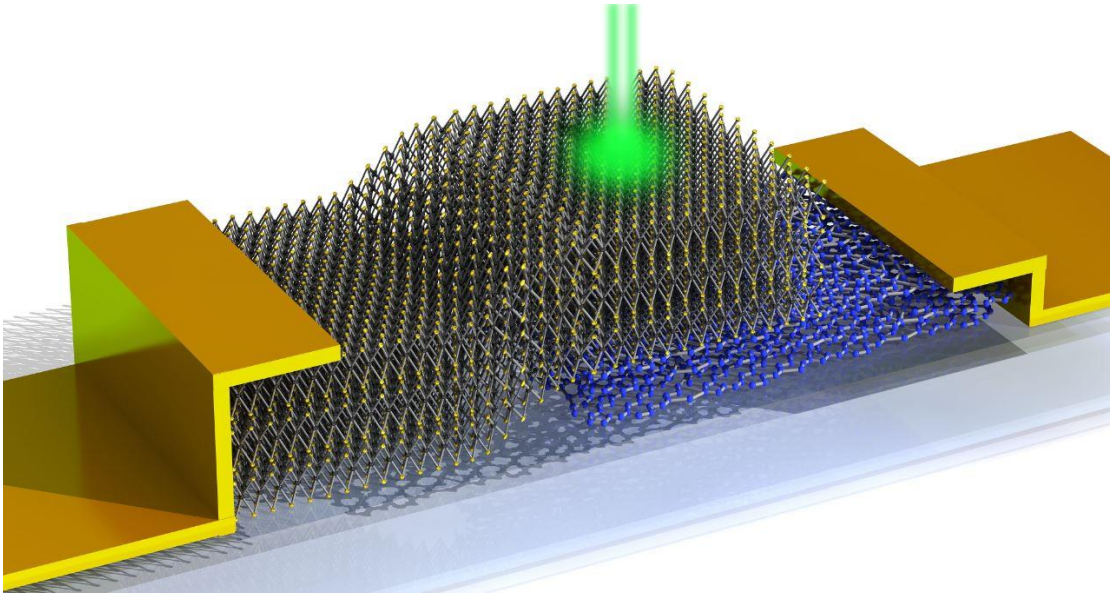

Figure 6.3 Schematic 3D diagram of the transparent device enabled by the MGH on quartz substrate.

6.2.4 Device measurement

The photoresponsive behaviour measurement under illumination was carried out with a Keithley 4200 semiconductor characterisation system equipped with monochromatic laser pointers as the illumination sources under ambient conditions. The incident optical power of laser pointers was extracted from the calibration GaAs solar cells with MGH/quartz covered. The measured practical laser power for red (656 nm), green (532 nm) and blue (405 nm) lights was set at 10.3 µW, 0.8 µW and 92.2 µW, respectively.

6.3 Results and Discussion

In figure 6.4a, both the HR-TEM image and the inset of selected-area electron diffraction (SAED) illustrate that the as-grown MoS_2 thin films possess high crystallinity. Figure 6.4b depicts the curved and mainly well-crystallised lattice structure of glassy-graphene but with a disordered plane, differing glassy-graphene from amorphous glassy carbon and pristine graphene.

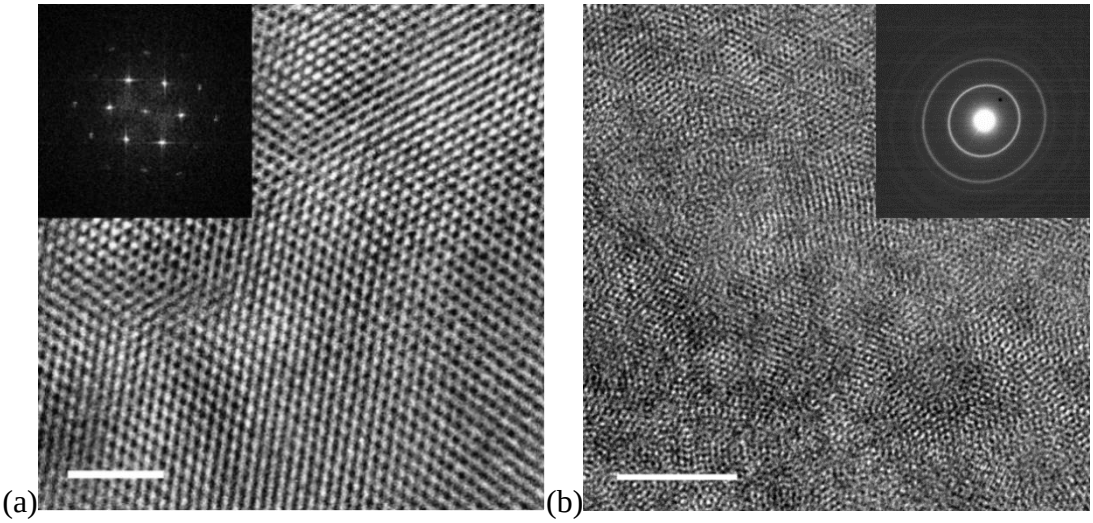

Figure 6.4 (a) HR-TEM images and SAED patterns (the inset) of the PAD-synthesised MoS_2 thin film. The scale bar is 2 nm. (b) HR-TEM images and SAED patterns (the inset) of the PAD-synthesised glassy-graphene thin film, showing the curved lattice structure. The scale bar is 5 nm.

Figure 6.5a is an optical image of the MGH/quartz obtained under the optical microscope. Due to the relatively poor optics contrast of MoS_2 and glassy-graphene thin films on quartz, only an unclear outline of the MGH is observed. AFM in combination with Raman spectroscopy were employed to characterise the as-prepared MGH properties. AFM height image was scanned at the dashed-circled domain in figure 6.5a, displayed in figure 6.5b. The surface morphology obviously depicts the stacked heterojunction domain, demonstrating the formation of the heterostructure. The inset shows the heights of MoS_2 and glassy-graphene thin films are 1.9 nm and 1 nm, respectively, indicating the trilayer nature of the MoS_2 thin films.[20,21]

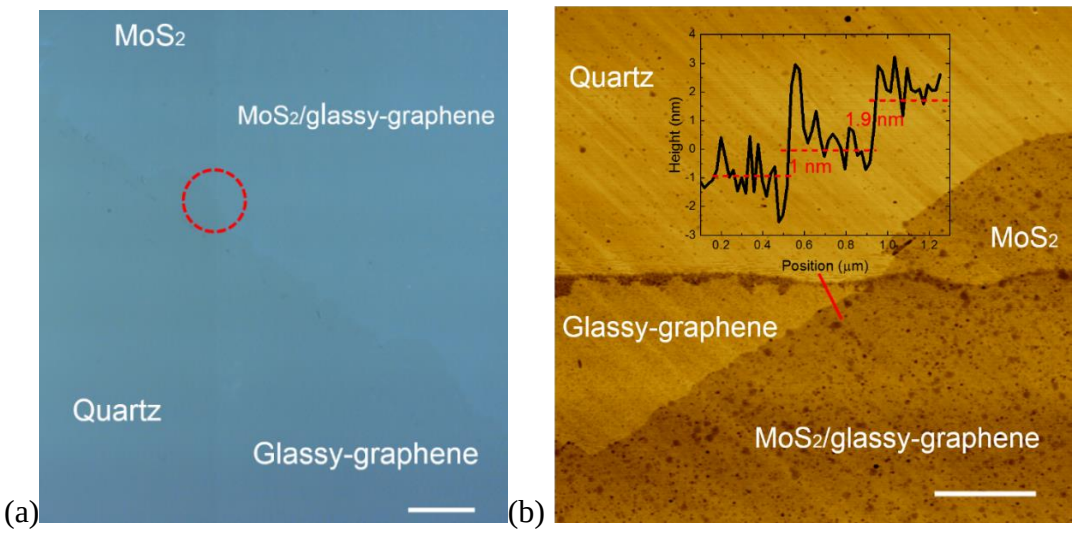

Figure 6.5 (a) Optical microscopy image of the MGH. The scale bar is 50 μm. (b) AFM height image measured at the domain labelled by the dashed red circle displayed in (a) and the inset illustrating the thickness variation along the dashed red line. The scale bar is 2 μm.

Figure 6.6 exhibits the corresponding Raman spectra of the as-prepared MGH, as-grown MoS_2 and as-grown glassy-graphene thin films, excited by a 532 nm laser. In the Raman spectrum of the MGH, the Raman-active phonon modes of both MoS_2 and glassy-graphene were resolved, further revealing the existence of the heterostructure. The two fingerprint peaks of MoS_2 in the MGH were evidently resolved at 384.8 cm^{-1} and 407.8 cm^{-1}, which corresponded to the E^1_{2g} (in-plane mode) and A_{1g} (out-of-plane mode) Raman-active phonon modes, respectively. The Raman shift difference (23 cm^{-1}) between the two Raman-active modes reveals the MoS_2 thin film possesses a three-layer configuration,[22] well consistent with the analysis result according to the AFM height result.

In comparison with the Raman signal of D, G, 2D and D + G modes attained from the as-grown glassy-graphene thin film without MoS_2 on the top (the blue curve shown in figure 6.6), those shown in the Raman spectrum of the MGH changes noticeably, including softened Raman frequency and widened full-width at half maximum (FWHM). This behaviour could be due to increased carrier concentration of the MGH, originated from the 532 nm Raman laser excited carriers.[23]

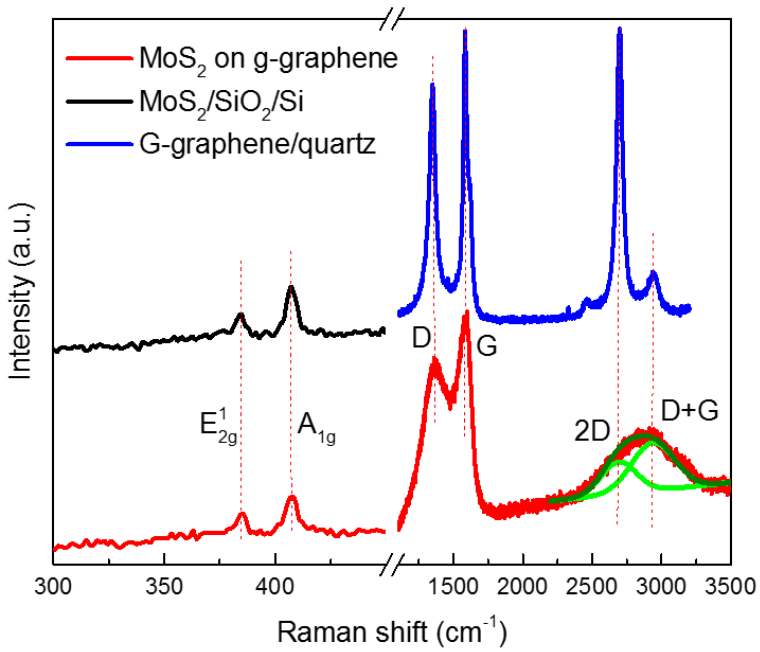

Figure 6.6 Raman spectrum of the as-prepared MGH, compared with those of the as-grown MoS_2 thin film on SiO_2/Si and glassy-graphene thin films on quartz. The Raman spectrum of the MGH was obtained at the heterostructure domain in the dashed red circle shown in figure 6.5a. The two green peaks denote fitted peaks of 2D and D + G, and the olive peak denotes the accumulative peak.

In contrast, figure 6.7a and b display the optical microscopy image, AFM surface morphology and height profile of the MGH with 9L MoS_2, respectively. With thickness increased, the MGH domain was observed clearly. The inset illustrates the thickness of glassy-graphene and MoS_2 is both 6 nm. This height of MoS_2 corresponds to approximate 9L.[20, 21] The Raman spectrum of the MGH with 9L MoS_2 is shown in figure 6.8. Obviously, the Raman peak intensity of MoS_2 thin films was strongly strengthened as the thickness increased from 3 nm to 9 nm. The Raman shift difference between the two eigen-peaks (E^1_{2g} and A_{1g} Raman modes) of MoS_2 is 24.6 cm^{-1}, revealing the approximate 9L configuration.

(a)

(b)

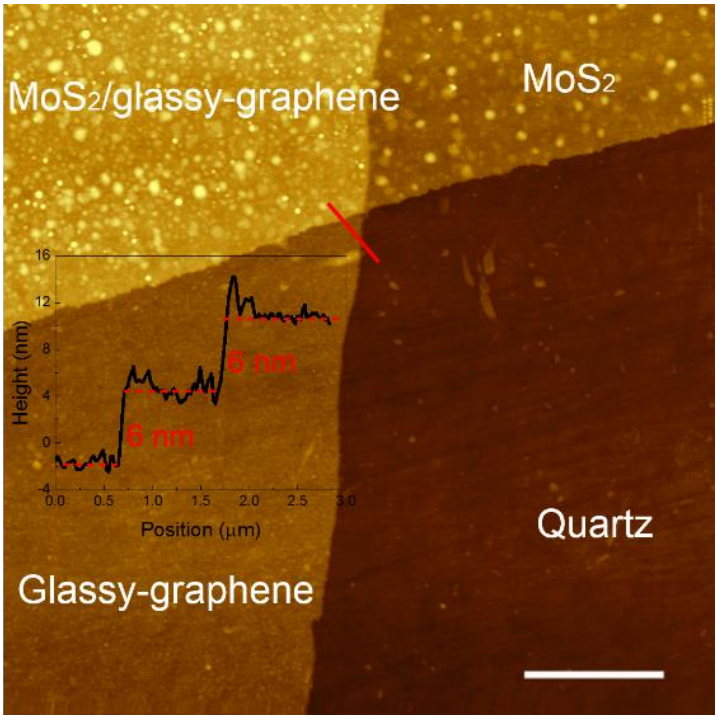

Figure 6.7 (a) Optical microscopy image of the MGH based on 9L MoS_2 thin films. The scale bar is 200 μm. (b) AFM surface morphology of the MGH and the inset showing the thickness variation along the solid red line, identify the thickness of 6 nm for both materials. The scale bar is 2 μm.

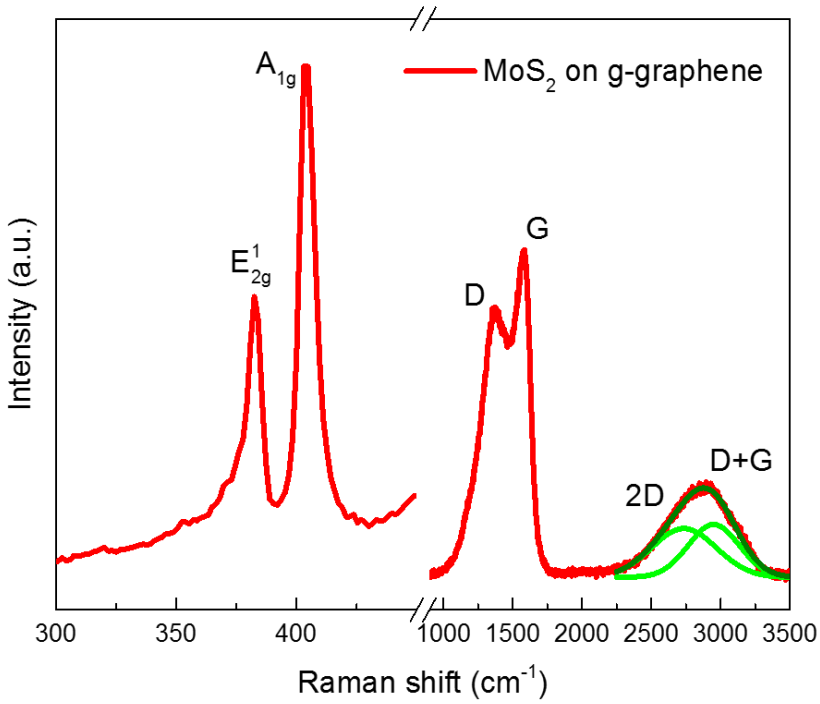

Figure 6.8 Raman spectrum of the MGH with 9L MoS_2. The two green peaks denote fitted peaks of 2D and D+G modes, and the olive peak denotes the accumulative peak. Both Raman-active phonon modes from MoS_2 and glassy-graphene were resolved at the heterojunction.

The transparent devices were electrically characterised using a semiconductor analysis system equipped with different excitation sources to explore their photoresponse performance under ambient conditions. Figure 6.9 shows the photo-induced current curve of the photodetector enabled by 3L MoS_2/1 nm glassy-graphene which was measured with the AM 1.5G one sun illumination. In comparison with the dark current curve, the photocurrent almost kept increasing by half with the varied bias voltage. Notably, both the dark current and photocurrent obtained between the respective metal electrodes at MoS_2 and glassy-graphene sides exhibit the symmetrically linear feature passing through the origin point, dependent on the applied voltage and suggesting ohmic contact features.

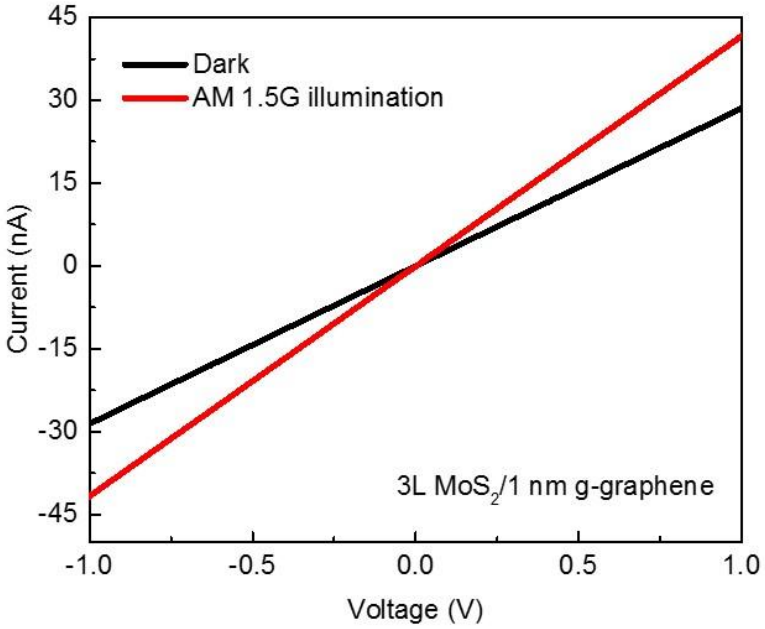

Figure 6.9 I-V curves of the photodetector enabled by the MGH with 3L MoS_2 measured in the dark and with AM 1.5G one sun illumination, respectively, showing ohmic contact behaviour.

The same current-voltage (I-V) relationship was observed at the photodetector enabled by 9L MoS_2/6 nm glassy-graphene as well (see figure 6.10). The linear behaviour reveals an ohmic contact was achieved at the interface between MoS_2 and glassy-graphene, instead of the formerly reported MoS_2/graphene heterostructure exhibiting Schottky junction features.[10-13] This behaviour can be attributed to the particularly well-aligned band structure of MGH.

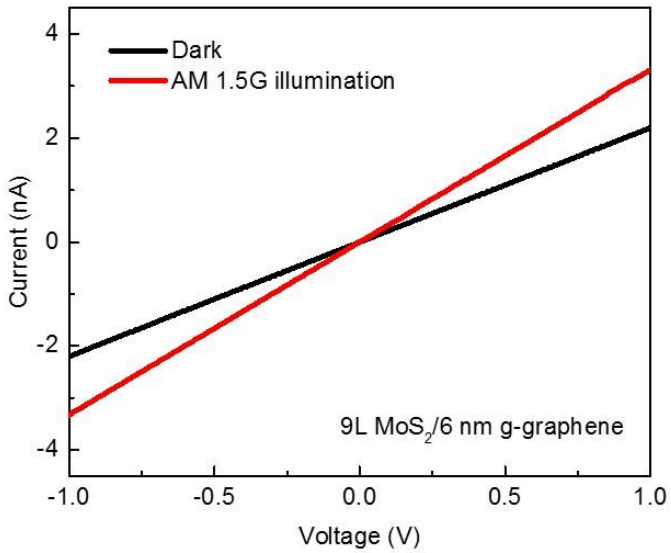

Figure 6.10 I-V curves of the photodetector enabled by the MGH with 9L MoS_2, measured in the dark and with AM 1.5G one sun illumination.

Photocurrent (defined as $I_{pc} = I_{illumination} - I_{dark}$) characteristic curves of devices illuminated by the monochromatic blue (λ: 405 nm), green (λ: 532 nm) and red (λ: 656 nm) lasers are displayed in figure 6.11 and 6.12. Because of the good transparency of devices, particularly for the device enabled by the MGH with 3L MoS_2, most of light was not absorbed by the MGH, which was either reflected or transmitted during the illumination process. As for the resulted energy loss, for example, it can reach up to ~ 94.5% for the 405 nm light illumination. Nevertheless, the three monochromatic lights were still responded with varied I_{pc} that all depends on the applied voltage values linearly. For the device enabled by the MGH with 3L MoS_2, the red laser of 532 nm exited the most photocarriers, and the largest I_{pc} value was obtained from the blue laser of 405 nm for the photodetector based on 9L MoS_2 thin film.

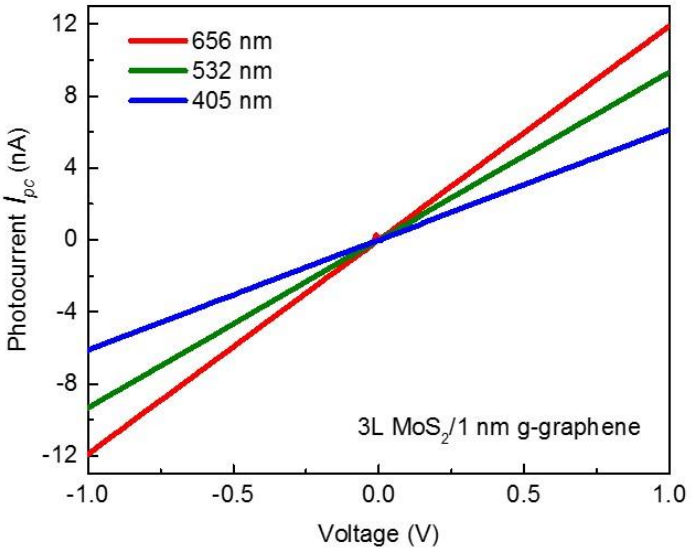

Figure 6.11 Photocurrent transfer curves of the photodetectors enabled by the MGH with 3L MoS_2 illuminated by the monochromatic blue (405 nm), green (532 nm) and red (656 nm) lights, respectively.

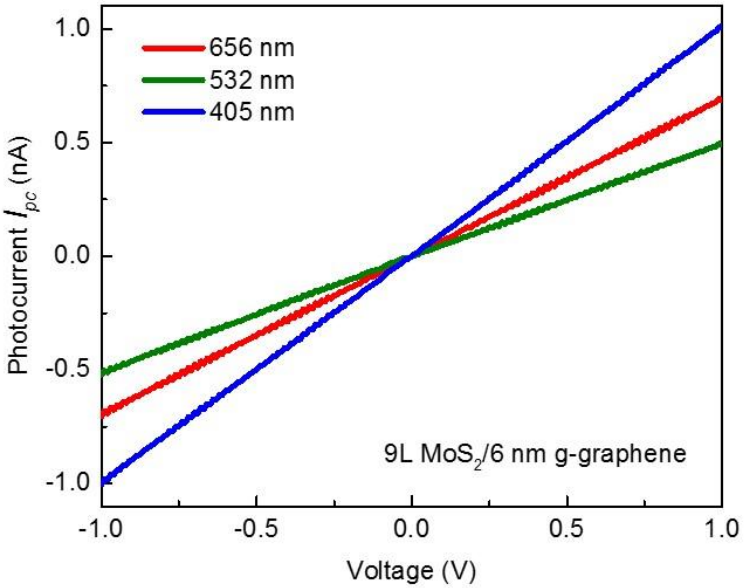

Figure 6.12 Photocurrent transfer curves of the photodetectors enabled by the MGH with 9L MoS_2 illuminated by the monochromatic blue (405 nm), green (532 nm) and red (656 nm) lights, respectively.

The respective photoresponsivity (R_A, defined as $R_A = I_{pc}/P$, here P represents incident optical power) of photodetectors was calculated, and the results were shown in figure 6.13 and 6.14 as a function of biased voltage values. The largest R_A of 12.3 mA/W was attained when the photodetector with 3L MoS_2 was excited by the green laser biased at 1 V (shown in figure 6.13). For the red and blue laser illumination, the R_A is 1.2 mA/W and 0.07 mA/W as the photodetector was applied with biased voltage of 1 V, respectively. At the similar measurement conditions, the R_A of the device is larger than that of pristine graphene nanosheet based photodetectors (0.25 mA/W),[24] single layer MoS_2 nanosheet based phototransistors (0.42 mA/W) and photosensors (1.1 mA/W).[7,25]

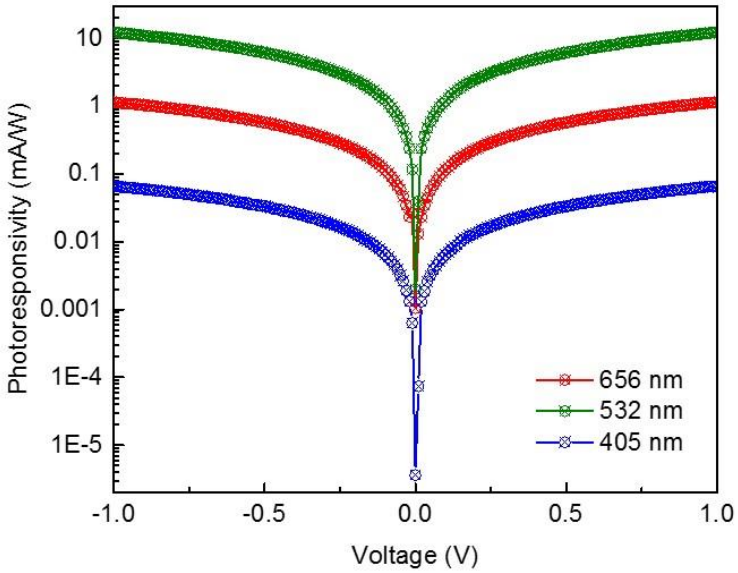

Figure 6.13 Photoresponsivity of devices enabled by the 3L MoS_2 under the monochromatic blue (405 nm), green (532 nm) and red (656 nm) light illumination, respectively, showing obvious wavelength selectivity.

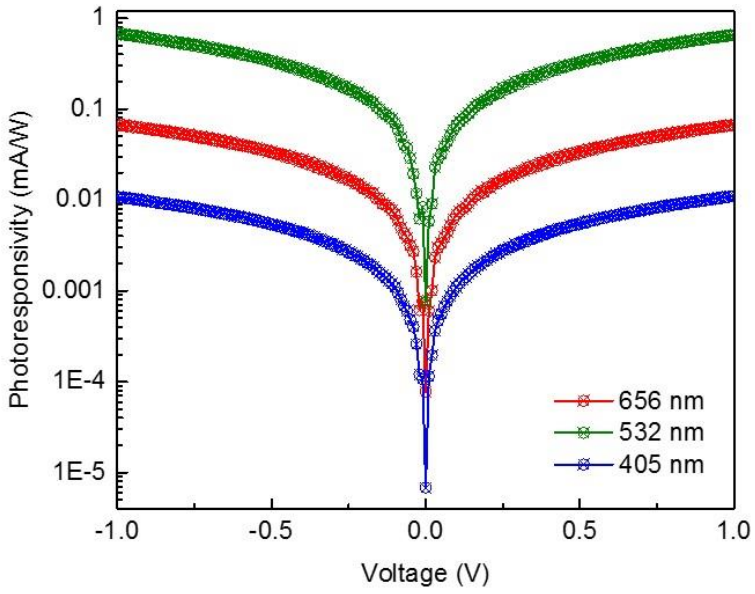

Figure 6.14 Photoresponsivity of the devices enabled by the 9L MoS_2 under the monochromatic blue (405 nm), green (532 nm) and red (656 nm) light illumination, respectively, showing obvious wavelength selectivity.

Moreover, it was pronounced that the photodetector shows changing R_A with different orders of magnitude for monochromatic light with different wavelength. This obvious wavelength selectivity property was also observed at the device with 9L MoS_2 (see figure 6.14), where the R_A is 0.65 mA/W, 0.07 mA/W and 0.01 mA/W for green, red and blue lights, respectively.

When illuminated by the 532 nm laser, both the photodetectors with different thickness exhibit the best photoresponsive capability and they are qualified for identifying 656 nm and 405 nm lights as well, realised with no gate modulation. The specific detectivity (D^*), which is another important figure of merit for photoresponse performance, is defined by the equation: $D^* = R(A/2qI_{dark})^{1/2}$. Here, A represents the active domain of the photodetector and q denotes the elementary charge. According to the obtained largest R_A, a high D^* up to 1.8×10^{10} Jones for 532 nm light illumination was achieved, comparable to the MoS_2/graphene nanosheet heterostructure based photodetectors (1.5×10^{10} Jones for 520 nm light) and multilayer MoS_2 nanosheet photodetectors ($\sim 10^{10}$ Jones for 532 nm light).[26,27]

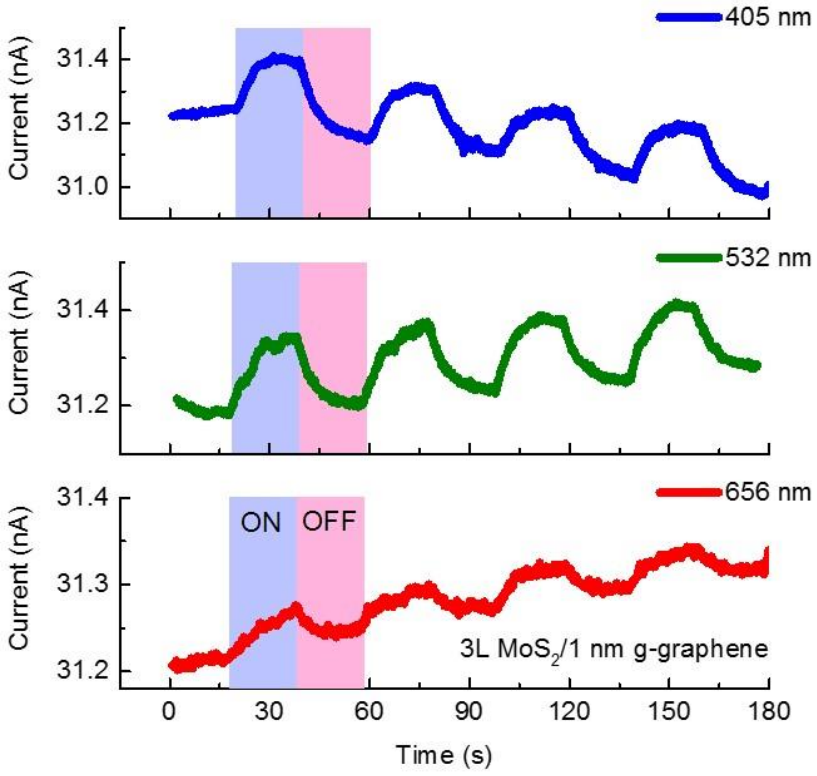

Figure 6.15 Photo-induced current on/off behaviour of the photodetectors enabled by the MGH with 3L MoS_2 under the monochromatic blue (405 nm), green (532 nm) and red (656 nm) light illumination, respectively. The biased voltage is 1 V. The time break between the each on-off photoswitching loop is 20 s.

The photo-induced current under on/off photoswitching was studied with time gap of 20 s when biased at 1 V was applied to the photodetectors, as displayed in figure 6.15 and 6.16. In figure 6.15, the photodetector responded to the monochromatic green and red lights with a rising tendency, exhibiting classical positive photoresponsive behaviour. Nevertheless, negative photoresponsive behaviour at ambient conditions, leading to reduced current value at off status, was resolved in the photodetector under the monochromatic blue light excitation. Considering the analysis of photocurrent obtained with the linear voltage sweeping (the blue IV curve plotted in figure 6.11), the photoexcited electrical conductivity of the photodetectors can either enlarge or reduce under the 405 nm light excitation, which was observed in the metal-nanoparticle low-dimensional materials and doped-graphene nanosheet photodetectors as well. [16,28] Such

behaviour could be resulted from the disorder-relevant localised states in glassy-graphene thin films and particularly evident in the low dimensional materials.[29,30]

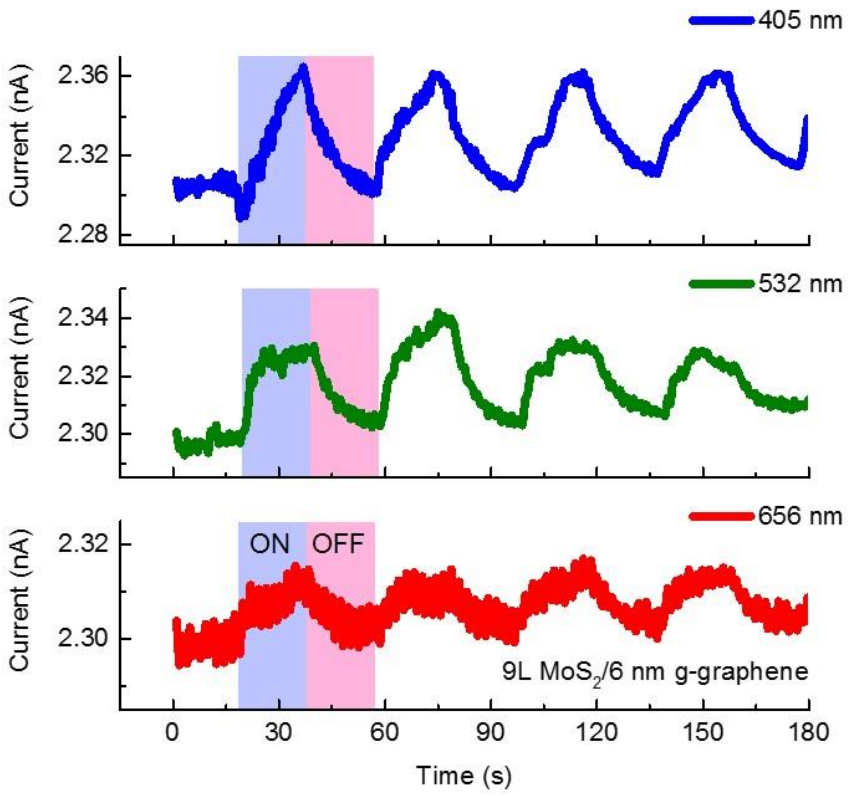

Figure 6.16 Photo-induced current on/off behaviour of the photodetectors enabled by the MGH with 9L MoS_2 under the monochromatic blue (405 nm), green (532 nm) and red (656 nm) light illumination, respectively. The biased voltage is 1 V. The time break between the each on-off photoswitching loop is 20 s.

In figure 6.16, likewise, the device shows traditional time-resolved photoresponse dynamics. The rising tendency and non-vertical rising and falling edges, on the one hand, could be due to the island domains on the surface of MoS_2 thin films (as shown in figure 6.5b) that trapped extensive photo-excited electrons.[31] On the other hand, it could originate from the surrounding or ambient influences (such as the bottom substrates, contact metals, *etc*.) on the photo-induced current dynamic cycles.[32] Figure 6.15 and 6.16 prove the stable reproducibility of the transparent photodetectors based on the MGH.

6.4 Conclusions

To sum up, novel few-layer and large-scale MGH were created and fabricated into large-scale transparent photodetectors. Wet transfer method using PMMA as the protection layer was used to prepare the 2D heterostructures. Detailed material characterisations were carried out to study this novel structure. Notably, ohmic contact formed at the junction interface between MoS_2 and glassy-graphene instead of reported traditional Schottky junction, which is of much importance for achieving true 2D device system that needs ohmic contact features. This feature was also repeated in MGH based on both 3L MoS_2 and 9L MoS_2 thin films. The photodetectors exhibited obvious wavelength selectivity regardless of large incident optical power loss due to the good transparency.

Both the devices enabled by the MGH with 3L MoS_2 and 9L MoS_2 possessed the best capability for detecting the 532 nm light. Thickness-induced impact on the device performance was also studied. The device with 3L MoS_2 showed the largest photoresponsivity of 12.3 mA/W and detectivity of 1.8×10^{10} Jones under the 532 nm light illumination. Moreover, unusual negative photoresponse was observed at the same device as illuminated by the 405 nm light. On/off photocurrent dynamics features indicated the stable reproducibility of the photodetectors.

6.5 References

(1) Novoselov, K. S.; Geim, A. K.; Morozov, S. V.; Jiang, D.; Zhang, Y.; Dubonos, S. V.; Grigorieva, I. V.; Firsov, A. A. Electric Field Effect in Atomically Thin Carbon Films. *Science.* **2004**, *306*, 666–669.

(2) Xia, F.; Wang, H.; Xiao, D.; Dubey, M.; Ramasubramaniam, A. Two-Dimensional Material Nanophotonics. *Nat. Photonics* **2014**, *8* (12), 899–907. https://doi.org/10.1038/nphoton.2014.271.

(3) Castellanos-Gomez, A. Why All the Fuss about 2D Semiconductors? *Nat. Photonics* **2016**, *10* (4), 202–204. https://doi.org/10.1038/nphoton.2016.53.

(4) Schwierz, F. Graphene Transistors. *Nat. Nanotechnol.* **2010**, *5* (7), 487–496. https://doi.org/10.1038/nnano.2010.89.

(5) Yin, Z.; Zhu, J.; He, Q.; Cao, X.; Tan, C.; Chen, H.; Yan, Q.; Zhang, H. Graphene-Based Materials for Solar Cell Applications. *Adv. Energy Mater.* **2014**, *4* (1), 1–19. https://doi.org/10.1002/aenm.201300574.

(6) Dai, X.; Wu, J.; Qian, Z.; Wang, H.; Jian, J.; Cao, Y.; Rummeli, M. H.; Yi, Q.; Liu, H.; Zou, G. Ultra-Smooth Glassy Graphene Thin Films for Flexible Transparent Circuits. *Sci. Adv.* **2016**, *2* (November), e1601574. https://doi.org/10.1126/sciadv.1601574.

(7) Yin, Z.; Li, H.; Li, H.; Jiang, L.; Shi, Y.; Sun, Y.; Lu, G.; Zhang, Q.; Chen, X.; Zhang, H. Single-Layer MoS2 Phototransistors. *ACS Nano* **2012**, *6* (1), 74–80. https://doi.org/10.1021/nn2024557.

(8) Tsai, M. L.; Su, S. H.; Chang, J. K.; Tsai, D. S.; Chen, C. H.; Wu, C. I.; Li, L. J.; Chen, L. J.; He, J. H. Monolayer MoS2 Heterojunction Solar Cells. *ACS Nano* **2014**, *8* (8), 8317–8322. https://doi.org/10.1021/nn502776h.

(9) Geim, A. K.; Grigorieva, I. V. Van Der Waals Heterostructures. *Nature* **2013**, *499* (7459), 419–425. https://doi.org/10.1038/nature12385.

(10) Tian, H.; Tan, Z.; Wu, C.; Wang, X.; Mohammad, M. A.; Xie, D.; Yang, Y.; Wang, J.; Li, L.-J.; Xu, J.; et al. Novel Field-Effect Schottky Barrier Transistors Based on Graphene-MoS2 Heterojunctions. *Sci. Rep.* **2014**, *4*, 5951. https://doi.org/10.1038/srep05951.

(11) Vabbina, P.; Choudhary, N.; Chowdhury, A.-A.; Sinha, R.; Karabiyik, M.; Das, S.; Choi, W.; Pala, N. Highly Sensitive Wide Bandwidth Photodetector Based on Internal Photoemission in CVD Grown P-Type MoS2/Graphene Schottky

Junction. *ACS Appl. Mater. Interfaces* **2015**, *7* (28), 15206–15213. https://doi.org/10.1021/acsami.5b00887.

(12) Kwak, J. Y.; Hwang, J.; Calderon, B.; Alsalman, H.; Munoz, N.; Schutter, B.; Spencer, M. G. Electrical Characteristics of Multilayer MoS2 FETs with MoS 2/graphene Heterojunction Contacts. *Nano Lett.* **2014**, *14*, 4511–4516. https://doi.org/10.1021/nl5015316.

(13) Yu, W. J.; Li, Z.; Zhou, H.; Chen, Y.; Wang, Y.; Huang, Y.; Duan, X. Vertically Stacked Multi-Heterostructures of Layered Materials for Logic Transistors and Complementary Inverters. *Nat. Mater.* **2013**, *12* (3), 246–252. https://doi.org/10.1038/nmat3518.

(14) Allain, A.; Kang, J.; Banerjee, K.; Kis, A. Electrical Contacts to Two-Dimensional Semiconductors. *Nat. Mater.* **2015**, *14* (12), 1195–1205. https://doi.org/10.1038/nmat4452.

(15) Jena, D.; Banerjee, K.; Xing, G. H. 2D Crystal Semiconductors: Intimate Contacts. *Nat. Mater.* **2014**, *13* (12), 1076–1078. https://doi.org/10.1038/nmat4121.

(16) Liu, N.; Tian, H.; Schwartz, G.; Tok, J. B. H.; Ren, T. L.; Bao, Z. Large-Area, Transparent, and Flexible Infrared Photodetector Fabricated Using P-N Junctions Formed by N-Doping Chemical Vapor Deposition Grown Graphene. *Nano Lett.* **2014**, *14* (7), 3702–3708. https://doi.org/10.1021/nl500443j.

(17) Zhang, H.; Jenatsch, S.; De Jonghe, J.; Nüesch, F.; Steim, R.; Véron, A. C.; Hany, R. Transparent Organic Photodetector Using a near-Infrared Absorbing Cyanine Dye. *Sci. Rep.* **2015**, *5*, 9439. https://doi.org/10.1038/srep09439.

(18) Xu, H.; Wu, J.; Feng, Q.; Mao, N.; Wang, C.; Zhang, J. High Responsivity and Gate Tunable Graphene-MoS2 Hybrid Phototransistor. *Small* **2014**, *10* (11), 2300–2306. https://doi.org/10.1002/smll.201303670.

(19) Zhu, J.; Wu, J.; Sun, Y.; Huang, J.; Xia, Y.; Wang, H.; Wang, H.; Wang, Y.; Yi, Q.; Zou, G. Thickness-Dependent Bandgap Tunable Molybdenum Disulfide Films for Optoelectronics. *RSC Adv.* **2016**, *6* (112), 110604–110609. https://doi.org/10.1039/C6RA22496B.

(20) Radisavljevic, B.; Radenovic, A.; Brivio, J.; Giacometti, V.; Kis, A. Single-Layer MoS2 Transistors. *Nat. Nanotechnol.* **2011**, *6* (3), 147–150. https://doi.org/10.1038/nnano.2010.279.

(21) Tsai, D.-S.; Liu, K.-K.; Lien, D.-H.; Tsai, M.-L.; Kang, C.-F.; Lin, C.-A.; Li, L.-

J.; He, J.-H. Few Layer MoS2 with Broadband High Photogain and Fast Optical Switching for Use in Harsh Environments. *ACS Nano* **2013**, *7* (5), 3905–3911. https://doi.org/10.1021/nn305301b.

(22) Li, H.; Zhang, Q.; Yap, C. C. R.; Tay, B. K.; Edwin, T. H. T.; Olivier, A.; Baillargeat, D. From Bulk to Monolayer MoS2: Evolution of Raman Scattering. *Adv. Funct. Mater.* **2012**, *22* (7), 1385–1390. https://doi.org/10.1002/adfm.201102111.

(23) Das, a; Pisana, S.; Chakraborty, B.; Piscanec, S.; Saha, S. K.; Waghmare, U. V; Novoselov, K. S.; Krishnamurthy, H. R.; Geim, a K.; Ferrari, a C.; et al. Monitoring Dopants by Raman Scattering in an Electrochemically Top-Gated Graphene Transistor. *Nat. Nanotechnol.* **2008**, *3* (4), 210–215. https://doi.org/10.1038/nnano.2008.67.

(24) Freitag, M.; Low, T.; Xia, F. N.; Avouris, P. Photoconductivity of Biased Graphene. *Nat. Photonics* **2013**, *7* (1), 53–59. https://doi.org/10.1038/nphoton.2012.314.

(25) Perea-López, N.; Lin, Z.; Pradhan, N. R.; Iñiguez-Rábago, A.; Laura Elías, A.; McCreary, A.; Lou, J.; Ajayan, P. M.; Terrones, H.; Balicas, L.; et al. CVD-Grown Monolayered MoS 2 as an Effective Photosensor Operating at Low-Voltage. *2D Mater.* **2014**, *1* (1), 011004. https://doi.org/10.1088/2053-1583/1/1/011004.

(26) Rathi, S.; Lee, I.; Lim, D.; Wang, J.; Ochiai, Y.; Aoki, N.; Watanabe, K.; Taniguchi, T.; Lee, G.-H.; Yu, Y.-J.; et al. Tunable Electrical and Optical Characteristics in Monolayer Graphene and Few-Layer MoS2 Heterostructure Devices. *Nano Lett.* **2015**, *15* (8), 5017–5024. https://doi.org/10.1021/acs.nanolett.5b01030.

(27) Choi, W.; Cho, M. Y.; Konar, A.; Lee, J. H.; Cha, G. B.; Hong, S. C.; Kim, S.; Kim, J.; Jena, D.; Joo, J.; et al. High-Detectivity Multilayer MoS2 Phototransistors with Spectral Response from Ultraviolet to Infrared. *Adv. Mater.* **2012**, *24* (43), 5832–5836. https://doi.org/10.1002/adma.201201909.

(28) Nakanishi, H.; Bishop, K. J. M.; Kowalczyk, B.; Nitzan, A.; Weiss, E. A.; Tretiakov, K. V; Apodaca, M. M.; Klajn, R.; Stoddart, J. F.; Grzybowski, B. A. Photoconductance and Inverse Photoconductance in Films of Functionalized Metal Nanoparticles. *Nature* **2009**, *460* (7253), 371–375. https://doi.org/10.1038/nature08131.

(29) Biswas, C.; Güneş, F.; Loc, D. D.; Lim, S. C.; Jeong, M. S.; Pribat, D.; Lee, Y. H. Negative and Positive Persistent Photoconductance in Graphene. *Nano Lett.* **2012**, *12* (12), 6505–6505. https://doi.org/10.1021/nl303926y.

(30) Liao, M.; Koide, Y.; Alvarez, J.; Imura, M.; Kleider, J. P. Persistent Positive and Transient Absolute Negative Photoconductivity Observed in Diamond Photodetectors. *Phys. Rev. B - Condens. Matter Mater. Phys.* **2008**, *78* (4), 1–9. https://doi.org/10.1103/PhysRevB.78.045112.

(31) Dolui, K.; Rungger, I.; Sanvito, S. Origin of the N-Type and P-Type Conductivity of MoS2 Monolayers on a SiO2 Substrate. *Phys. Rev. B - Condens. Matter Mater. Phys.* **2013**, *87* (16), 1–7. https://doi.org/10.1103/PhysRevB.87.165402.

(32) Lopez-Sanchez, O.; Lembke, D.; Kayci, M.; Radenovic, A.; Kis, A. Ultrasensitive Photodetectors Based on Monolayer MoS2. *Nat. Nanotechnol.* **2013**, *8* (7), 497–501. https://doi.org/10.1038/nnano.2013.100.

Chapter 7 Conclusions and Future Work

7.1 Summary

As presented in the former chapters, research focused on molecular beam epitaxy (MBE) growth, material characterisations, device fabrication and device measurements for 2D materials and their corresponding nanoelectronic and optoelectronic applications has been carried out systematically. The studied 2D materials contain glassy-graphene thin films, black phosphorene quantum dots (BPQDs), $MoS_{2(1-x)}Se_{2x}$, WSe_2 and MoS_2/glassy-graphene van der Waals heterostructures, and their device applications include nanoscale photodetectors, phototransistors and field-effect transistors (FETs). The corresponding obtained results presented in this thesis are summarised below.

Firstly, few-layer BPQDs were grown on Si substrates directly using the MBE method for the first time, which was performed in the MBE system based in the department of electronic and electrical engineering at UCL. Epitaxial growth of BPQDs with phase transition from white phosphorus was performed on both Si(111) and Si(100), and the

full deoxidization for the substrates to remove the native surface oxides was carried out at 20 °C and 15 °C, respectively. Systematic material characterisations were performed to demonstrate the formation of few-layer BPQDs on Si substrates. The obtained atomic force microscopy (AFM) images revealed that the BPQDs on Si(111) exhibited an average radius of 27.5 ± 5 nm and height of 3.1 ± 0.6 nm, formed in a uniform pyramid configuration, and the edge steps on the Si(111) surface were the preferred sites for BPQD crystallisation. In contrast, AFM results indicated that the BPQDs on non-deoxidized Si(100) were distributed densely and randomly with an average radius between 8 and 14 nm and height between 1 and 2 nm. This was caused by the absence of surface steps on Si(100) with native oxides covered. The ambient condition induced property degradation of BPQDs was also studied by exposing the samples to air for more than 6 months.

Secondly, self-powered and high-performance phototransistors enabled by the spatially bandgap-graded $MoS_{2(1-x)}Se_{2x}$ homojunctions, which were synthesised by a fast and low-cost chemical solution deposition method, were studied in detail. The spatially graded bandgaps, resulted from the in-plane Se-composition and thickness gradient within a single homojunction alloy domain, were tuned from 1.83 eV to 1.73 eV, forming a homojunction with a built-in electric field. As a result, a strong and sensitive photovoltaic effect controlled by gate voltage was achieved, enabling the in-plane homojunction phototransistors to deliver a photoresponsivity of 500 mA/W under the self-powered working mode. When working under biased conditions, the devices yielded a remarkable photoresponsivity of 8.4 A/W, a specific detectivity of 2.2 $\times 10^{12}$ Jones, an ultrahigh photoconductive gain of 10^6 ~10^7, and a fast photoresponsive time in the order of ~50 ms.

Thirdly, possessing the self-assembled oxidised edge domains that inevitably generated in air, a series of back-gated FETs on SiO_2/Si substrates were fabricated and studied enabled by long-term air-exposed bilayer (BL) WSe_2 with self-passivation. Detailed material characterisations were carried out, and proved the existence of WO_x/WSe_2 heterojunctions around edges of BL WSe_2. It was noticed that the internal domains of WSe_2 nanosheets were nearly unaffected by ambient air. With air-induced WO_x passivating dangling bonds at edges of WSe_2 and acting as a buffer layer between contact metals and WSe_2 nanosheets, the FETs possessed ohmic contact and exhibited unconventional n-type behaviour from 77 K to 300 K, high conductivity up to ~ 2600

S/m, ultra-low leakage gate current as small as ~ 10^{-12} A and noticeable robustness for large bias.

Fourthly, 2D MoS_2/glassy-graphene heterostructures (MGH) on quartz were prepared with the wet layer-by-layer vertical stacking technique, and the detailed material characterisations were carried out. Transparent photodetectors enabled by these novel van der Waals heterostructures were illuminated by monochromatic 405 nm, 532 nm and 656 nm laser for studying their photoresponsive features, respectively, showing noticeable wavelength selectivity for visible lights. Based on the photocurrent characteristic results, it is notable that the interface between MoS_2 and glassy-graphene is ohmic contact, different from the previously reported one between MoS_2 and graphene where Schottky junction was formed. The highest specific detectivity of 1.8×10^{10} Jones and the best photoresponsivity of 12.3 mA/W were achieved. In the on/off switched photocurrent dynamics results, stable device reproducibility was obtained and unusual negative photoresponse under the 532 nm light was observed, which could be relevant to the localised states in glassy-graphene thin films.

7.2 Future work

2D layered metal dichalcogenides (MDs), such as MoS_2, WSe_2, SnS_2, $SnSe_2$, *etc*., are an emerging class of materials with intriguing electrical features and a broadband absorption from the ultraviolet (UV) to visible (VIS) to near-infrared (NIR) spectral region, making them highly attractive both for fundamental studies of growth mechanisms and novel physical properties and for electronics and optoelectronics applications[1-3]. These atomically thin nanoflakes exhibit strong light-matter coupling and thickness-dependent band structures. Typically, the bandgap of MoS_2 gets smaller when the thickness increases from monolayer (1.8 eV) to bulk (1.2 eV), and oppositely, the bandgap of SnS_2 gets larger from monolayer (2.1 eV) to bulk (2.3 eV)[4,5]. Recently, to achieve high performance devices to duplicate Si-based ones, bandgap engineering technique has been applied to MDs. This has been realised by fabricating vertical and lateral heterostructures, such as exfoliated-restacked $MoTe_2/MoS_2$ and epitaxially-grown in-plane WS_2-$MoSe_2$, even though they are involved with complicated fabrication and there exist abrupt band structures.[2,6]

Indeed, 2D ternary MDs, $MX_{2(1-x)}Y_{2x}$ ($0 \leq x \leq 1$), with spatially graded composition of element Y in the same parent nanoflake, ideally form a homojunction that possesses continuously tuned band structures and thus offer great flexibility in terms of changing their electronic properties. For instance, Group VI metal based MD $SnS_{2(1-x)}Se_{2x}$ is expected to show a gradually tunable bandgap within a single domain from 2.1 eV (x =0, pristine SnS_2) to 1.0 eV (x = 1, pristine $SnSe_2$) by *in-situ* varying the Se content.[5,7-9] Being earth-abundant and eco-friendly, this ternary MD is particularly suitable for sustainable applications.

For the transition metal based MD like $MoS_{2(1-x)}Se_{2x}$, it is expected to show a spatially graded bandgap from 1.9 eV (x= 0, pristine MoS_2) to 1.5 eV (x=1, pristine $MoSe_2$) by *in-situ* varying the Se composition proportion, which is very desirable for use in tunable wavelength photodetectors. Moreover, these in-plane graded homojunctions grown by one-step processing can be an innovative technology to achieve what can be accomplished in either Si or III-V material systems. Nonetheless, the synthesis for such as-grown graded homojunctions, particularly in large scale, is barely studied. To date, the involved growth mechanisms, including doped-atom substitution process, crystal defects induced impacts on the crystallisation, *etc*., still remain unexplored.

In addition to inspire bandgap engineering, the ability of synthesising 2D in-plane homojunctions in a given $MX_{2(1-x)}Y_{2x}$ not only opens up a novel avenue for device engineering at the atomistic scale but also shows the potential to revolutionise electronics and optoelectronics applications, especially considering the rapid development of the Internet of Things (IoT). Notably, fuelled by the huge global market value of IoT, the demand for flexible electronics (FE) is ever-increasing.[10,11] Phototransistors are critical to colour imaging, optical communication, environmental monitoring and security surveillance, and thus the essential components of complex logic building blocks in integrated multistage circuits and FE.

Thanks to the outstanding properties, such as atomic scale thickness, transparency, flexibility, good conductivity, tunable broadband absorption, *etc*., these 2D ternary MDs will come into play for the flexible phototransistors and potentially for the self-powered flexible devices resulted from the built-in electric fields in the homojunctions. In terms of successful large scale synthesis, it is expected to fabricate ternary MD phototransistor

arrays for the promising use of integrated FE, such as flexible display, flexible sensors, flexible digital optoelectronic chips, *etc*., as depicted in Figure 7.1. Therefore, the integrated FE technology based on novel 2D crystals is to be explored and flexible phototransistor array fabrication is planned to be carried out.

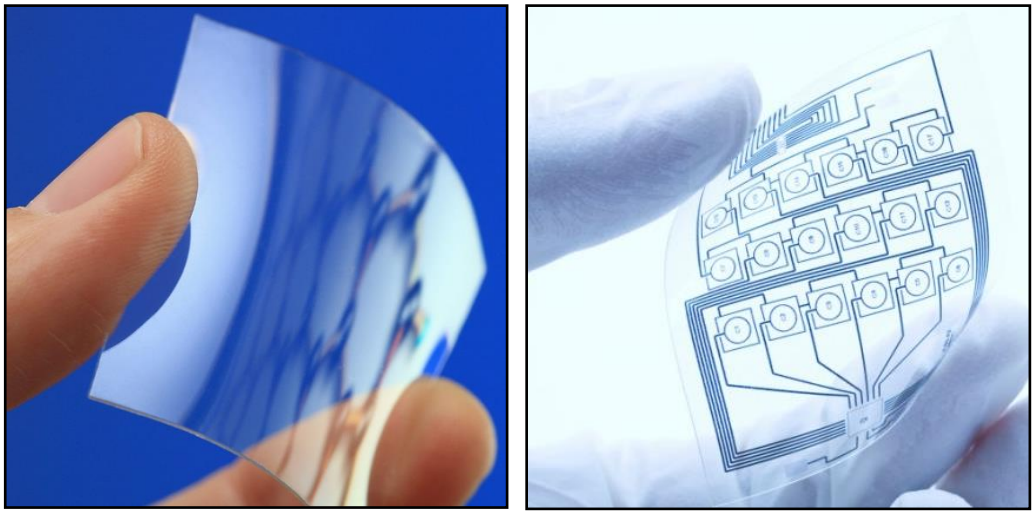

Figure 7.1 An example of (left) the 2D material on flexible substrate and (right) the flexible devices and circuits based on the 2D material. Reprint with no permission required: https://genesisnanotech.wordpress.com/2015/02/02/graphene-displays-clear-prospects-for-flexible-electronics-u-of-manchester/, https://www.nist.gov/image/flexible-printed-electric-circfrontjpg.

A single phototransistor based on as-grown materials on a conventional (300 nm) SiO_2/Si substrate will be firstly fabricated as the reference to study the processing recipes and device performance, and then to arrays on flexible polyethylene terephthalate (PET) substrates. SiO_2/Si and PET substrates will be purchased from the commercial supplier directly. All the involved device fabrication will be carried out in the cleanroom of London Centre for Nanotechnology (LCN). This work plan contains the following four tasks.

Task 1 *Fabricating phototransistors on SiO_2/Si substrates and further optimisation.*

The single and array-layout phototransistors with back gate will be correspondingly studied in this task. The specific photomask will be designed and ordered for creating device arrays. Conventional photolithography processing, followed by the metallisation will be performed to define the drain and source electrodes. In addition, different metal contact, such as Ti/Au, Ni/Au and Cr/Au, induced impacts on device performance will be studied, which is expected to obtain varied electrical conductivity, rectifying features and carrier mobility.

Task 2 *Transferring ternary MDs nanoflakes onto flexible PET substrates.*

As-grown MDs will be transferred onto target polyethylene terephthalate (PET) substrates using a wet transfer technique, in which Poly(methyl methacrylate) (PMMA) will be used as the carrier and the substrates will be etched away efficiently in KOH solution. The objective of this task is to obtain flat and smooth large scale MD nanoflakes on PET substrates, which is an important factor for achieving high-performance of phototransistors. Therefore, this task is expected to be carried out properly to optimise the attained material quality. Afterwards, material characterisations, including Raman spectroscopy, AFM, transmittance and spectral absorption test will be performed.

Task 3 *Fabricating phototransistor arrays on PET substrates and further optimisation.*

This part work will be carried out based on the previous experiment focused on the fabrication on SiO_2/Si substrates but top gate will be used instead. Conventional photolithography processing and the subsequent metallisation and dielectric layer deposition will be further optimised to fit the fabrication on flexible substrates.

Task 4 *Measuring optoelectronic performance of devices both on SiO_2/Si and PET substrates.*

Device performance measurement will be performed based in the Back End Lab in LCN. The Keithley 4200 is equipped with a tunable laser source from UV to NIR, which will be used to characterise the electrical and photoresponsive behaviour of flexible phototransistors. Bending radius and times induced impacts on the performance will also be studied.

7.3 References

(1) Manzeli, S.; Ovchinnikov, D.; Pasquier, D.; Yazyev, O. V.; Kis, A. 2D Transition Metal Dichalcogenides. *Nat. Rev. Mater.* **2017**, *2*, 17033. https://doi.org/10.1038/natrevmats.2017.33.

(2) Novoselov, K. S.; Mishchenko, A.; Carvalho, A.; Castro Neto, A. H. 2D Materials and van Der Waals Heterostructures. *Science* **2016**, *353* (6298), 9439. https://doi.org/10.1126/science.aac9439.

(3) Xie, C.; Mak, C.; Tao, X.; Yan, F. Photodetectors Based on Two-Dimensional Layered Materials Beyond Graphene. *Adv. Funct. Mater.* **2017**, *27* (19), 1603886. https://doi.org/10.1002/adfm.201603886.

(4) Roy, K.; Padmanabhan, M.; Goswami, S.; Sai, T. P.; Ramalingam, G.; Raghavan, S.; Ghosh, A. Graphene-MoS2 Hybrid Structures for Multifunctional Photoresponsive Memory Devices. *Nat. Nanotechnol.* **2013**, *8* (11), 826–830. https://doi.org/10.1038/nnano.2013.206.

(5) Huang, Y.; Sutter, E.; Sadowski, J. T.; Cotlet, M.; Monti, O. L. A.; Racke, D. A.; Neupane, M. R.; Wickramaratne, D.; Lake, R. K.; Parkinson, B. A.; et al. Tin Disulfide-an Emerging Layered Metal Dichalcogenide Semiconductor: Materials Properties and Device Characteristics. *ACS Nano* **2014**, *8* (10), 10743–10755. https://doi.org/10.1021/nn504481r.

(6) Zhang, W.; Wang, Q.; Chen, Y.; Wang, Z.; Lee, A. T. S. Van Der Walls Stacked 2D Layered Materials for Optoelectronics. *2D Mater.* **2016**, *3* (2), 022001. https://doi.org/10.1088/2053-1583/3/2/022001.

(7) Pei, T.; Bao, L.; Wang, G.; Ma, R.; Yang, H.; Li, J.; Gu, C.; Pantelides, S.; Du, S.; Gao, H. J. Few-Layer SnSe2 Transistors with High On/off Ratios. *Appl. Phys. Lett.* **2016**, *108* (5), 053506. https://doi.org/10.1063/1.4941394.

(8) Su, Y.; Ebrish, M. A.; Olson, E. J.; Koester, S. J. SnSe2 Field-Effect Transistors with High Drive Current. *Appl. Phys. Lett.* **2013**, *103* (26), 263104. https://doi.org/10.1063/1.4857495.

(9) Pan, T. S.; De, D.; Manongdo, J.; Guloy, A. M.; Hadjiev, V. G.; Lin, Y.; Peng, H. B. Field Effect Transistors with Layered Two-Dimensional SnS2-xSex Conduction Channels: Effects of Selenium Substitution. *Appl. Phys. Lett.* **2013**, *103* (9), 093108. https://doi.org/10.1063/1.4819072.

(10) Pu, J.; Funahashi, K.; Chen, C.-H.; Li, M.-Y.; Li, L.-J.; Takenobu, T. Highly

Flexible and High-Performance Complementary Inverters of Large-Area Transition Metal Dichalcogenide Monolayers. *Adv. Mater*. **2016**, *28*, 4111–4119. https://doi.org/10.1002/adma.201503872.

(11) Nassar, J. M.; Khan, S. M.; Villalva, D. R.; Nour, M. M.; Almuslem, A. S.; Hussain, M. M. Compliant Plant Wearables for Localized Microclimate and Plant Growth Monitoring. *npj Flex. Electron.* **2018**, *2* (1), 24. https://doi.org/10.1038/s41528-018-0039-8.